PIEZOELECTRIC ENERGY HARVESTING FROM WIND-INDUCED FLUTTER

A thesis submitted in fulfilment of the requirements for the degree of
Doctor of Philosophy

Arvind Deivasigamani
B.Tech.

School of Aerospace, Mechanical and Manufacturing Engineering
College of Science, Engineering and Health
RMIT University
Melbourne, Australia
September, 2014

To a few special people, whose sacrifices, free-flowing love and emotional strength have helped me complete this work.

Declaration

I certify that except where due acknowledgements have been made, the work is that of the author alone; the work has not been submitted previously, in whole or in part, to qualify for any other academic award; the content of the thesis is the result of work which has been carried out since the official commencement date of the approved research program; and, any editorial work, paid or unpaid, carried out by a third party is duly acknowledged.

Arvind Deivasigamani

Friday the 26th of September, 2014

Acknowledgments

The author gratefully acknowledges his parents for all their support, care and concern. Without them, this work would have remained as a dream. The author would also like to thank his brother and sister-in-law for their support at home during the course of this research.

Prof. Sabu John and Prof. Simon Watkins, primary and secondary supervisors respectively, have imparted precious knowledge and wisdom during the course of this research. The useful advice and suggestions provided by them will never be forgotten. The author is eternally gratefully for all their support and guidance.

This research was funded through an Australian Research Council (ARC) Linkage Grant (No.: LP100200034) in conjunction with Fabrics and Composites Science and Technology (FCST) Pty. Ltd. The author would like to heartily thank ARC and Dr. Floreana Coman, the Managing Director of FCST, for the financial support provided.

As a part of this Linkage Grant, a complementary research work was conducted by Jesse M. McCarthy. His constant support during the experiments, and significant contributions in the computational analysis presented here were very valuable. The author would like to sincerely thank him for his efforts and help.

The author would like to thank Mr. Gilbert Atkins and Mr. Sebastian Naselli, technical staff at RMIT University, for their support and guidance in designing the testing rigs and electrical circuits respectively.

The author would like to sincerely thank Mr. Phred Petersen from the RMIT University School of media and communication for his assistance in capturing the smoke-wire flow visualization videos.

Last but not the least; the author would like to thank the Almighty for Everything.

Abstract

Energy harvesting has gained importance over the last two decades due to the depletion of fossil fuels. Renewable resources such as solar, wind and ocean thermal have been explored and put to use for different applications across the world. Although these renewable energy resources can help generate significant amounts of power, most of these resources do not help in developing a self-sustaining urban environment. Devices like windmills are increasingly being subjected to objections from environmental, health and housing development groups on grounds of avian casualties from turbine blade strike and noise generated from these rotary systems.

Piezoelectric materials have been used to generate small amounts of electricity from mechanical pressure and vibration. Although these piezoelectric materials are extensively used for microbalances, sound detection, high frequency generation and Structural Health Monitoring (SHM), researchers have recently utilised these piezoelectric materials for energy harvesting from vibrations produced in machines and environment.

The purpose of this work was to develop a scalable energy harvesting system for use in an urban environment to power Ultra Low Power (ULP) devices like sensors and LED lights. In this regard, a "leaf and stalk" construct was investigated to harvest energy from wind-induced flutter. Fundamental Fluid Structure Interaction (FSI) studies were carried out to experimentally determine the dependence of physical properties of highly compliant cantilever beams on their flutter onset velocity and flutter frequency. The results clearly indicated the variation of flutter characteristics with respect to physical properties of the cantilever beam. The results also showed that theoretical two-dimensional scaling laws for flutter frequency and flutter onset velocity can be extended to a three-dimensional beam with suitable proportionality constants. Theoretical and experimental analyses were also carried out to understand flutter characteristics of slender connected body systems consisting of a revolute hinge, when located at various positions along the beam. The results revealed that the existence of a revolute hinge aids in energy harvesting by reducing the onset velocity and that the position of hinge along the beam was critical in achieving flutter in the fundamental mode of the beam.

Several leaf-stalk configurations were experimentally tested to investigate the possibility of energy harvesting from coupled bending-torsional flutter. High-speed videos were also used to identify and differentiate the flutter modes of the configurations to validate the power output results. It was found that asymmetrical configurations, when excited by wind, were more prone to chaotic flapping, and that this reduced the average power output. Also, configurations subjected to excessive bending strains increased the power output but were more prone to fatigue and fracture.

Two similar harvesters were placed in stream-wise, cross-stream and vertical directions to identify the proximity effects of these harvesters on their power output. It was found that the power output of the downstream harvester increased by up to 40% compared to its stand-alone case, when displaced from the upstream harvester by one harvester length in the stream-wise direction. Smoke-wire flow visualization results indicated that there existed a beneficial vortex interaction between the harvesters to produce a specific phase lag at given wind speed, thereby causing an increase in the power output of the downstream harvester.

The outcomes of this research resulted in five journal papers, eight conference papers and a book chapter.

TABLE OF CONTENTS

LIST OF FIGURES

LIST OF TABLES

LIST OF SYMBOLS

P_A	Power available (μW, mW, W)
t	Time (s)
ρ_s	Density of solid (kg/m^3)
ρ_f	Density of fluid (kg/m^3)
A	Area (mm^2, cm^2, m^2)
A_{swept}	Swept area (mm^2, cm^2, m^2)
v	Velocity (m/s) or non-dimensional critical flutter speed (Chapter 3)
η_b	Betz limit
Q_m	Mechanical quality factor
k_{eff}^2	Effective electromagnetic coupling coefficient
d_{ij}	Piezoelectric charge coefficient in *ij* mode (C/N)
g_{ij}	Piezoelectric voltage coefficient in *ij* mode (Vm/N)
ε	Dielectric constant (F/m)
ε_0	Permittivity of free space (8.85 x 10^{-12} F/m)
d	Separation distance between electrodes (Chapter 2) or separation distance between harvesters (Chapter 5) (mm)
C	Theodorsen's functional (Chapter 3)
C_p	Capacitance of piezo (pF, μF)
E	Electric field strength (N/C) or Elastic modulus (MPa, GPa)
D	Electric displacement field (C/m^2)
S	Mechanical strain
T	Mechanical stress (N/m^2)
T_n	Cycle time for n^{th} cycle (Chapter 5) (s)
c	Damping coefficient (N-s/m) or mechanical compliance (m^2/N)
V	Voltage (V)
V_{RMS}	Root mean square voltage (V)
m	Mass (mg, g, kg)
I	Moment of Inertia (mm^4, m^4)
h	Thickness of beam (mm, cm, m)
l	Width of beam (mm, cm, m)
F	Input force (N)

x, y, z	Displacement in respective orthogonal directions (mm, cm, m)
M	Bending moment (N.m)
k	Spring stiffness (N/m)
ζ	Damping ratio
ω	Flutter frequency (Hz)
ω_n	Natural frequency (Hz)
ω_i	Natural frequency of i^{th} mode (Hz)
a	Acceleration (m/s^2) or offset distance (mm, cm, m) (Chapter 4)
$L(f(t))$	Laplace transform of function f
Y	Vibration amplitude (mm, cm, m)
L	Cantilever length of beam (mm, cm, m)
U	Free-stream velocity (m/s)
U_c	Critical flutter speed / Flutter onset speed (m/s)
μ	Mass ratio
R_L	Load resistance (Ω, kΩ, MΩ)
ΔP	Pressure difference (Pa)
P_{nc}	Non-circulatory pressure (Pa)
P_γ	Circulatory pressure (Pa)
$\emptyset_{nc}$	Non-circulatory velocity potential (m^2/s)
$\emptyset_\sigma$	Circulatory velocity potential (m^2/s)
σ	Circulation (m^2/s)
γ	Vortex strength (Chapter 3) or torsional power ratio (Chapter 4)
θ	Angular displacement or phase lag (deg., rad.).
η	Non-dimensional hinge position
$C_{1,2\ldots8}$	Equation coefficients (Chapter 3)
$\lambda_{1,2\ldots}$	Eigen values (Chapter 3)
λ	Normalized power output
R_i	Natural frequency ratio of i^{th} mode (Hz)
K_1	Flutter onset constant of proportionality
K_2	Flutter frequency constant of proportionality
I_p	Polar moment of inertia (mm^4, m^4)
R	Torsional rigidity (Chapter 4) (N-m/rad)
R_1	Warping rigidity (Chapter 4) (N-m/rad)

G	Shear modulus (MPa, GPa)
f_n	Frequency of n^{th} cycle (Hz)

LIST OF ACRONYMS

ABL	Atmospheric Boundary Layer
AC	Alternating Current
AWT	Aeronautical Wind Tunnel
BC	Boundary Condition
BOM	Bureau of Meteorology
DAQ	Data Acquisition
DC	Direct Current
EIE	Extraneously-Induced Excitation
FSI	Fluid Structure Interaction
HAWT	Horizontal Axis Wind Turbine
IPCC	Intergovernmental Panel on Climate Change
KDP	Potassium Dihydrogen Phosphate
LCO	Limit-Cycle Oscillations
LED	Light Emitting Diode
LHS	Left Hand Side
MFC	Macro-Fibre Composite
MIE	Movement-Induced Excitation
PIV	Particle Image Velocimetry
PVDF	Polyvinylidene Fluoride
PZT	Lead Zirconate Titanate
RHS	Right Hand Side
RMS	Root Mean Square
UDF	User Defined Functions
ULP	Ultra Low Power
VAWT	Vertical Axis Wind Turbine

Chapter 1

Introduction

1.1 Background

1.1.1 Need for sustainability

"Sustainable development is development that meets the needs of the present without compromising the ability of future generations to meet their own needs" as stated by the Brundtland Commission of the United Nations on March 20, 1987. This becomes all the more important in the field of energy resource planning. Natural energy resources like coal and petroleum are limited on earth and an excessive use of these resources have led to the energy crisis. Environmentalists, scientists and engineers have started to raise concerns, as the natural energy resources are getting depleted at a very rapid rate. Thus, it is very important to have a sustainable environment for the welfare of the future.

It is also a known fact that social harmony and economy of a nation depends on the environment. In other words, the economy is a subsystem of human society, which is itself a subsystem of the biosphere and hence, a gain in one sector is a loss from another (Porritt, 2006). This can be represented as three concentric circles as shown in Figure 1.1.

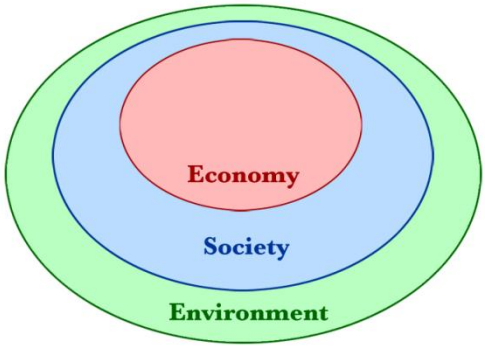

Figure 1.1: A diagram indicating the relationship between the three pillars of sustainability suggesting that both economy and society are constrained by environmental limits (Porritt, 2006).

Figure 1.2 shows that oil and coal together contribute 58% of the world's energy consumption. The growing scarcity of natural energy resources has resulted in the acute rise of fuel prices in most countries across the world. This has resulted in many countries starting

to suffer from socio-economic problems. The only solution to all these issues is to have a sustainable environment where the usage of these non-renewable resources is minimized.

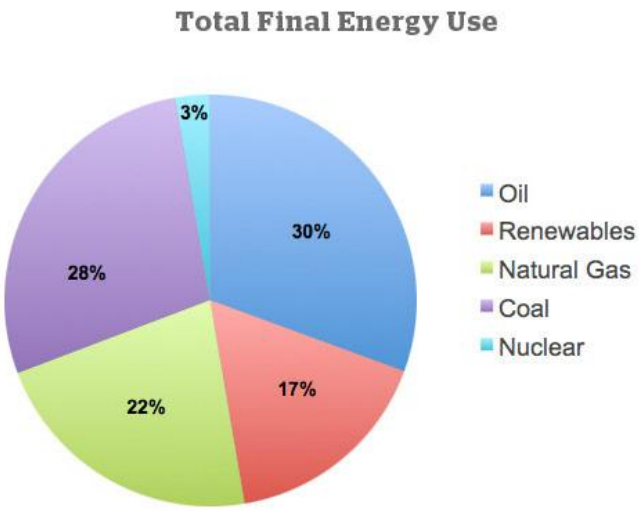

Figure 1.2. World primary energy consumption by fuel type (Cutler Cleveland, 2010).

On the other hand, global warming and climate change are of increasing concerns today, even for a common man. Due to the increasing use of fossil fuels for power generation and transportation purposes, gases like CO_2, CO and CH_4 are released into the atmosphere causing a gradual increase in the earth's temperature and depletion of the ozone layer.

Different countries have imposed various policies to control carbon emissions into the atmosphere. For example, Australia had implemented a carbon tax effective from 2012 to reduce the carbon emissions from the use of fossil fuels. Thus, in order to have a sustainable environment which suits the global economy and society; it is highly important to identify other options for power generation. Intergovernmental Panel on Climate Change (IPCC), an international organisation, releases reports every year on climate change and emphasises the extensive use of renewable energy resources.

In summary, development of a sustainable environment is very important not only for containing growing environmental issues such as global warming but also to protect the socio-economic status of countries around the world from increasing costs due to limited availability of non renewable resources such as fossil fuels.

1.1.2 Renewable energy resources

Renewable energy is the energy derived from resources which are naturally replenished unlike fossil fuels which have limited availability. It is very encouraging to note that about 16% of the global energy resources are from these renewable energy resources (REN21, 2013). However, 10% of these resources consist of biomass which is generally used for heating purposes.

Resources such as tidal, hydroelectric and geothermal energy are very location specific and are not installed in urban environments. The power generated is usually supplied to the grid to reach the urban residents. Due to the population growth and the recent development of cities across the world, the population in the cities have increased significantly. Thus, in order to avoid cabling and poling costs, self-sustaining buildings, capable of harvesting their own energy, would prove to be efficient. Thus, it is important to develop energy harvesting devices from renewable resources suitable in urban setting.

1.2 Wind energy harvesting in urban areas

Wind energy has been converted to usable energy for day-to-day activities since the 19th century. Today, there are several wind farms around the world harvesting energy from wind. However, these wind farms and windmills are usually positioned in rural areas where vast pieces of land are available. Wind energy harvesting faces a wide range of challenges when employed in urban areas.

The major issue with wind energy harvesting in urban areas is the low wind speed. The average wind speed in urban areas, closer to the ground, is usually lower than in open areas due to the existence of buildings and other man-made constructs. Therefore, the windmills have to be designed to be able to harvest energy from low wind speeds. This would require modifications in blade sizes and arrangements. Also, as the wind speed reduces, the efficiency of most windmills significantly reduces.

The other major issues usually associated with wind mills are cost effectiveness, noise and safety. Due to the low power output, the return on investment is generally low. Also, certain commercial and residential councils do not permit wind mills to be installed since the noise produced by windmills exceeds the allowable limit, and safety concerns have been raised due to the proximity of humans.

Recently, aesthetics of these windmills has become important. Councils do not generally approve conventional urban windmills as they do not fit in well with the surroundings. Thus, considering the challenges, it is essential to develop an alternative technology to harvest energy from wind in urban settings. The following section gives a brief overview of piezoelectric energy harvesting, which forms the basis of this research. The limitations of wind turbines in urban areas are explained in detail in Chapter 2.

1.3 Piezoelectric energy harvesting from fluid flow

Piezoelectric materials are special type of materials which have the ability to produce electric charge in response to applied mechanical strain. The reverse effect also holds true. These materials mechanically deform in response to applied electric charge. Piezoelectric effect in materials like quartz, topaz and rochelle salt were first discovered in 1880 by Pierre Curie and Jacques Curie. Since then, these materials have been slowly moved from laboratories to practical devices. Piezoelectric materials today are found in scientific instruments like microbalances, accelerometers, strain sensors, etc.

However, in recent years, importance has been given to piezoelectric energy harvesters which can make use of the ambient surroundings to generate electrical energy. There have been several new concepts developed by researchers in the last 15 years to harvest electrical energy from wind using piezoelectric materials. However, one interesting concept in this regard was proposed by Dickson (2008), where the device consisted of piezoelectric membrane ("stalk") and a polymeric membrane ("leaf") coupled by a hinge to form the energy harvesting system. These leaf-stalk systems could then be scaled up to form an energy harvesting tree, as shown in Figure 1.3. The tree could be placed in an area where there is sufficient wind, thereby allowing the aerodynamic forces to impinge on the leaves, making the piezoelectric stalks to flutter, and hence generate electrical energy.

Currently, there are several Ultra Low Power (ULP) energy harvesting devices which cannot supply to the grid, but could be used to power a variety of sensor nodes and LED lights. Raju (2008) stated that the power density of these harvesting devices could be between 4-100$\mu W/cm^2$. Li and Lipson (2009) performed experiments with devices similar to the ones proposed by Dickson (2008) and the results indicated that at a particular wind speed, for a specific configuration, the power density was found to be 45$\mu W/cm^2$. Whilst low in terms of

conventional wind turbines, these power densities suggest that piezoelectric flapping system has promising potential for local applications.

Figure 1.3: Concept of a piezoelectric tree (Dickson, 2008)

Since return on investment is an important parameter, it is important to consider power densities and cost of piezoelectric materials. Polyvinylidene Fluoride (PVDF) type piezoelectric materials cost only around 6¢/cm^2 (PPC 2009). On the other hand, Macro-Fibre Composite (MFC) type piezoelectric materials cost significantly more. However, Churchill et al. (2003) noted that the power density of these MFCs could be as high as 0.44 mW/cm^2. Thus, in terms of power density and cost effectiveness, this system could match existing urban wind turbines and overcome their limitations at the same time.

Piezoelectric energy harvesting from fluid flow requires knowledge and understanding of several fields of study. Since the leaf-stalk system should be designed to flutter in the wind, an understanding of fluid-structure interaction is required if such systems are to be optimised. Thus, it is important to combine aspects of structural dynamics and aerodynamics. On the other hand, the electric charge produced by the piezoelectric membrane is dependent on the rate of change of strain experienced by it. This involves a combination of electrical and structural engineering. Thus, the design demands a deep knowledge in the inter-connectivity of structural, aerodynamic and electrical aspects. Figure 1.4 shows the same as a schematic represented by Akaydin et al. (2010).

The piezoelectric membrane when coupled with a polymeric leaf by a hinge, acts as a single unit, capable of fluttering in the wind. The leaf is believed to act as a vibration amplifier, thereby increasing the strains on the piezoelectric stalk. Thus the geometry, material and orientation of the leaf and stalk system are important for energy harvesting. Figure 1.5 shows the working concept of the piezoelectric leaf-stalk system.

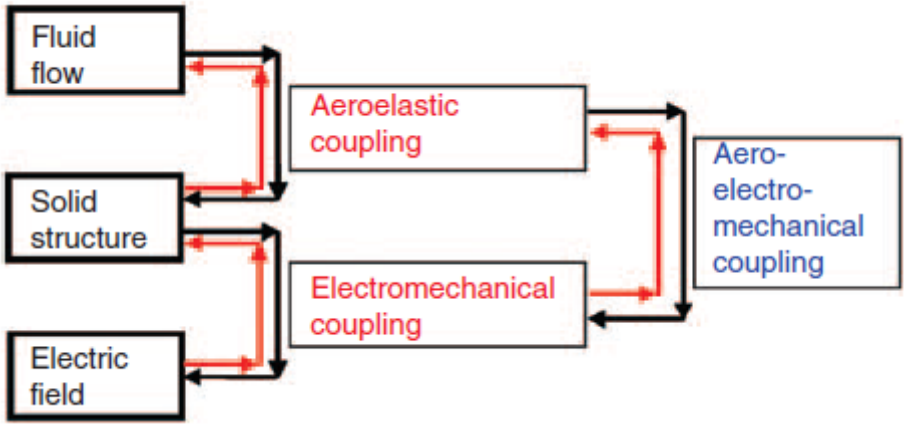

Figure 1.4: Schematic 3-way interaction between flow, structure and electric field (Akaydin et al., 2010)

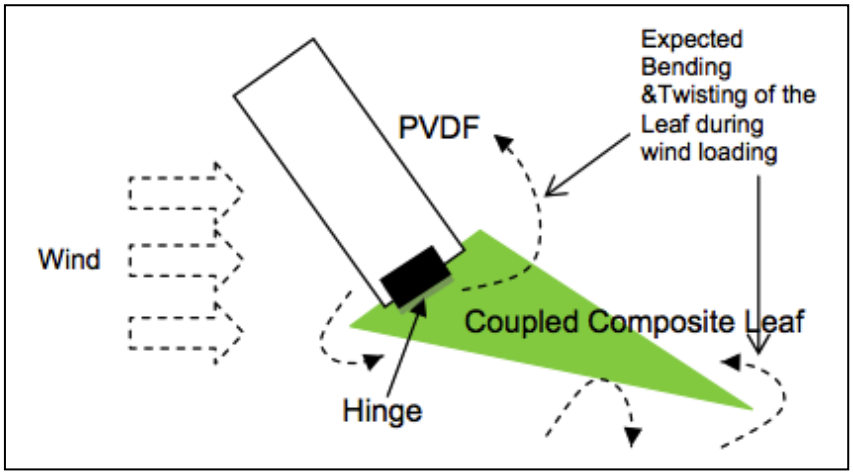

Figure 1.5: A diagram showing the conceptual operation of a single piezoelectric leaf/stalk system (Source: ARC grant: LP100200034 - S John & S Watkins).

There is substantial literature available in the above mentioned fields which have to be understood before investigating and optimizing the harvester system for its maximum power output. The literature involves certain fundamental concepts, definitions, analytical and computational modelling, analysis and experiments performed elsewhere relevant to this work. Chapter 2 reviews some of the important literature useful to understand the work described in this thesis.

1.4 Objectives

The broad objective of this research is to investigate an aesthetically pleasing energy harvesting system suitable for urban environment using piezoelectric materials. Since the system should be capable of working at very low wind speeds, a fundamental understanding of the interaction between solid and fluid is required. Thus, determining the dynamic properties responsible for flutter onset and frequency forms a part of this research. Also, determining the flutter characteristics of a connected body system is useful to optimise the harvester.

Since the harvester would consist of a piezoelectric material coupled with an amplification device ('leaf'), the choice of the piezo and leaf material plays an important role in the power output of the system. Also, investigation of several configurations and arrangements of these harvesters and their effect on the power output are addressed in this work.

In order to harvest sufficient amount of energy to power ULP devices, several harvesters have to function in tandem. As it is likely there will be interaction effects between closely-spaced harvesters, the effect of one harvester on another, when placed next to each other, in terms of their power outputs is investigated in this research. The performance of these harvesters in turbulence is also addressed.

1.5 Methodology

In order to address the Fluid Structure Interaction (FSI) issues associated with the work, complete analytical solutions are derived for the connected body systems to understand the relationship between the natural frequencies and their respective flutter onset velocities. Also, theoretical scaling laws for flutter onset and frequency are experimentally validated to obtain a conclusive estimate of the flutter onset and frequency based on the solid properties.

Extensive wind-tunnel tests are conducted by varying the leaf area and geometry and measuring the power output from the piezoelectric material at several wind speeds. Once the geometry is optimised, several configurations of the leaf and stalk system are tested for their power output to obtain the best possible configuration. High speed video results and computational analysis are used wherever essential to support the experimental results.

In order to scale up the number of piezos, proximity effects of two similar harvesters are experimentally determined. Power outputs are recorded simultaneously to observe the

increase or decrease of the power output from the piezos due to their operation in tandem. Power output data are used to obtain the phase lag between the harvesters when operating together. Smoke wire flow visualization is carried out to understand the flow structures around the harvesters and to support the power output results. The findings are explained in detail in the chapters of this thesis.

1.6 Structure of Thesis

Chapter 1: Introduction

In this introductory chapter, the rationale for this research was explained. Concepts such as the need for sustainability in today's scenario, renewable energy resources to supplement the power requirements and wind energy as the potential source in urban environment were discussed. The current concerns regarding operation of wind turbines in urban areas and piezoelectric energy harvesting from fluid flow as a potential alternative were established. The broad objectives and methodology were outlined.

Chapter 2: Literature review

The important concepts in piezoelectricity, vibration based energy harvesting, fluid-structure interaction and energy harvesting from fluid flow are explained. These concepts include some fundamental terms, phenomenon and review of important analysis and experiments performed by researchers in this field which are useful in the context of this thesis. At the end of the chapter, specific research scope and objectives are identified which are answered in the forthcoming chapters.

Chapter 3: Flutter of Simple Cantilevered and Interconnected Beams with Hinges

A detailed analytical modelling of flutter of cantilevered beams is provided along with factors influencing the flutter onset and flutter frequency. Experiments performed to validate the theoretical relationships are explained. Simple cantilevered beams with hinges at variable positions in a connected body system are analysed in detail. The body of work includes theoretical modelling, computational validation and experiments to understand the effect of hinge on flutter onset and frequency.

Chapter 4: Horizontal symmetrical, asymmetrical and vertical leaf-stalk configurations

The variation of "leaf" area and aspect ratios for a simple horizontal piezo leaf-stalk configuration and their effects on power output are discussed. Governing equations of motion on coupled-bending torsional vibrations for simple beams are reviewed. Experimental results comparing a symmetrical configuration with asymmetrical configuration are investigated, including the advantages and limitations of a vertical "L" shaped configuration.

Chapter 5: Proximity of energy harvesters

Two horizontal stalk configurations were displaced in stream-wise, cross-stream and vertical directions, one at a time, and the effect of one harvester on another in terms of their power outputs is established. Smoke-wire flow visualisation was carried out for a specific configuration and the results are provided. Simultaneous voltage measurements were carried out to estimate the phase lag between the harvesters and the results are discussed. Also, a proof of concept to demonstrate the working of multiple harvesters in smooth flow was constructed and evaluated.

Chapter 6: Conclusions and recommendations

In the final chapter, specific objectives are restated and the major conclusions deduced from this work are stated. Recommendations for the future research are also considered.

1.7 Publications resulted from this research

Journal articles

1. **A. Deivasigamani**, J. McCarthy, S. John, S. Watkins, F. Coman, and P. Trivailo. Flutter of cantilevered interconnected beams with variable hinge positions. Journal of Fluids and Structures, 38:223 - 237, April 2012.
2. **A. Deivasigamani**, J. McCarthy, S. John, S. Watkins, F. Coman, and P. Trivailo. Piezoelectric energy harvesting from wind using coupled bending-torsional vibrations. Journal of Modern Applied Sciences, Vol. 8, No. 4, 2014.
3. J. McCarthy, **A. Deivasigamani**, S. Watkins, S. John, F. Coman, and P. Petersen. Downstream flow structures of a fluttering piezoelectric energy harvester. Experimental Thermal and Fluid Science, 51: 279 - 290, 2013.
4. J. McCarthy, **A. Deivasigamani**, S. Watkins, S. John, F. Coman, and P. Petersen. On the visualization of flow structures downstream of fluttering piezoelectric energy

harvesters in a tandem configuration. Experimental Thermal and Fluid Science, 57: 407 - 419, 2014.

5. J. McCarthy, S. Watkins, **A. Deivasigamani**, S. John, and F. Coman. Piezoelectric energy harvesters in smooth and turbulent flows: How well might they perform in outdoor, real-world conditions? (*Accepted*). Journal of Wind Engineering and Industrial Aerodynamics, 2014.

Book Chapter

6. J. McCarthy, **A. Deivasigamani**, S. Watkins, S. John, and F. Coman. Nonlinear Approaches in Engineering Applications 2, chapter 6, pages 169 - 211. Springer Science & Business Media, New York, 2014.

Conference proceedings

7. **A. Deivasigamani**, J. McCarthy, S. Watkins, S. John, and F. Coman. Flow-induced flutter of slender cantilever high-compliance plates. In 28th International Congress Of The Aeronautical Sciences, ICAS 2012, September 23 - September 28, number 863, Brisbane, Australia, 2012.

8. **A. Deivasigamani**, J. McCarthy, S. John, S. Watkins, and F. Coman. Energy harvesting from fluid flow using coupled bending-torsion flutter of a thin composite piezoelectric beam. In 19th International Conference on Composite Materials, Montreal, Canada, July 2013.

9. **A. Deivasigamani**, J. McCarthy, S. John, S. Watkins, and F. Coman. Proximity effects of piezoelectric energy harvesters in fluid flow. In 29th Congress of the International Council of the Aeronautical Sciences, ICAS 2014, September 7 - 12, St. Petersburg, Russia, 2014.

10. **A. Deivasigamani**, J. McCarthy, S. John, S. Watkins, and F. Coman. Investigation of asymmetrical configurations for piezoelectric energy harvesting from fluid flow. In Proceedings of ASME 2014 Smart Materials, Adaptive Structures and Intelligent Systems, Rhode Island, USA, September 2014. American Society of Mechanical Engineers.

11. J. McCarthy, **A. Deivasigamani**, S. John, S. Watkins, and F. Coman. The effect of the configuration of the amplification device on the power output of a piezoelectric strip. In ASME Conference on Smart Materials, Adaptive Structures and Intelligent Systems, SMASIS2012, September 19 - September 21, number Paper No. 7951, Stone Mountain, Georgia, USA, 2012. American Society of Mechanical Engineers.

12. J. McCarthy, **A. Deivasigamani**, S. Watkins, S. John, and F. Coman. A parametric study of wind- induced flutter of piezoelectric patches for energy harvesting. In 15th Australian International Aerospace Congress, AIAC15, Paper No. 194, Melbourne, Australia, February 2013.

13. J. McCarthy, **A. Deivasigamani**, S. Watkins, S. John, and F. Coman. Piezoelectric energy harvesting utilising flutter: An overview of key findings to date (*Abstract submitted*). In 8th Australasian Conference on Applied Mechanics, Melbourne, Australia, November 2014. Engineers Australia.

14. J. McCarthy, S. Watkins, **A. Deivasigamani**, S. John, and F. Coman. A study of piezoelectric energy harvester in smooth and turbulent flows: how might they perform in real-world conditions? (*accepted*). In 19th Australasian Fluid Mechanics Conference, Melbourne, Australia, December 2014.

Chapter 2
Literature Review

2.1 Introduction

Energy harvesting from fluid-induced flutter using piezoelectric materials, as discussed in the previous chapter, involves knowledge and understanding across several fields, namely piezoelectricity, fluid-structure interaction, electrical loading and structural dynamics. It is essential to understand the basic concepts of all these fields independently, and then in conjunction, as the fields would be coupled.

The following section briefly explains the history of wind energy harvesting, techniques, current trends and concerns which lead to understanding some basic concepts of alternative energy harvesting techniques, such as piezoelectric energy harvesting. The working principle, materials and coupling equations involved with piezoelectricity are studied. Later, fluid-structure interaction and aerodynamic concepts involved in flutter of slender beams are studied. Energy harvesting from vibrations are examined in detail, and some of the electrical aspects involved with piezoelectric energy harvesting are discussed.

2.2 Wind energy harvesting

Wind energy has been put to useful work for thousands of years. Early sailors used wind power to navigate their sail boats. This principle was later utilized to create a sail type windmill to harvest power from winds. Windmills were initially used for driving machines which could grind grains or pump water. It was only in late nineteenth century that it was used to generate electrical power (Burton et al., 2001). As time progressed, the technology of the blades slowly improved, moving from fabrics to light metals. The rotor diameter increased and aerodynamics came into picture. During the Second World War, it was noted that Denmark had installed eighty-eight windmills to produce 18,000MWh of energy (Golding, 1955).

Figure 2.1: Steel-bladed water pumping windmill in American Midwest in late 1800s (Image courtesy: http://telosnet.com/wind/early.html)

During the late twentieth century, due to the increasing demand for renewable energy, experts from countries like U.S.A., Sweden, Canada, etc. started experimenting with different types of windmill blades and factors which could lead to scaling up these windmills to have a wind farm generating large amounts of power.

Today, there are different types of windmills with a wide variety of rotor diameters, shapes and orientations. Large wind farms have been setup at few places generating high amount of electricity. As of November 2010, the Roscoe Wind Farm is the largest onshore wind farm in the world, with a capacity of 781.5 MW of power, followed by the Horse Hollow Wind Energy Centre (735.5 MW). The Thanet Offshore Wind Project in United Kingdom is the largest offshore wind farm in the world at 300 MW, followed by Horns Rev II (209 MW) in Denmark (WWEA, 2011).

Figure 2.2: Roscoe wind farm, Texas, U.S.A. (Image courtesy: http://www.examiner.com/article/wind-energy-powers-investors)

The above mentioned wind farms are located outside the urban settings and are specifically designed for large scale energy production. Although they are extremely important to supplement the demands and requirements of domestic and commercial establishments, the focus of this research is on tapping the wind energy resource in urban areas. In this regard, windmills have to be designed to work at velocities which are commonly observed in cities. However, before proceeding to the wind velocity statistics in urban areas, it is important to understand the amount of energy available in the wind.

The potential power available in the wind is given by:

$$P_A = \frac{1}{2}\rho A_{swept} v^3 \tag{2.1}$$

Where P_A - Power available in the fluid flow; ρ - Density of fluid; A_{swept} - Swept area of the rotor blades; v - Velocity of the fluid flow.

It is well known that the amount of power extracted in an unbounded fluid is limited by Betz Limit (η_b) which is given as 0.593 (Betz, 1966). Therefore, the maximum extractable wind power using a wind turbine is given by:

$$P_{max} = \frac{1}{2}\rho A_{swept} v^3 \eta_b \quad (2.2)$$

Where P_{max} - Maximum power extractable from the fluid flow.

From the above equations, it is observed that the power generated from wind is proportional to velocity cubed. Therefore, it is essential to design the wind turbines to work within the range of wind speeds available in a particular location.

2.2.1 Wind speeds in urban locations

From equation (2.2), in urban environments, generally the power generated from winds would be reduced compared to non-urban areas. This is because, due to the presence of tall buildings and lack of open space, the average wind speeds are generally very low along the ground. Also, due to flow pattern around buildings, there are certain building-specific over-speed and under-speed locations. This makes it challenging to design wind turbines which could work in urban settings and generate power to the grid. Small scale wind turbines are placed on top of the buildings where over-speed effects are observed, and the power generated is used for certain lighting purposes in the buildings directly. However, when the wind direction is reversed, the same location is subjected to under-speed effect, thereby producing significantly lower amounts of power. In the sections below, the average wind speeds of cities are discussed. Also, the challenges faced in designing a small scale windmill are discussed.

Wind characteristics in different cities across the world are well recorded over very long periods of time. Anemometers and sensors are placed at different locations which can provide wind speed and wind direction statistics over a period of time. For example, The Bureau of Meteorology (BOM), Australia provides complete information regarding wind and temperature statistics at various locations across Australia over a period of 60 years. Figure 2.3 shows the annual wind speeds in Melbourne and Sydney from 1955 to 2009.

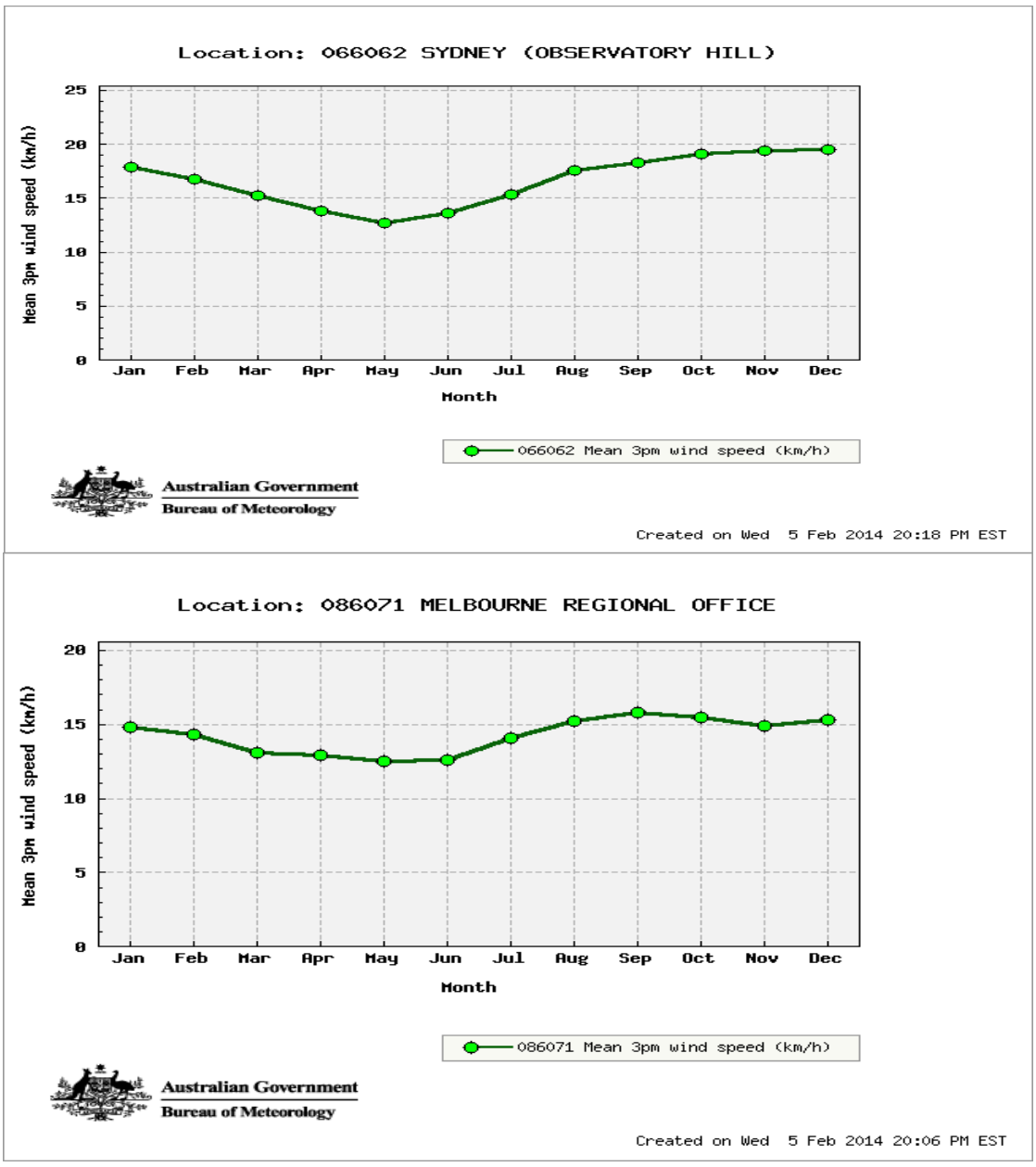

Figure 2.3: Mean wind speed data recorded from 1955 to 2009 at Sydney and Melbourne (Source: www.bom.gov.au)

The above figure shows the wind speed data at 3 pm everyday throughout the year. It is important to note that average wind speeds would vary at different times of the day and at various altitudes. In addition to the wind speed data, wind direction and turbulence intensity data are required to understand the wind behaviour at a specific location to design any wind energy harvesting system.

2.2.2 Present concerns with wind turbines in urban areas.

Since the average wind speeds in cities are very low (3-6 m/s), to suit this wind speed, the wind rotor diameters, materials and blade angles have to be designed differently to those found in larger wind turbines found in wind farms. By doing so, it is observed that the efficiency and performance significantly reduces. In 2007, about 25 locations were selected for roof top wind mill installations across several parts of United Kingdom. At each location, anemometers were first installed and the wind data were collected. Based on the data, windmills were designed and manufactured by different manufacturers. Since the theoretical modelling of wind turbines are well developed over years, the power output of each of these windmills were first theoretically estimated and later on compared with the actual power output values of the installed units. It was disappointing to note that at low wind speeds, the windmills performed well below the theoretical estimation. (Encraft, 2009).

Apart from the poor performance, another aspect which is closely related to its performance is its cost effectiveness. Due to the low power output of these urban small scale windmills, the payback period would be very long. This was in fact statistically reported in some studies (Webb, 2007; Wilson, 2009). Also, in order to meet the maintenance cost, the power output has to be sufficiently high to cut down the electricity bills. Thus it is observed that the cost effectiveness depends on the power output as sufficiently high return on investment is necessary. Also, in order to achieve high power outputs, the wind speeds have to be relatively higher which is highly unlikely in urban environment. These are often the major concerns during investment in such renewable energy resources implemented in urban areas.

Small wind turbines often produce noise similar to the noise produced by the indoor pedestal and table fans. Large windmills rotate at lower speeds and hence the noise produced is lesser in amplitude and frequency. However, in urban environments, the windmills have smaller diameters and are designed to be lighter to rotate in low wind speeds. Thus, the rotation per minute (rpm) is generally higher, thus causing more noise.

In urban residential areas, often the councils have an upper limit to the sound levels which should not be exceeded for peaceful living environment. For example, a wind turbine in Wellington, New Zealand recorded a sound power level of 54dBA, when the legal limit in the area was 45dBA (Gipe 2003).

The vibration of the turbine can also create problems when rigidly mounting the turbine to a building structure. The vibrations in a wind turbine generally do not originate from the blade rotation, as the design process usually eliminates blade imbalance. However, vibrations may result from blade wake interactions with support structures and cause resonance in the turbine gearbox. This stress and vibration may be transmitted to the building on which the turbine is mounted (Wilson 2009), and depending on the building materials and design, could be inconvenient to the occupants and also affect the structural integrity. Some small wind turbine manufacturers even state that their wind turbines are only suitable for mounting on concrete structures, to eliminate vibration concerns (Wilson 2009).

In urban areas, importance to aesthetics is generally higher. Although this aspect is very subjective, devices which blend well with the surroundings are considered aesthetically well designed. Some suburban councils refuse to accept the installations of simple Horizontal Axis Wind Turbines (HAWT) due to their appearance. This recent aspect of design has imposed challenges to the windmill manufacturers as they are forced to design their blades and structure to suit well with the surroundings keeping the aerodynamic and efficiency aspects intact. This often increases the cost of design and manufacture. Nowadays, windmill manufacturers are trying to mimic nature in their designs. Attempts are being made to design Vertical Axis Wind Turbines (VAWT), which blend well with the environment and also produce the required power output. Figure 2.4 shows some of the common VAWT existing in urban areas.

Thus, it is clear that there are many major concerns regarding the implementation of windmills in urban areas. In order to overcome the above mentioned limitations, either the windmill designs have to be significantly improved, or a completely alternative technique has to be implemented to harvest energy from the wind in urban settings. One such alternative approach is piezoelectric energy harvesting from wind-induced vibrations. The following section gives a brief overview of some fundamental terms and concepts involved with piezoelectricity.

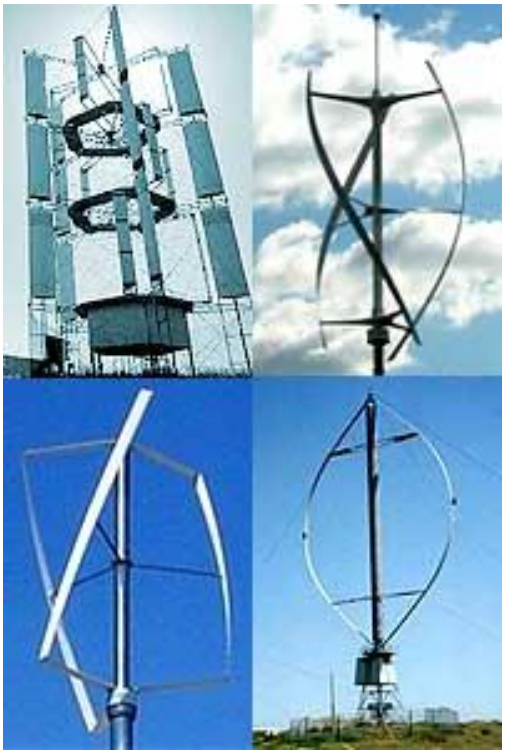

Figure 2.4: Some of the VAWT designed for urban environment.
(Source: http://www.lowcarboneconomy.com)

2.3 Piezoelectricity

Piezoelectricity is usually defined as the ability of certain crystalline materials to develop an electric charge proportional to an applied mechanical stress. This phenomenon was first discovered in 1880 by Pierre and Jacques Curie during their study of the effects of pressure on the generation of electrical charge by crystals such as quartz, tourmaline and Rochelle salt. The term 'piezoelectricity' was first given by W. Hankel, and the converse effect was mathematically deduced by Gabriel Lipmann from fundamental thermodynamic principles. However, piezoelectricity remained as a laboratory phenomenon until 1917, when Paul Langevin and his colleagues designed an ultrasonic submarine detector, which consisted of a transducer made of thin quartz crystals carefully glued between two steel plates, and a hydrophone to detect the returned echo. By emitting a high-frequency chirp from the transducer, and measuring the amount of time it takes to hear an echo from the sound waves bouncing off an object, one could calculate the distance to that object (Kholkin et al., 2002; Cady, 1964). This success opened up the opportunities for piezoelectric materials in a variety of applications such as ultrasonic transducers, microphones, accelerometers, etc. Figure 2.5 shows the schematic working of a piezoelectric material.

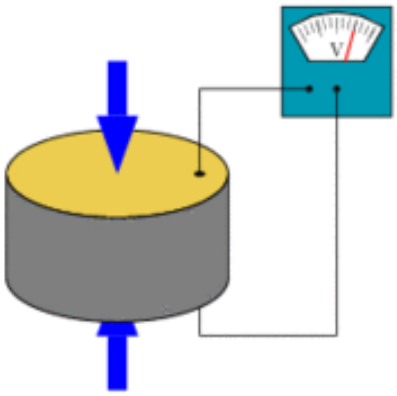

Figure 2.5: Schematic working of a piezoelectric material. Generation of electrical charge upon mechanical stress (Source: http://en.wikipedia.org/wiki/Piezoelectricity).

2.4 Piezoelectric materials

In 1935, Busch and Scherrer discovered piezoelectricity in potassium dihydrogen phosphate (KDP) and its isomorph. However in 1940-1943, unusually high dielectric properties were found in $BaTiO_3$. After this discovery, modifications of $BaTiO_3$ led to high voltage output. Piezoelectric transducers based on $BaTiO_3$ ceramics became well established in a number of devices.

2.4.1 Lead Zirconate Titanate

In 1950s, it was found that the PZT (Lead Zirconate Titanate) system could exhibit strong piezoelectric effects. Since then, the PZT system containing various additives has become the dominant piezoelectric ceramic for various applications (Zhu, 2010). The unit cell of PZT is shown in the diagram below (Figure 2.6).

PZTs are manufactured in strips and plates of various thicknesses based on the application. However, these strips have a specific stiffness which restricts use for various applications which require flexibility of piezoelectric materials. Moreover, PZT strips are brittle in nature and thus, do not have the ability to handle large deformations. In the previous chapter, it was mentioned that the piezoelectric materials must have the ability to flutter in the wind for energy harvesting purposes. To achieve this, the material must have sufficient compliance which is not available in the current commercially existing PZT strips. Thus, it is important to look for other alternatives which suit this research project.

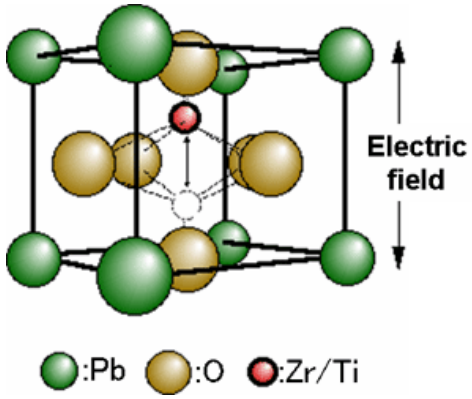

Figure 2.6: The structure of a PZT molecule (Source: YTC America Inc., 2008)

2.4.2 Macro Fibre Composites

In order to overcome the above limitations, several forms of PZT have been developed for various applications which are flexible to handle large amounts of strain. One such modification of PZT is called as Macro Fibre Composite (MFC). "The MFC consists of rectangular piezo ceramic rods sandwiched between layers of adhesive, electrodes and polyimide film (Figure 2.7). The electrodes are attached to the film in an interdigitated pattern which transfers the applied voltage directly to and from the ribbon shaped rods. This assembly enables in-plane poling, actuation and sensing in a sealed and durable, ready to use package. As a thin, surface conformable sheet it can be normally bonded to various types of structures or embedded in a composite structure" (Smart Material Corp., 2012). These MFCs are very precisely engineered materials having high energy densities and output. However, these sensors and actuators are very expensive due to the manufacturing complexities involved with the materials.

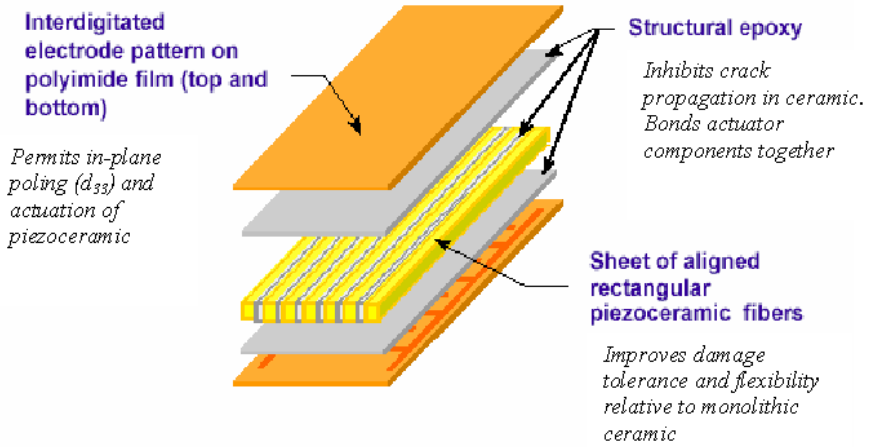

Figure 2.7: Components of MFC
(Source: http://www.eng.newcastle.edu.au/eecs/fyweb/Archives/2005/c2003191/larc.htm)

2.4.3 Poly-vinylidene fluoride (PVDF)

In 1969, strong piezoelectricity was observed in PVDF. Since then, PVDFs are used for various applications in place of PZTs due to its availability, cost and other piezoelectric parameters. PVDF has a glass transition temperature (T_g) of about −35 °C and is typically 50–60% crystalline. To give the material its piezoelectric properties, it is mechanically stretched to orient the molecular chains and then poled under tension. PVDF exists in several forms: alpha (TGTG'), beta (TTTT), and gamma (TTTGTTTG') phases, depending on the chain conformations as trans (T) or gauche (G) linkages. When poled, PVDF is a ferroelectric polymer, exhibiting efficient piezoelectric and pyroelectric properties. These characteristics make it useful in sensor and battery applications (Zhang, 2002).

Commercially available PVDF films are extremely flexible compared to the MFCs. Also, the MFCs are about ten times as expensive compared to the PVDFs, thereby making it not viable for this energy harvesting application. It is to be noted that the MFCs are very well engineered products and hence, are capable of providing an order of magnitude higher power outputs compared to the PVDFs. In chapter 4, preliminary experiments comparing MFCs and PVDFs are shown where it was evident that for the application in this project, MFCs were not suitable due to their high costs and lower fatigue life. There are several other synthetically manufactured piezoelectric materials such as Active Fibre Composites (AFC) and Quickpacks™ which are becoming increasingly available for various applications. However, it is well known that PVDF exhibits the maximum flexibility and longer fatigue life. Lee et al. (2004, 2005) performed experiments to compare PZTs and PVDFs for energy harvesting applications and found that PVDF with a certain electrode configuration proved to have the longest fatigue life and hence more suitable for energy harvesting.

In the next section, some of the important piezoelectric parameters are discussed. These parameters decide the efficiency of the device in terms of energy output and ability to convert mechanical energy to electrical energy and vice versa. Some of the expansion, compression and bending effects of piezos are also discussed.

2.5 Piezoelectric parameters

The parameters that are of interest when considering the electromechanical effects of piezoelectric materials, are the piezoelectric coupling factor k (e.g. $k_{33}, k_{31}, k_p \; and \; k_t$),

mechanical quality factor (Q_m) and piezoelectric coefficients, such as the d and g coefficients which describe the interaction between mechanical and electrical behaviour of piezoelectric ceramics. The effective electromechanical coupling coefficient k_{eff} describes the ability of the transducer to convert one form of energy to another, which is defined by the equation:

$$k_{eff}^2 = \frac{mechanical\ energy\ converted\ to\ electrical\ energy}{input\ mechanical\ energy}$$

or

$$k_{eff}^2 = \frac{electrical\ energy\ converted\ to\ mechanical\ energy}{input\ electrical\ energy} \tag{2.3}$$

This parameter is a function in equations for electrical/mechanical energy conversion efficiency in actuators, in bandwidth and insertion loss in transducers, and signal processing devices, and in the location and spacing of critical frequencies of resonators. Since the energy conversion is always incomplete, k^2 is (and thus also k) is always lower than 1.0 (Zhu, 2010).

The mechanical quality factor Q_m, representing the degree of mechanical loss of piezoelectric resonator at resonance, is defined as

$$Q_m = \frac{stored\ mechanical\ energy\ at\ resonance}{mechanical\ dissipated\ energy\ per\ resonant\ cycle} \tag{2.4}$$

Although these factors give an overall idea about the efficiency of the piezoelectric material, it is very important to understand the piezoelectric coefficients as they play a crucial role in converting mechanical strain into electrical energy and vice versa. However, in a solid, strain could be in different directions. Hence, the conversion coefficient in the direction of the strain is responsible for its corresponding energy conversion.

Figure 2.8 shows the direction of forces and polarization in a piezoelectric material. The direction of polarization is generally along the z axis. Since the piezoelectric ceramic is anisotropic, the piezoelectric coefficients (d and g constants) are related to the direction of the applied force and the direction perpendicular to it. Therefore, the coefficients have two subscript numbers representing the polarization and strain direction.

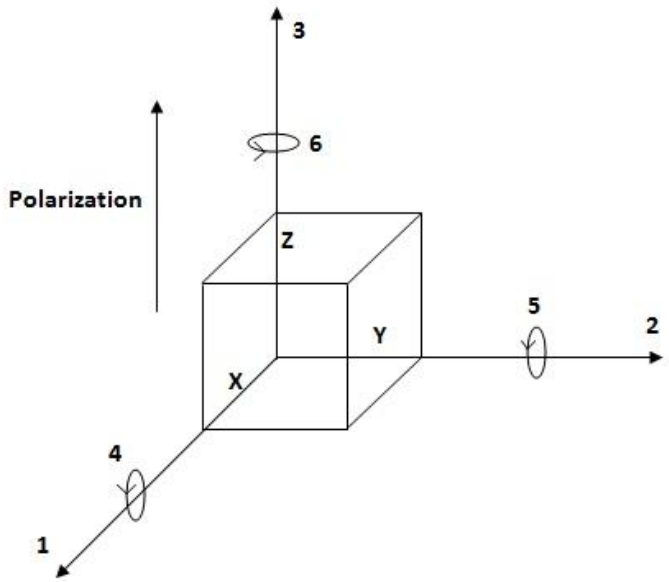

Figure 2.8: Direction of forces affecting a piezoelectric material.

2.5.1 Piezoelectric charge coefficient (*d* constant)

The piezoelectric charge coefficient is defined as the ratio between the electrical charge generated per unit area and the applied stress. It is expressed generally as Coulombs/Newton (C/N).

$$d = \frac{generated\ charge\ density}{applied\ mechanical\ stress} \tag{2.5}$$

Alternatively, it can be defined as the ratio between the strain developed in a piezoelectric material and the applied electrical field. Table 2.1 indicates the nomenclature for the charge coefficient in a piezoelectric material (APC International, Ltd., 2014).

$$d = \frac{mechanical\ strain\ developed}{applied\ electric\ field} \tag{2.6}$$

2.5.2 Piezoelectric voltage coefficient (*g* constant)

The piezoelectric voltage coefficient is defined as the ratio between the electrical field developed per unit area and the applied mechanical stress. It is expressed generally as Volt.meter/Newton (V.m/N).

$$g = \frac{electric\ field\ developed}{applied\ mechanical\ stress} \tag{2.7}$$

Alternatively, it can be defined as the ratio between the mechanical strain developed in a piezoelectric material and the applied charge density (Piezo Systems, Inc., 2014). The nomenclature for this coefficient is similar to the ones shown in Table 2.1.

$$g = \frac{mechanical\ strain\ developed}{applied\ charge\ density} \tag{2.8}$$

Table 2.1: Nomenclature explanation for '*d*' constant (APC International, Ltd., 2014)

d_{33}	induced polarization in direction 3 (parallel to direction in which ceramic element is polarized) per unit stress applied in direction 3 **or** induced strain in direction 3 per unit electric field applied in direction 3
d_{31}	induced polarization in direction 3 (parallel to direction in which ceramic element is polarized) per unit stress applied in direction 1 (perpendicular to direction in which ceramic element is polarized) **or** induced strain in direction 1 per unit electric field applied in direction 3
d_{15}	induced polarization in direction 1 (perpendicular to direction in which ceramic element is polarized) per unit shear stress applied about direction 2 (direction 2 perpendicular to direction in which ceramic element is polarized) **or** induced shear strain about direction 2 per unit electric field applied in direction 1

2.5.3 Dielectric Constant (Relative Permittivity)

The dielectric constant (ε) is defined as the ratio of the permittivity of the material to the permittivity of free space. This is generally measured well below the mechanical resonance. The dielectric constant is derived from the static capacitance measurements at 1 kHz using a standard impedance bridge. The relations are expressed by the associated equation,

$$\varepsilon = \frac{C_p d}{\varepsilon_0 A} \tag{2.9}$$

where C_p is the capacitance of the piezoelectric material; d is separation distance between the electrodes; A is the area of the electrodes; ε_0 is the permittivity of free space (8.854 x 10^{-12} F/m).

The above-mentioned parameters are very essential to determine the quality and effectiveness of the piezoelectric material for various applications. However, it is important to understand the role of these parameters in the conversion of mechanical strain to electrical field and vice versa. Thus, the following section describes the relationship between the mechanical stress, strain and electrical field with the help of these piezoelectric coefficients.

2.6 Piezoelectric constitutive equations

Piezoelectricity combines the electrical and mechanical behaviour of a material. Thus, the fundamental electrical and mechanical equations are combined to arrive at the constitutive equation. The fundamental equation which relates the electric displacement (D) and electric field strength (E) is given by,

$$D = \varepsilon E \tag{2.10}$$

where ε is the electrical permittivity. On the other hand, the well known Hooke's law which relates mechanical stress (T) and strain (S) is given by,

$$S = cT \tag{2.11}$$

where c is compliance. These two equations are combined in a piezoelectric material to arrive at the coupled equations:

$$\begin{aligned} \{S\} &= [c^E]\{T\} + [d^t]\{E\} \\ \{D\} &= [d]\{T\} + [\varepsilon^T]\{E\} \end{aligned} \tag{2.12}$$

Here, d is piezoelectric charge coefficient for the direct effect and d^t is the charge coefficient for the inverse effect (superscript t stands for the transposition of the matrix). The superscripts E and T refer to the values measured at a constant electric and stress field respectively (Dragon, 1998).

As the equations (2.12) suggest, all the parameters depend on the direction and poling and hence are written in the matrix form. The electric displacement and electric field are first-rank tensors while mechanical stress and strain are technically second-rank tensors. The

dielectric permittivity is also a second-rank tensor while the piezoelectric coefficient being a third-rank tensor and compliance, a fourth-rank tensor. However, there is an inconsistent notation system for expressing these matrices (Zhu, 2010). This research does not aim to deal with the fundamental design of the piezoelectric material and hence an overall understanding of these constitutive relationship equations would be sufficient in the current context.

2.7 Applications of piezoelectric materials

The constitutive equations (2.12) in the previous section suggest that these piezoelectric materials could be used as a sensor and an actuator. An applied stress or strain could result in producing an electric field and hence, an output voltage. Thus, these materials could be used as sensors to detect impact loads and damages in structures.

An interesting application here is the use of piezoelectric materials to characterize the dynamic behaviour of a mechanical system. It was established in the previous section that applying a mechanical stress or strain would result in an output voltage. However, the piezoelectric material provides an output voltage only during the process of mechanical strain, i.e. the output voltage (V_{OUT}) is proportional to time rate of change of mechanical strain (S). Nam and Sasaki (2002) investigated the use of piezoelectric material as a strain rate sensor and used the method developed by Dosch et al. (1992) which clearly showed that for a sensor operating in the bending mode (*31* mode),

$$V_{OUT} \propto \frac{\partial S}{\partial t} \tag{2.13}$$

This knowledge opens up a wide range of sensor applications to measure the dynamic characteristics of a system such as amplitude, frequency and damping. This concept is also the basis for piezoelectric energy harvesting from vibrations.

On the other hand, piezoelectric materials could be used as actuators by making use of the inverse piezoelectric effect. Some of the common applications of piezoelectric materials are listed below:

- Detection and generation of sonar waves.
- Piezoelectric microbalances
- Automotive fuel injection systems
- Loudspeakers

- Piezoelectric motors
- Atomic force microscopes and scanning tunnelling microscopes
- Inkjet printers
- Active vibration control using amplified actuators.
- X-ray shutters.
- Solenoid valve controls
- Strain and dynamic sensing applications
- Accelerometers
- Energy harvesting systems

Of all the above mentioned applications, piezoelectric energy harvesting is studied in detail in this thesis. In the following section, some of the fundamental concepts involved in conversion of mechanical vibration energy to electrical energy are explained. Also, some of the recent techniques to harvest energy from vibrations are reviewed.

2.8 Piezoelectric energy harvesting from mechanical vibrations

The best possible way to achieve a continuous time rate of change of strain is through vibrations. There are several modes in which a solid can vibrate. For example, a solid beam could be subjected to axial compression and expansion, transverse bending or torsional vibrations. These vibration modes cause strains in different directions across the solid. Before different forms of energy harvesting are investigated, it is important to understand some basic concepts behind vibrations of continuous beams.

2.8.1 Euler-Bernoulli Beam Theory

Euler-Bernoulli beam theory explains vibrations in beams with the help of fundamental governing equations. In this section, a beam undergoing transverse vibration is investigated. According to this theory, the governing equation for forced transverse bending vibration is written as (Timoshenko, 1953)

$$m\frac{\partial^2 y}{\partial t^2} + EI\frac{\partial^4 y}{\partial x^4} = F \tag{2.14}$$

Where $m = \rho_s hl$; *m*- Mass per unit length of the beam; ρ_s- density of the beam; *h*- thickness of the beam; *l*- width of the beam. *E*- Elastic modulus; *I*- moment of inertia; and *F*- input forcing function.

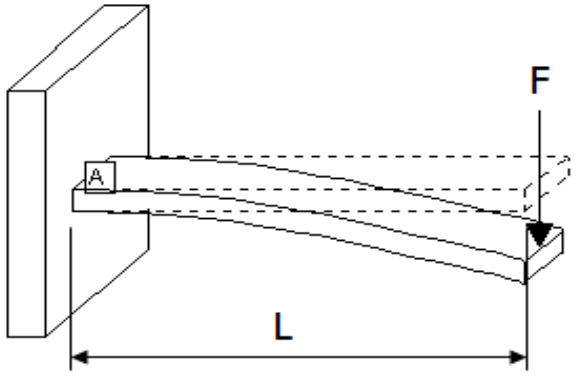

Figure 2.9: A cantilevered beam subjected to transverse bending.

Thus the mechanical stress (*T*) and strain (*S*) induced from these vibrations are given by,

$$T = \frac{Mz}{I} = -zE\frac{\partial^2 y}{\partial x^2}$$
$$S = -z\frac{\partial^2 y}{\partial x^2} \tag{2.15}$$

where *M* – bending moment, *I* – moment of inertia, *z* – distance from the neutral axis to the point of interest (Timoshenko, 1953). It is these stress and strain experienced by the piezo, that get converted into electrical energy governed by the coupling equations discussed previously (equation (2.12)).

2.8.2 Power available from vibrations

Since vibrations prove to be the easiest source of obtaining continuous, periodic strain rates, it is essential to understand the power available from vibrations. It is vital to understand the dependency of power on some of the fundamental characteristics of vibrations such as amplitude, frequency and damping ratio. To derive the power equation, a very simple spring-mass damper system is considered as shown in Figure 2.10. Priya (2007) established the relationship for power available from vibrations as a function of vibration parameters. A detailed derivation of the same is shown in this section. Here, *m* is the mass of the system, *k* is the spring constant and *c* is the damping coefficient. The over-dots in the following equations denote the derivative with respect to time.

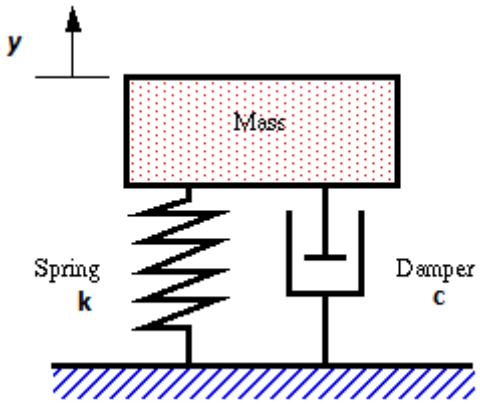

Figure 2.10: A simple spring-mass-damper system.

For forced vibrations, the governing equation for a lumped parameter system is given by,

$$\begin{aligned} m\ddot{z} + c\dot{z} + kz &= -m\ddot{y} \\ \ddot{z} + \frac{c}{m}\dot{z} + \frac{k}{m}z &= -\ddot{y} \\ \ddot{z} + 2\zeta\omega_n\dot{z} + \omega_n^2 z &= -\ddot{y} \end{aligned} \tag{2.16}$$

where damping ratio, $\zeta = \frac{c}{2\sqrt{mk}}$ and natural frequency, $\omega_n = \sqrt{\frac{k}{m}}$,

The Laplace transform of a function is given by,

$$\begin{aligned} L\big(z(t)\big) = Z(s) &= \int_0^\infty e^{-st} z(t)dt \\ Z(s) &= \left[\frac{e^{-st}z(t)}{-s}\right]_0^\infty - \int_0^\infty \frac{e^{-st}\dot{z}(t)}{-s}dt \\ Z(s) &= \left[\frac{z(0)}{s}\right]_0^\infty + \frac{1}{s}L\{\dot{z}(t)\} \end{aligned} \tag{2.17}$$

Now, rearranging terms give:

$$L\big(\dot{z}(t)\big) = sL\big(z(t)\big) - z(0) = sZ(s) - z(0) \tag{2.18}$$

Similarly,

$$\begin{aligned} L\big(\ddot{z}(t)\big) &= s^2Z(s) - sZ(s) - z(0) \\ L\big(\ddot{y}(t)\big) &= s^2Y(s) - sY(s) - Y(0) \end{aligned} \tag{2.19}$$

Now, substituting equations (2.18) and (2.19) in equation (2.16) with initial position at 0, yields:

$$s^2Z(s) + 2\zeta\omega_n sZ(s) + \omega_n^2 Z(s) = -s^2Y(s) \tag{2.20}$$

Rearranging it yields:

$$\left|\frac{Z(s)}{Y(s)}\right| = \frac{s^2}{s^2 + 2\zeta\omega_n s + \omega_n^2}$$

$$Z(s) = \frac{s^2}{s^2 + 2\zeta\omega_n s + \omega_n^2} L(Y \sin \omega t) \tag{2.21}$$

Using Laplace formula for sine, we get:

$$Z(s) = Y\left(\frac{s^2}{s^2 + 2\zeta\omega_n s + \omega_n^2}\right)\left(\frac{\omega}{s^2 + \omega^2}\right) \tag{2.22}$$

Now, applying inverse Laplace transform by using partial fractions will yield:

$$z(t) = \frac{\left(\frac{\omega}{\omega_n}\right)^2}{\sqrt{\left(1 - \left(\frac{\omega}{\omega_n}\right)^2\right)^2 + \left(\frac{2\zeta\omega}{\omega_n}\right)^2}} Y\sin(\omega t - \varphi) \tag{2.23}$$

The equation (2.23) is the position equation. If differentiated, we obtain velocity, *v* as,

$$v = \dot{z}(t) = \frac{\left(\frac{\omega}{\omega_n}\right)^2 Y\omega}{\sqrt{\left(1 - \left(\frac{\omega}{\omega_n}\right)^2\right)^2 + \left(\frac{2\zeta\omega}{\omega_n}\right)^2}} \tag{2.24}$$

and the acceleration, *a*,

$$a = \ddot{z}(t) = \frac{\left(\frac{\omega}{\omega_n}\right)^2 Y\omega^2}{\sqrt{\left(1 - \left(\frac{\omega}{\omega_n}\right)^2\right)^2 + \left(\frac{2\zeta\omega}{\omega_n}\right)^2}} \tag{2.25}$$

(Note that the maximum values are taken by neglecting sine and cosine functions)

Therefore, Power is the product of force and velocity given by (Priya, 2007):

$$P = m\ddot{z}(t)\dot{z}(t) = \frac{\left(\frac{\omega}{\omega_n}\right)^4 Y^2\omega^3 m}{\left(1-\left(\frac{\omega}{\omega_n}\right)^2\right)^2 + \left(\frac{2\zeta\omega}{\omega_n}\right)^2} \tag{2.26}$$

During resonance (when $\omega = \omega_n$),

$$P = \frac{Y^2\omega^3 m}{4\zeta^2} \tag{2.27}$$

From the above analysis, three aspects of power from vibrations are observed:

- Power available from vibrations is directly proportional to the square of its amplitude.
- Power available from vibrations is directly proportional to the cube of its frequency.
- During resonance, the amplitude is at its maximum and so is the power available from vibrations.

Thus, during the design of an energy harvesting system, equation (2.27) should form the basis to arrive at a configuration which would have a vibrating frequency and amplitude such that the power available from its vibration is maximized. In the following section, some of the techniques and experiments performed by researchers in the recent past to harvest energy from vibrations using piezoelectric materials are reviewed.

2.9 Energy harvesting configurations

There are several different ways in which these piezoelectric materials can be arranged and configured to harvest energy from vibrations. Since the vibrations could be from any machine source or periodic movement, the piezo members could be fixed and aligned differently based on the application such that the forcing function could act at different locations on the piezo beam. Also, as mentioned before, there are several modes of operation of these piezos depending on the direction of applied mechanical strain. The geometry of the piezoelectric material could also be altered to obtain a required stress distribution, frequency and amplitude of vibration which maximizes the power output.

2.9.1 Modes of operation

The piezoelectric beam can be clamped, pinned or hinged at both ends or just at one end to form a cantilever configuration. In this case, the piezoelectric material is subjected to transverse bending. On the other hand, when one surface of the piezo is clamped completely

and load is applied on the opposite surface, the piezo is subjected to axial compression and expansion. When the piezo is subjected to transverse bending, the piezo is found to be operating in the d_{31} mode and when the piezo is subjected to axial compression; it is found to be operating in the d_{33} mode. These notations are not always the same and are based on the poling direction with respect to the axis system. Figure 2.11 shows the schematic of these modes of operation. In d_{31} configuration the poling direction and direction of force are perpendicular while in d_{33} mode, they are in the same direction.

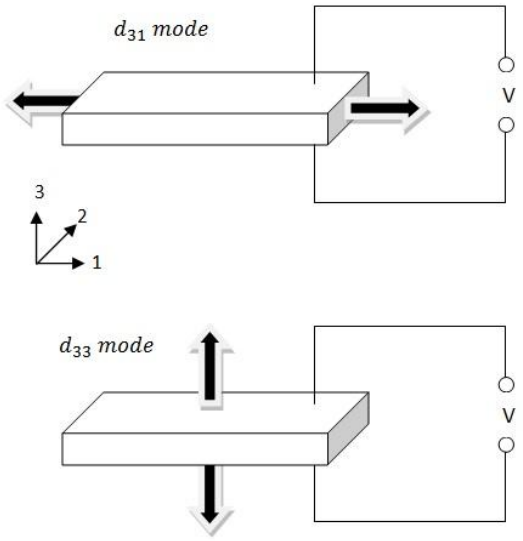

Figure 2.11: Two commonly found modes of operation for a piezoelectric material.

There are also few other modes of operation like d_{32}, d_{15}, etc. but they are not very common. Also, most commercially available piezoelectric materials are also designed to work only in the conventional d_{33} and d_{31} modes. Although the mode of operation depends to a certain extent on the location and loading nature of the harvester system, it is still useful to compare the behaviour of piezo in these two predominant modes for energy harvesting applications.

The coupling coefficient (k) of a piezo operating in the d_{31} mode is found to be lower than the one operating in d_{33} mode. Bakers et al. (2005) tested three different piezoelectric materials and found that the k-value was lower for all the piezos operating in the d_{31} mode. However, when equal volumes of the same piezo were taken and subjected to d_{31} and d_{33} modes, the cantilever configuration operating in d_{31} provided two orders of magnitude more power output. The d_{33} operation mode was found to be robust and having a higher k-value. However, it required very high force amplitude and vibration levels to strain the solid due to its high stiffness. On the other hand the cantilever operating in d_{31} mode required much lesser

amount of force to strain and provide electrical power. Also, Roundy et al. (2003) stated that harvesters operating in d_{31} mode have lower fundamental natural frequency and hence are capable of performing better in low frequency natural environments. These conclusions are important as they lead to designing energy harvesters in the cantilever configuration operating in d_{31} mode.

2.9.2 Location of forcing functions

In cantilever based energy harvesters, there are predominantly two different configurations. One common technique is base excitation where the piezo beam is clamped to a structure which vibrates at one end and the other end is left free. In the other configuration, the base is completely clamped and the force is applied at the free end. Figures 2.12 & 2.13 show the schematic of these configurations.

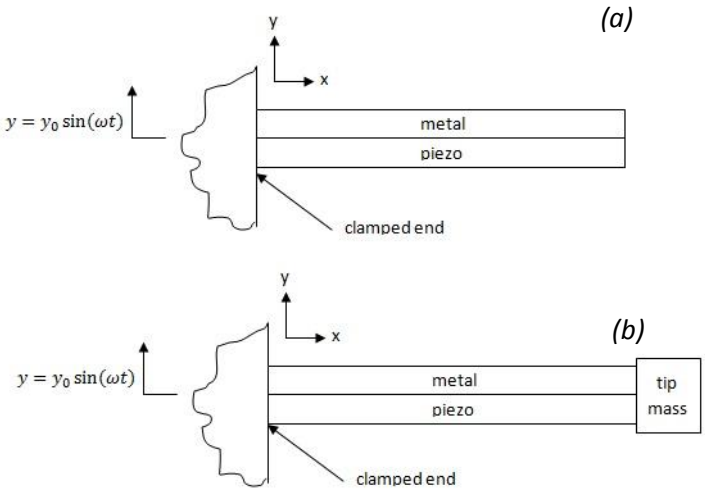

Figure 2.12: Schematic of a base excitation case (*a*) without tip mass and (*b*) with tip mass.

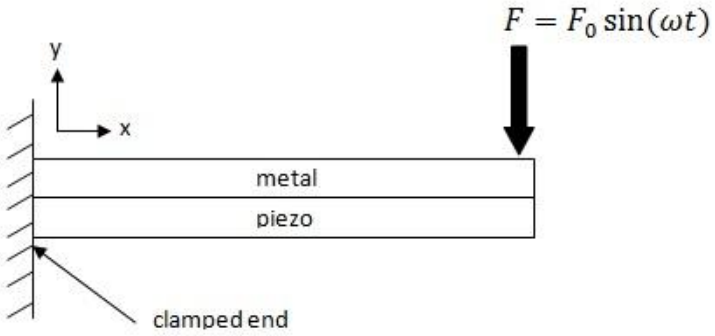

Figure 2.13: Schematic of a simple cantilevered piezo harvester with force applied at the free end.

In Figure 2.12, as indicated, the base of the cantilever is attached to the vibrating structure. It is also important to note that the base of the piezo is clamped to the structure such that all the degrees of freedom are arrested. This is essential to obtain large amounts of strain on the piezo at the base. It can also be seen from the same figure that the piezo is bonded to the metal beam. This is usually done as the piezo-ceramics are brittle and are not capable of handling high strain. Thus, a carefully chosen metal beam with a specific bending rigidity could support the piezo and also bring the natural frequency of the composite beam close to the input frequency.

In certain cases, it could be a challenge to choose the correct stiffness of the reinforcing metal beam. Alternatively, a simple solution could be found by attaching a tip mass (or a proof mass) at the end of the cantilever, as shown in Figure 2.12b. This mass can be easily chosen to tune the fundamental natural frequency to the excitation frequency. Also, the tip mass helps in achieving the required inertial characteristics and improves dynamic flexibility. An example of a cantilever harvester in the base excitation configuration with a tip mass can be found in Roundy and Wright (2004); Erturk and Inman (2011).

Figure 2.13 shows the schematic of the harvester where the loading is at the free end of the beam. This is another commonly found configuration where the system is very simple to analytically model and optimize its parameters. In certain cases, a two stage harvesting system could be developed to convert a base excitation system to the tip excitation system. Rastegar et al. (2006) developed a two stage system (as shown in Figure 2.14) where the first stage had a simple mass and spring system which acted as the energy transfer unit from the base structure to the piezo beams. By adopting such a configuration, the energy at a low frequency level could be transferred to the harvester beams having orders of magnitude higher natural frequencies. However, the choice of loading and excitation is purely governed by the vibration source and installation location. That said, these concepts contribute to the fundamental understanding of cantilever piezoelectric energy harvesters.

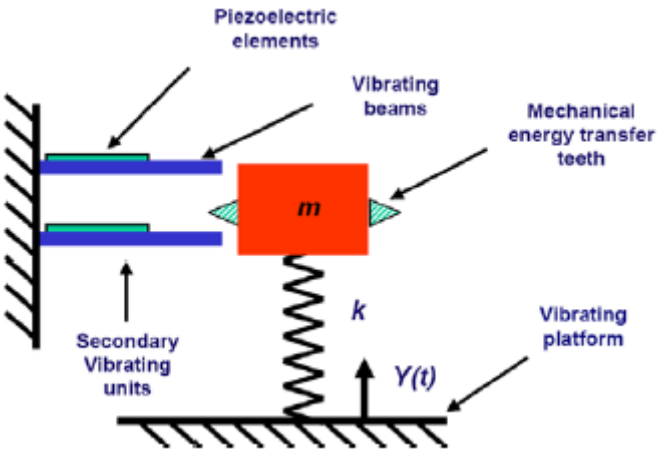

Figure 2.14: Schematic of the two-stage harvester (Rastegar et al., 2006).

2.9.3 Stacking of Piezos

In order to increase the energy harvesting abilities of these cantilever-type piezoelectric harvesters, multiple piezoelectric layers are often added. This process is called stacking. Stacking provides more area of the piezo material and hence help in greater energy conversion. However, adding layers often increase the mechanical stiffness of the system and hence avoid large amounts of strain. Figure 2.15 shows schematic of some basic stacking methods of these harvesters.

In Figure 2.15a, a homogenous bimorph is shown where the two piezos are bonded together and made to act as a vibrating beam. This is often done when the input vibration levels are high in power and frequency. This homogenous bimorph, although provides greater volume of the piezo, increases the stiffness and are only suitable for higher vibration levels. Also, the stiffness of the beam is purely governed by the mechanical properties of the piezos and hence often cannot be tuned to the input frequency. To solve this issue, a pre-calculated tip-mass could be used to tune the frequency of the system.

Figure 2.15b shows a heterogeneous bimorph where two piezo layers are bonded to a metallic beam. The applications are similar to the homogenous bimorphs, the difference being that the stiffness and mass of the metal beam could be tuned to the required frequency. Another interesting arrangement is shown in Figure 2.15c. Here, two piezos are separated where no metal beam is in-between. This arrangement is called an air-spaced bimorph. In this arrangement, the bending rigidity could be altered by varying the separation distance. The major advantage of this arrangement is that the piezo layers are shifted away from the neutral bending axis and hence help in providing large amounts of strain. Mateu and Moll (2005)

performed experiments to compare a unimorph, heterogeneous bimorph and homogeneous bimorph and concluded that the unimorph performed better under low input amplitude and frequency conditions while the bimorphs performed better under high input frequency conditions.

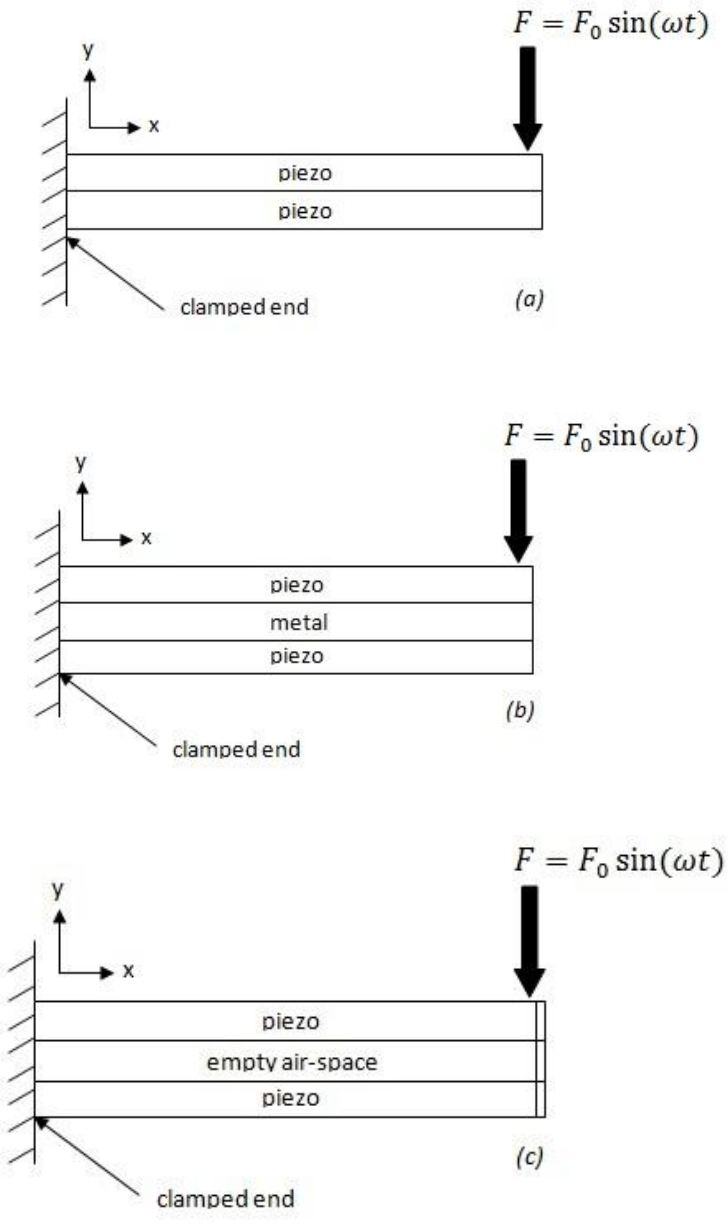

Figure 2.15: Schematic of (a) homogeneous bimorph (b) heterogeneous bimorph and (c) air-spaced bimorph.

When using multiple piezo layers, there are two ways in which these piezos could be connected electrically. They could either be connected electrically in series or in parallel. Ng and Liao (2004, 2005) performed experiments to compare a unimorph with two heterogeneous bimorphs; one connected in parallel and the other in series. When connected in

series or parallel, it was found that the result depended on the electrical load resistance of the circuit. The optimal load resistance had to be calculated according to the circuit and matched with the impedance of the piezos (explained later in this chapter). Results indicated that the unimorph performed the best under low load and frequency conditions. In bimorph configuration, the parallel connection had higher power outputs under medium loading conditions and series connection had higher power output under high loading conditions. This was due to the fact that when the piezos were connected electrically in series, the effective internal impedance of the piezo increased and hence required a higher load for better performance. Thus, it was concluded that in bimorphs, electrical loading and associated circuitry plays an important role in the power output of the system.

2.9.4 Geometry of piezos

A cantilever based harvester with a uniform rectangular cross-section is the most common configuration usually employed. However, efforts have been made to change the geometry of the piezo beam to exploit its bending characteristics and generate more power. For example, Mateu and Moll (2005) analytically compared a rectangular cantilever beam with a triangular cantilever and stated that for a given load, the triangular beam will be subjected to higher strain values and hence will be capable of harvesting more power compared to a conventional rectangular cantilever harvester.

Roundy et al. (2005) suggested a trapezoidal shaped cantilever harvester instead of a rectangular cantilever. It was stated that the trapezoidal shape would help in providing uniform strain distribution across the beam and hence are capable of providing more than twice the energy than a rectangular beam. Followed by this work, experiments were performed by Bakers et al. (2005) to compare a trapezoidal cantilever with a rectangular cantilever. It was found that for a given volume of the piezoelectric material, the trapezoidal cantilever was capable of providing up to 30% more power output. A schematic of the design is shown in figure 2.16. However, in all these analysis and findings, the effect of the geometry on fatigue was not considered. It is to be mentioned that as the strain values increase, the power output increases, but at the same time the fatigue life usually reduces.

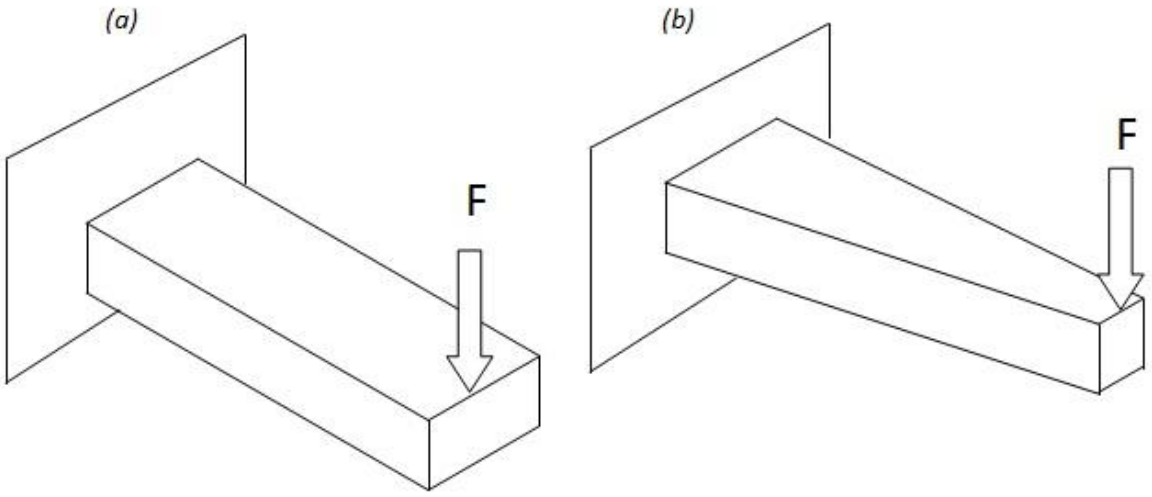

Figure 2.16: Schematic of (a) rectangular harvester (b) trapezoidal harvester.

There are several other shapes investigated for energy harvesting such as pre-stressed piezoelectric curved beams, circular ring type harvester, a piezoelectric circular 'cymbal' to name a few. Apart from geometry, boundary conditions and stacking, there are several other techniques employed by researchers across the world in this field. These peripheral techniques, yet relevant to the body of work explained here, can be found in Sodano et al. (2005), Priya (2007) and Anton and Sodano (2007), where a detailed review and comparison of vibration based piezoelectric energy harvesters are provided.

To summarize, this section has the following conclusions:

- Piezoelectric materials operating in the d_{31} mode is found to be the most effective under low vibration level conditions.
- A cantilever harvester is the most commonly used design where the input forcing function could be made to act at the base or at the free end. However, the loading condition purely depends on the nature of the vibration source.
- Cantilever bimorphs could be effective under high vibration frequency and amplitude inputs. While having a bimorph design, importance must be given to the electrical circuitry as the electrical load resistance should be matched to the effective impedance of the piezoelectric system.
- Geometry of the piezoelectric harvester could be altered to harvest more energy from the vibration source. However, it is important not to reduce the fatigue life of the harvester.

Having reviewed the various design techniques of the harvesters, it is important to bring them to the current context of this thesis. As mentioned before, this research is to exploit the possibility of using piezoelectric materials to harvest energy from wind in urban environment, in which case, the vibration should originate from fluid flow. Thus, it is vital to use the pre-existing body of knowledge in vibration-based energy harvesting to design a piezoelectric harvester to generate energy from fluid flow. The following section deals with energy harvesting from fluid flow where some of the fundamental FSI concepts and some of the recent work done by researchers in this field across the world are reviewed.

2.10 Piezoelectric energy harvesting from fluid flow

Whenever a fluid flows around a solid, there is always an interaction between the solid and the fluid and if that results in periodic solid deflection, then the fluid flow could well act as a source of input forcing function on the piezoelectric solid to harvest energy. Thus, before reviewing some of the existing techniques to design the harvester system, it is important to understand some concepts related to FSI. This section first highlights FSI terms and concepts related to this research and then reviews the harvesting techniques experimented by researchers till date.

2.10.1 Fluid-Structure Interaction (FSI)

Fluid-Structure Interaction (FSI) is physical interaction that takes place whenever a fluid in motion impinges on a solid body, whether rigid or deformable. The interaction may be one-way, meaning that the resulting deformation of the solid body (however minuscule) does not significantly affect the fluid flow; or the interaction may be two-way, meaning that the solid-body deformation is such that the flow field is affected significantly enough to instigate a continuing cycle of fluid-structure energy transfer, the manifestation usually being solid-body vibration (McCarthy et al. (2013)).

FSI can be found in everyday lives and in day to day activities. Flutter of flags, vibrations of poles and antennas on buildings and flutter of blinds over windows are trivial events that occur every day, but impose a serious challenge to the scientific and research community to understand the complex aero-elastic phenomenon behind it (Paidoussis (1998)).

Flutter of flags have been always been a topic of research for a very long time. It was long believed that flag flutter could be attributed to two phenomena: (1) Von-Karman vortex shedding at the trailing edge of the flag and (2) Kelvin-Helmholtz instability problem. Von-

Karman vortex shedding is a repeating pattern of swirling vortices caused by unsteady separation of flow of a fluid around blunt bodies (Von Karman, 1963). A classic Von-Karman vortex shedding behind a circular cylinder is shown in Figure 2.17. Kelvin-Helmholtz instability is the instability that occurs due to a velocity shear or a velocity difference across the interface between two fluids (Kelvin, 1871; Helmholtz, 1868).

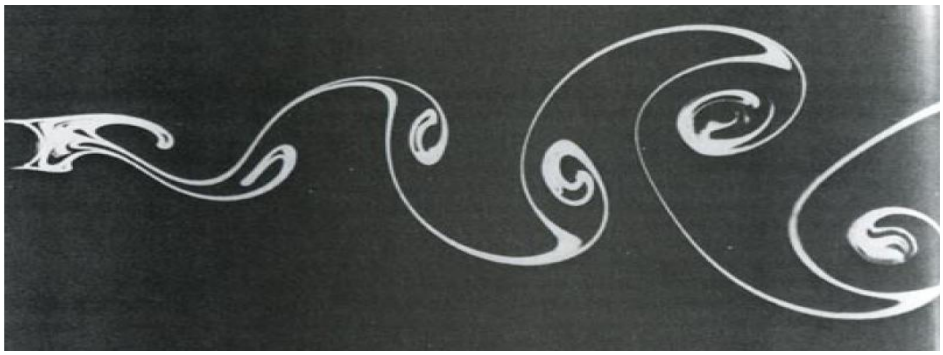

Figure 2.17: Von-Karman vortex shedding behind a circular cylinder (Van Dyke, 1982).

However, upon reconsideration, it was found that the flutter of flags is not governed by either of these two phenomena (Argentina and Mahadevan, 2005). The existence of a flexible solid boundary in the middle separates the shear layer of the working fluid on either side. This realization rules out the Kelvin-Helmholtz instability initiating flutter. Also Jun et al. (2000) performed flow visualization experiments of a flexible filament in flowing soap film. The images indicated that the vortices shed at the trailing edge of the fluttering filament were at a much higher frequency compared to the flutter frequency of the filament (Figure 2.18). This clearly indicated that the flutter frequency is not influenced by the Von-Karman vortex street.

Flutter of slender beams and plates have always been an interesting area of study for decades. Some of the earliest work was carried out by Rayleigh (1878) where a slender plate flutter was theoretically modelled. However, the plate under consideration was of infinite dimensions (in length and breadth). Thus, although this work provided a fundamental understanding of flutter, this theory could not be applied for plates of finite dimensions.

Figure 2.18: Vortex shedding at the wake of a flapping filament in a two-dimensional, parallel flow (Jun et al., 2000).

However, due to the advent of high speed aircrafts, it was highly important to analyse and characterize wing flutter. In this regard, Theodorsen (1935) explained wing flutter using analytical potential flow methods. Incompressible, inviscid and irrotational flow conditions were considered over an aerofoil. Theodorsen stated that there are two important factors to be considered during a flutter onset and sustenance:

1. The non-circulatory velocity potential, which described the pressure distribution over an aerofoil.
2. The circulatory velocity potential, which described the vortex shedding at the trailing edge of the finite plate.

Since a detailed analysis performed by Argentina and Mahadevan (2005), which was an adaptation of Theodorsen's work, is explained later in Chapter 3, a detailed analysis is not presented here. However, the "Theodorsen's functional" derived in this work is still used today as it quantifies the unsteadiness in a flow during flutter.

Since Theodorsen's equations were capable of modelling flutter of finite plates, researchers have widely used them to estimate two important aspects of flutter, namely critical flutter speed and flutter frequency. Critical flutter speed is defined as the speed at which onset of flutter occurs, i.e. the solid transitions from a static state to a limit-cycle harmonic oscillation state. Flutter frequency is defined as the frequency of the fluttering solid. Kornecki et al. (1976) examined the critical flutter speed and flutter frequency of a plate having two different boundary conditions (clamped-clamped and clamped-free). Three different theories were used to predict the two parameters and it was noted that the theories predicted flutter frequency very well, but the critical flutter speed prediction did not align well with the experiments.

Huang (1995) attempted to predict the critical flutter speed and flutter frequency in a similar manner to Kornecki et al. (1976). However, the application here was to understand palatal flutter which resulted in human snoring. A linear two dimensional model was used and experiments were performed to compare the results. It was clearly shown that the critical flutter speed depended upon the cantilever length and stiffness of the plate. Also, it was stated that steady state fluttering motion is mainly a combination of first two in-vacuo mode shapes. Figure 2.19 shows the first few transverse bending mode shapes and equation 2.28 shows the critical flutter speed (U_c) formula derived in this work.

$$U_c = (\pi\beta_i)^2 \sqrt{\frac{dB}{2\rho_f L^3}} \tag{2.28}$$

where $B = \frac{Eh^3}{12}$

E - Elastic modulus

h - Thickness of plate

d - Non-dimensional dynamic head

L - Cantilever length of plate

ρ_f - Density of the fluid flowing around the plate

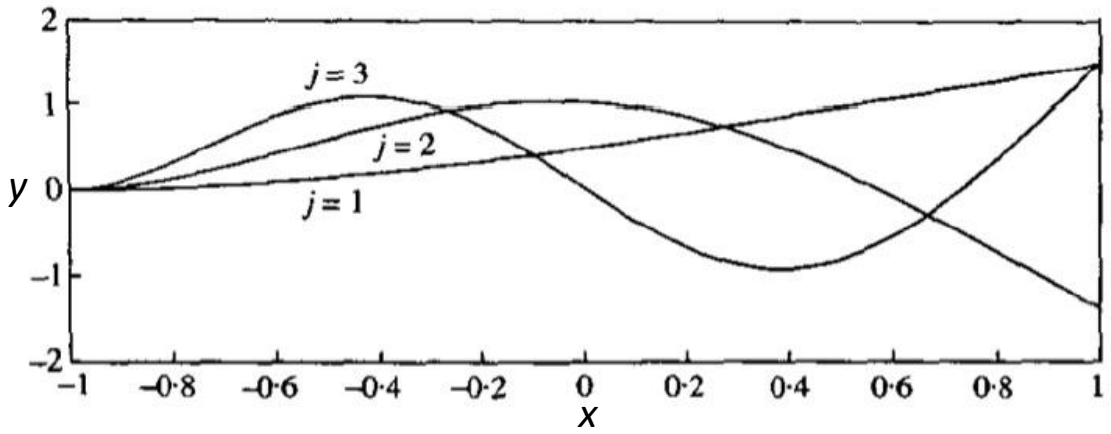

Figure 2.19: In-vacuo bending mode shapes for a cantilever beam (Huang, 1995).

Argentina and Mahadevan (2005) performed a theoretical analysis to model the flutter of thin cantilever plate of finite length. This analysis did not account for the nonlinearities in the geometry of the system. The pressure difference determined in this analysis was valid for an inviscid, incompressible flow for small amplitude motions. However, this analysis accounted for fluid added mass. A detailed mathematical model developed in this work is given later in Chapter 3. However, the two important two dimensional scaling laws which explain the flutter frequency (ω) and critical flutter speed (U_c) are given in equations (2.29 & 2.30).

$$\omega \approx \sqrt{\frac{\rho_f U^2}{\rho_s h L}} \tag{2.29}$$

$$U_c \approx \sqrt{\frac{E h^3}{\rho_f L^3}} \tag{2.30}$$

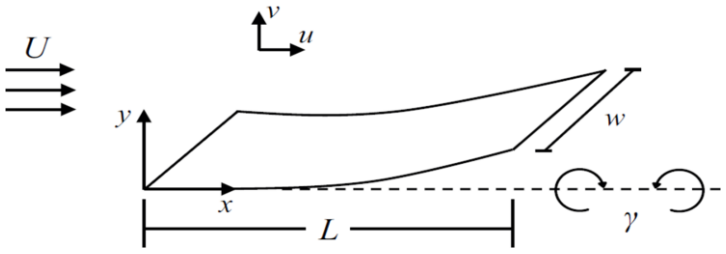

Figure 2.20: Schematic of a cantilever slender beam fluttering in parallel flow.

The symbols used here are similar to the ones used in equation (2.28). These equations are very critical as they clearly indicate the parameters influencing the critical flutter speed and flutter frequency. From equation (2.27) explained in Section 2.8.2, it is clear that for the

piezoelectric membrane fluttering in a fluid, the power output would be higher if the fluttering frequency is increased. At the same time, as mentioned in the previous chapter, wind speeds in the urban areas are usually 3-6 m/s and hence it is also important that these membranes flutter in this range. In this regard, these equations would be very useful to design the fluttering harvesters. However, it is to be noted that these scaling laws are two dimensional, i.e. the laws do not account for a finite width (w) of the plate. Thus, these scaling laws have to be experimentally validated to confirm the effects of physical properties of the solid on U_c and ω. Also, the validity of these 2D scaling laws in real 3D environment should also be experimentally validated.

Using piezoelectric beams to harvest energy from the wind would seem more encouraging at high wind speeds since equations (2.27 & 2.29) indicate that as the wind speed increases, flutter frequency would increase leading to high power output. However, this is only possible if the solid continues to flutter in its steady state. Connel and Yue (2007) stated three distinct flutter regimes:

1. Fixed point stability (no flutter)
2. Limit-cycle flapping (steady flutter)
3. Chaotic flapping (random flapping)

The existence of a solid plate in one of these three regimes will depend on the solid and fluid properties, namely stiffness, density and geometry of the solid plate/beam, density and velocity of the fluid. Experts in this field of research usually predict the fluttering mode shape and regime by defining a mass ratio (μ), which is given as:

$$\mu = \frac{\rho_s h}{\rho_f L} \tag{2.31}$$

Figure 2.21 shows the tip displacement of membranes flapping in the aforementioned regimes depending on the μ value. A more interesting observation is the difference in the power spectrum of the membranes flapping in these three flutter regimes. Figure 2.22 shows the power spectrum of these membranes and it can be clearly seen that the membrane operating in limit-cycle flapping has the maximum power while the membrane in chaotic flapping exhibits a more broadband behaviour.

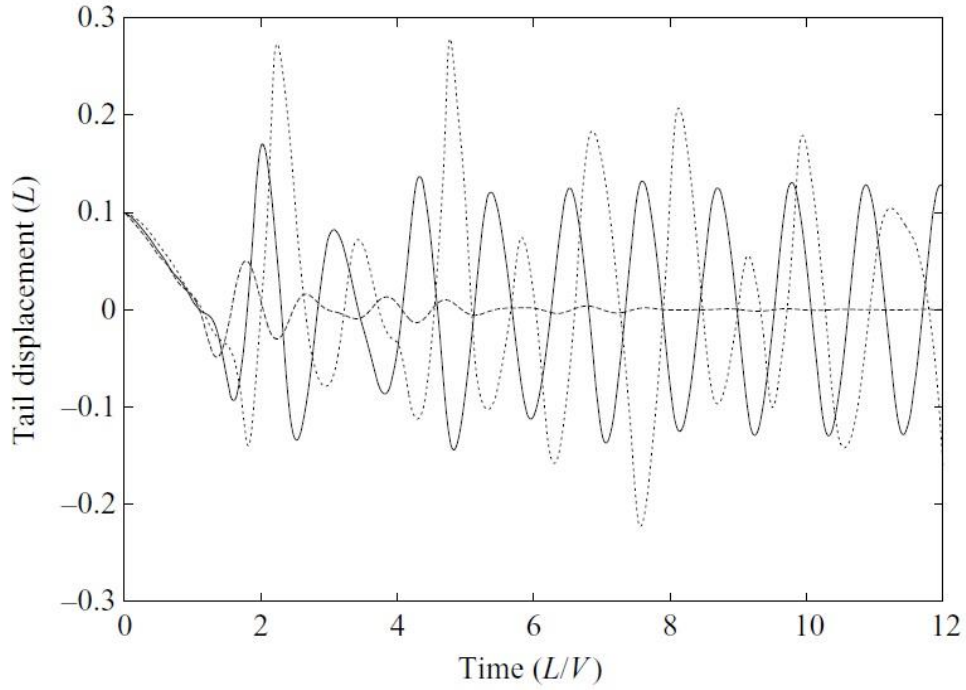

Figure 2.21: Trailing edge displacement plotted against non-dimensional time for (a) fixed point stability with μ = 0.025 (- - -), (b) limit-cycle flapping with μ = 0.1 (___) and (c) chaotic flapping with μ = 0.2 (. . .) (Connel and Yue, 2007).

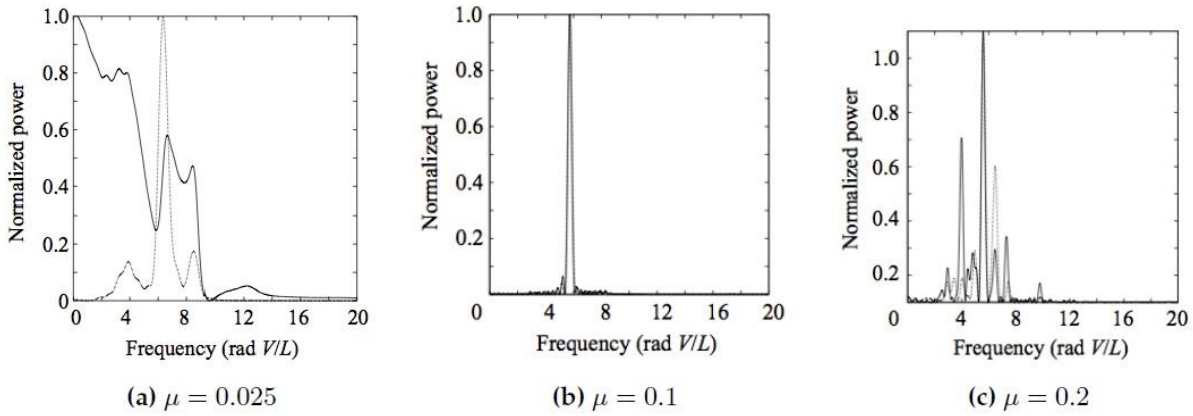

Figure 2.22: Normalized power spectrum of the trailing edge displacement for the μ values described in figure 2.21 (Connel and Yue, 2007).

Also, it has been found that depending on the mass ratio, the forcing pressure differential may excite different bending modes. Yamaguchi et al. (2000) characterised the flutter response based on three distinct mass ratio regimes:

1. For μ>0.7, they found that the flutter closely resembled the second-order in vacuo mode shapes, with travelling waves superimposed.

2. For $0.05< \mu <0.7$, they found that the oscillation modes greatly deviated from the in vacuo mode shapes, and the mode shapes were close to third-order.

3. For $\mu<0.05$, they found that the mass ratio became insignificant, and oscillatory motion was chiefly governed by frictional effects and the surrounding fluid mass.

Figure 2.23 shows the time varying membrane deformation, pressure distribution and vortex strength for two different cases having $\mu = 2.92$ and $\mu = 0.04$.

Naudascher and Rockwell (1980, 1994) classified mainly two types of flutter in their work based on the excitation mechanism. One type of flutter is Movement-Induced Excitation (MIE) flutter where the flutter of a beam immersed in a fluid flow is initiated by the fluid exciting a resonant instability in the beam, either bending or torsional. This is a self excited phenomenon without any external force being required to initiate flutter. Another type of flutter is Extraneously-Induced Excitation (EIE) flutter where the flutter of a beam immersed in a fluid flow is initiated by external, time-varying pressure gradients, such as those generated by vortex shedding off of a bluff body.

The FSI concepts explained here are put in context later when some of the analytical and experimental work performed in this research is explained. Thus, having analysed some of the important concepts involved in fluid-induced flutter, the next section reviews some of the important literature on energy harvesting from fluid flow.

2.10.2 Review of current energy harvesting techniques

One of the earliest investigations of energy harvesting from fluid flow was carried out by Taylor et al. (2001). They developed a so called 'energy harvesting eel' which consisted of a long slender PVDF bimorph material. In order to make this material have the motion of a swimming eel, a bluff body was placed upstream to the harvesting eel. As the fluid passed the bluff body, alternating vortices were shed on either side. This resulting pressure differential in water caused the bimorph to 'wave' similar to the motions of an eel. This type of flutter results from EIE as explained in the previous section. The prototype eel tested in this work was 9.5 inches long, 3 inches wide and 150 μm thick. The results showed that the power output could be maximized when the flapping frequency of the membrane was matched with the vortex shedding frequency from the upstream bluff body. In this work, the main focus was on optimizing the electrical sub-system and the work indicated that a maximum

mechanical-to-electrical energy conversion of 37% could be achieved. However, the beam flutter characteristics were not examined in detail.

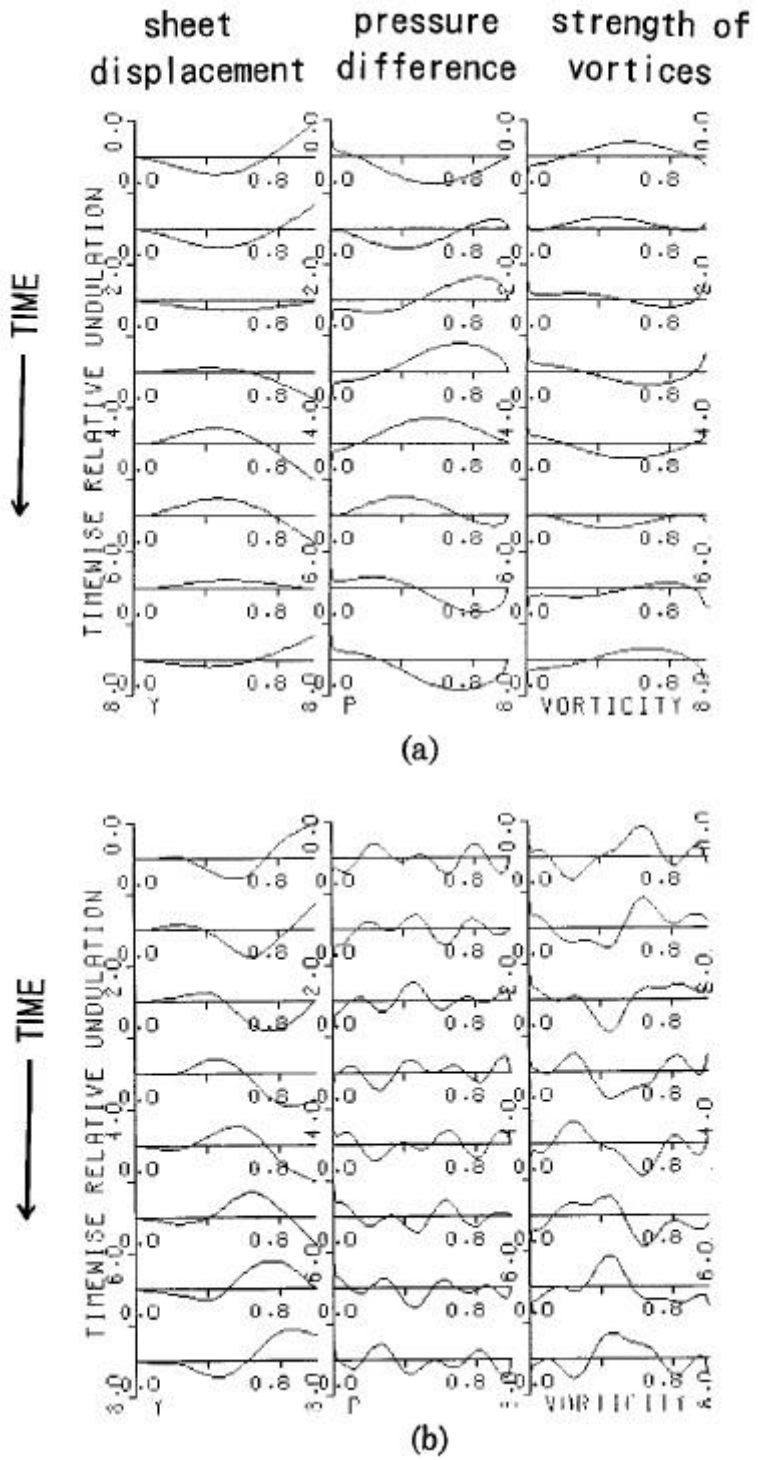

Figure 2.23: Time-varying beam deformation, pressure and vorticity results for (a) $\mu = 2.92$ and (b) $\mu = 0.04$ (Yamaguchi at al., 2000).

In order to understand the fluid-induced flutter characteristics of this energy harvesting eel, Allen and Smits (2001) performed a detailed analysis. They noted that in order for the

vortices to influence the motion of the beam, the beam must have low bending rigidity. They used different beam materials with different bending rigidities and differing lengths and conducted a Particle Image Velocimetry (PIV) flow visualization investigation to determine the effect of the vortices impinging on the beam. A schematic of the beam is shown in Figure 2.24. In this work, the size of the bluff body *D* was varied in order to effectively change the Reynolds number. However, *s/D* ratio was kept constant at unity throughout the experiments. Figure 2.25 shows the PIV images of the flapping plate with and without an upstream bluff body.

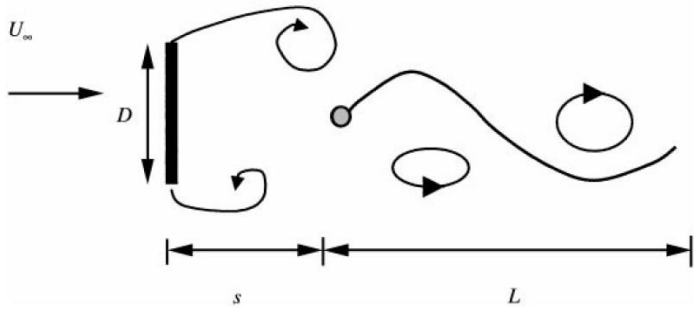

Figure 2.24: Schematic of the flapping plate behind a bluff body (Allen and Smits, 2001).

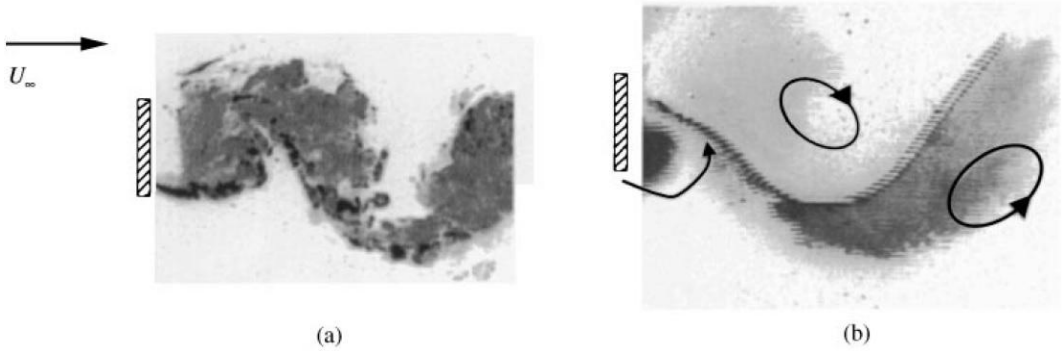

Figure 2.25: Formation of Von Karman vortex street behind a bluff body (a) without membrane and (b) the formation of a coherent beam with flexible membrane (Allen and Smits, 2001).

In 2004, Pobering and Schwesinger conducted experiments with a harvester similar to the one found in Taylor et al. (2001) (schematic shown in Figure 2.26 & 2.27). A PVDF flag and a cantilever bimorph configuration were tested. At first, theoretical calculations were performed to determine the power harvesting capabilities of the harvester submerged in rivers. It was estimated that the piezoelectric materials were capable of harvesting 140 W/m^2 with a river water speed of 2 m/s. Having analysed both the configurations, it was found that flag was capable of generating 11-32 W/m^2 of energy while the cantilever bimorph having dimensions of 5 mm length, 3 mm width and 60 μm thickness was capable of generating 6.1 μW.

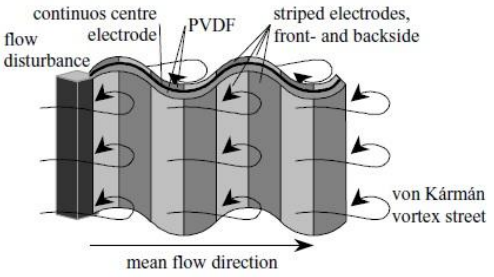

Figure 2.26: Schematic of PVDF flag generator (Pobering and Schwesinger, 2004).

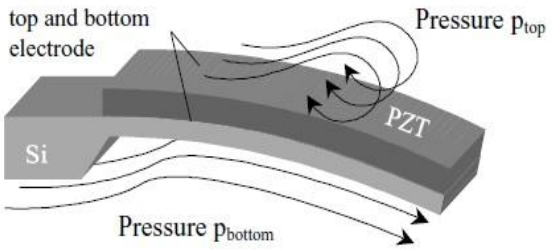

Figure 2.27: Cantilevered bimorph generator (Pobering and Schwesinger, 2004).

In this work, a calculation was shown in this work to combine multiple such harvesters to create a large scale generator. It was suggested that 100,000 cantilever elements could be arranged in an area of 1 m^2. Based on this suggested arrangement and power output estimation from one cantilever harvester, it was calculated that this large scale generator could deliver approximately 68 W/m^3 of power. This value was compared with a state of the art wind turbine having a power density of 34 W/m^3 to show that piezoelectric energy harvesting from fluid flow was more capable compared to the advanced wind turbines. A schematic of the generator is shown in Figure 2.28.

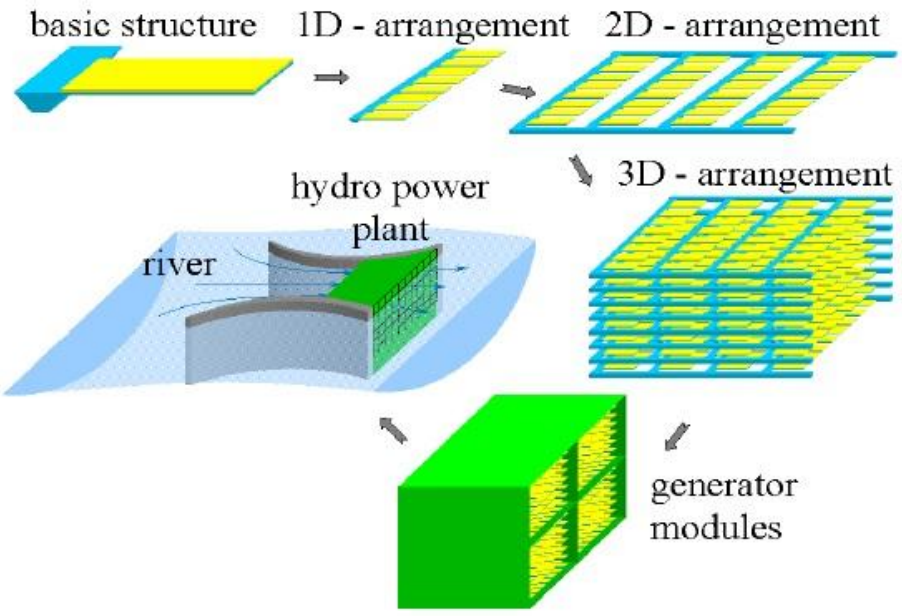

Figure 2.28: Piezoelectric array concept proposed by Pobering and Schwesinger, (2004).

Although this work showed a lot of promise, a closer look revealed several issues associated with this design. At first, the theoretical calculations were not validated. The calculations were roughly based only on the energy available in the fluid flow. A detailed analytical

analysis based on the fluid forcing function on the piezoelectric material, beam theory and mechanical strain to electrical energy conversion was not performed. Also, during scaling of the harvesters, the volume calculation was incorrect as the separation space between two consecutive harvesters was not taken into account. In reality, two harvesters cannot be immersed physically in contact with each other as it would restrict their free fluttering motion. Another important aspect not considered here is the proximity effect of the harvesters. A cantilever harvester flapping in a fluid would change the fluid flow pattern in lateral, vertical and longitudinal direction. For example, a harvester placed in close proximity downstream to the existing harvester upstream would have different flutter characteristics due to the difference in the fluid flow pattern and vortices shed from the upstream harvester impinging on the downstream one.

The aforementioned models were analysed to harvest energy predominantly from water flow. Although some useful concepts were derived from their work, the main focus in this research is to harvest energy from ambient wind in urban settings. One way to use piezoelectric materials to harvest energy from wind is to design a special piezoelectric windmill. In this regard, Priya et al. (2005) designed a device which consisted of a conventional fan that rotated in wind. The output shaft of this fan was connected to the input shaft of the piezoelectric windmill. This piezoelectric windmill consisted of 12 piezoelectric bimorphs in a circular array where one end of each of the bimorph was clamped and the free end was made to brush a rubber stopper connected to the input shaft. Thus, as the fan rotated in the wind, the power was transmitted to the rubber stopper which acted as the vibration source to the bimorphs. The experimental setup is shown in Figure 2.29.

The result indicated that when the bimorph oscillated at a frequency of 6 Hz, a maximum power of 10.2 mW was obtained through a load resistance of 4.6 kΩ. In order to further investigate the scope of this windmill, Priya (2005) used the same windmill with 10 bimorphs. It was found that at a wind speed of 10 mph (4.47 m/s), a maximum power output of 7.5 mW could be obtained. However, it was indicated that at wind speeds greater than 12 mph (5.36 m/s), the piezoelectric materials could be potentially damaged. This was mainly due to the fact that the piezoelectric materials used (PZTs) were not capable of handling large tip displacements. Thus, PZTs, although capable of providing high power outputs, were not suitable for this application.

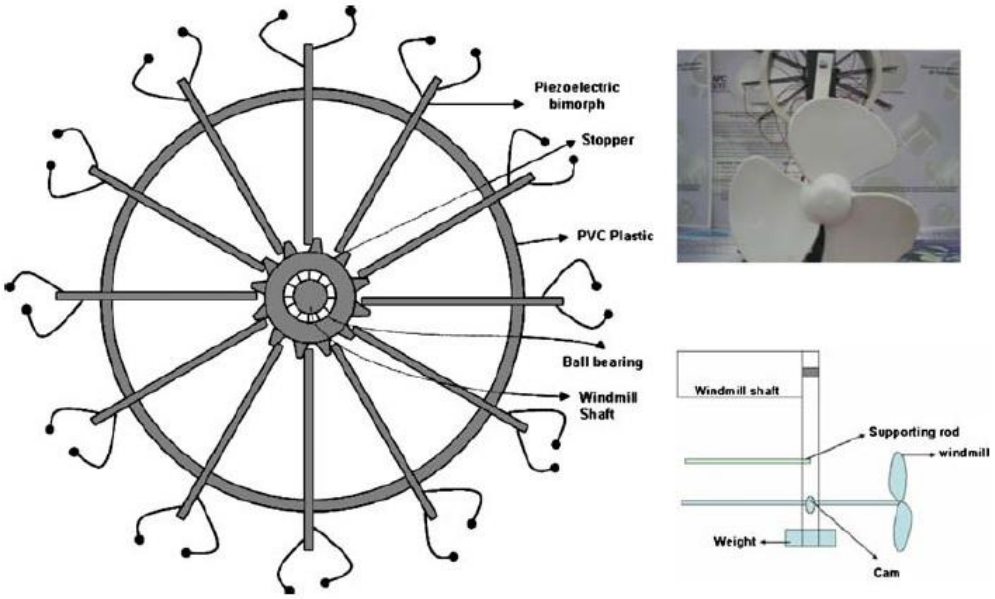

Figure 2.29: The piezoelectric windmill developed by Priya et al. (2005).

More recently, Karami et al. (2011) proposed a piezoelectric windmill using a small Vertical Axis Wind Turbine (VAWT). Permanent magnets were placed at the base of the windmill and four vertical piezoelectric PZT beams were placed from the bottom, the base being clamped and the tip containing magnets. Thus, as the windmill rotated in wind, the magnets repelled, creating an oscillatory motion in the PZT beams. This arrangement was better compared to the previous design shown in Priya (2005) in the sense that there was no physical contact and hence, friction in the current model. The experimental setup of Karami et al. (2011) is shown in Figure 2.30.

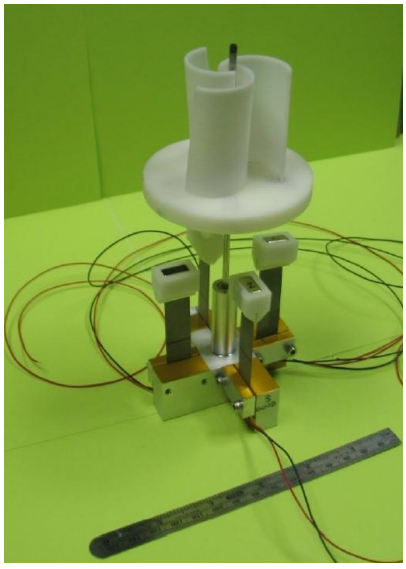

Figure 2.30: Experimental setup of wind energy harvester (Karami et al., 2011).

It was stated that this configuration was capable of producing 10 mW of power at a wind speed of only 2.3 m/s. However, it was noted that the effective magnetic coupling depended on the wind speed and rpm. Also, the use of PZT here again had the same fatigue and fracture issue. Use of PVDF might solve the fatigue issue, but would reduce the power output drastically at the same time. More importantly, it needs to be noted that the existence of a windmill does not negate the limitations of urban wind turbines previously discussed in Section 2.2. Thus, it is necessary to investigate alternative designs to harvest energy from the wind.

Hobeck and Inman (2011) came up with a "piezoelectric grass" concept to harvest energy from fluid flow. The so called "grass" consisted of vertical arrays of piezoelectric materials which could flutter in a fluid flow. Two types of piezoelectric materials were tested, namely PVDF and PZT QuickPacks™. The idea was proposed to harvest energy from rivers and other water streams having very low velocity (approximately 0.5 m/s) under highly turbulent conditions. Wind-tunnel tests were performed to investigate the feasibility of this harvester and the results indicated that PVDF "grass" provided only up to 1 μW per cantilever at 7m/s while the PZT was capable of proving up to 1mW per cantilever at 11.5 m/s. The experimental setup is shown in Figure 2.31.

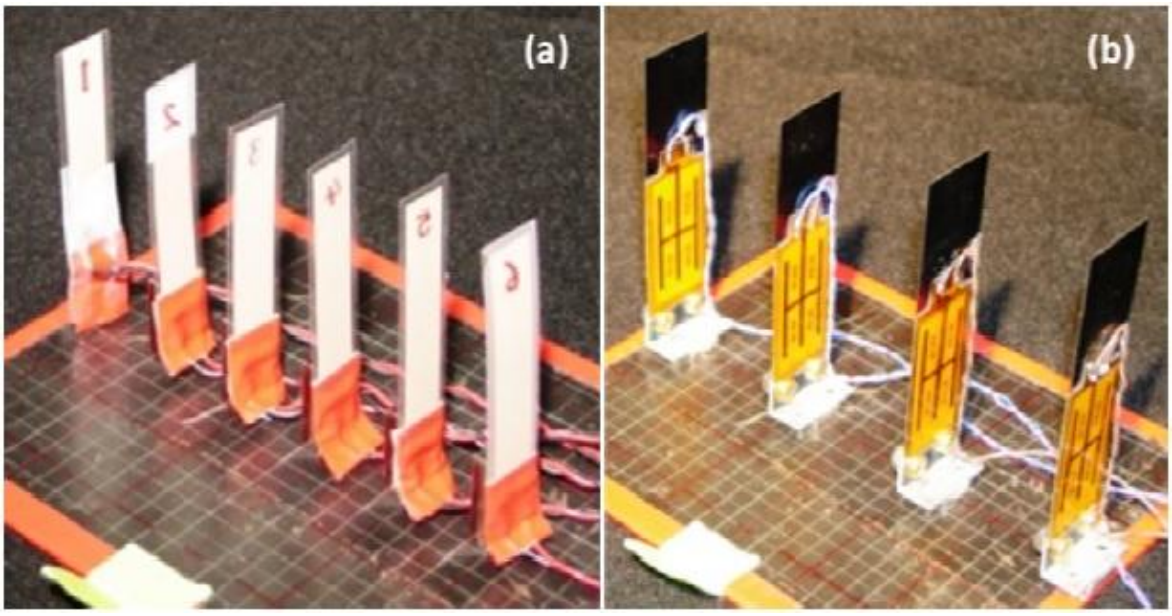

Figure 2.31: Piezoelectric grass concept with (a) PVDF array and (b) QuickPacks™ piezo array (Hobeck and Inman, 2011).

However, there are certain limitations related to this work in the context of this thesis. In urban areas, the wind speeds do not generally exceed 8 m/s. Also, the data was recorded

under very high turbulence intensity (> 25%), the rationale behind this choice not well established. Also, a bluff body upstream was used in the experiments and the aerodynamic influence of it on the flutter characteristics was not well established. However, since most of the previous works were carried out in smooth flow conditions, this work was novel as it indicated that turbulent flow conditions could assist energy harvesting.

Sirohi and Mahadik (2011) proposed a design based on galloping of a bar with triangular cross-section attached to cantilever beams bonded with piezoelectric materials. Thus, as the triangular bar galloped in the wind, the cantilever beams with piezoelectric materials converted mechanical energy to electrical energy. In this work, a complete analytical model was developed which included aerodynamic, structural and electro mechanical parameters. Experiments were performed to validate the analytical model and the result indicated that the analytical model, although had a fairly rough estimation, needed to be refined to match the experimental results. The schematic of the galloping harvester is shown in Figure 2.32. Although this device was capable of providing high power outputs (up to 53 mW) at a nominal wind speed of 5 m/s (the turbulence level not mentioned), the major disadvantage was attributed to the fatigue life of the PZTs. It was noted that the device had tip displacement of about 40 mm which are found to be extremely large for PZTs to handle over many cycles. Also, the wind must be incident on the flat surface of the triangular bar to initiate galloping motion. However, in reality, wind could approach the device from any direction.

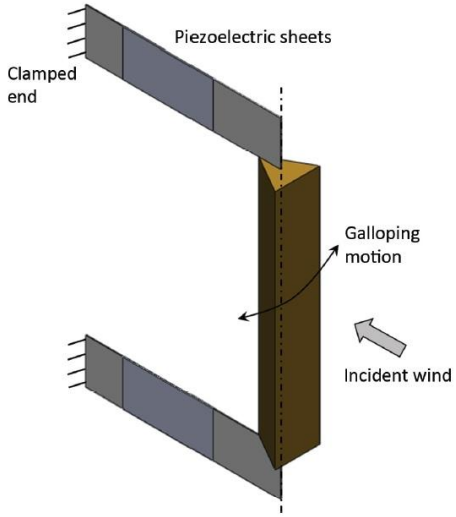

Figure 2.32: Schematic of the wind energy harvester developed by Sirohi and Mahadik (2011).

When modelling FSI, it is always a challenge to analytically model the interactions when the solid body is highly compliant. PVDF films flapping in fluid flow is one such case where deformations in structure are non-linear. The problem is even more complex when the fluid-structure model is combined with electro-mechanical model. Computational analysis could be an alternative approach to solve this problem. However, commercially available packages are generally not capable of handling large non-linear deformations during fluid and structure coupled analysis. User Defined Functions (UDF) might be required to solve the coupled multi-physics problem.

Akaydin et al. (2011) investigated energy harvesting from highly unsteady flow using piezoelectric materials. A complete computational analysis was performed and the results were experimentally validated. In this work, a PVDF piezo film was placed downstream at the wake of a circular cylinder to exploit the vortex shed off the bluff body. The leading edge of the PVDF was kept free while the trailing edge was clamped. Smoke flow visualization indicated that the vortices shed from the cylinder interacted beneficially with the PVDF to harvest useful electrical energy. A Single Degree Of Freedom (SDOF) model was used and the analysis was carried out using FLUENT (Ansys, Inc.) with the help of UDF. The computational result of the vortex shed from the cylinder impinging on the PVDF beam is shown in Figure 2.33. The computational results matched reasonably well with the experiments. It was mentioned that in order to improve the computational model, a stronger fluid-structure coupling method and a 3D analysis were required. However, that would make it significantly more computationally expensive. Also, it was noted that in order to accurately model the system, the electrical circuit connected to the piezo had to be numerically modelled as it was found elsewhere that it had significant effect on the results (Erturk and Inman, 2008). Thus, it is clear that a complete closed form analytical or computational solution to the existing multi-physics problem is highly challenging and has its own limitations in its current state.

Most of the work done to date to harvest energy from the wind using piezoelectric materials did not investigate the possibility of varying the geometry and configuration of the fluttering slender beam. Varying the geometry or attaching elements to the fluttering cantilever beam could enhance flutter characteristics to harvest more power. In this regard, one of the most important works was done by Li and Lipson (2009). They developed a novel flapping piezo-leaf generator to harvest energy from ambient wind. The device consisted of a PVDF

piezoelectric material (called the "stalk") clamped at its leading edge. A triangular polymeric material was attached to the other end of the stalk with the help of a revolute hinge. The concept behind this design was that the triangular artificial "leaf" would act as a "pendulum" amplifier to enhance flutter deformations, and hence enhance power output. The schematic of the concept is shown in Figure 2.34.

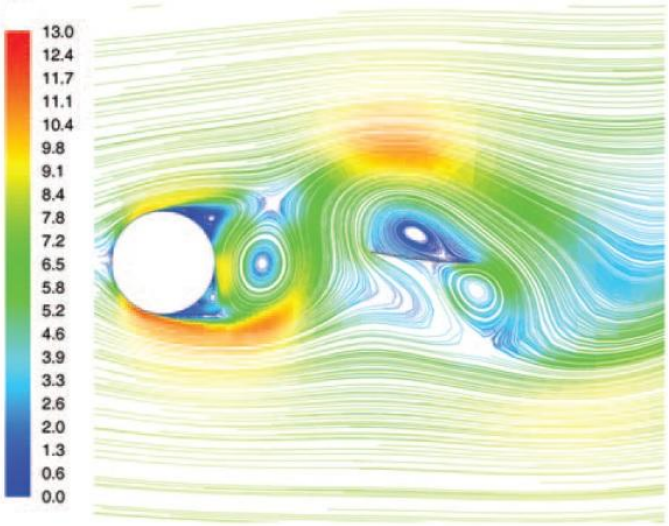

Figure 2.33: The coloured pathlines indicating the vortex shed from the bluff body reaching the top surface of the piezo flapper (Akaydin et al., 2011).

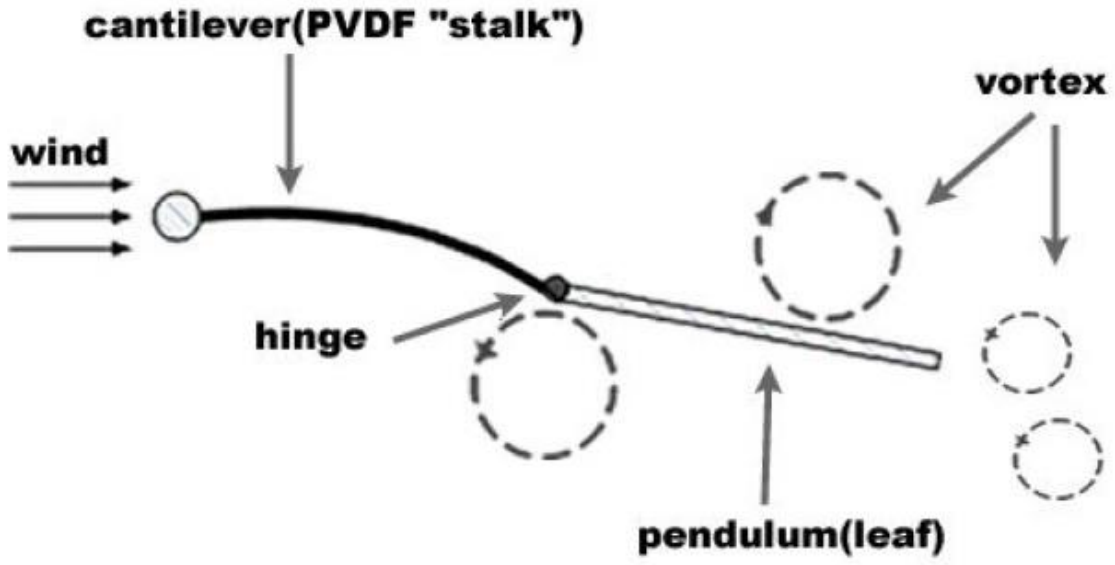

Figure 2.34: Working principle of the leaf-stalk system (Li and Lipson, 2009).

For the geometry of the "pendulum" leaf, several other shapes such as square, rhombus and trapezium were tested and it was found that the triangular shape with base and height, each 8 cm, helped in providing the maximum power output. It was believed that the vortices shed

along the edges of the triangle helped in enhancing flutter amplitude and hence more strain on the PVDF. However, the rationale behind the existence of a revolute hinge and its effect on the flutter characteristics were not explained.

This design of PVDF stalk-hinge-leaf configuration was named as horizontal configuration. Several configurations were experimented for the stalk. A single PVDF layer bonded with a plastic beam, metal beam and even PVDF bimorphs were experimented and the results revealed that a single PVDF layer by itself proved to be the most efficient design for the range of wind speeds tested (2-8 m/s).

In order to increase the power output of the device, a vertical configuration was introduced where the PVDF stalk was held vertical with respect to the horizontal flow while the triangular leaf remained the same as compared to the horizontal configuration. This configuration was also called the L-shaped configuration. Several types of stalks were experimented and it was found that a commercially available shorter PVDF stalk provided a maximum power output of 300 μW at 8 m/s. In general, the vertical configuration provided significantly higher power outputs compared to the horizontal configuration. Figure 2.35 shows both the horizontal and vertical configuration tested by Li and Lipson (2009). Figure 2.36 shows the power outputs of the long and short vertical configurations tested.

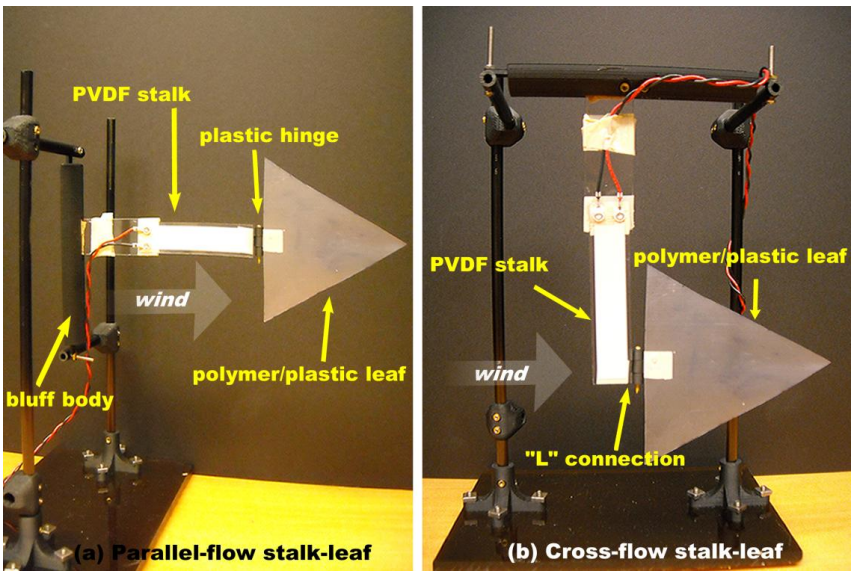

Figure 2.35: The two configurations investigated by Li and Lipson (2009) (a) Horizontal stalk and (b) Vertical stalk.

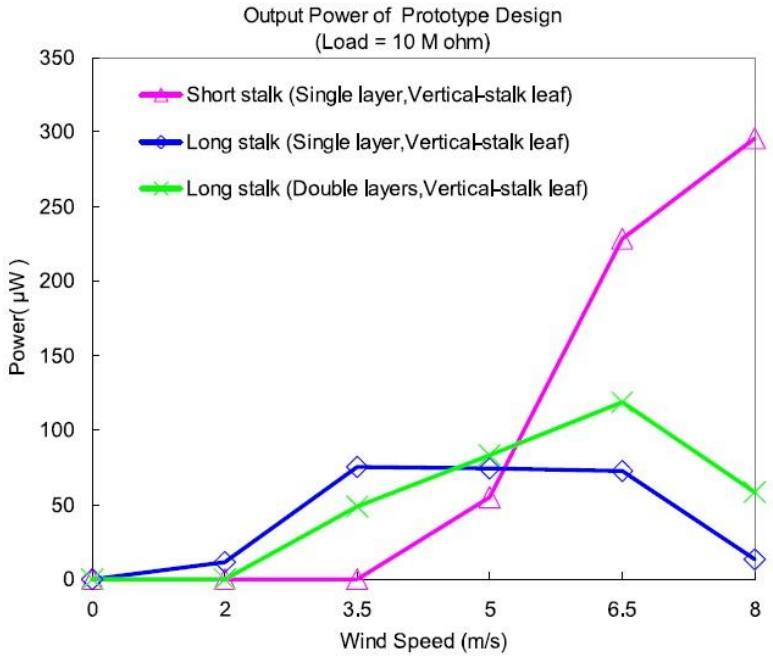

Figure 2.36: Power output of the vertical stalk configuration. Maximum power is obtained in the short stalk at higher wind speeds (Li and Lipson, 2009).

This work appeared promising as the device had an artificial leaf-like appearance and at the same time was capable of providing greater power output compared to the current piezoelectric harvesters. This leaf-like arrangement could be scaled to form an artificial tree which could blend well with the urban settings and harvest energy at the same time. However, further work is required to understand the working of this device. It was postulated that the higher power output of the vertical stalk could be attributed to coupled bending and torsional vibrations. Thus, further experiments would be required to visualize the motion of this vertical stalk to understand the reason behind the increased power output. At the same time, the triangular leaf's area and aspect ratio has to be varied to observe the effect of the leaf's geometry on the power output. This work by Li and Lipson (2009) forms the basis of this research.

The configuration of the piezoelectric beam, hinge and flapping plate was also investigated by Bryant et al. (2011). In this work, a QuickPacks™ piezoelectric material was bonded to a flexible steel beam. The leading edge of the beam was clamped while the trailing edge of the beam was attached to a thin rectangular balsa plate using a revolute plastic hinge. The harvester configuration is shown in Figure 2.37. The overall harvester length was 360 mm and the tests were performed at a Reynolds number of 175000 (which would correspond to approximately 7-8 m/s). It was found that the harvester was capable of providing 1.49 mW at this wind speed.

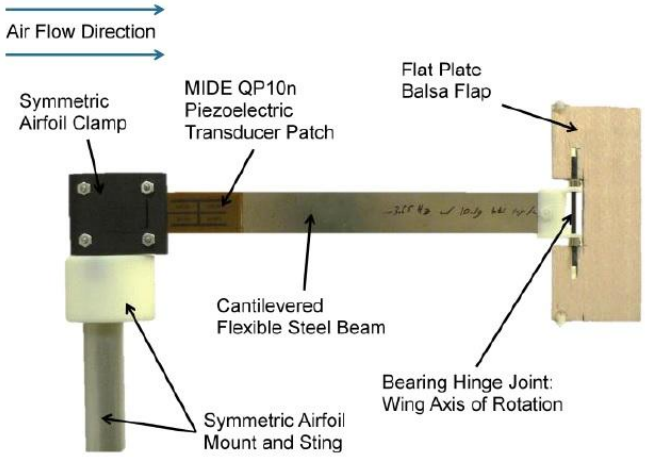

Figure 2.37: Harvester configuration developed by Bryant et al. (2009).

In order to scale up these harvesters and have several harvesters working in tandem, proximity effects of these harvesters were studied in detail. In this regard, Bryant et al. (2011, 2012) continued their work by having two similar harvesters immersed in fluid flow and displaced the harvesters in the stream-wise and cross-stream direction (Schematic is shown in Figure 2.38). It was observed that the power output of the leading (upstream) harvester was independent of the position of the trailing (downstream) harvester in the stream-wise or cross stream direction. Interestingly, it was found that the downstream harvester had a beneficial aerodynamic interaction with upstream harvester when it was displaced from 0 to 3 times the body length of the harvester downstream. It was noted that at a stream-wise non-dimensionalized distance of 2 (X/L=2 and Y/L=0), the downstream harvester provided 30% more power compared to its stand-alone case. However, cross-stream separation (Y/L) did not have any effect on the power output of the harvesters.

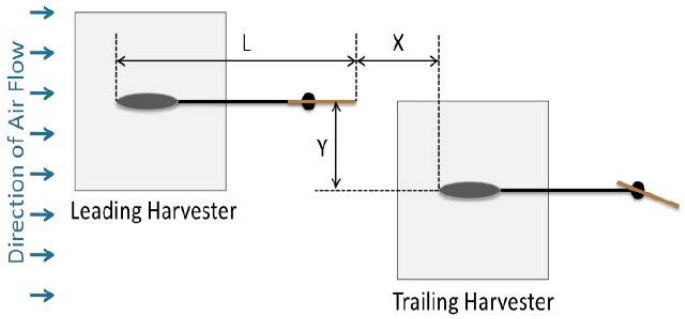

Figure 2.38: Schematic of setup for proximity experiments (Bryant et al., 2011).

In order to understand this beneficial interaction, smoke wire flow visualization experiments were conducted and based on the visual data, it was concluded that synergistic effects occurred due to an inverted drafting wake interaction phenomenon. Later, four similar

harvesters were placed in the stream-wise direction and the separation distance between them were varied. It was found that at a separation distance of *X/L*=0, all the harvesters provided more power output compared to their stand-alone cases. Figure 2.39 shows the non-dimensionalized power output of all the four harvesters when displaced at different *X/L* values between them. Although the harvesters had slightly different flapping frequencies in their stand-alone tests, when operating in tandem, they were found to be flapping at the same frequency with increased amplitude. It was also observed that there existed a specific phase difference between the harvesters and it varied linearly with the stream-wise separation distance for a given Reynolds number.

This work appears promising as unlike scaling of wind turbines, these vibration-based harvesters are found to have beneficial interactions when placed in line. All the aforementioned experiments were performed at a constant Reynolds number. In reality, wind speed is an important variable and hence the effect of wind speed on this wake interaction has to be further understood. Also, the possibility of extending this phenomenon to devices having different geometry and mechanical properties would appear to be a worthy area of research. This is due to the fact that harvesters with different mechanical stiffness and geometries would flap at different frequencies and hence would shed vortices which could be different in nature.

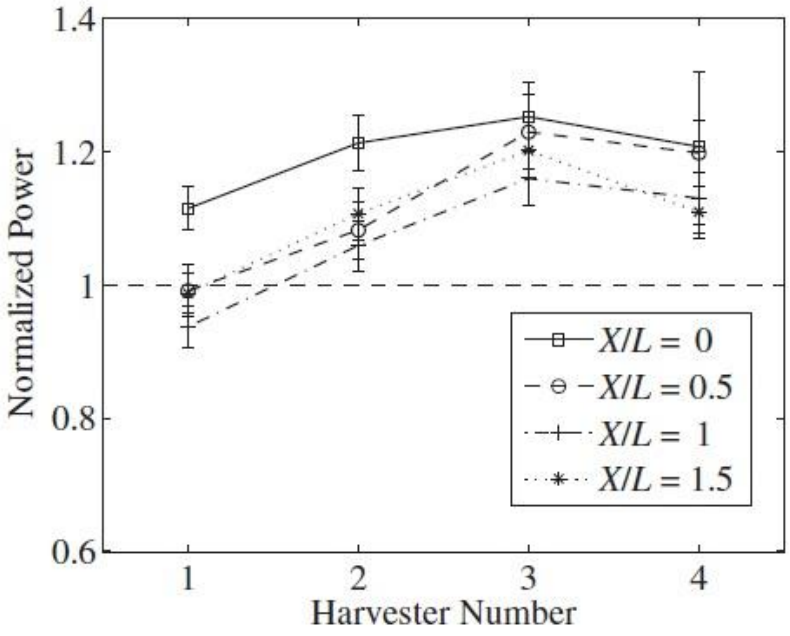

Figure 2.39: Performance of the four harvesters operating in tandem (Bryant et al., 2011).

Thus, having reviewed all the relevant literature in this area, some very promising and useful works carried out by researchers in the last decade are noted. Also, some specific research gaps in piezoelectric energy harvesting from wind-induced vibrations are clearly visible. However, before stating the specific research objectives of this thesis, it is important to understand some fundamental concepts related to the electrical circuitry involved in piezoelectric energy harvesters.

2.11 Electrical circuitry in piezoelectric energy harvesting

In piezoelectric energy harvesting from fluid flow, the first step is to convert the ambient energy into vibration energy in the harvester. However, it is also important to convert and condition the electric charge produced by the harvester to a form which could be stored or used later by an ULP device. Figure 2.40 shows the energy flow schematically (Erturk and Inman, 2011).

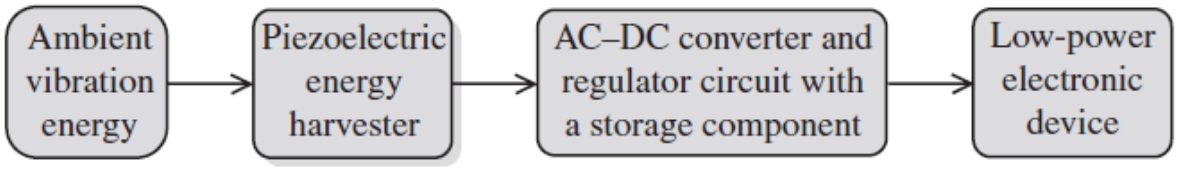

Figure 2.40: Steps involved in energy flow in piezoelectric energy harvesting (Erturk and Inman, 2011).

Thus, the third component in the flow chart is vital in the harvesting process. Figure 2.40 indicates that the AC voltage from the piezo has to be converted to DC voltage to be used by any sensor or battery. The nature of voltage generated from piezoelectric material is AC due to the fact that the strain induced in the material is always alternating when subjected to vibrations. Figure 2.41 shows a standard piezoelectric harvester circuit consisting of a full-wave rectifier, smoothing capacitor, and matching load resistance (Shu and Lien, 2006). The capacitor is used to smooth the DC voltage from the rectifier by charging and discharging based on the requirement. Most times, the DC voltage converted must be conditioned to a form suitable for the end device. However, the DC-DC conversion is not studied in detail here as it is beyond the scope of this thesis.

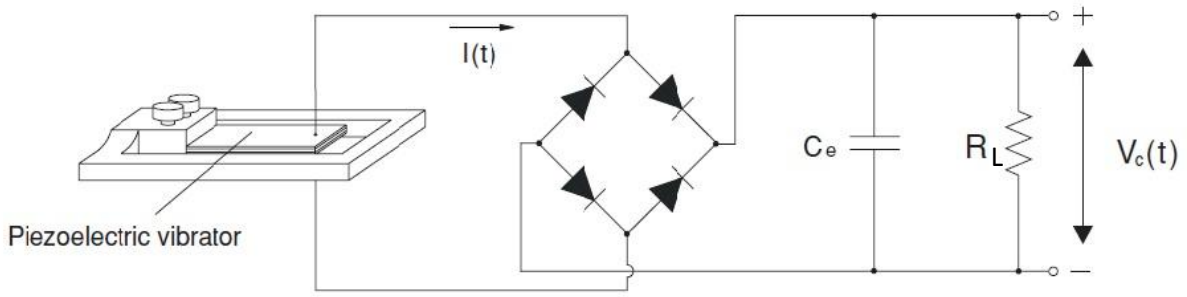

Figure 2.41: Fundamental electric circuit for piezoelectric energy harvesting system (Shu and Lien, 2006).

The load resistance (R_L) plays an important part in maximizing the power output from the harvester. To understand this, the internal circuit of a piezoelectric material has to be understood. A piezoelectric material is ideally a device consisting of an internal capacitor (C_p) and resistor (R_p) as indicated in Figure 2.42 (Ramadass and Chandrakasan, 2010).

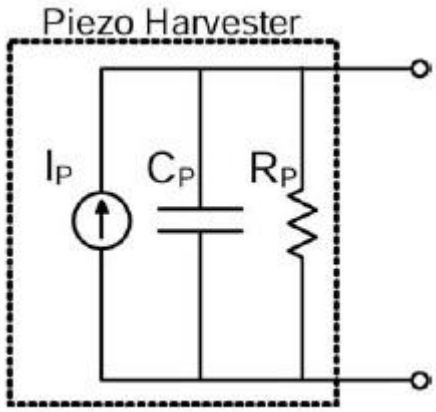

Figure 2.42: Electrical equivalent circuit of a piezoelectric material (Ramadass and Chandrakasan, 2010).

Thus, this RC circuit, when vibrates, requires an optimal load resistance (R_L) to maximize the power output. One approximate way to identify the optimal R_L for a piezoelectric harvester operating at a specific mechanical frequency (ω) is given by the following equation:

$$R_L \approx \frac{1}{C_p \omega} \tag{2.32}$$

The equation (2.32) is however an approximate estimate as it does not account for the mechanical and electrical damping associated with the system. To determine the accurate R_L theoretically, complex calculations are required. An easier alternative to identify this R_L can be done through simple experiments. A wide range of resistance values could be connected

across the harvester vibrating at a specific frequency to measure the output Root Mean Square (RMS) voltage. The power output could then be calculated according to the following equation:

$$P_{OUT} = \frac{(V_{RMS})^2}{R_L} \tag{2.33}$$

These voltage and power values could then be plotted against the load resistance values to obtain the optimal R_L which would correspond to the maximum point of the power curve. Typical voltage and power curves in a load matching experiment are shown in Figure 2.43.

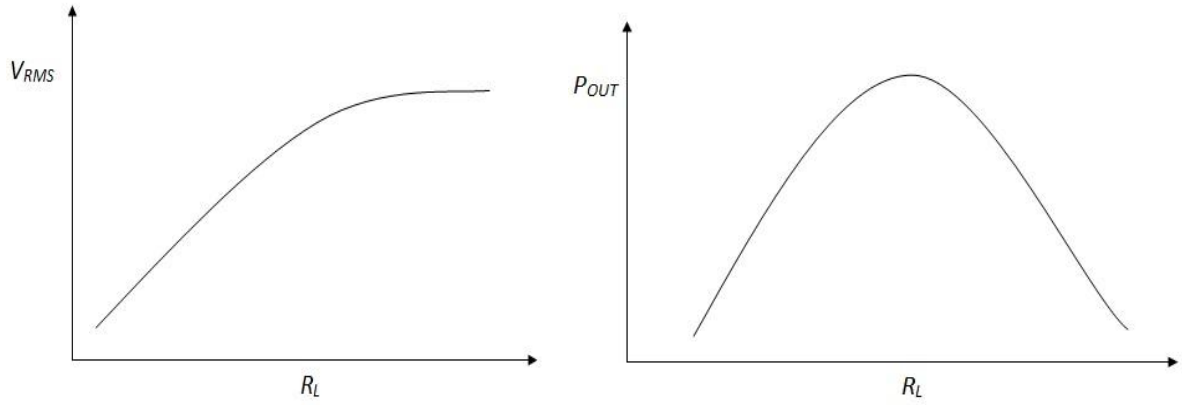

Figure 2.43: Standard voltage and Power curves plotted against load resistances for load matching.

Several research works have been carried out over the last decade to enhance the power output by investigating different circuits. While this peripheral aspect is not discussed in detail in this thesis, an extensive analysis of associated electronics can be found in Ottman et al. (2002), Guyomar et al. (2005), Sodano et al. (2004), Guan and Liao (2007) and Kong et al. (2010). Thus, having reviewed the necessary fundamental concepts involved in the electrical circuitry of the harvesting system, all the important literature related to this research have been discussed in detail. The next section states the specific research objectives of this thesis which will be addressed in the later chapters.

2.12 Scope and Objectives

Having reviewed the previous work in this research field, it is clearly evident that there are a number of questions which need to be addressed in order to have a better understanding in this area (as discussed in the previous section). These questions or gaps in research lead to the scope and objectives of this research.

In order to understand the feasibility, practicality and most importantly, the science behind piezoelectric energy harvesting from wind-induced vibrations, some of the questions which would be addressed in this body of work are as follows:

1. How are the physical and geometric properties of a three-dimensional highly compliant beam affecting its flutter onset and flutter frequency in a simple cantilever system?

2. What is the effect of the hinge, when placed at different positions along a beam, on the flutter frequency and onset velocity in a connected body system?

3. What is the possibility of increasing the power output using vertical leaf-stalk and other asymmetrical configurations for energy harvesting applications under smooth fluid flow conditions?

4. What are the proximity effects of two identical flapping piezo-leaf systems in smooth flow on their power outputs when displaced in three orthogonal directions?

In order to achieve the above mentioned tasks, the research method would include theoretical modelling of the structure and piezo, experimental work to understand FSI and computational work to supplement the experimental results.

Due to the vastness of this multi-disciplinary project, along with the need for a large test matrix, the scope of this research was limited only to the above mentioned questions. Thus, some of the aspects related to this research, but **not addressed** in this work, include:

- Development of an analytical model of the aerodynamic forces inducing flutter in the piezo-leaf system.

- The effect of fatigue of the system on the power output.

- The effect of outdoor environment including moisture and ultra-violet radiation.

- Optimization of power conditioning circuitry to suit ULP devices (i.e. battery charging, loading and associated electronics).

There are other key aspects to be addressed pertaining to this research. Some of them include:

- Visualising the three-dimensional flow characteristics downstream of a harvester, and determining the cause(s) of greater power outputs from a trailing harvester placed in tandem.

- Determining the behaviour of a single harvester when the wind is capable of approaching from an off-parallel direction.

- Understanding how the power output of single harvester varies when immersed in replicated ABL turbulence, as contrasted with the case of immersion in smooth flow.

These aspects are addressed through the outcomes of a complementary research project, undertaken by Jesse M. McCarthy. Some of the results from McCarthy's work, with due acknowledgement, will be shown later in Chapters 4 and 5 to provide a complete picture of the work required to understand the performance of these harvesters.

Chapter 3

Flutter of Simple Cantilevered and Interconnected Beams with Hinges

3.1 Introduction

Flutter analysis involves a detailed understanding of the interactions between the solid body and the fluid flowing around it as the deformation of the solid displaces the fluid and vice versa. In the case of energy harvesting from fluid flow using piezoelectric materials, understanding the science behind flutter is important to maximise flutter amplitude and frequency. In Chapter 2, equation (2.27) indicated that the power output is proportional to the square of the amplitude and cube of the frequency at resonance. This indicates that it is important to design these harvester systems in order to increase their flutter amplitudes and frequencies. Thus, it is important to understand the physical properties of the solid and fluid affecting the flutter amplitude and frequency.

Theodorsen (1935) provided mathematical explanations to the theory of flutter and aerodynamic instability. Since then, substantial work has been carried out to determine the flutter behaviour analytically, numerically and also experimentally (Datta and Gottenberg, 1975; Kornecki et al., 1976; Paidoussis, 2004; Eloy et al., 2007 and references therein). Argentina and Mahadevan (2005) investigated the flutter behaviour of cantilevered plates in axial flow using linear beam model and a simplified model based on Theodorsen's theory of flutter. The pressure difference determined in this analysis is valid for an inviscid, incompressible flow for small amplitude motions. It also accounts for finite length of the plate, vortex shedding and fluid added mass. More interestingly, they provided simple scaling laws for critical flutter velocity and flutter frequency and mentioned the relationship between the critical flutter onset velocity and the plate's natural frequency. It is also evident that these scaling laws match with the findings from other researchers. However, these are two dimensional theoretical laws and hence have to be experimentally validated for a three dimensional beam (as discussed in Chapter 2).

In this chapter, the theory of flutter experienced by simple cantilever beams are explained analytically in accordance to the model described by Argentina and Mahadevan (2005) using Theodorsen's principles. The two dimensional scaling laws derived in this work are explained. Later, these scaling laws are experimentally validated by varying some of the solid properties and geometries to investigate the extension of these scaling laws in the three dimensional environment.

Also, in order to understand the flutter behaviour of a connected body with a hinge, natural frequencies of the connected body system with variable hinge positions are derived analytically from fundamental equations. This analytical model is computationally validated and the relationship between the natural frequency of a beam and its critical flutter speed is theoretically established. Later, the critical flutter speeds of the connected bodies with several hinge positions are experimentally determined and compared with the theoretical model. The theoretical analysis, experimental setup and results are discussed in detail in the following sections.

3.2 Theory of Flutter

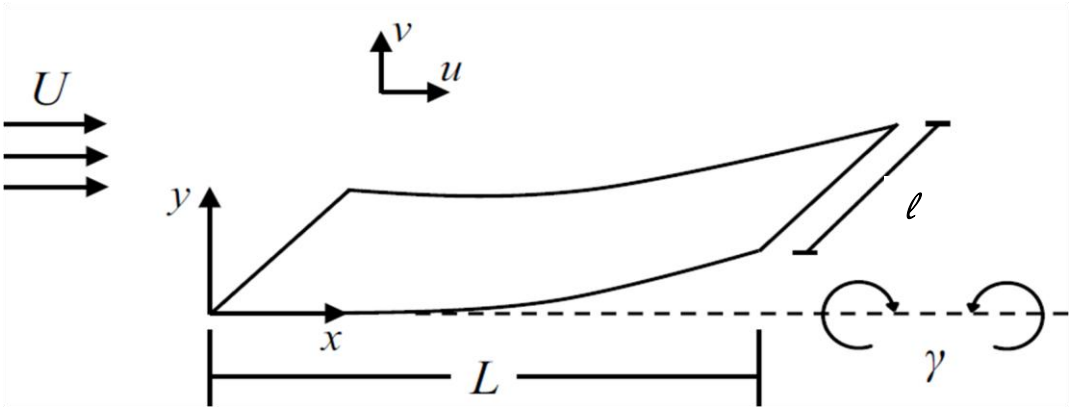

Figure 3.1: Schematic of a fluttering cantilever beam

The governing equations of flutter of a simple cantilever plate of finite length were provided by Argentina and Mahadevan (2005). A detailed explanation and derivation of the same are provided here since fluid-induced flutter forms the basis of this research. The analysis here is considered two dimensional by assuming L<<*l* (width of the flexible beam is considered to be very large compared to the finite length of the beam, thereby essentially involving a two-dimensional system). The flow considered in this two-dimensional analysis is inviscid and incompressible. Although it does not include the non-linearities in the system, it accounts for

the finite length of the beam, vortex shedding at the trailing edge and the fluid-added mass. The basic theory and equations of this work are given below.

The causation of flutter here is the pressure difference across the upper and lower surfaces of the beam. The Euler-Bernoulli beam equation of motion is given by

$$m\frac{\partial^2 y}{\partial t^2} + EI\frac{\partial^4 y}{\partial x^4} = l\Delta P \tag{3.1}$$

Where $m = \rho_s hl$

m- Mass per unit length of the plate; ρ_s- density of the plate; *h*- thickness of the plate; *l*- width of the plate.
E- Youngs modulus; *I*- moment of inertia; ΔP- pressure difference across the plate due to the fluid flow.

The pressure difference across the beam is divided into two parts according to Theodorsen's approach of fluid induced flutter. Therefore,

$$\Delta P = P_{nc} + P_{\gamma} \tag{3.2}$$

Where P_{nc}- non-circulatory pressure due to the transverse motion of the beam; P_{γ}- circulatory pressure due to vortex shedding at the trailing edge.

Non-circulatory pressure analysis

For a small deflection of the plate, the transverse velocity according to the classical airfoil theory is given by

$$v = \frac{\partial y}{\partial t} + U\frac{\partial y}{\partial x} \tag{3.3}$$

If this transverse velocity is assumed to vary slowly along the plate, then the approximate non-circulatory velocity potential is given by,

$$\emptyset_{nc} = Y\left(\frac{\partial y}{\partial t} + U\frac{\partial y}{\partial x}\right) \tag{3.4}$$

Where $Y \approx \sqrt{x(L-x)}$; *L*- length of the plate.

The linearized Bernoulli relation for non-circulatory pressure is given by,

$$P_{nc} = -2\rho_f \left(\frac{\partial \emptyset_{nc}}{\partial t} + U\frac{\partial \emptyset_{nc}}{\partial x}\right) \tag{3.5}$$

Where ρ_f- density of the fluid.

On differentiating equation (3.4) with respect to time and space, and substituting in the linearized Bernoulli equation (3.5) yields,

$$P_{nc} = -2\rho_f \frac{\partial^2 y}{\partial t^2}\sqrt{x(L-x)} + \frac{\rho_f U(2x-L)}{\sqrt{x(L-x)}}\left(\frac{\partial y}{\partial t} + U\frac{\partial y}{\partial x}\right) \tag{3.6}$$

Circulatory pressure analysis

According to Kelvin's theorem, vorticity has to be conserved in an inviscid flow of a given topology (Kundu and Cohen, 2002). Therefore, to conserve the total vorticity, if there is a vortex at the trailing edge, it should be balanced by a bound vortex in the beam with opposite strength (as shown in figure 3.1).

The position of the vortex at the trailing edge is considered as $\frac{L}{2}(1+X_o)$ and thus, to compensate, the position of the bound vortex is given by $\frac{L}{2}\left(1+\frac{1}{X_o}\right)$. Here X_O is a non-dimensional number. $X_o \in [1,\infty)$. Thus as the vortex at the trailing edge leaves the plate, the bound vortex gets further into the beam to conserve the vorticity. When X_o=1, both the vortices are exactly at the trailing edge of the beam.

The circulatory potential is given by:

$$\emptyset_\sigma = -\frac{\sigma}{2\pi}(\theta_1 - \theta_2) \tag{3.7}$$

Where σ- circulation. Therefore,

$$\emptyset_\sigma = -\frac{\sigma}{2\pi}\left[\tan^{-1}\left(\frac{Y}{X-\frac{L}{2}(1+X_o)}\right) - \tan^{-1}\left(\frac{Y}{X-\frac{L}{2}\left(1+\frac{1}{X_o}\right)}\right)\right] \tag{3.8}$$

When $X = x, y = \sqrt{x(L-x)}$ Thus,

$$\emptyset_\sigma = -\frac{\sigma}{2\pi}\tan^{-1}\left(\frac{\sqrt{x(L-x)}L\left(X_o - \frac{1}{X_o}\right)}{\frac{L^2}{2}\left(\frac{1}{X_o} + X_o + 2\right) - 2Lx\left(X_o + \frac{1}{X_o}\right)}\right) \tag{3.9}$$

Let $X_o + \frac{1}{X_o} = 2x_o$. Therefore, $X_o - \frac{1}{X_o} = 2\sqrt{x_o^2 - 1}$

Thus, the center of vorticity is given by $\frac{L(1+x_0)}{2}$.

Therefore,

$$\emptyset_\sigma = -\frac{\sigma}{2\pi}\tan^{-1}\left(\frac{\sqrt{x(L-x)}\sqrt{x_o^2-1}}{\frac{L}{2}(1+x_o) - xx_o}\right) \tag{3.10}$$

For a circulatory flow, if the vortex velocity is assumed the same as the fluid flow velocity, then,

$$\frac{\partial \emptyset_\sigma}{\partial t} = U\frac{\partial \emptyset_\sigma}{\partial x_o} \tag{3.11}$$

Substituting the above equation (3.11) in the linearized Bernoulli relation (3.5) gives

$$P_\sigma = -2\rho_f U\left(\frac{\partial \emptyset_\sigma}{\partial x_o} + \frac{\partial \emptyset_\sigma}{\partial x}\right) \tag{3.12}$$

Differentiating the velocity potential function (3.10) with respect to x and x_o and substituting in (3.12) yields

$$P_\sigma = \frac{-2\rho_f U\sigma}{2\pi}\left[\frac{2x + L(x_o - 1)}{L\sqrt{x_o^2-1}\sqrt{x(L-x)}}\right] \tag{3.13}$$

For a distribution of vortices along the horizontal axis of strength γ,

$$\sigma = \gamma\left(\frac{L}{2}\right)dx_o \tag{3.14}$$

Therefore,

$$P_\gamma = \frac{-\rho_f U}{2\pi\sqrt{x(L-x)}} \int_1^\infty \frac{2x + L(x_o - 1)}{\sqrt{x_o^2 - 1}} \gamma dx_o \tag{3.15}$$

The vortex sheet strength is determined by the Kutta condition which states that the horizontal component of the velocity does not diverge at the trailing edge. This implies that the total velocity potential has a finite variation at the trailing edge of the beam. Thus,

$$\frac{\partial}{\partial x}\left(\emptyset_\gamma + \emptyset_{nc}\right) = finite\ (when\ x = L) \tag{3.16}$$

On differentiating the velocity potential equations (3.4) and (3.10) and substituting in the above equation (3.16) yields

$$\frac{1}{2\pi} \int_1^\infty \sqrt{\frac{x_o + 1}{x_o - 1}} \gamma dx_o = \frac{\partial y}{\partial t} + U \frac{\partial y}{\partial x} \tag{3.17}$$

Multiplying by the RHS and dividing by the LHS of the above equation (3.17) to the RHS of equation (3.15) yields

$$P_\gamma = \frac{-\rho_f U}{\sqrt{x(L-x)}} \left(\frac{\partial y}{\partial t} + U \frac{\partial y}{\partial x}\right) \left[\frac{2x \int_1^\infty \frac{\gamma dx_o}{\sqrt{x_o^2 - 1}}}{\int_1^\infty \sqrt{\frac{x_o+1}{x_o-1}} \gamma dx_o} + L \frac{\int_1^\infty \frac{x_o \gamma dx_o}{\sqrt{x_o^2 - 1}}}{\int_1^\infty \sqrt{\frac{x_o+1}{x_o-1}} \gamma dx_o} - \frac{L \int_1^\infty \frac{\gamma dx_o}{\sqrt{x_o^2 - 1}}}{\int_1^\infty \sqrt{\frac{x_o+1}{x_o-1}} \gamma dx_o} \right] \tag{3.18}$$

Here, the Theodorsen functional, C, is defined as

$$C = \frac{\int_1^\infty \frac{x_o \gamma dx_o}{\sqrt{x_o^2 - 1}}}{\int_1^\infty \sqrt{\frac{x_o+1}{x_o-1}} \gamma dx_o} \tag{3.19}$$

Thus,

$$1 - C = \frac{\int_1^{\infty} \frac{\gamma dx_o}{\sqrt{x_o^2 - 1}}}{\int_1^{\infty} \sqrt{\frac{x_o + 1}{x_o - 1}} \gamma dx_o} \tag{3.20}$$

On substituting equation (3.19) and (3.20) in equation (3.20), the equation yields

$$P_\gamma = \frac{-\rho_f U}{\sqrt{x(L-x)}} \left(\frac{\partial y}{\partial t} + U \frac{\partial y}{\partial x} \right) [L(2C - 1) + 2x(1 - C)] \tag{3.21}$$

By adding equations (3.6) and (3.21), the total pressure is given by

$$\Delta P = -2\rho_f UC \left(\sqrt{\frac{L-x}{x}} \right) \left(\frac{\partial y}{\partial t} + U \frac{\partial y}{\partial x} \right) - 2L\rho_f \frac{\partial^2 y}{\partial t^2} \left(\frac{\sqrt{x(L-x)}}{L} \right) \tag{3.22}$$

Substituting (3.22) in (3.1) gives the equation of motion as,

$$m \frac{\partial^2 y}{\partial t^2} + EI \frac{\partial^4 y}{\partial x^4} = -l \left[2\rho_f UC \left(\sqrt{\frac{L-x}{x}} \right) \left(\frac{\partial y}{\partial t} + U \frac{\partial y}{\partial x} \right) + 2L\rho_f \frac{\partial^2 y}{\partial t^2} \left(\frac{\sqrt{x(L-x)}}{L} \right) \right] \tag{3.23}$$

The equation (3.23) describes the complete motion of the cantilever beam subjected to fluid-induced flutter. It is seen that, even after a two dimensional analysis, linearization and other assumptions in the analytical model, the final governing equation is fairly complex. Thus, developing a complete analytical solution for a very three dimensional realistic fluttering high compliant beam is highly challenging. Also, due to the assumptions, the analytical model usually is not reliable and do not match well with experiments. Moreover, the analytical model gets very complex for a connected body system investigated by Li and Lipson (2009) and Bryant et al. (2011).

However, as mentioned earlier, in the case of piezoelectric energy harvesting, the two most important factors to be considered during the design of the harvester system are critical flutter speed and flutter frequency. Thus, it could be sufficient to derive an analytical model that determines the critical flutter speed and flutter frequency of a fluttering beam. When a cantilever beam is placed in a fluid flow and the flow velocity is increased, the beam initially remains statically stable and then begins to flutter at a particular fluid velocity. This velocity

is called as the critical flutter velocity (U_c). Argentina and Mahadevan (2005) provided a simple explanation to determine the system parameters responsible for flutter frequency and critical flutter velocity. According to this explanation, when a rigid cantilever beam (hinged at the leading edge) oscillates, the fluid pressure through a small angle should equal to the inertia of the oscillating plate.

Fluid pressure through a small angle, $\theta = \rho_f U^2 \theta$

The inertia of the oscillating plate = $\rho_s h \omega^2 L \theta$

By equating the above two terms, the flutter frequency is scaled as

$$\omega \approx \sqrt{\frac{\rho_f U^2}{\rho_s h L}} \tag{3.24}$$

However, for the onset of flutter, the flutter frequency should be equal to the lowest bending mode vibration frequency (ω_b) which is given by

$$\omega_b \approx \sqrt{\frac{E h^2}{\rho_s L^4}} \tag{3.25}$$

Therefore, the critical flutter onset velocity is given by,

$$U_c \approx \sqrt{\frac{E h^3}{\rho_f L^3}} \tag{3.26}$$

where E - elastic modulus; h - thickness of plate; L - cantilever length of plate; ρ_f - density of the fluid flowing around the plate; ρ_s - density of beam. Please note that the nomenclature remains the same for the entire section. The system parameters affecting the critical flutter velocity are clearly stated here. Also, the relationship between the critical flutter velocity and the natural frequency of the plate is established. Since the pressure across the plate should be able to excite the lowest resonant bending mode, the critical flutter velocity is directly proportional to the plate's natural frequency. Huang (1995) also stated the critical flutter velocity as a function of beam's stiffness, density and its cantilever length, which matches with the above scaling laws (3.24) and (3.26).

However, there are some key questions to be answered in order to utilize these scaling laws for designing the energy harvesting system. Some of the questions include:

- Are these theoretical laws experimentally validated to determine the relationship of the flutter velocity and flutter frequency in terms of the physical properties of the beam?
- Are these two-dimensional scaling laws applicable for three-dimensional beams?
- Is there a specific relationship between the natural frequency of the beam and its critical flutter speed? If so, can this relationship be extended to a connected body system?

In the following sections, attempts are made to answer these questions. At first, theoretical and computational analyses are conducted on the connected body system to derive its natural frequencies for the first few modes of interest. Later, experiments are connected on simple cantilevered cantilever beams and connected bodies to validate the theoretical scaling laws and derivations.

3.3 Flutter of a connected body

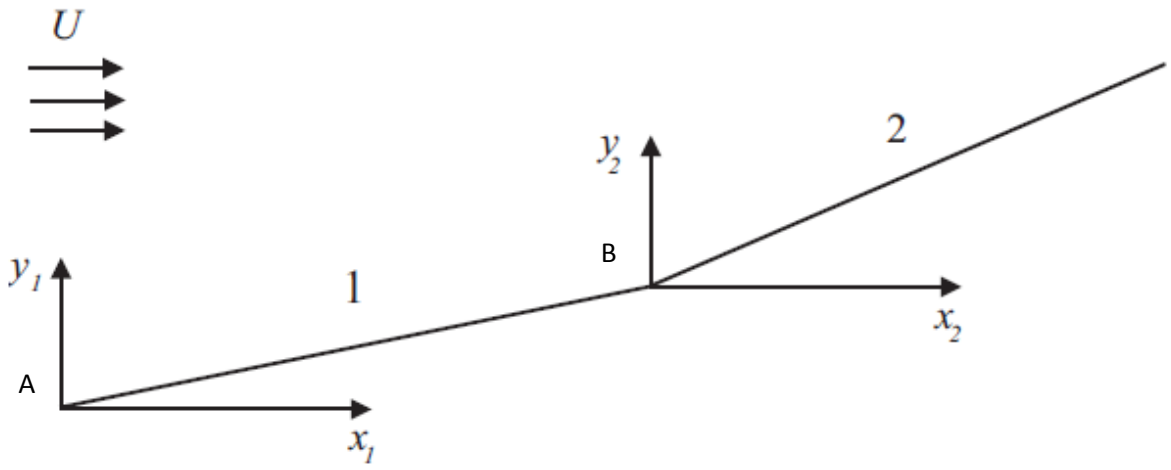

Figure 3.2: Schematic of a connected body

In the previous section, equations (3.25) and (3.26) clearly indicate that the critical flutter velocity is directly proportional to the natural frequency of the fluttering beam. Thus, instead of attempting to achieve a complete analytical solution on the connected body which is extremely challenging, a simple natural frequency analysis of a connected body, by placing the hinge at several positions, would indicate the flutter onset behaviour as a function of hinge position within the connected body system. In this regard, the author performed the natural frequency analysis and the derivation is shown in this section.

In the figure 3.2, the connected body considered for a free vibration analysis is shown. The two elements (elements 1 and 2) are joined at B with a free hinge. The element 1 considered is clamped at A. For this analysis both the elements of the beam were considered to have the same material properties and geometry in order to isolate the effect of a hinge on the cantilever beam dynamics. In the below derivation, the overall total length of the beam was considered to be *L* and the non-dimensional hinge position, $\eta = \frac{x}{L}$, where *x* is the horizontal position of the hinge along the beam. The cantilever lengths of the elements 1 and 2 were L_1 and L_2 respectively, where $L_1 = \eta L$ and $L_2 = (1-\eta)L$.

According to Euler-Bernoulli beam theory for element 1,

$$m\frac{\partial^2 y_1}{\partial t^2} + EI\frac{\partial^4 y_1}{\partial x_1^4} = 0 \tag{3.27}$$

and for element 2,

$$m\frac{\partial^2 y_2}{\partial {t_2}^2} + (EI)\frac{\partial^4 y_2}{\partial x_2^4} = 0 \tag{3.28}$$

The variable separable method was used to solve the partial differential equations with respect to time and space. Thus,

$$\begin{aligned} y_1 &= Y_1(x)T_1(t) \\ y_2 &= Y_2(x)T_2(t) \end{aligned} \tag{3.29}$$

The general solution for the space functions in equation (3.29) is given by,

$$\begin{aligned} Y_1(x) &= C_1\cos\beta x + \mathrm{C}_2\sin\beta x + C_3\cos h\beta x + C_4\sin h\beta x \\ Y_2(x) &= C_5\cos\beta x + \mathrm{C}_6\sin\beta x + C_7\cos h\beta x + C_8\sin h\beta x \end{aligned} \tag{3.30}$$

where $\mathrm{C}_{1,2,\ldots 8}$ are constants and $\beta^4 = \frac{\rho_s A\omega^2}{EI}$.

Therefore,

$$\omega = (\beta L)^2\sqrt{\frac{EI}{\rho_s AL^4}} \tag{3.31}$$

where E - Young's modulus of the beam; ρ_s - density of the solid beam; *I* - moment of inertia of the beam; *A* - cross-sectional area of the beam; *L* - cantilever length of beam.

Now, the Boundary Conditions (BC) to solve for the constants, and also to determine the natural frequencies, are stated below.

BC at A (clamped):

$$y_1(0,t) = 0; \qquad \frac{\partial y_1}{\partial x_1}(0,t) = 0 \tag{3.32}$$

BC at B (free hinge):

$$\frac{\partial^2 y_1}{\partial x_1^2}(L_1,t) = 0; \quad y_2(0,t) = y_1(L_1,t); \quad \frac{\partial^2 y_2}{\partial x_2^2}(0,t) = 0\,; \quad \frac{\partial^3 y_1}{\partial x_1^3}(L_1,t) = \frac{\partial^3 y_2}{\partial x_2^3}(0,t) \tag{3.33}$$

BC at C (free end):

$$\frac{\partial^2 y_2}{\partial x_2^2}(L_2,t) = 0; \quad \frac{\partial^3 y_2}{\partial x_2^3}(L_2,t) = 0 \tag{3.34}$$

Now, applying boundary conditions at A to the general solution (3.30) yields

$$\begin{aligned} C_1 + C_3 &= 0 \\ C_2 + C_4 &= 0 \end{aligned} \tag{3.35}$$

Applying boundary conditions at B yields

$$\begin{aligned} C_7 - C_5 &= 0 \\ C_1(\cos\eta\beta L - \cos h\,\eta\beta L) + C_2(\sin\eta\beta L - \sin h\,\eta\beta L) - 2C_5 &= 0 \\ C_1(\cos\eta\beta L + \cos h\,\eta\beta L) + C_2(\sin\eta\beta L + \sin h\,\eta\beta L) &= 0 \\ -C_2(\cos\eta\beta L + \cos h\,\eta\beta L) + C_1(\sin\eta\beta L - \sin h\,\eta\beta L) + C_6 - C_8 &= 0 \end{aligned} \tag{3.36}$$

Applying boundary conditions at C yields

$$\begin{aligned} C_5(\cos h\,(1-\eta)\beta L - \cos(1-\eta)\beta L) - C_6\sin(1-\eta)\beta L + C_8(\sin h\,(1-\eta)\beta L) &= 0 \\ C_5(\sin(1-\eta)\beta L + \sin h\,(1-\eta)\beta L) - C_6\cos(1-\eta)\beta L + C_8\cos h\,(1-\eta)\beta L &= 0 \end{aligned} \tag{3.37}$$

Now the equations (3.35), (3.36) and (3.37) had to be solved simultaneously to obtain the solution. However, from equations (3.35) and (3.36), it is deduced that

$$C_3 = -C_1$$

$$C_4 = -C_2 \tag{3.38}$$

$$C_7 = C_5$$

Thus, equations (3.35), (3.36) and (3.37) reduced to five simultaneous equations which could be solved simultaneously to obtain the solutions. The homogenous equation can be written as $[C]\{z\} = 0$, where *C* is the coefficient matrix. However, determining the natural frequencies of system involved solving the equations for a non trivial case. Thus, the determinant of the coefficient matrix of these homogenous equations had to set to zero, i.e. $det[C] = 0$.

The determinant of the simplified coefficient matrix is given by,

$$\begin{vmatrix}
\cos\eta\lambda & \sin\eta\lambda & -2 & 0 & 0 \\
-\cos h\,\eta\lambda & -\sin h\,\eta\lambda & & & \\
\cos\eta\lambda & \sin\eta\lambda & 0 & 0 & 0 \\
+\cos h\,\eta\lambda & +\sin h\,\eta\lambda & & & \\
\sin\eta\lambda & -\cos\eta\lambda & 0 & 1 & -1 \\
-\sin h\,\eta\lambda & -\cos h\ \eta\lambda & & & \\
0 & 0 & \cos h\,(1-\eta)A & -\sin(1-\eta)A & \sin h\,(1-\eta)A \\
 & & -\cos(1-\eta)A & & \\
0 & 0 & \sin(1-\eta)A & -\cos(1-\eta)A & \cos h\,(1-\eta)A \\
 & & +\sin h\,(1-\eta)A & &
\end{vmatrix} \tag{3.39}$$

where $\beta L = \lambda$

Therefore, the determinant, when equated to zero yielded the characteristic equation for the connected body system. For a simple comparison, a hinge position of $\eta = 0.5$ is taken as an example here. Therefore, the characteristic equation reduces as:

$$8\cos h\,(0.5\lambda)\,.\sin h\,(0.5\lambda).\cos(0.5\lambda)^2 - 8\sin(0.5\lambda)\,.\cos h\,(0.5\lambda)^2\,.\cos(0.5\lambda) = 0 \tag{3.40}$$

Roots of this equation yield:

$$\lambda_1 = 0, \quad \lambda_2 = 3.14, \ \lambda_3 = 7.83 \quad \lambda_4 = 9.42, \ \lambda_5 = 14.14 \ \ldots\ldots \tag{3.41}$$

Where the natural frequency from equation (3.31) can be re-written as

$$\omega = (A_i)^2 \sqrt{\frac{EI}{\rho A L^4}} \quad i = 1,2,3 \ldots \tag{3.41}$$

The roots of equation (3.40) were obtained numerically in the MATLAB® Symbolic Math Toolbox™ where an equation root discovery algorithm employing a mixture of secant stepping, bi-sectioning, and quadratic interpolation was used (MATLAB®, 2010).

It should be noted that the general solutions for the time functions in equation (3.29) were not considered, because a steady-state, sinusoidal undulations of the multi-element beam was considered, the transient vibrational effects were ignored. This can be justified given the non-temporal nature of the energy harvesters considered in this study.

3.3.1 Comparison of connected body to a simple cantilever beam

In order to quantify the impact of a hinge on the natural frequencies of a cantilever beam, the roots in equation (3.41) were compared to the standard clamped-free cantilever beam modes. The characteristic equation for a clamped-free Euler-Bernoulli beam was a very simple to derive and hence was obtained from a standard handbook (Blevins, 1979) as

$$\cos(\lambda)\,.\cos h\,(\lambda) = -1 \tag{3.42}$$

The roots of the equation yield

$$A_1 = 1.87, \quad A_2 = 4.69, \ A_3 = 7.85 \quad A_4 = 10.99, \ A_5 = 14.13 \ \ldots. \tag{3.43}$$

where the natural frequency is given by equation (3.41). A comparison of the roots obtained from equations (3.41) and (3.43) is shown in Table 3.1.

A modal natural frequency ratio, R_i is defined as,

$$R_i = \frac{\omega_{i,hinge}}{\omega_{i,uniform}} \tag{3.44}$$

where $\omega_{i,hinge}$ is the i^{th} hinged-beam natural frequency and $\omega_{i,uniform}$ is the i^{th} uniform-beam natural frequency. Table 3.2 presents the beam properties that are used herein, and Figure 3.3 shows *Ri* plotted against η for the second through fourth vibration modes. Since $R_1 = 0$ for all η considered, it was excluded from this analysis (the rigid body mode for the connected/hinged system was not considered in the analysis). In this analysis, only R_2 (fundamental flexible mode) is considered for comparison. The behaviour of R_2 in Figure 3.3 is explained along with Figures 3.5 & 3.6 in the following section (Section 3.4).

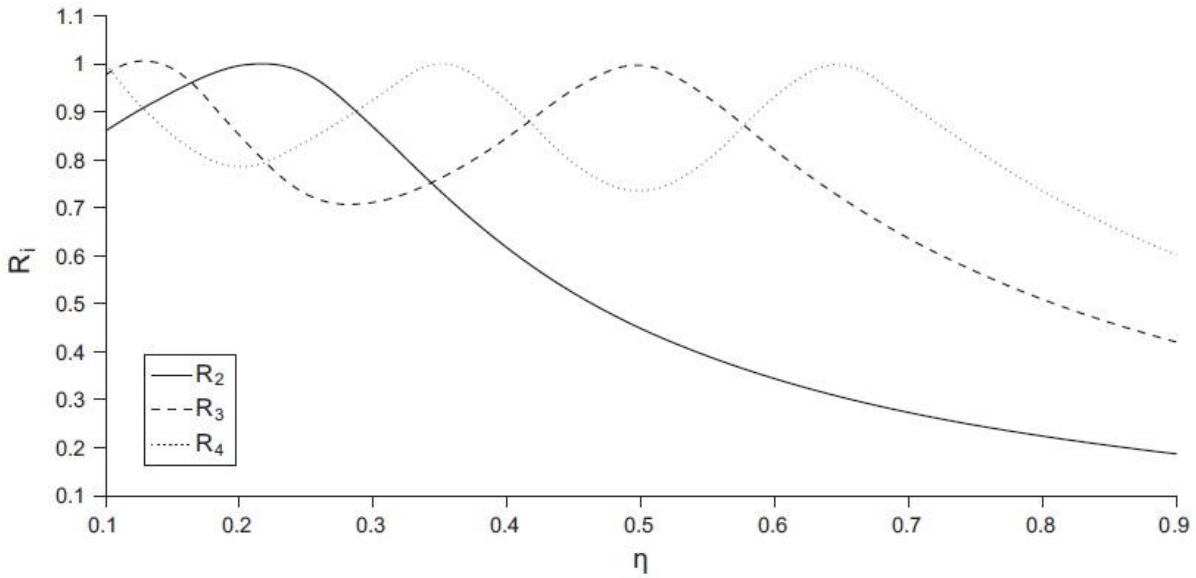

Figure 3.3: Natural frequencies calculated for R_1, R_2 and R_3 for all hinge positions.

Table 3.1: Comparison of characteristic equation roots with $\boldsymbol{\eta = 0.5}$

Mode number	Uniform beam	Hinged beam
λ_1	1.87	0 (rigid body mode)
λ_2	4.69	3.14
λ_3	7.85	7.83
λ_4	10.99	9.42

Table 3.2: Properties of beam used in connected body analysis

Property	Symbol	Value
Stiffness	EI	2.7 x 10^{-4} Nm^2
Beam density	ρ_s	995 kg/m^3
Cross-sectional area	A	21 mm^2
Beam length	L	236 mm
Beam thickness	h	0.35 mm
Beam width	w	60 mm
Mass ratio	μ	1.19

3.4 Computational modelling

Substantiation of the analytical model was accomplished through the use of the modal analysis capabilities in ANSYS® Mechanical™ (Release 13.0). The beam geometry was clamped at the leading edge ($x = 0$), free at the trailing edge ($x = L$) and had a revolute hinge at η as per the analytical model in Section 3.3. No modal or viscous damping was applied to the model. In Figure 3.4, the computational setup is illustrated.

Figure 3.4 indicates the mesh fineness and given the simplicity of the analysis, this was considered sufficient. A stress and strain solution were not desired, nor was the geometry complex, therefore uniform mesh sizing and density were selected (see Appendix A for mesh details). In a modal analysis, the shifted Block Lanczos algorithm was used by default (ANSYS®, 2010) to directly extract the Eigen values and Eigen vectors of a structural model containing rigid-body modes. The interested reader may find details of the algorithm in Grimes et al. (1994).

The first four bending-mode Eigen values and vectors of the system were extracted; transverse and torsional vibration modes were neglected, despite the fact that with the present boundary conditions, they were inherently obtained in the solution process. The uniform beam solutions were determined first, so that the computational natural frequency ratio $R_{i,comp}$ could be evaluated at discrete beam hinge locations, for the second through fourth modes, as shown in Figure 3.5.

There was excellent correlation between the computational and analytical models. Given that the boundary conditions were well defined, the geometry is relatively elementary, and no fluid-forcing term was present, it was expected that the two solutions corresponded to this degree, even with the two distinct numerical solution methods utilised between the analytical and computational models. The second normalised mode shapes are displayed for the cases where $\eta = 0.2$ (Figure 3.6a) and $\eta = 0.9$ (Figure 3.6b), corresponding to the points where R_2 was maximum and minimum, respectively. A free hinge introduced an additional degree of freedom to the system, providing greater flexibility. When the hinge was positioned at $\eta = 0.1$, the leading element was very short and hence the system behaved similarly to a hinged-free beam. Thus, the natural frequency was lower than the clamped-free uniform beam and $R_2 < 1$. When $\eta = 0.2$, the hinge did not affect the mode shape (Figure 3.6a), therefore rendering $R_2 \approx 1$. However, as η increased, the leading element length increased thus permitting greater flexibility; consequently, R_2 decreased. This was because the trailing element became shorter and stiffer compared to the leading element. Also, the maximum displacement of the second mode shape occurred at the hinge location, as the hinge was shifted towards the trailing edge (Figure 3.6b)).

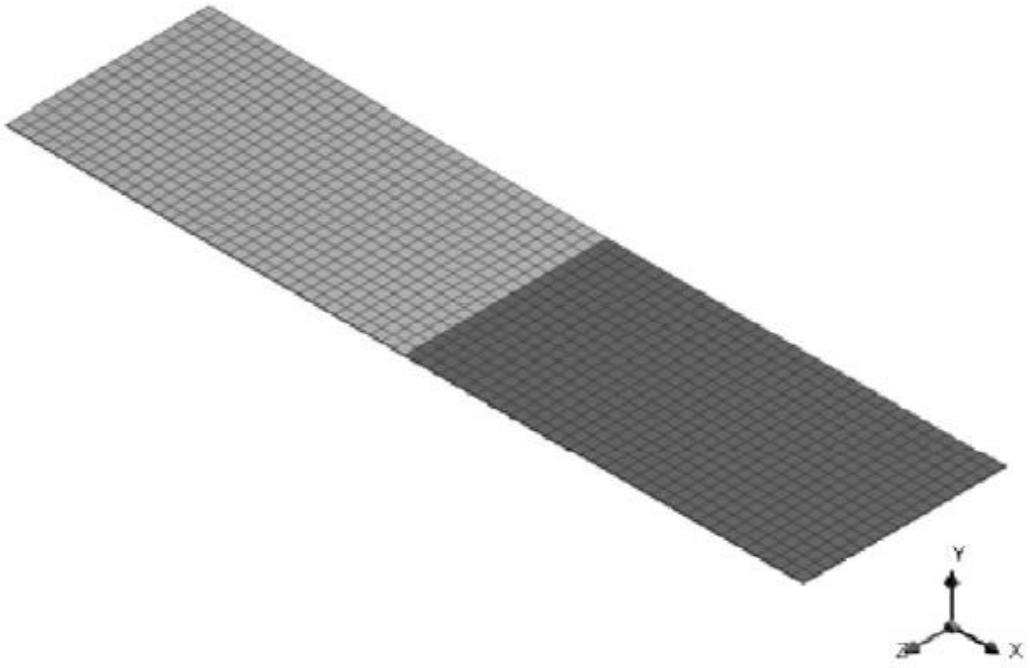

Figure 3.4: Computational setup of the connected body with $\boldsymbol{\eta = 0.5}$

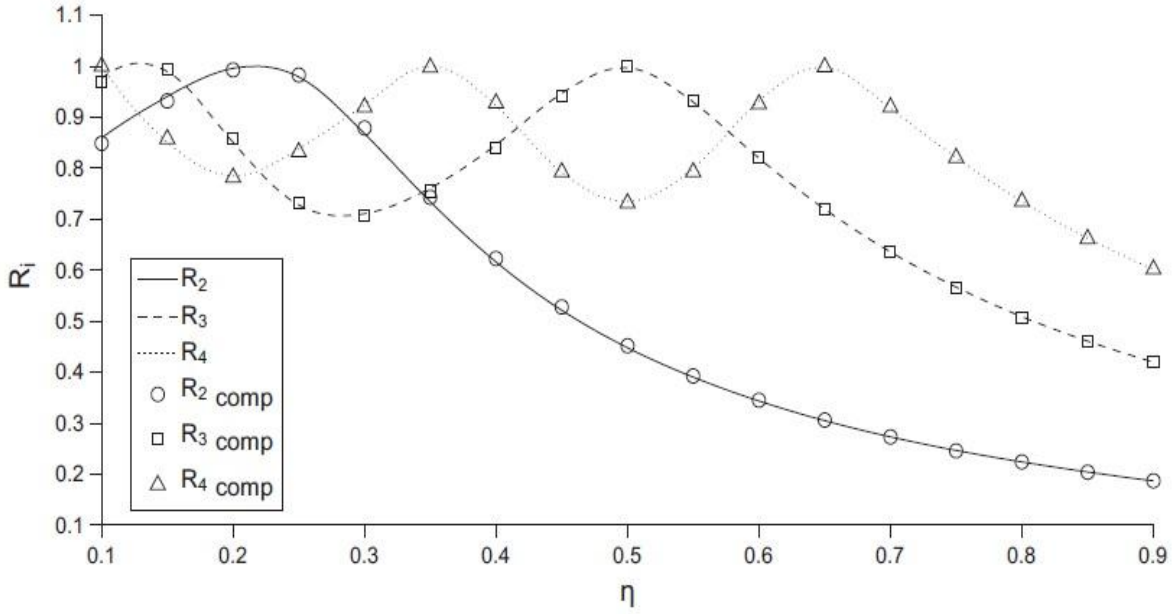

Figure 3.5: Computational and analytical R_i comparison.

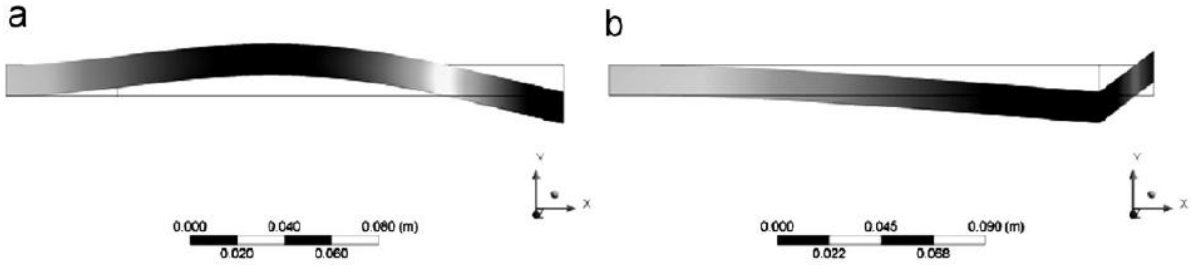

Figure 3.6: Computationally determined mode shapes for the hinge positions which give (a) maximum R_2 ($\boldsymbol{\eta = 0.2}$) and (b) minimum R_2 ($\boldsymbol{\eta = 0.9}$).

3.5 Experimental rationale

Experimental studies were conducted to validate the theoretical analysis. The experiments were divided into two parts. At first, experiments were conducted to validate the theoretical scaling laws (equations (3.24) and (3.26)). To validate the theoretical scaling laws, different materials with varying cantilever lengths were used and tested for their critical flutter speed and flutter frequency. Later, experiments were performed to validate the theoretical analysis and the effect of hinge at different positions on their critical flutter speed.

Equations (3.24) and (3.26) can be re-written as:

$$U_c = K_1 \sqrt{\frac{Eh^3}{\rho_f L^3}} \tag{3.45}$$

$$\omega = K_2 \sqrt{\frac{\rho_f U^2}{\rho_s h L}} \tag{3.46}$$

where the constants of proportionality K_1 and K_2 can be experimentally derived. By performing experiments with different materials and cantilever lengths, and by experimentally determining the critical flutter speed and frequency, it could be verified if a constant K value exists in each equation (3.45) and (3.46), respectively. By obtaining a constant K value, it could be concluded that these scaling laws are indeed valid and also applicable for a three dimensional case.

On the other hand, equations (3.25) and (3.26) suggest that the critical flutter frequency of a beam is proportional to its natural frequency. In Section 3.3, natural frequencies of the first few modes of a connected body system with hinges at different positions along the beam were analytically determined. Thus, by determining the critical flutter speeds of these connected beams experimentally, this proportionality of critical flutter speed and natural frequency could be verified.

Similar to the non-dimensional natural frequency ratio mentioned in equation (3.44), the critical flutter speed of these connected beams were compared with a uniform cantilever beam of the same cantilever length, thus establishing a non-dimensional critical flutter speed ratio, v, defined as

$$v = \frac{U_{C,hinge}}{U_{C,uniform}} \tag{3.47}$$

$$R_i \propto v \tag{3.48}$$

where $U_{C,uniform}$ and $U_{C,hinge}$ are critical flutter speed of the uniform cantilever beam and hinged/connected beam respectively; R_i is the natural frequency ratio. Thus, the proportionality (equation (3.48)) could be verified experimentally and would prove to be very crucial in the understanding of the flutter characteristics of a connected body. In the following sections, the experimental setup, methodology and results are discussed in detail.

3.6 Experimental setup

3.6.1 Wind tunnel

Experiments were carried out in smooth, parallel-flow, free-stream conditions. The tests were conducted in RMIT University's Aeronautical Wind Tunnel, which is a closed-circuit tunnel having a test section 1.32 m high, 1.07 m wide and 2.7 m long. The wind tunnel was powered by an 100kW-DC motor driving a six-bladed fan. The maximum speed of the wind tunnel was 45m/s, and anti-turbulence screens coupled with a contraction ratio of 4:1 gave longitudinal turbulence intensity levels of less than 0.5%.

A pitot-static tube was mounted in the wind tunnel, and connected to an MKS® Baratron™ pressure transducer for flow-speed measurements. Experiments were conducted over a series of weeks, and thus the air density in the wind tunnel fluctuated over the course of time. Therefore, an error analysis was conducted to evaluate the consequence of standardising the density to an International Standard Atmosphere value of 1.23kg/m^3. A maximum error in velocity measurements of 0.5% was found, and as this is considered negligible, the air density in the flow velocity calculations was standardised.

3.6.2 Clamping stand

A base stand was securely fastened into the wind-tunnel test section, and a steel strip having a height of 600 mm, a stream-wise dimension of 12 mm, and a transverse dimension of 1.75 mm, was clamped to the base stand at the top, and bolted to the wind tunnel floor at the bottom. The beams were then clamped at the leading edge using another shorter steel strip fastened to the longer one, so that the transverse dimension (the width) of the base clamping system was 3.5 mm. The schematic figure of the transverse clamping width and stream-wise length of the strip is shown in Figure 3.8. The effect of the clamping base geometry on the critical flutter speed of these beams was evaluated, and by incrementally increasing the width of the clamp past 3.5 mm for the given clamp geometry, the critical flutter speed increased gradually. Nevertheless, the increase in critical flutter speed from a theoretically infinitesimally thin clamping base, to the width used here was found to be negligible (McCarthy et al., 2014). The beams were placed well outside of the test-section boundary layer, and far enough away from the base stand so that no aerodynamic interference could occur. The clamping base was guyed to the wind-tunnel walls so that no transverse vibrations

manifested during the testing process. In Figure 3.7, an image of the wind-tunnel configuration for the experiments is shown.

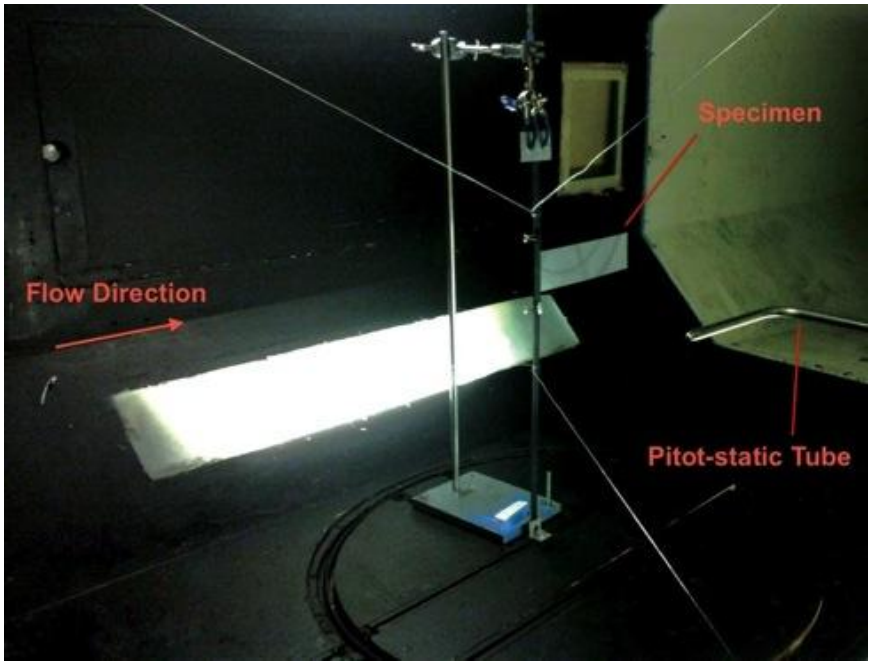

Figure 3.7: Experimental setup in the wind tunnel.

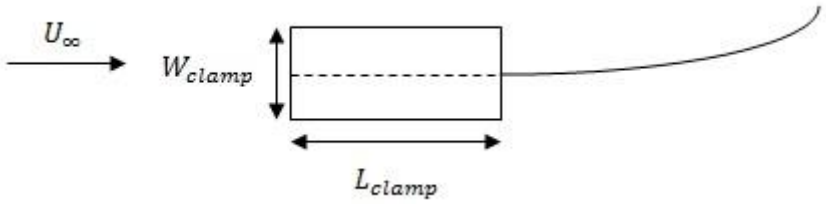

Figure 3.8: Schematic cross-sectional view of clamping strip (clamping base enlarged for clarity).

3.6.3 High-speed imaging

In order to experimentally determine the flutter frequency of the simple cantilever beams and verify equation (3.46), high speed cameras were utilized in the wind tunnel to capture the fluttering motion of the beams and deduce its fluttering frequency. A high-speed camera (IDT X-Stream XS4) was placed far downstream facing the samples in order to shoot the flutter at 1000 frames per second, which was high enough to capture the flutter frequency of all the samples. The camera captured and stored the images locally, obviating any buffering time delay. However, in order to capture the motion at such high frame rates in a small, dark test section, powerful lights were required to light up the samples. Two 100W garden lights were placed downstream inside the wind tunnel facing the upstream test samples. Figure 3.9 shows the setup of the lights in the wind tunnel.

Figure 3.9: Lighting setup in the wind tunnel for high-speed imaging.

The camera was positioned in between the two lights facing the upstream sample. Although the actual sample did not cause any significant blockage, the camera with its stand and lights influenced the tunnel flow. Thus, after the test rig and camera were setup in the wind tunnel, another pitot-static tube was placed at the position of the actual sample to compare the pressure values with the wind tunnel's standard pitot tube. A calibration factor of 1.1 was observed and this factor was incorporated in all the results. Figure 3.10 shows a screenshot from the high speed video recorded for a fluttering sample.

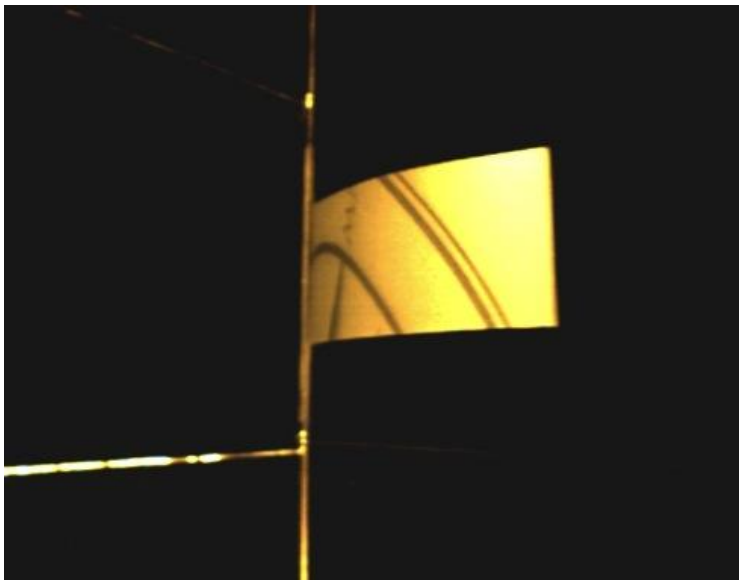

Figure 3.10: Screen shot of polypropylene (cantilever length of 200 mm) in motion.

While carrying out the connected/hinged beam experiments, no video recording was required and hence the internal light setup was removed. However, in order to capture the fluttering mode shapes of these connected bodies, a camera was placed on the floor of the wind tunnel directly facing up at the samples. A Canon® 550D digital SLR camera was utilised to capture still images of the mode shapes for various hinge positions. A 28 mm lens was used, and the camera was set to a shutter speed of 1/640s and an aperture value of f/4.0. Due to lower lighting conditions, and the desire to avoid an intrusive lighting setup within the wind tunnel, the light sensitivity of the camera sensor was increased. The captured images were desaturated, cropped, and the highlight tones were boosted so that the beams were accentuated in the image. No other processing was required.

3.7 Methodology

In order to validate equations (3.45) and (3.46), different material properties were required. Thus, the test samples used for experiments included polypropylene, paper and Mylar. Tensile tests were performed to obtain the modulus for these materials (see Appendix B). Properties of these materials are listed in Table 3.3. All the test samples used for the experiments had a common width of 60 mm and thickness of 0.35 mm. The cantilever lengths of these materials were varied from 118mm (considered as L_b) to 283.2mm ($2.4L_b$). The normalised length (L/L_b) was varied from 1 to 2.4 in steps of 0.1, thereby providing 15 samples of each material. Schematic in Figure 3.11 shows the test sample geometry used herein. While paper and polypropylene were used to determine the K values in equations (3.45) and (3.46), specific sample lengths of Mylar were used to validate the experimentally determined K values.

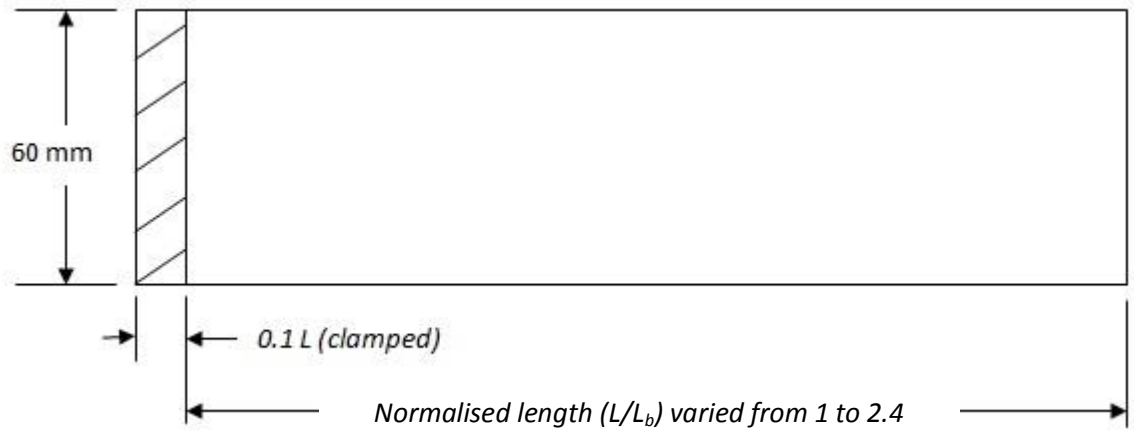

Figure 3.11: Schematic of test sample geometry.

Table 3.3: Properties of the materials used in experiments.

Material	Elastic Modulus (Mpa)	Density (kg/m^3)
Polyproylene	1261	995
Paper	2124	773
Mylar	3000	1400

For the connected beam experiments, there were nine identical polypropylene beams fabricated (with properties and dimensions shown in Table 3.2) and each beam had exactly one hinge; thus, for the experiments performed, η ranged from 0.1 to 0.9. The revolute hinges were prepared by sewing threads with an '8' pattern at the top, middle and bottom to connect the beam elements (figure 3.12). This hinge construction technique was chosen as it was the most ideal solution for replicating a zero-mass hinge (i.e. the mass of the thread is deemed negligible), and the '8' pattern ensured that the thread did not loosen during flutter of the beam. Two different hinge thread materials were evaluated – Kevlar and cotton, such that the effect of hinge material on the results, if any, could be identified. It was found that between the cotton and Kevlar thread, there was a minor difference in hinge torsional stiffness (see Appendix C). The cotton-threaded beams were used as their torsional stiffness was lower than the Kevlar-threaded beams, and thus more readily approximated the ideal case of zero-torsional stiffness.

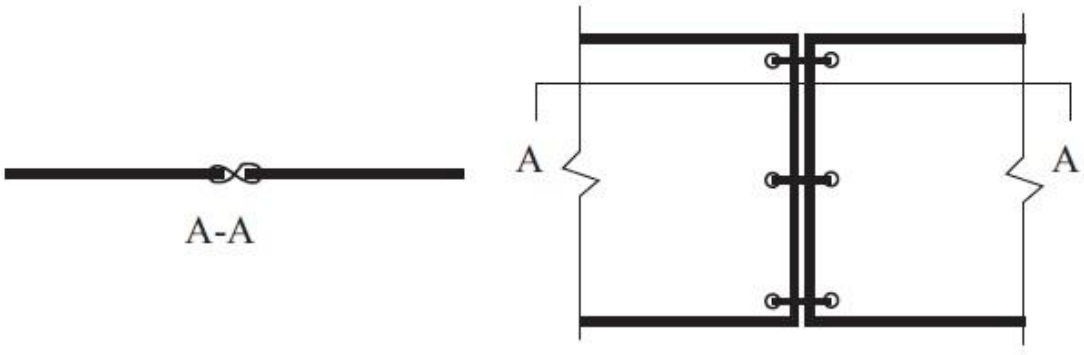

Figure 3.12: The side and top view of the hinge sewing method. The gap between the connected bodies is exaggerated for clarity.

3.8 Results and Discussion

Based on the experiments conducted, the results are discussed here in detail. This section is divided into two parts. The first part shows the results to validate the scaling laws for critical flutter velocity and frequency. The second part shows the results for the effect of hinge on the critical flutter speed of connected body.

3.8.1 Validation of scaling laws

In order to validate equations (3.45) and (3.46), tests were conducted using paper, polypropylene and Mylar for 15 different lengths as explained in the previous section. However, Mylar being the most rigid material of all three, the shorter samples had a very high critical flutter speed (beyond the safe testing limit of the wind tunnel). Also, due to the high flexural rigidity and plastic nature of the material, longer samples had a snapping tendency while fluttering. Thus, Mylar sample results were not included along with paper and polypropylene. However, certain random samples of Mylar were considered to validate the experimentally determined K values from the results. The below section shows the results of critical flutter speed and flutter frequency tests.

3.8.1.1 Critical flutter speed

It is well known from theory that critical flutter velocity (U_c) is a unique velocity at which the structure transitions from the static condition to steady state flapping. Thus, the transition to flapping state was visually observed for each sample and the corresponding flow speed was noted. These observed values were plotted against the non-dimensional lengths of the samples. Figure 3.13 shows the results of the critical flutter velocity of polypropylene and paper of normalised lengths, 1 to 2.4.

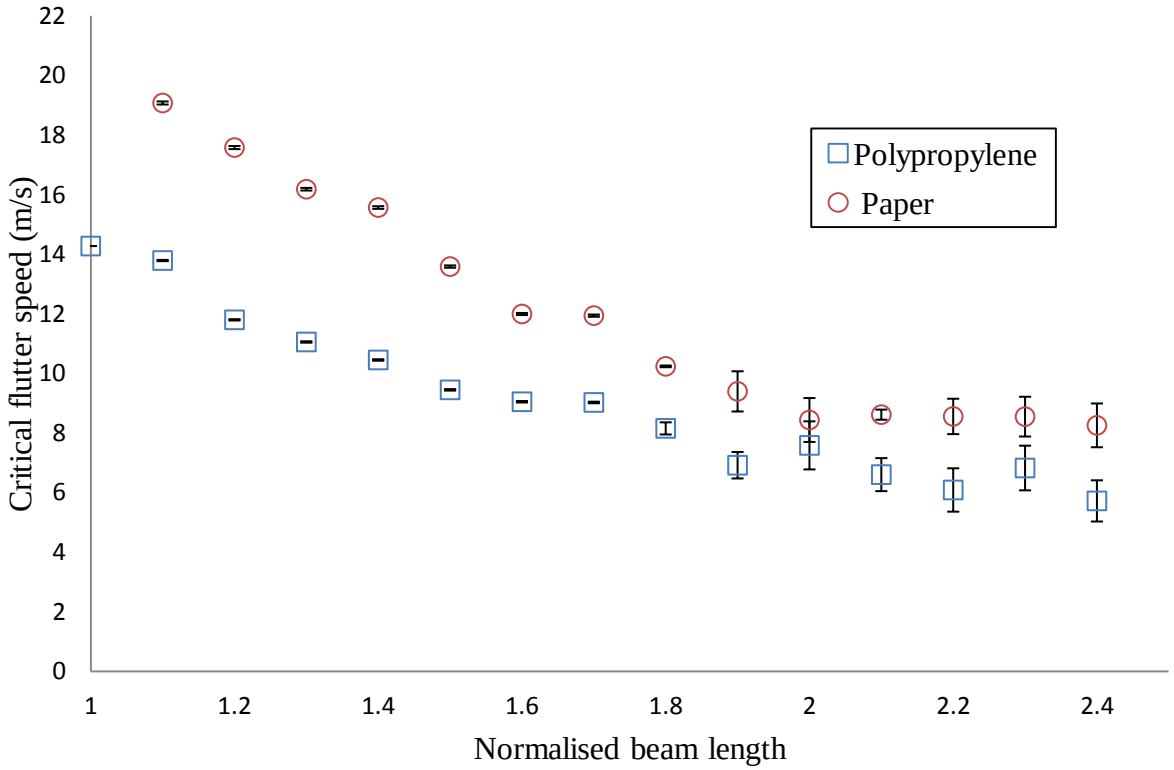

Figure 3.13: Experimental critical flutter speed of polypropylene and paper of different lengths.

From Figure 3.13, it is evident that as the cantilever length increases, U_c decreases for both paper and polypropylene. When the lengths of the samples were shorter, U_c was distinctively higher and clearly determined as the transition from static stability to flutter occurred instantaneously. However, as the cantilever length is increased, the transition from static stability to steady flapping took few seconds making it difficult to define U_c. Also, the flow velocity was very low indicating that the samples of longer lengths were highly unstable. This could be attributed for the values not following a specific trend when lengths of samples were longer. Also, it was clearly visible that paper, being rigid, fluttered at higher U_c. A shorter test sample, when clamped in the stand, was tested twice for its U_c and since the data points were found to be exactly same, the repeatability was established.

In Figure 3.14, the experimental results are compared with the theoretical two-dimensional scaling laws for U_c of polypropylene and paper. The equation (3.45) is rewritten here:

$$U_c = K_1 \sqrt{\frac{Eh^3}{\rho_f L^3}} \tag{3.49}$$

where K_1 is a constant of proportionality. The scaling law U_c values were plotted with $K_1 = 1$. It was clearly evident that the experimental results clearly followed the same trend of the

scaling laws. This implied that there existed a constant of proportionality, K_1 irrespective of the structure material and cantilever length.

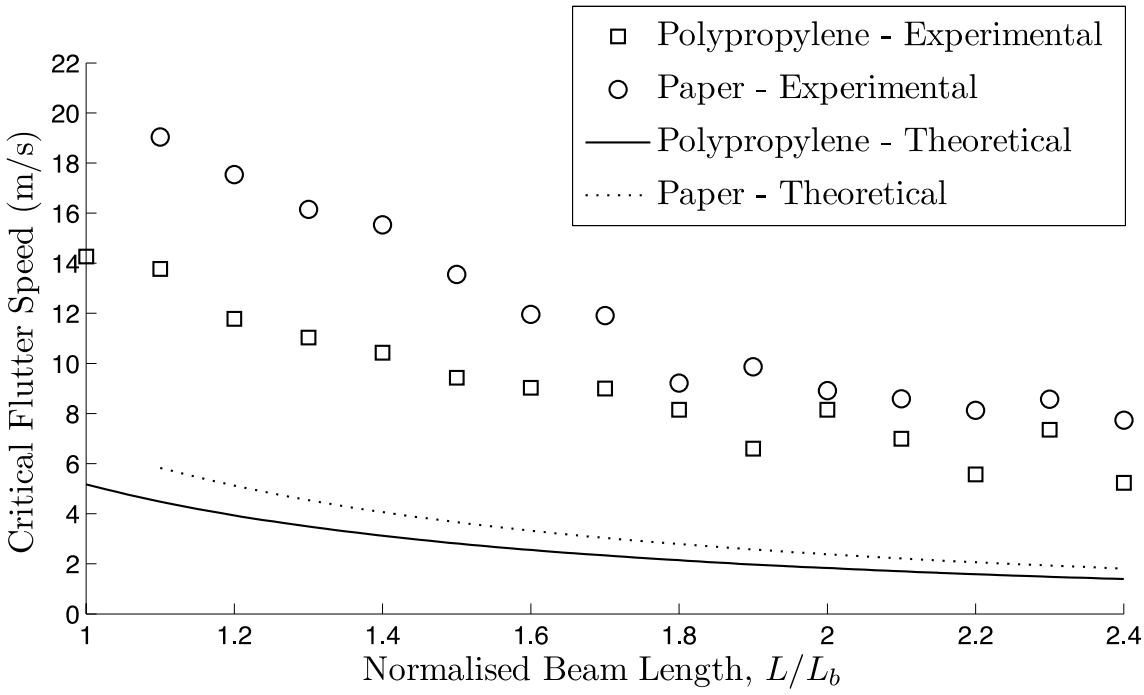

Figure 3.14: Comparison of experimental results of critical flutter speed with corresponding scaling laws.

Based on the experimental results, the constant of proportionalities were worked out for every sample by calculating the ratio of experimental U_c to theoretical U_c. It was observed that the average K_1 value for polypropylene was 3.62 and that of paper was 3.78. Ideally, the values should have been exactly the same. However, since the critical flutter speed could not be clearly defined for long lengths, it could have resulted in a small difference in K_1 values. The K_1 values of both the samples of different lengths are shown in Figure 3.15. It was seen clearly that the values were relatively stable as expected. Thus, this constant value could be used to predict the critical flutter speed for any material of wide range of cantilever lengths, while maintaining a constant width.

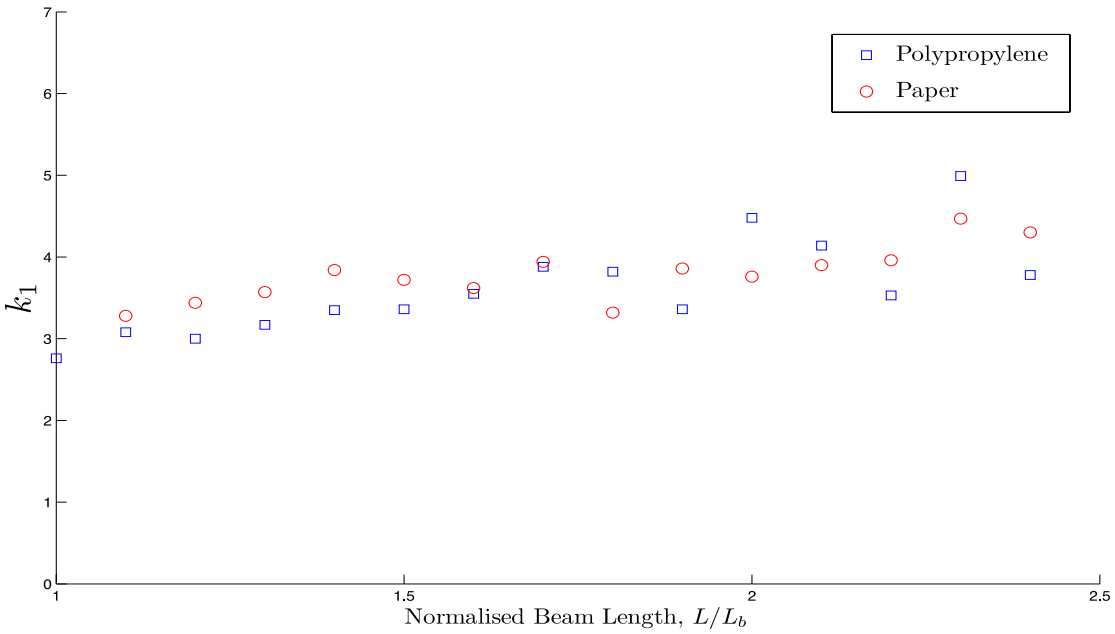

Figure 3.15: *K* values of critical flutter speed for different samples versus its normalized lengths.

3.8.1.2 Flutter frequency

Flutter frequency of a structure induced by fluid flow could be measured only after the structure transitions from static stability to steady state flapping. Also, in order to determine the flutter frequency as a function of material properties and geometry, it is important to record the flutter frequencies at a constant wind speed for each material. It is also known that as the flow velocity increases, the structure transitions to chaotic flapping. Therefore, longer lengths of these samples transitioned to chaotic flapping and hence had to be neglected for this analysis.

Figure 3.16 shows the flutter frequency of paper and polypropylene of different normalized lengths. From the figure, it is clear that as the cantilever lengths increase, the flutter frequency reduces as expected from the scaling laws. Also, since paper had a high modulus, the flutter frequencies were higher compared to that of polypropylene. The cantilever lengths were chosen such that the frequencies could be recorded at constant wind speed. The shorter lengths (1, 1.1, etc.) commenced fluttering at very high speeds and this flutter speed had to be kept constant while recording the flutter frequency of the longer lengths as well. While doing so, the longer lengths (2, 2.1, etc.) transitioned to chaotic flapping and hence were not included in the results or calculations.

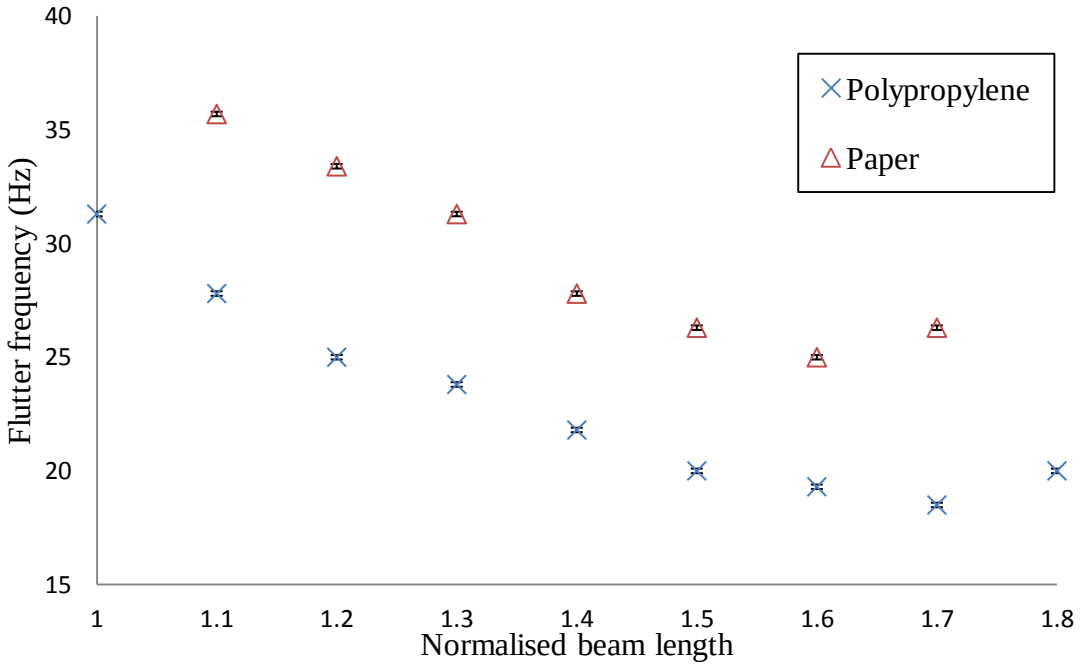

Figure 3.16: Experimental flutter frequency of polypropylene and paper of different lengths.

In Figure 3.17, these experimental flutter frequency values are compared with theoretical scaling laws. The equation (3.46) is rewritten here:

$$\omega = K_2 \sqrt{\frac{\rho_f U^2}{\rho_s h L}} \tag{3.50}$$

where K_2 is a constant of proportionality. The scaling laws were plotted for K_2 = 1. It was evident that the experimental results followed the same trend of scaling laws. This indicated that a constant of proportionality could be worked out for flutter frequency irrespective of the material properties and cantilever lengths for a given width.

The K_2 values were determined in a similar manner as that of K_1 and it was observed that the average K_2 values were constant irrespective of the material stiffness and geometry. It was observed that the average K_2 value for polypropylene was 2.02 and that of paper was 1.81. Ideally, the values should have been exactly the same. This difference in the values could be attributed to the inaccuracies in high-speed footage. Also, the longer lengths could have fluttered in a combination of modes making it difficult to determine the frequencies accurately. The K_2 values of both the samples of different lengths are shown in Figure 3.18. It is seen clearly that the values were relatively stable as expected. This indicated that for a given width of the plate of any material, flutter frequency could be predicted for a wide range of cantilever lengths.

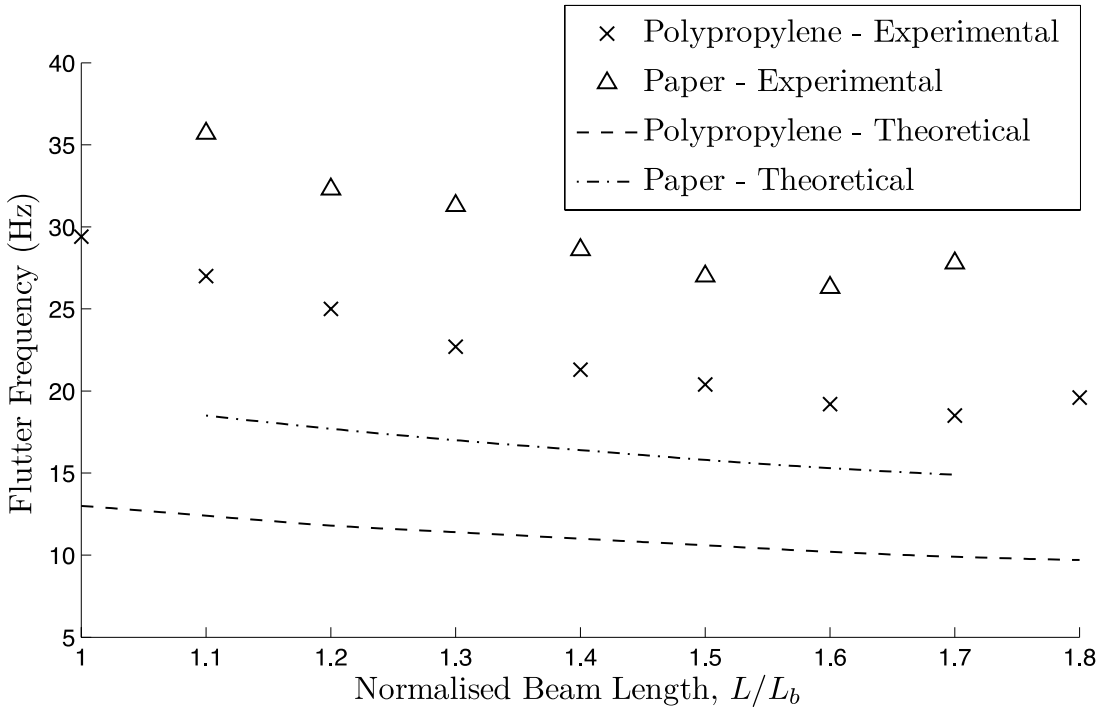

Figure 3.17: Comparison of experimental results of flutter frequencies with corresponding scaling laws.

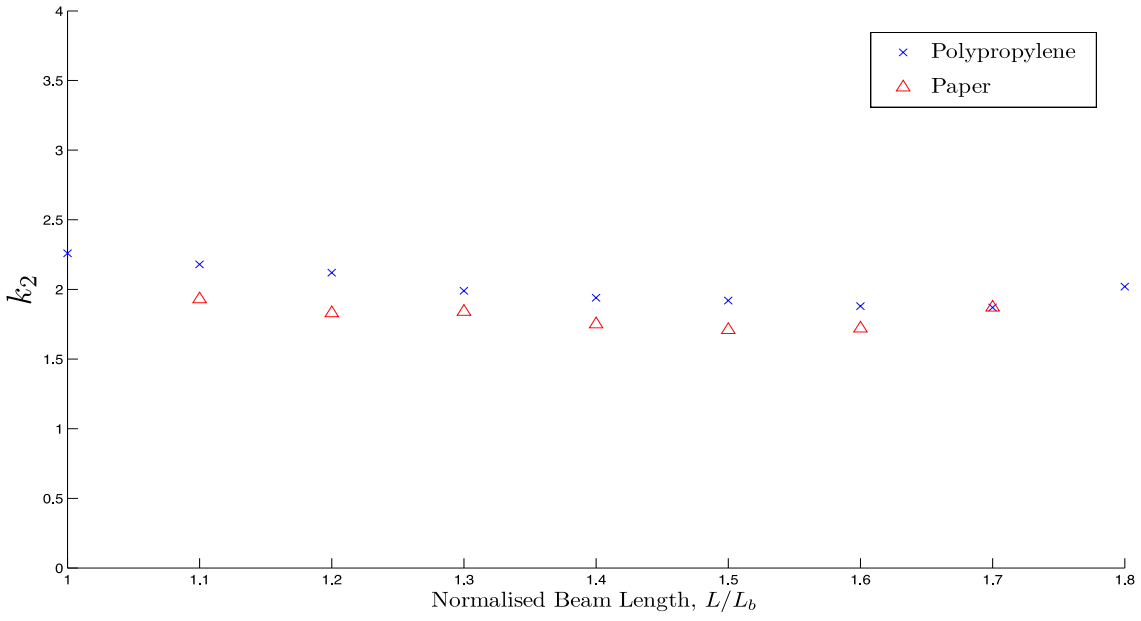

Figure 3.18: *K* values of flutter frequency for different samples versus its normalized lengths.

Based on the *K* values calculated, some of the Mylar samples' flutter frequencies were theoretically predicted and compared with the experimental results. Some of the findings are listed in Table 3.4. The predictions matched closely with the obtained results.

Table 3.4: Comparison of experimental and theoretical results for 3 samples of Mylar

Normalized lengths	Observed flutter frequency (Hz)	Predicted flutter frequency (Hz)	Error (%)
1.6	21.3	21.2	0.4
1.7	20	20.4	2
1.8	18.8	20	6.3

One aspect that has not been studied is the width of these test samples. In all the tests, the width of the sample was maintained constant. This was because, the theoretical scaling laws were obtained based on a two-dimensional analysis. However, the results clearly indicate that the two dimensional scaling laws are valid for a three-dimensional cantilever beam with empirical correction. Increasing the width of the sample is postulated to produce a different K value. Conducting several experiments with different width values could lead to an understanding of dependence of the K values on the width of the fluttering beam. However, it is important to note that the main focus of this work was to validate the scaling laws and to obtain an estimate of the critical flutter speed and frequency based on the material properties.

Since the experimental results shown here are repeatable, this work proves to be vital in choosing the material for energy harvesting purpose. The scaling laws could be used to identify the dependence of material and geometric properties on flutter characteristics. Thus, for a given width and length of a sample, the K value could be experimentally determined once. Then, the empirically determined K value could be used for any material and cantilever length (keeping the width constant) to exactly determine the flutter frequency and onset velocity.

3.8.1.3 Connected body experiments

The relationship between v and η obtained experimentally is shown in Figure 3.19. Each experimental replicate is plotted to substantiate repeatability of the results. Additionally, in Figure 3.20, both the second modal natural frequency ratio R_2 and v are plotted against η. The trend of R_2 was examined more in-depth, since in previous spectral analyses it was found that

maximum power was contained in the lowest flexible bending mode (Alben and Shelley, 2008; Connell and Yue, 2007; Hobeck and Inman, 2011). It is important to note that R_1 is the rigid body mode (0 for a hinged body) and hence R_2 is the lowest flexible bending mode.

When the hinge was at $\eta = 0.1$, the leading beam element was seen to remain essentially rigid, while the trailing element fluttered as a uniform hinged-free beam in the wind tunnel. This was due to the higher stiffness and shorter length of the leading element compared to the trailing element. When the hinge was moved to $\eta = 0.2$, virtually no discontinuity was observed at the hinge position, and the entire system fluttered as a uniform cantilever beam. This was evidenced from the normalised critical flutter speed value, $v \approx 0.9$ (Figure 3.19), and was elucidated previously in figure 3.6 from the mode shape. As the hinge was shifted towards $\eta = 0.5$, the critical flutter speed decreased monotonically. In fact, it is evident from Figure 3.20 that for the domain $0.1 \ll \eta \ll 0.5$, v outlines the same trend as R_2. This was due to flutter eventuating in the lowest flexible bending mode for these hinge positions, suggesting that the relationship in equation (3.48) indeed holds true for these hinge positions. In figure 3.21, the mode shapes captured in the wind tunnel and the computational mode shapes are compared, for η = 0.1 and 0.2.

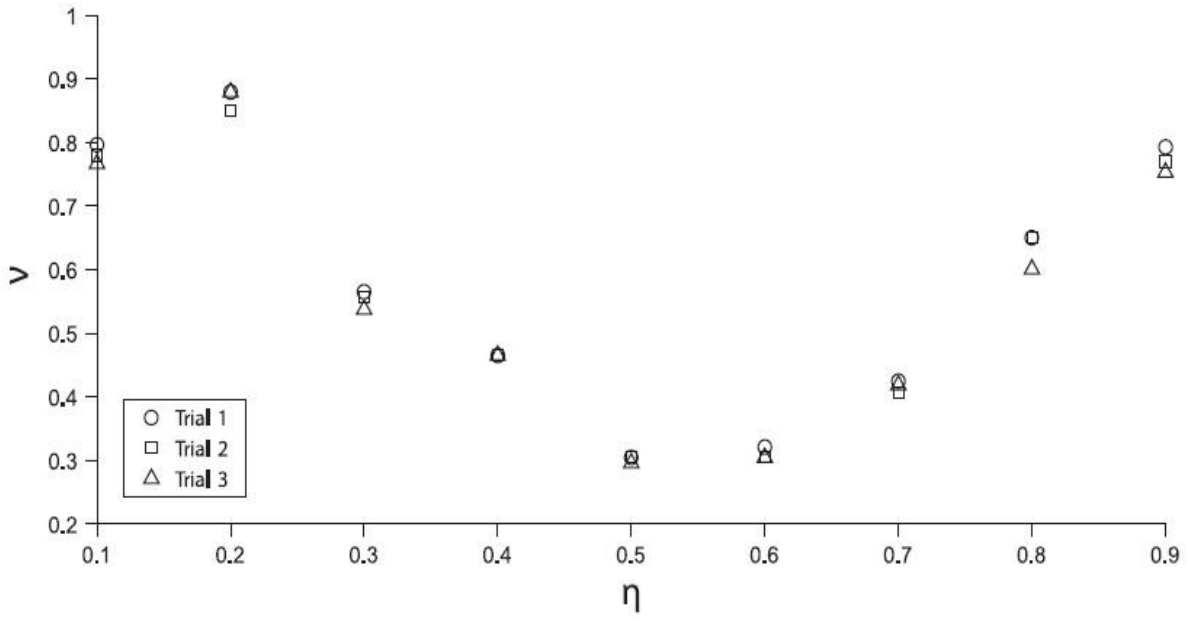

Figure 3.19: Normalized critical flutter speed v against $\boldsymbol{\eta}$.

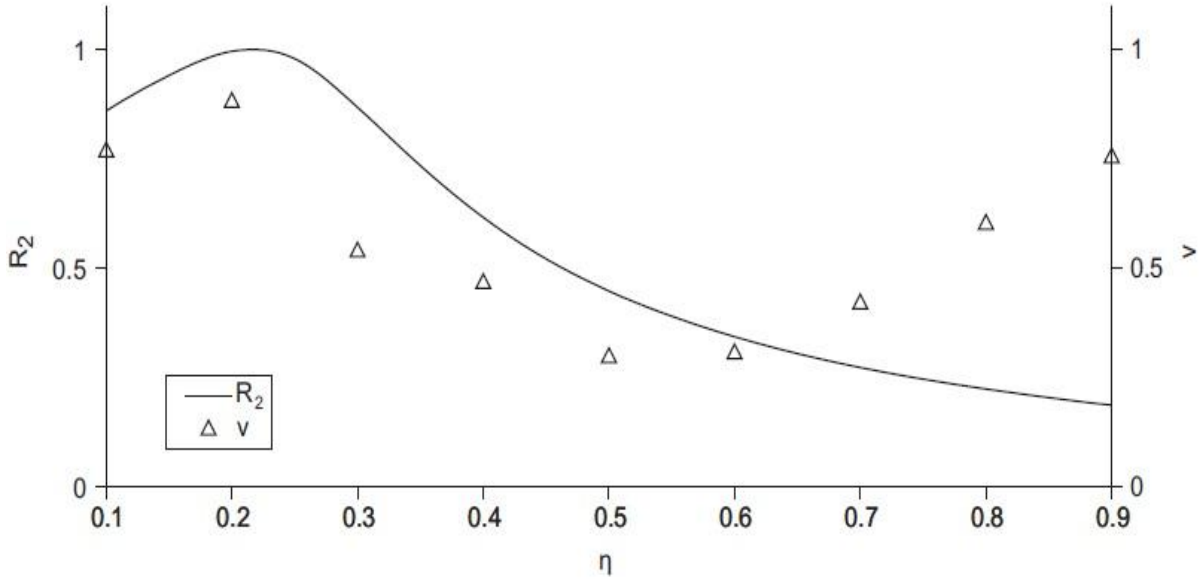

Figure 3.20: R_2 (left ordinate axis) and v (right ordinate axis) plotted against $\boldsymbol{\eta}$.

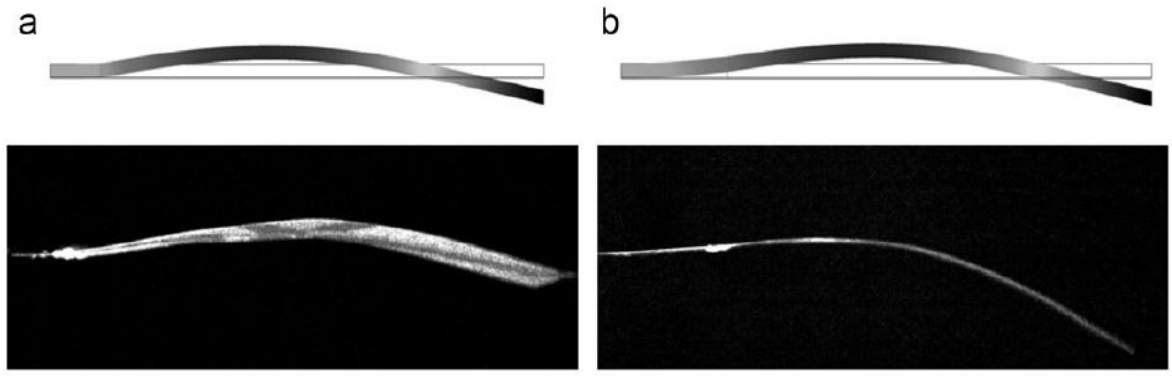

Figure 3.21: Experimental and computational mode shape comparison for (a) $\boldsymbol{\eta = 0.1}$ and (b) $\boldsymbol{\eta = 0.2}$.

For $\eta > 0.5$, v started to increase and deviated from the R_2 curve, which continued to decrease. For these hinge positions, an intriguing observation emerged; it was seen that the specimens began to flutter in higher-order mode shapes, and not the lowest flexible bending mode. This phenomenon occurred due to the relative stiffness and length between the leading and trailing elements. When the hinge position was beyond $\eta > 0.5$, the hinged beam was able to flutter in higher-order modes because the leading element became longer compared to the trailing element. In Figure 3.22, the mode shapes are compared for η = 0.5 and 0.8. Given the presence of a hinge, the system was possessed with an additional degree of freedom, which acted to enhance system stability by transitioning flutter occurrence into higher-order modes and thus delaying flutter onset. As the flexibility of the leading element increased with increasing length, combined with the added degree of freedom imparted by the hinge, the

system began to transition to a higher mode shape. This transitional behaviour has been previously observed by Watanabe et al. (2002) for both the flutter frequency and the critical flutter speed, for a varying mass ratio of a uniform beam.

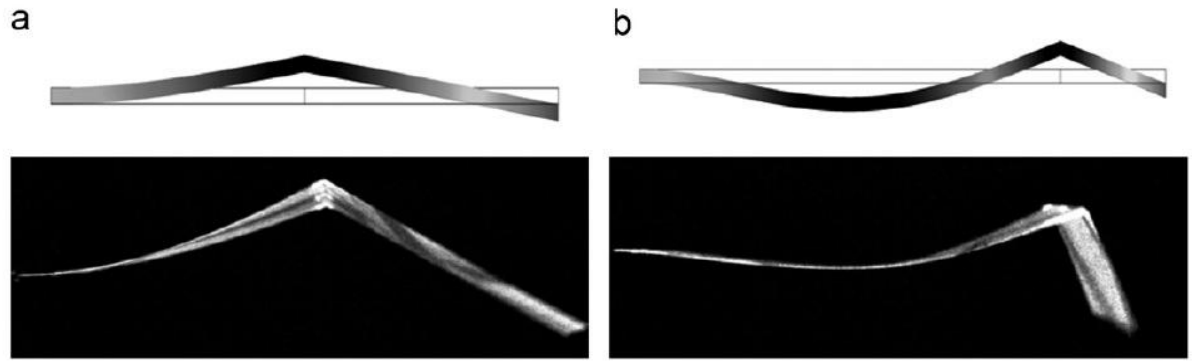

Figure 3.22: Experimental and computational mode shape comparison for (a) $\boldsymbol{\eta = 0.5}$ and (b) $\boldsymbol{\eta = 0.8}$.

The derivation of the critical flutter speed scaling law was revisited, to clarify this behaviour. Argentina and Mahadevan (2005) stated that the natural frequency of the lowest flexible bending mode scales as

$$\omega_b \approx \sqrt{\frac{Eh^2}{\rho_s L^4}} \tag{3.51}$$

In equation (3.51), the mode coefficient λ_i is neglected. Considering a general case with a possibility of higher order modes, the equation can be re-written as

$$\omega_b \approx \lambda_i^2 \sqrt{\frac{Eh^2}{\rho_s L^4}} \tag{3.52}$$

Thus, equating equation (3.52) to the flutter frequency scaling law (equation (3.26)), provided a more generalized critical flutter speed scaling law as

$$U_c \approx \lambda_i^2 \sqrt{\frac{Eh^3}{\rho_f L^3}} \tag{3.53}$$

Equation (3.53) is dependent on the mode shape coefficient. Thus the critical flutter speed is now unbounded from occurring in the lowest flexible bending mode, since $\lambda_{1,2,3\ldots}$. Given that all other parameters in equation (3.53) remained constant while varying the hinge position, the implication is that λ is some non-linear function of η. The three distinct regions of flutter for a varying hinge position are shown in Figure 3.23.

Regarding real-world implications, the work here provides a preliminary insight into the hinge placement for piezoelectric energy harvesters immersed in fluid flow. Such devices are envisioned for deployment in urban areas, where prevalent wind velocities are generally very low (e.g., Sustainable Energy Authority Victoria, 2003); notwithstanding the fact that the wind is turbulent and may approach from any direction. It is vital for such harvesters to operate at low wind speeds, and thus have low critical flutter speeds. Since maximum energy is extracted when the beam is fluttering in the lowest flexible bending mode (λ_2-mode), it would be ideal to restrict the hinge position to $\eta \leq 0.5$ for the case presented here consisting of two identical beam elements. Within this λ_2-mode and at this mass ratio, the flutter frequency is approximately equal to the natural frequency since it was found previously that unsteady lift effects did not significantly influence flutter (Watanabe et al., 2002). Therefore, as the hinge moved from $\eta = 0.5$ towards the leading edge, both the critical flutter speed and flutter frequency increased (Figure 3.23). Recalling that at resonance, the power output of a piezoelectric material varies as the flutter frequency cubed, there is a trade-off between early start-up of the system (i.e. low U_c), and higher frequency vibrations. This trade-off study, along with consideration of the vibration amplitude, differing trailing-element materials, and effects of non-parallel flow on the system, will be a recommendation for future work.

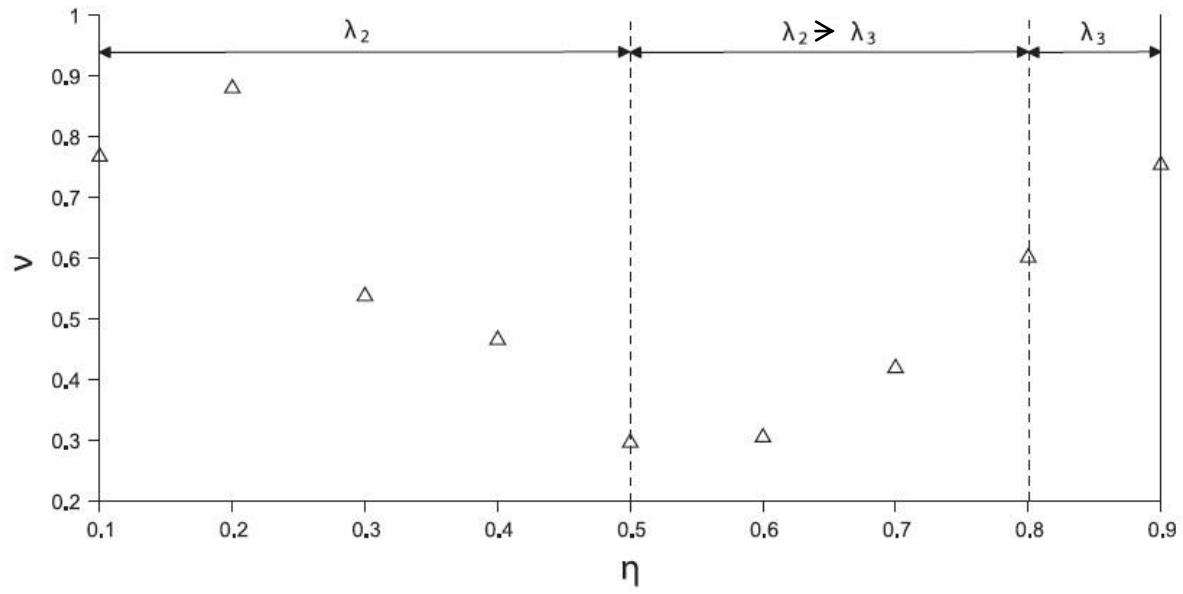

Figure 3.23: The three distinct regions in which the flutter mode changes from the lowest flexible bending mode for $\boldsymbol{\eta} < 0.5$, to a transitional combination of modes for $\mathbf{0.5} < \eta < 0.8$, to the third mode for $\boldsymbol{\eta} > \mathbf{0.8}$.

3.9 Summary

This chapter involved fundamental understanding of fluid-induced flutter of simple cantilevered beams. Following the method of Argentina and Mahadevan (2005), derivation of governing equations, concerning circulatory and non-circulatory pressure, were explained in detail. More importantly, the two dimensional scaling laws for critical flutter speed and flutter frequency were mentioned.

Since some of the recent research work on energy harvesting from fluid flow involved a use of a free revolute hinge, the effect of the hinge on a simple cantilever beam was discussed in detail. At first, a complete analytical natural frequency analysis was carried out for a clamped-hinged-free connected beam to obtain its natural frequency for the first few modes. The hinge position was varied along the beam to obtain a relationship between the hinge positions and their corresponding natural frequencies.

Two sets of experiments were carried out to validate the two dimensional scaling laws and the effect of hinge on a fluttering connected body, respectively. Three different materials, namely polypropylene, paper and Mylar were used with 15 different cantilever lengths for each material to validate the scaling laws. The results indicated that for a given width of the cantilever beam, the two dimensional scaling laws for critical flutter speed and flutter frequency were indeed valid in a three dimensional environment. Thus, the scaling laws could be used as a basis to choose the fluttering material and cantilever lengths for energy harvesting purposes. Also, of all the materials, polypropylene provided the lowest critical flutter speed and most repeatable results. Thus, polypropylene was chosen for further experimental analysis.

Experimental samples for the connected bodies were prepared with varying hinge positions along the beam and tests were conducted to measure the critical flutter speed for each sample. The results indicated that the critical flutter speeds followed the same trend as natural frequencies as the hinge position was varied from the leading edge to the middle of the beam. The lowest critical flutter speed was observed when the hinge was exactly at the middle of the beam. As the hinge position approached closer to the trailing edge, it was observed that the system transitioned to higher modes and hence fluttered at a higher speed. This was believed to be due to the increased flexibility and length of the leading edge compared to the trailing edge, making it possible to flutter at higher modes. Thus, it was clear that the position of the hinge and relative stiffness between the leading and trailing edge of the beams would

be crucial in affecting the flutter onset and flutter mode shapes, and hence the power output from an energy harvesting device. The results and their practical implications were discussed in detail in this chapter. Also, based on these results, the hinge position was determined for the harvester systems explained in Chapter 4 and in subsequent chapters.

Chapter 4

Horizontal Symmetrical, Asymmetrical and Vertical Leaf-stalk Configurations

4.1 Introduction

As the title suggests, this chapter focuses on investigating several configurations of the harvester to maximize the power output. While the previous chapter answered some fundamental questions pertaining to FSI, this chapter explores the possibility of employing certain specific piezoelectric leaf-stalk configurations which might improve efficiency, when excited by fluid flow. Detailed analyses of the power output and flutter characteristics of each configuration are carried out to understand the cause and effect of its performance.

In the previous chapter, experimental validation of theoretical scaling laws governing flutter frequency and critical flutter was established. Thus, the choice of material for the 'leaf' was based on this analysis. Also, the connected body analysis indicated that the presence of a hinge in the harvester system reduced the critical flutter speed, thereby providing an opportunity to harvest more power at lower wind speeds. The analysis also indicated that the hinge position plays a crucial role in the flutter mode. Therefore, these findings are taken into consideration in the design of the harvester system, as later explained in this chapter.

Although the main interest is to optimize the design to increase power output, it is extremely important to understand the performance of every configuration to be able to determine the aspects which could affect the power output, when excited by wind. In this regard, detailed analyses of power output data and high speed videos of fluttering motions are combined to determine the aspects affecting the power output.

As mentioned earlier, a complementary research was carried out which focussed on optimizing the leaf geometry, performance of these harvesters in turbulence and the effect of wind approaching from different directions on power output. Some of the results are shown here to obtain an overall understanding of the project and some of the design choices made in this section of the thesis.

4.2 Rationale for experiments

Li and Lipson (2009) investigated two configurations: Horizontal stalk and vertical stalk configurations as shown in Figure 4.1. In both the configurations, a triangular leaf was utilized to increase the flutter motion and reduce the flutter onset velocity. Out of the two configurations, it was reported that the vertical stalk configuration was capable of providing relatively higher power output compared to the horizontal stalk.

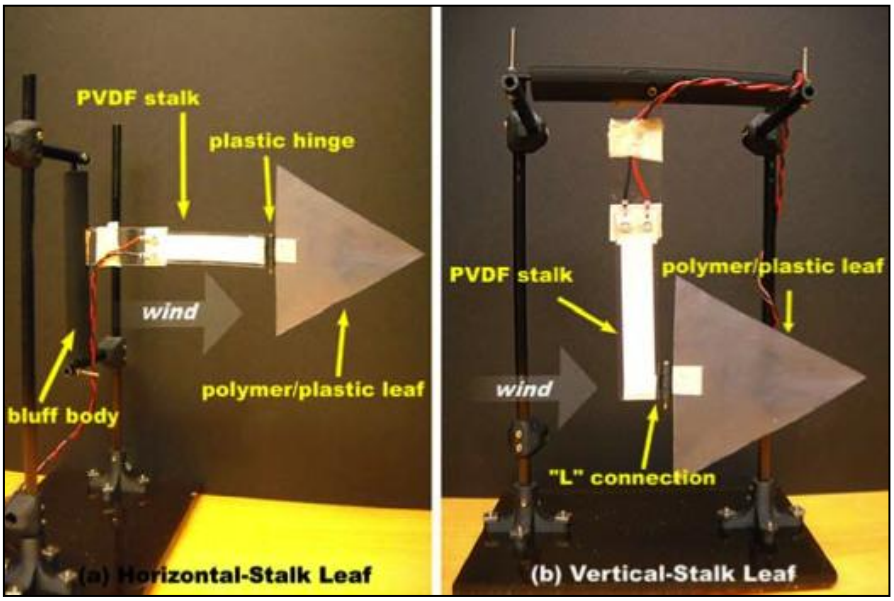

Figure 4.1: Horizontal and vertical leaf-stalk configuration (Li and Lipson, 2009).

However, Li and Lipson did not clearly establish the reasons behind the configuration's increased power output. They suggested that the higher power output could be attributed to coupled bending-torsional strains experienced by the piezoelectric stalk. This led to them suggesting that coupled bending-torsion could increase the power output compared to a pure bending case. Thus, it was important to understand the flutter behaviour and hence the cause for increased power output.

Abdelkefil et al. (2011) investigated a piezoelectric cantilever beam subjected to coupled bending–torsional vibrations via base excitation, due to an imposed offset between the beam centre of mass and shear centre. The offset was created by placing two masses asymmetrically at the tip of the beam (Figure 4.2). It was shown analytically that a piezoelectric beam subjected to coupled bending-torsional vibration produced nearly 30% more power than a beam subjected to conventional transverse bending. It was mentioned that the bending strains induced from the torsional mode increased the power output. However, no experiments were performed to validate their results.

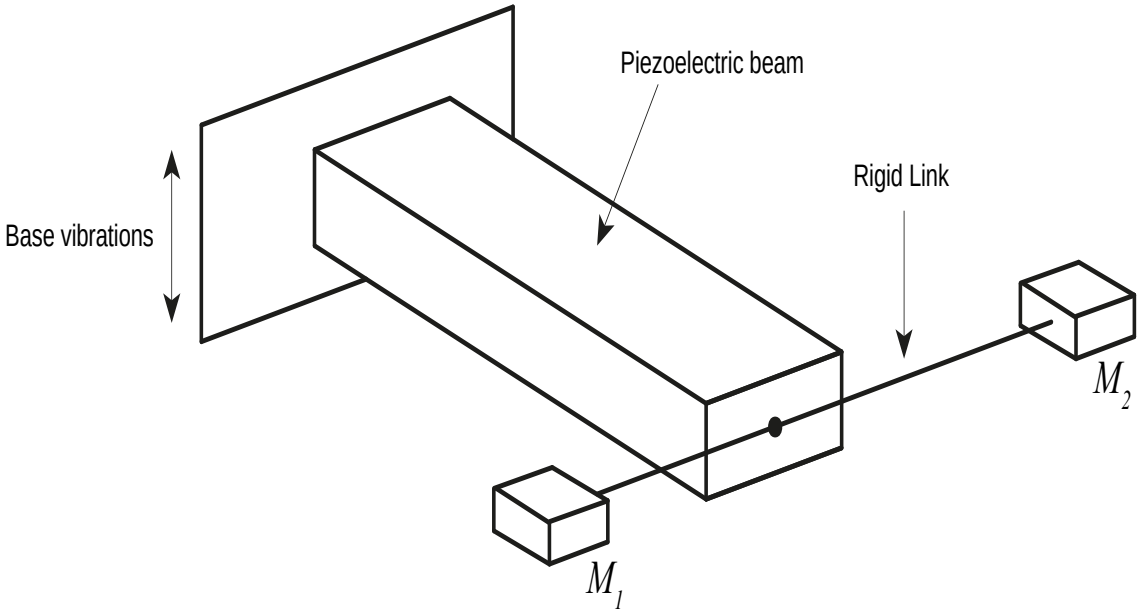

Figure 4.2: Schematic diagram of asymmetrical energy harvesting system (Abdelkefil et al., 2011).

It is important to note that in their work the harvester configuration was excited by simple base mechanical vibrations. However, the harvester system investigated here has to be excited by fluid flow. A thorough literature review indicated that to date, no investigative studies were conducted with regards to asymmetrical configurations immersed in fluid flow.

Thus, some pertinent questions answered in this chapter include:

- Is energy harvesting from smooth fluid flow using coupled bending-torsional vibrations possible?
- Why does the vertical leaf-stalk configuration output more power than the horizontal leaf-stalk configuration?

4.3 Theoretical concept of coupled bending-torsional vibrations

When a beam is subjected to a transverse loading on its centroidal axis (Figure 4.3), the beam is subjected to pure bending vibrations. However, when the same input force is applied at an offset distance, the loading can be equivalently modeled as a force-couple system (Figure 4.4). Thus, when the beam experiences transverse loading away from its centroidal axis, it is subjected to coupled bending and torsion.

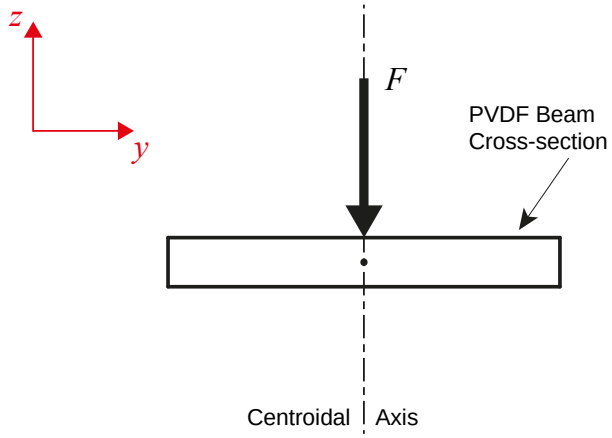

Figure 4.3: Schematic of beam subjected to pure transverse bending.

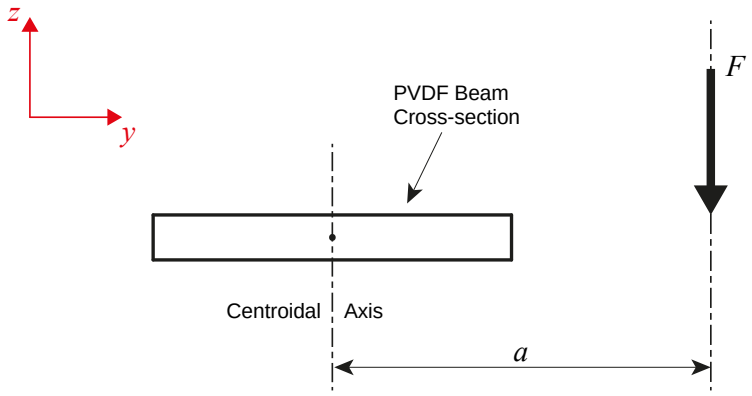

Figure 4.4a: Schematic of asymmetric loading at an offset distance.

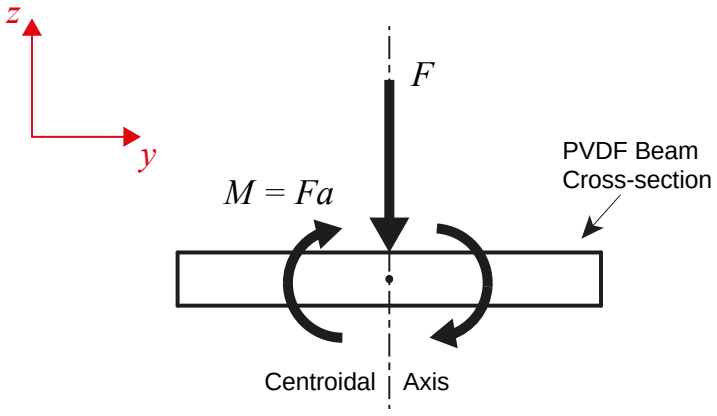

Figure 4.4b: Equivalent representation with a force and couple system.

This means that instead of a single bending equation, the motion is actually governed by a system of two equations that need to be solved simultaneously (due to translational and rotational degree of freedom). The equations are given by Weaver et al. (1990) as:

$$m\frac{\partial^2(y-a\theta)}{\partial t^2}+EI\frac{\partial^4 y}{\partial x^4}=f(t) \tag{4.1}$$

$$ma\frac{\partial^2(y-a\theta)}{\partial t^2}+R\frac{\partial^2\theta}{\partial x^2}-R_1\frac{\partial^4\theta}{\partial x^4}-\rho_s I_p\frac{\partial^2\theta}{\partial t^2}=f(t) \tag{4.2}$$

where $m = \rho_s hl$, the mass per unit length of the beam; ρ_s - density of the beam; h - thickness of the beam; l- width of the beam; E- elastic modulus; I- moment of inertia; $f(t)$ - transverse loading function; a - distance between the centroidal axis of the beam and its shear center; I_p - polar moment of inertia; R - torsional rigidity and R_1 - warping rigidity.

The stress (T) and the strain (S) induced from coupled bending-torsion are then:

$$T=\frac{Mz}{I}=-z\left(E\frac{\partial^2 y}{\partial x^2}+G\frac{\partial^2\theta}{\partial x^2}\right) \tag{4.3}$$

$$S=-z\left(\frac{\partial^2 y}{\partial x^2}+\frac{\partial^2\theta}{\partial x^2}\right) \tag{4.4}$$

where G - shear modulus and z - distance from neutral axis to the point of interest. The stress and strain induced via the beam vibrations are related to the electric field and displacement by (Erturk and Inman, 2011):

$$\begin{aligned}\{S\}&=[c]\{T\}+[d^t]\{E\}\\ \{D\}&=[d]\{T\}+[\varepsilon]\{E\}\end{aligned} \tag{4.5}$$

Where D – electrical displacement; c – compliance; d- direct piezoelectric coefficient; d^t – transverse piezoelectric coefficient, ε- permittivity; E - electric field strength.

It is non-trivial to obtain a closed-form solution for equations (4.1), (4.2) and (4.5). The solution becomes more complex for a connected body system with varying geometry and stiffness. Also, it is quite challenging to model the aerodynamic forcing function in the system.

Since piezoelectric energy harvesting involves conversion of mechanical energy to electrical energy, it could be sufficient to perform a theoretical analysis on the mechanical energy produced in transverse bending and compare it with the mechanical energy produced in coupled bending-torsion. This analysis could later be verified with the electrical power output

obtained from the experimental and computational studies. However, there are certain drawbacks in doing so: firstly, all of the strain energy is not harvestable. Since the piezoelectric beam acts as a strain integrator over the piezoelectric area, the shear strains produced from torsion do not contribute to the overall harvestable energy unless the piezoelectric membrane is designed to work in the *15*-mode (which converts shear strains into electrical energy). Secondly, it is important to note that the static strain energy equations do not consider the vibration frequency and damping present in any dynamic system.

Therefore, it was important to perform experiments and simulations to identify the effect of coupled bending-torsion vibrations on the power output. In the following sections, the methodology, experimental setup and results are explained in detail.

4.4 Methodology

In order to investigate the effect of bending and torsion on power output, two different set of analyses were conducted. At first, simple dynamic tests were performed using a shaker. This test involved use of symmetrical and offset configurations of piezoelectric materials. The purposes of these tests were to observe the power output for a simple cantilever piezoelectric beam with a known input force and to observe the power output with the same input force, applied at specific distances away from the centroidal axis. Two offset configurations were tested to determine the effect of offset distance on the power output.

Computational analysis was carried out in conjunction with these dynamic experimental results. A dual field analysis, comprising structural and electrical components of the system, was undertaken in ANSYS®. Also, structural damping in the system was computationally varied as a parameter to observe the effect of damping on the power output of the system.

These dynamic tests would clearly indicate the effect of bending and torsion on the power output of the system. However, the main purpose here was to investigate the performance of asymmetrical configurations when immersed in fluid flow. In this regard, the same pure bending and offset configurations were coupled with an amplification device (the 'leaf') and immersed in smooth wind flow.

Voltage output was recorded at every wind speed to determine the power output. In order to understand the flutter characteristics of each of the configuration, high speed cameras were utilised to capture the motion in the wind tunnel and later post process the images to extract useful information. The following sections explain the experimental setup in detail.

4.5 Experimental setup

All the wind-tunnel tests were conducted in RMIT's Aeronautical Wind Tunnel (AWT). The specifications of AWT were mentioned earlier in Chapter 3. Since the average wind speeds in cities are between 3-8 m/s (Australian Bureau of Meteorology, 2011), the configurations were tested for the same wind speed range. The dynamic test setup, configuration setup, electrical circuitry and data logging information are provided in this section.

4.5.1 Piezoelectric material

The piezoelectric material used in the experiments was a commercially available rectangular PVDF (LDT-028K/L with rivets, Measurement Specialties: Figure 4.5). The piezo was a laminated film, measuring 72 mm long, 16 mm wide and 205 μm thick, with leads attached at the ends. The lamination was such that the actual PVDF film was offset from the neutral axis to provide a cumulative electrical charge during transverse bending. (However, due to proprietary reasons, the offset distance was not revealed by the manufacturer). The lamination also provided sufficient sturdiness to ensure repeatable power outputs. PVDF was chosen over other piezoelectric materials for its higher flexibility and cheaper costs (information on other piezoelectric materials can be found in Chapter 2). Properties of PVDF used here are listed in Table 4.1.

Figure 4.5: LDT - 028K/L PVDF film with leads (Source: Measurement Specialties Inc.)

Table 4.1: PVDF properties (Measurement Specialties Inc., 2006)

PVDF properties (LDT2-028K/L)	
Electromechanical coupling factor k_t	14%
Capacitance (nF @1kHz)	2.78
Young's Modulus (GPa)	4.0
Piezo stress coefficient, g_{31} (Vm/N)	0.216
Piezo stress coefficient, g_{32} (Vm/N)	0.003
Piezo stress coefficient, g_{33} (Vm/N)	-0.33
Density (kg/m^3)	1780
Poisson's ratio	0.34

4.5.2 Dynamic tests

Dynamic tests were performed using three different configurations of the PVDF patch. The first configuration consisted of PVDF only (Figure 4.6), with the base completely clamped and the free end attached to a shaker (LS 100 - Ling Electronics) to input known transverse displacements at a specific frequency. The second configuration consisted of the PVDF clamped at one end, with a Mylar strip bonded orthogonally at the PVDF free end (Figure 4.7). The free end of the Mylar was then connected to the shaker. The purpose of the Mylar strip was to create an offset between the centroidal axis of the PVDF and the shaker location. The length of the Mylar strip from the centroidal axis of the PVDF to the shaker was 36mm (*a* - half of the overall length of the PVDF patch). The third configuration was similar to the second configuration except that the offset distance was 72mm (*2a*). Mylar was used here due to its relatively high specific modulus. Ideally, given the high flexibility of PVDF, a material of zero mass and infinite stiffness would be desirable. However, it is challenging to practically obtain such a material. In this regard, Mylar was considered as the best choice to create the offset. The three cases tested are summarized in Table 4.2, and the properties of Mylar are given in Table 4.3.

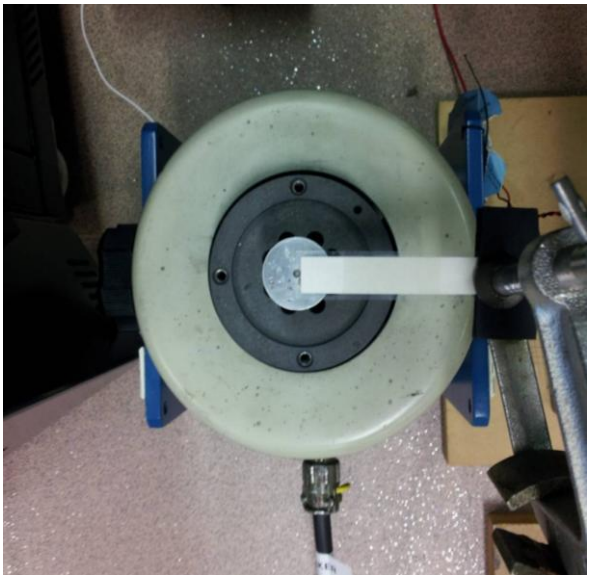

Figure 4.6: Setup of bending configuration.

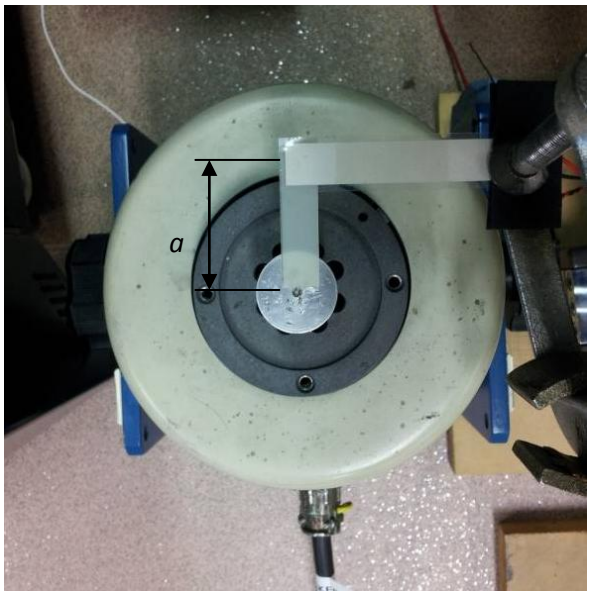

Figure 4.7: Setup of asymmetric loading with offset distance of *a*.

Li and Lipson (2009) stated that their harvester system had flapping frequencies in the range of 8-20 Hz. Thus, the shaker was configured to input a constant sinusoidal displacement amplitude of 13mm at a frequency of 15Hz for all three cases. Given the shaker limitations, and that all the configurations were compliant and low in mass, a low, constant input displacement amplitude was chosen. Also, it was visually observed that the deformations on Mylar strips appeared highly nonlinear for input amplitudes greater than 13 mm, and hence leading to an inefficient energy transfer to the piezo. The orientation of the tests was such that negligible sagging of the beams due to gravity occurred; the scope of this work excluded a study on the influence of gravity in these systems.

Table 4.2: A summary of the configurations tested in the experiments.

Configuration 1	PVDF beam subjected to bending.
Configuration 2	PVDF beam subjected to bending and torsion with the shaker offset at *a* (36mm) via Mylar.
Configuration 3	PVDF beam subjected to bending and torsion with the shaker offset at 2*a* (72mm) via Mylar.

Table 4.3: Properties of Mylar (offset material)

Mylar properties	
Width (mm)	10
Thickness (mm)	0.35
Young's Modulus (GPa)	5.0
Density (kg/m^3)	1400

4.5.3 Computational modelling

4.5.3.1 Overview

In order to corroborate the experimental results from the dynamic tests, a computational analysis was conducted utilising ANSYS® R14.0; specifically, the dual-field, piezoelectric capabilities of the code. Three different scenarios were investigated, matching the three cases outlined in Table 4.2; bending, bending and torsion with offset *a*, and bending and torsion with offset 2*a*. A steady-state harmonic analysis was carried out for each case, with the following assumptions made:

1. The material model was linearly elastic, and no material nonlinear effects were taken into account.
2. Transient vibrational effects (i.e. start-up effects) were ignored.
3. The effect of gravity was negligible (as mentioned earlier).
4. No material viscoelastic or electrical damping was considered.

The geometry was modeled as per the experimental shaker setup, see Figure 4.6 & 4.7, with the PVDF patch clamped at one end and either free, as in the bending case, or bonded to the Mylar beam at the other end. A displacement boundary condition forcing the transverse displacement degree-of-freedom was implemented, so as to replicate the shaker's effect. All

other degrees of freedom were fixed at the location of the imposed displacement. The forced displacement was applied as a sinusoidal input with an amplitude of 13mm and a frequency of 15Hz.

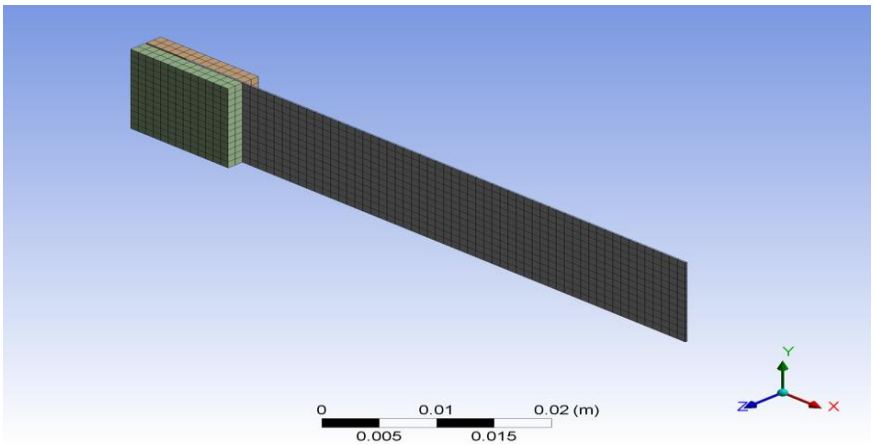

Figure 4.8a: Computational bending configuration

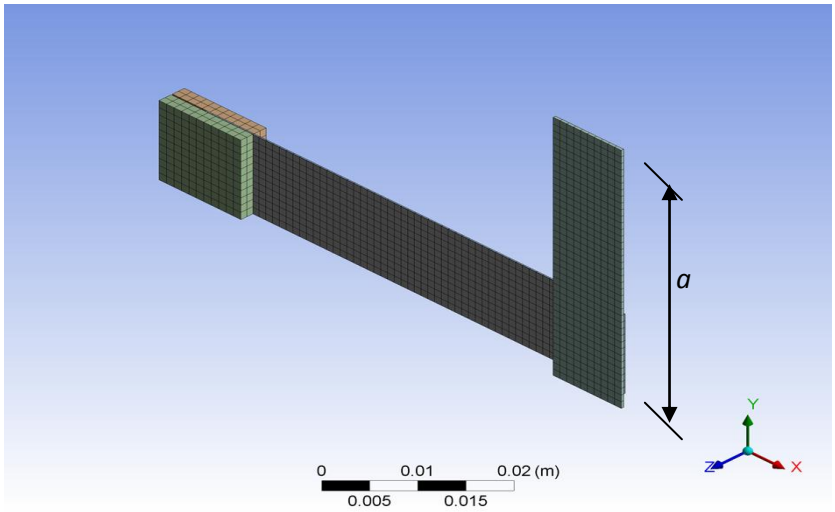

Figure 4.8b: Computational asymmetric loading case with offset distance *a*.

The steady-state power output from the PVDF patch was measured by connecting a resistance element (with resistance 5.6MΩ, explained later in Section 4.5.5) to the two terminals of the patch, and recording voltages across this resistance element. A mesh sensitivity analysis revealed that large changes in the mesh sizing did not significantly affect the output power, and so a relatively fine mesh sizing was chosen, and kept constant across the three test cases (Figure 4.8) so as to isolate the effect of the increasing offset distance, and adequately capture the strains experienced during the loading. During the solution process, the equations of motion governing the harmonic response of the beam were solved directly, as iterative solvers caused poor performance with the dual-field elements meshed to the

PVDF-beam geometry. See Appendix D for user-defined functions used in ANSYS® for this analysis.

Instead of applying a clamped end condition to the PVDF beam, the actual clamps from the experiments were modeled in order to simulate the fact that a small section of the PVDF beam was clamped (Figure 4.8). The clamps were then fixed on all four edges to enforce the clamping end condition of the PVDF beam.

4.5.3.2 Structural Damping Analysis

The total amount of damping present in the experimental model would involve structural damping, fluid-added damping and electrical damping. Given the experimental setup, the fluid-added mass effects could be considered negligible. However, electrical damping could affect the dynamics of the system, especially when the load resistance is matched to the operating piezo (Sodano et al., 2001). Since the load resistance was maintained constant across the configurations, this damping effect was not considered in this analysis. Here, only the structural damping was taken into account, as:

$$\zeta_s = \frac{c}{c_{crit}} \tag{4.6}$$

where ζ_s is the global structural damping ratio, c is the user-defined structural damping applied, and c_{crit} is the structural critical damping coefficient, as calculated internally by the solver. The structural damping here is proportional to the strain induced in the structure, and is independent of the forcing frequency; whereas viscoelastic damping is proportional to the velocity of the structure, and can be shown to be linearly dependent on the forcing frequency (Beards, 1996). Here, ζ_s ranged from 0 to 1.4 (from no damping to an extremely over-damped case), and both the power output and torsional power ratio γ for each damping-ratio case were plotted. Here, a torsional power ratio, γ, is defined as:

$$\gamma = \frac{P_{2a} - P_{bending}}{P_a - P_{bending}} \tag{4.7}$$

where P_{2a} is the power output at $2a$ offset, P_a is the power output at a offset, and $P_{bending}$ is the power output from bending only.

4.5.4 Configuration setup for wind-tunnel tests

The symmetrical harvester configuration used in the experiments is similar to the one investigated by Li and Lipson (2009). The harvester consists of a PVDF 'stalk', a revolute hinge and an amplification device, called 'leaf', thereby forming the leaf-stalk system.

4.5.4.1 Revolute hinge

Connected body analysis (shown in Chapter 3) clearly indicated that the presence of hinge reduces the flutter onset velocity. Also, for a simple connected body system, the onset velocity was the lowest when the hinge was placed exactly at the middle of the beam span. However, as the hinge was placed closer to trailing edge, the system transitioned to higher mode flutter. Thus, based on the connected body analysis, a revolute hinge was used in the harvester system, approximately at the middle of the overall harvester length.

A simple nylon pinned hinge (18 mm x 26 mm) was used in the harvester system. The hinge was bonded with the leaf and stalk with the help of electrical tapes. The hinge mass constituted up to 14% of the overall mass. McCarthy conducted a simplified study on the effect of hinge mass on the flutter characteristics, details of which can be found in McCarthy et al. (2012). The main finding was that the hinge mass helped in reducing the flutter onset velocity, but also reduced the flutter frequency, Due to this trade off, it was estimated that there would be no significant effect on the power output.

Figure 4.9: Nylon revolute hinge (Source: www.hobbyking.com)

4.5.4.2 Polymeric leaf

Li and Lipson (2009), in their experiments, concluded that the leaf acts as an amplification device to increase the flutter amplitude, and hence the strain on the PVDF stalk. They suggested that the leaf would increase surface area of the harvester system, thereby capturing more dynamic pressure and increasing flutter amplitude.

Li et al. (2011) conducted experiments with different geometrical shapes of leaf and concluded that a triangular leaf had the best results in terms of power output. McCarthy et al. (2012) conducted experiments with different triangular geometries to determine the optimal leaf shape in order to maximise the power output. Since the author was closely involved with the experiments and data analysis, some of the key results are shown in this section.

A simple horizontal symmetrical configuration was used for the experiments (as seen in Figure 4.10). In order to maintain symmetry about the central axis of the system, isosceles triangles were used. The leaf was cut from a 305 μm thick polypropylene sheet (properties listed in Table 3.3). Polypropylene was chosen based on the experimental results shown in Chapter 3. Four different leaf areas were tested for their effect on the power output: 18 cm^2, 32 cm^2, 50 cm^2 and 72 cm^2 (*b* x *h* - 6 x 6, 8 x 8, 10 x 10 and 12 x 12 cm). Figure 4.11 shows the power output of these configurations at different wind speeds.

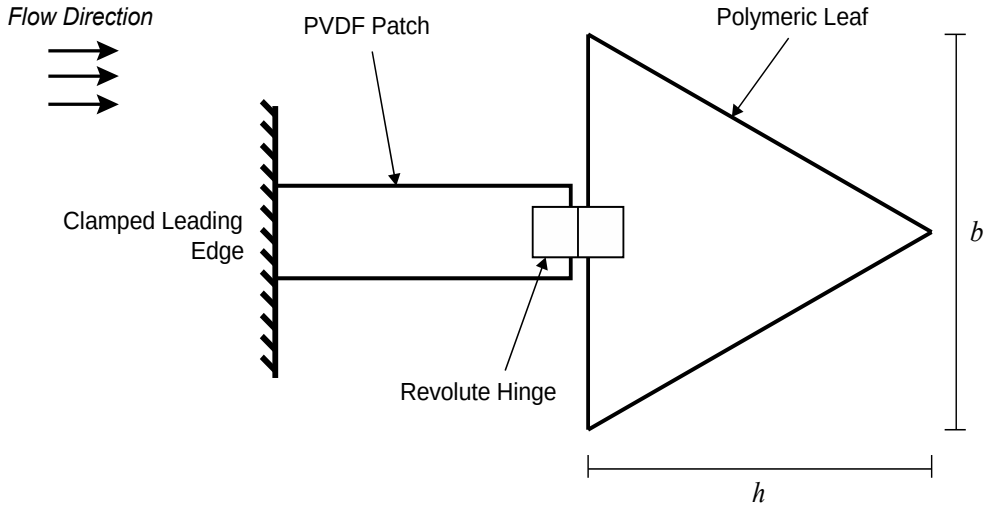

Figure 4.10: Schematic of horizontal symmetrical configuration

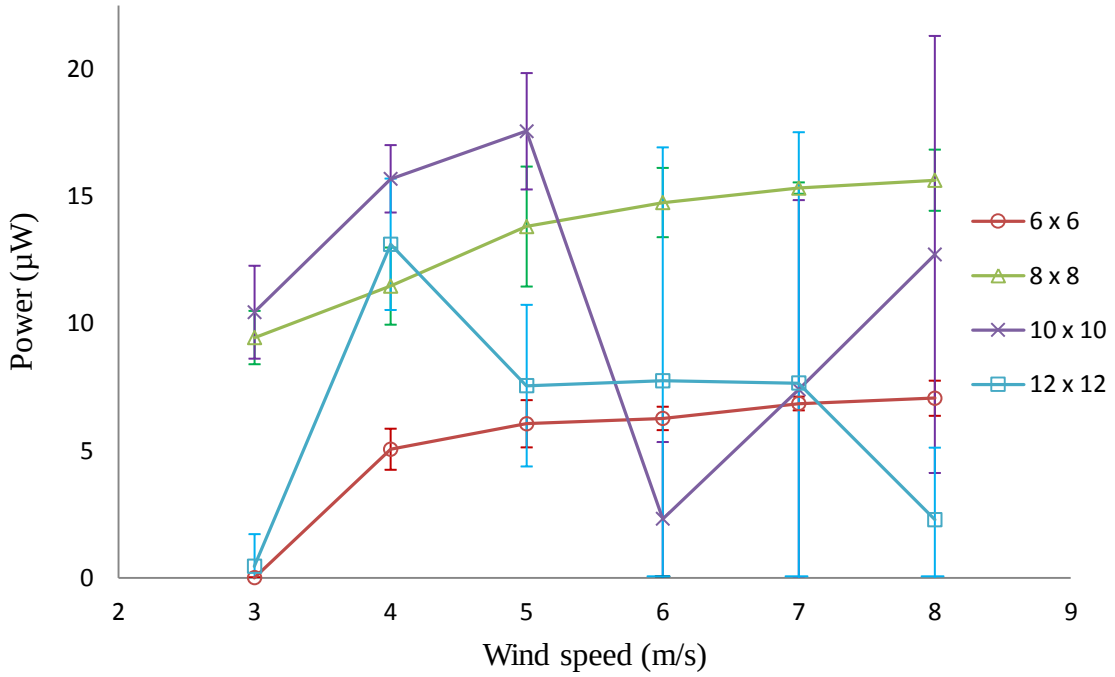

Figure 4.11: Leaf area variation results (Legend: *b* x *h* cm).

From Figure 4.11, it is clear that for the given wind-speed range, the 8 x 8 (32 cm^2) leaf performed the best compared to the other leaf areas. Thus, in the next set of experiments, this leaf area was kept constant and the aspect ratio (*h/b*) was varied. Four different aspect ratios were tested: 0.25, 0.86, 1 and 4. Figure 4.12 shows the aspect ratio variation results.

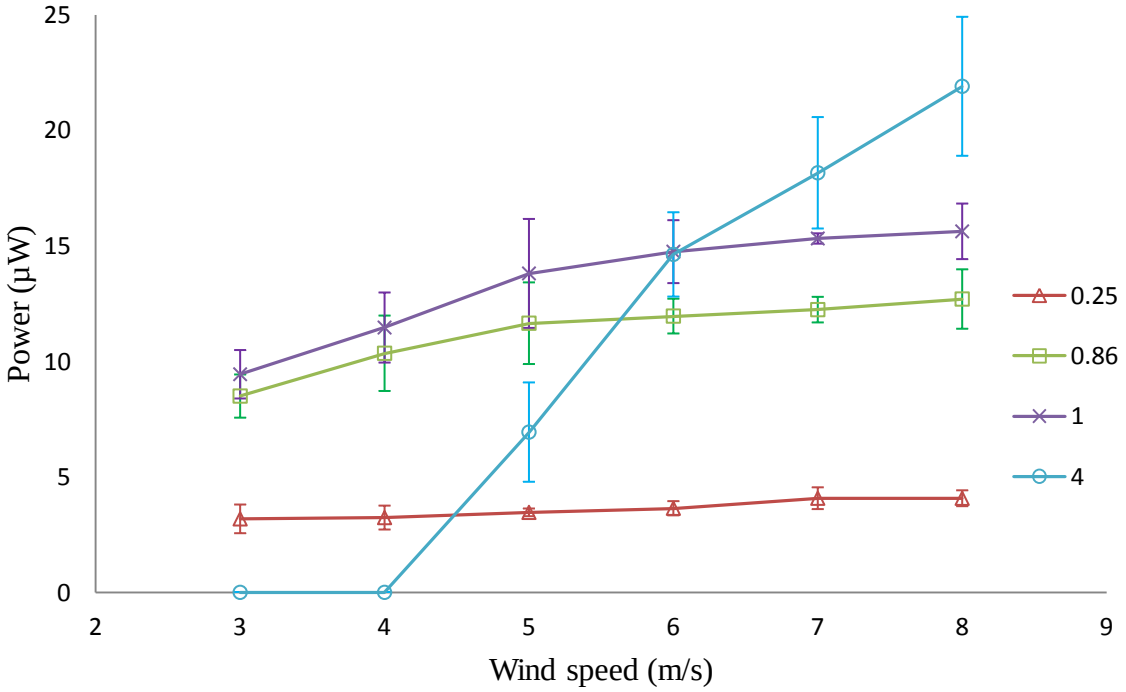

Figure 4.12: Leaf aspect-ratio variation results (Legend: Aspect ratio - *h/b*).

From Figure 4.12, it is clear that up to 6 m/s, the aspect ratio of 1 performed the best. Although, the aspect ratio of 4 performed better at higher wind speeds, it had a higher start-up speed (with no flutter at wind speeds of 3 and 4 m/s). Thus, in the experiments explained in this chapter, an isosceles triangle of base and height 8 cm each was used. A detailed discussion of the geometry choices, results and repeatability can be found in McCarthy et al. (2012). It is also important to note that the focus here was the median wind speed (5.5 m/s), and hence the electrical load was matched at this wind speed (as explained later in Section 4.5.5).

4.5.4.3 Harvester configurations

In the symmetrical configuration, the PVDF patch was directly connected to the leaf via a revolute hinge as per Figure 4.10. In the asymmetrical configurations, Mylar was used to create an offset between the axis of the leaf and the centroidal axis of the piezo (Figure 4.13). The offset distances were kept the same as the ones used in simple dynamic tests (i.e. *a* was 36 mm and *2a* was 72 mm).

Also, since the reason for the increased power output of a vertical-stalk configuration was not discussed in detail by Li and Lipson (2009), a horizontal-stalk configuration was compared with the vertical-stalk configuration for its power output in this work. Figure 4.14 shows the schematic of the vertical-stalk configuration where the axis of the PVDF is perpendicular to the direction of flow.

The leading edge of the PVDF patch was clamped using metal strips having a thickness of 1.75mm. The stand was guyed to the walls of the wind tunnel using thin-gauge wires, to avoid any transverse vibrations during the experiments. Previous flow visualization work indicated that the clamping strip and binder clips did not have any significant aerodynamic interference with the harvester (McCarthy et al., 2013).

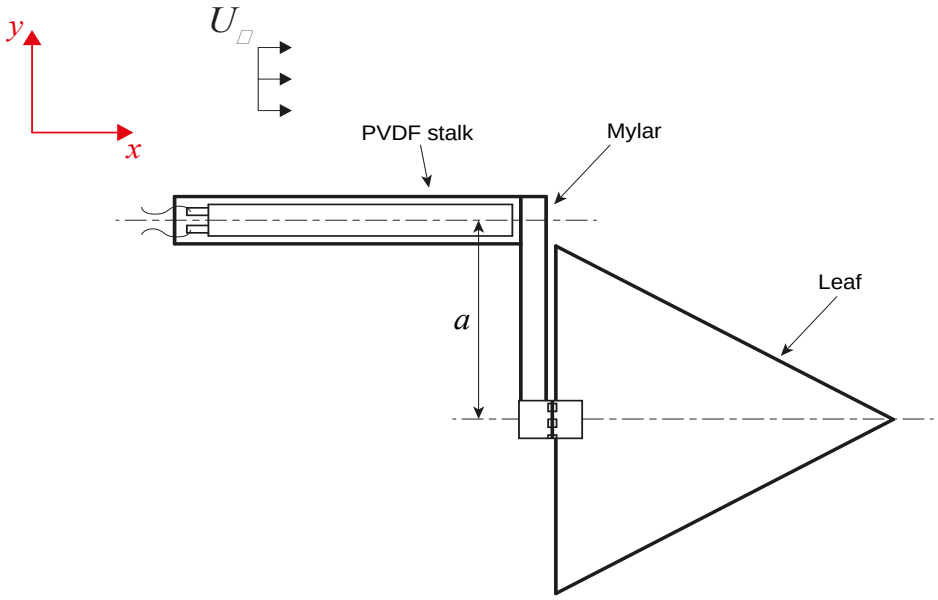

Figure 4.13: Schematic of the asymmetric (*a*-offset) configuration.

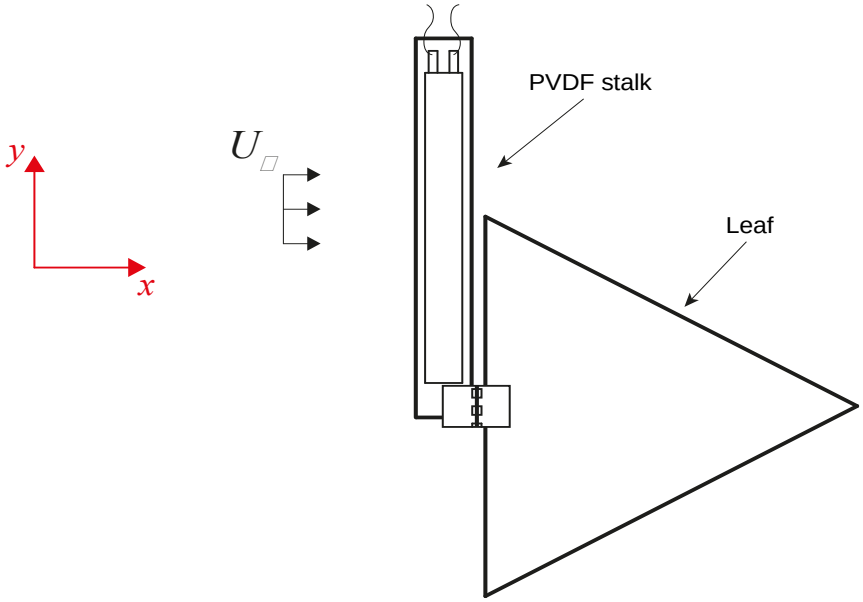

Figure 4.14: Schematic of vertical-stalk configuration.

4.5.5 Load matching and data logging

In order to record the electrical power output from the PVDF patch, the patch was connected to a simple circuit. The power output of a piezoelectric material depends on the external load resistance across which the voltages are measured (as mentioned earlier in Chapter 2). The optimal load resistance R_{Lopt} for a piezoelectric material in operation for maximum power output is restated here as:

$$R_{L\,opt} \approx \frac{1}{\omega C} \tag{4.8}$$

where ω - operational frequency of the piezoelectric material and C - internal capacitance of the piezoelectric material.

In the case of wind-tunnel tests, the patch was tested for its power output from 3-8m/s. Thus, the optimal load resistance was experimentally determined for a velocity of 5.5m/s, the median wind speed. Ideally, a specific optimized load for every wind speed would be preferred. In reality, this would mean that the load has to be actively tuned in accordance to the wind speed. However, Mateu and Moll (2005) performed experiments on active resistance tuning and stated that it would not be beneficial to do so. The power required for tuning resistance was noted to be higher than the power harvested from the piezo system. Thus, no active tuning was designed for the harvesters used in this body of work.

The horizontal symmetrical configuration was connected to different load resistances ranging from 1-60MΩ in parallel. This circuit was connected across a differential probe (Elditest, GE8115) before linking the circuit to the DAQ board (National Instruments, BNC 2110). The use of a differential probe with a very high internal impedance ensured that the AC voltage from the leaf-stalk was measured across the load resistance, and also that the voltage was scaled down to the maximum allowable voltage of the DAQ board. The circuit diagram is shown in Figure 4.15.

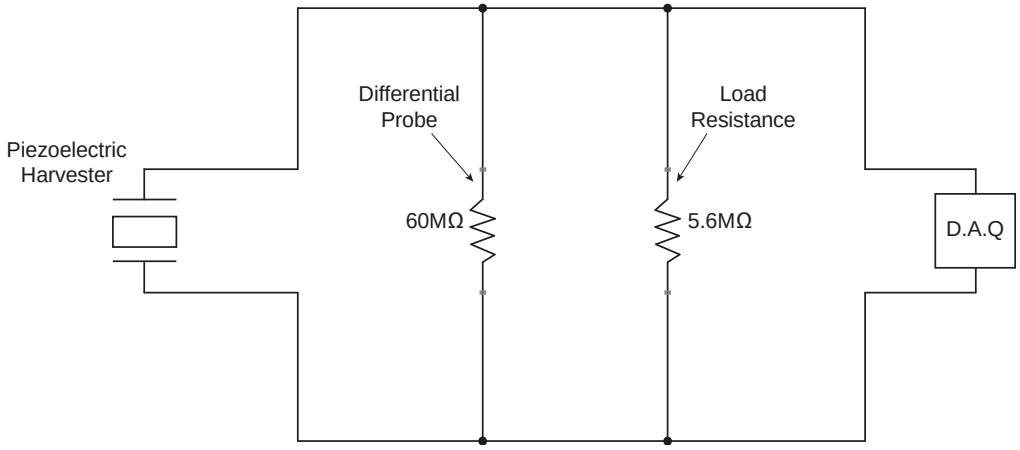

Figure 4.15: Energy-capture circuit used for power measurement.

The AC voltages were recorded at a sampling rate of 1kHz, for a period of 2 minutes, to ensure good resolution. A LabView® program was written to measure the voltage output from the piezo at every instant. The electrical power output was then calculated for each data value as:

$$P_i = \frac{V_{RMS}^2}{R_L} \tag{4.9}$$

where V_{RMS} - root-mean-square voltage from the leaf-stalk. The average power for the 2 minute period was calculated as

$$P_{avg} = \frac{1}{1200} \sum_{i=1}^{1200} P_i \tag{4.10}$$

The load matching experiments were carried out for the horizontal-stalk configuration. The circuit was setup and the voltage data were recorded after setting the wind speed at 5.5 m/s. Different load resistances were connected one by one and their corresponding power outputs were calculated. The output average RMS voltages were plotted against different load resistances and the graph is shown in Figure 4.16.

It is clear that as the load resistance was increased from 1MΩ, the voltage increased initially and then saturated at resistance of around 20MΩ. In order to determine the optimum value of load resistance, the output power was plotted against the load resistance (shown in Figure 4.17).

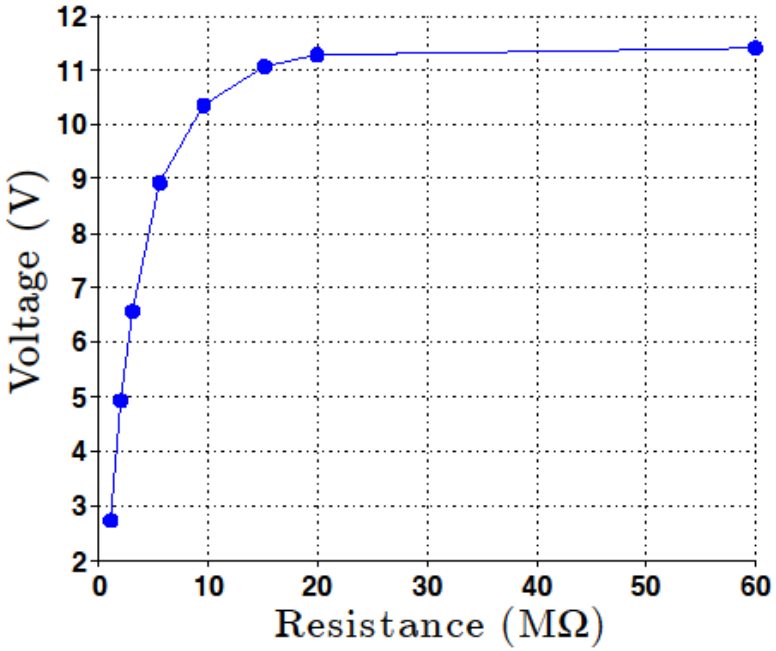

Figure 4.16: RMS Voltage vs. Load resistance at 5.5 m/s wind speed.

The optimal load resistance value for this case was found to lie between 3.4 MΩ and 5.6MΩ. It is important to note that at lower wind speeds, as equations (4.6) and (4.7) suggest, high

load resistances are beneficial in increasing the power output. Thus, a 5.6MΩ load resistor was used for all the experiments conducted, given that average wind speeds in urban areas are generally less than 5.5 m/s. It is to be noted that input frequency in dynamic tests, and flutter frequency for a vertical-stalk arrangement would be different, and hence would require a different optimal resistance value. However, in order to have a common ground for comparison between the two different configurations, the same load resistance was used while measuring the voltage output. It is important to note that the same load resistance (5.6MΩ) was also used in the computational analysis.

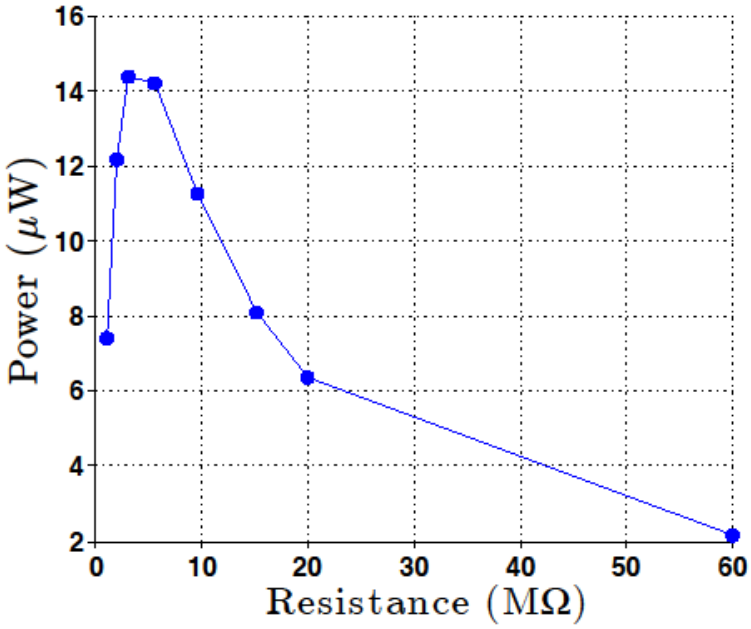

Figure 4.17: Output power vs. load resistance at 5.5 m/s.

4.5.6 High-speed image capture

In order to highlight the flutter modes of all four configurations (horizontal symmetrical, two asymmetrical (*a* and *2a*) and vertical stalk configurations), high speed footages were captured for all the tested wind speeds. A high-speed camera (IDT X-Stream XS-4) was placed downstream of the specimen. An image of the setup is shown in Figure 4.18. The footage was acquired at 1000 frames/second to ensure good resolution of the leaf-stalk flutter and the specimen was lit with a 300W studio light from outside the wind tunnel, thereby not requiring any re-calibration of the wind tunnel). The electrical circuit and data acquisition methods were the same as in the dynamic tests.

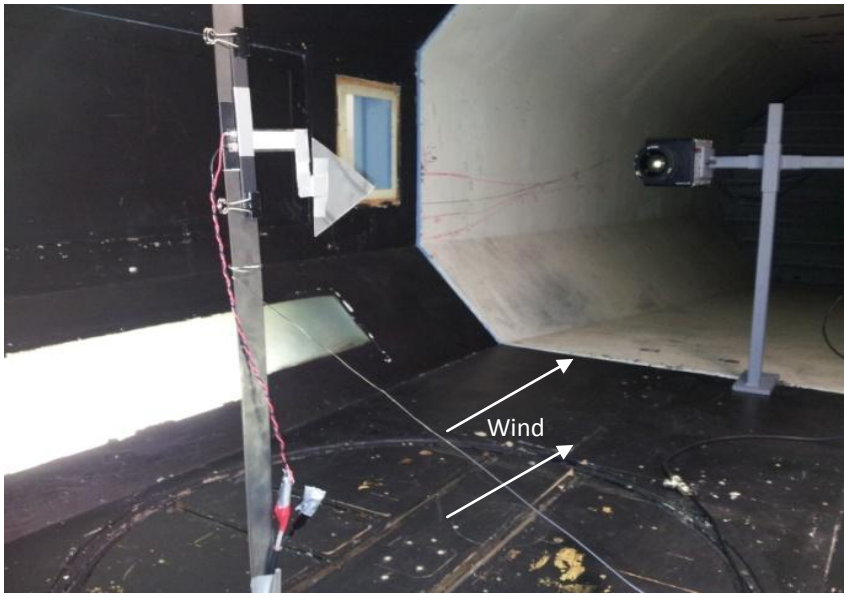

Figure 4.18: Asymmetrical configuration with camera setup in wind tunnel.

4.6 Results and discussion

4.6.1 Dynamic tests

It is known from Section 2.8.2 in Chapter 2 that the harvestable power from mechanical vibrations at resonance is given by:

$$P = \frac{mY^2\omega^3}{4\zeta_s^2} \tag{4.11}$$

where m - mass of the structure; Y - amplitude of vibration; ω - frequency of vibration; ζ_s - structural damping ratio of the system. The general, off-resonance condition is likewise defined as:

$$P = \frac{\left(\frac{\omega}{\omega_n}\right)^4 Y^2\omega^3 m}{\left(1-\left(\frac{\omega}{\omega_n}\right)^2\right)^2 + \left(\frac{2\zeta_s\omega}{\omega_n}\right)^2} \tag{4.12}$$

where ω_n is the natural frequency of the system. In the experimental analysis, an input displacement frequency of 15Hz was maintained for all three configurations and the power output recorded for two minutes. As seen in equations (4.11) and (4.12), it was vital to maintain a constant frequency, as the input frequency would affect the power output, though the effect of changes in input frequency were not quantified in the analyses. Furthermore, damping is inversely proportional to power output. In the experiments, the structural damping

ratio ζ_s for all the configurations was not measured and so in the computational analysis, it was varied from 0 to 1.4. For ζs = 0.7, the computational results corresponded almost exactly with the experimental results (Figure 4.19), indicating that the experiments could have indeed been in a 70% under-damped state.

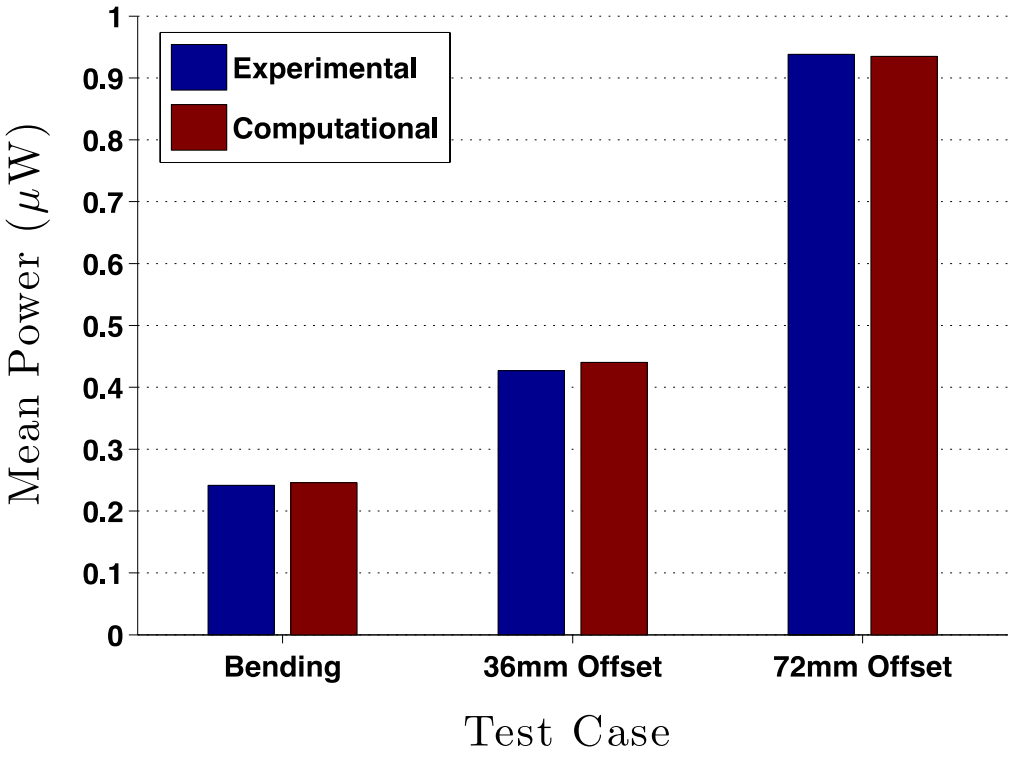

Figure 4.19: Comparison of experimental and computational shaker results for ζs = 0.7.

The offset configurations provided more power output compared to the bending case, as expected. The power outputs, in general, were low due to the relatively small applied displacements. The experimental power ratio (as defined in equation (4.7)) was found to be 3.76 while the computational power ratio for ζs = 0.7 was 3.54. The computationally determined output power and power ratio for the three cases are compared against a varying damping ratio in Figure 4.20.

It was evident that the effect of the structural damping ratio was more pronounced for the *2a* offset case. This was probably due to the higher strains sustained in the Mylar due to inertia. A material with infinite stiffness and zero mass would have been preferred to achieve the offset; but this cannot be practically achieved.

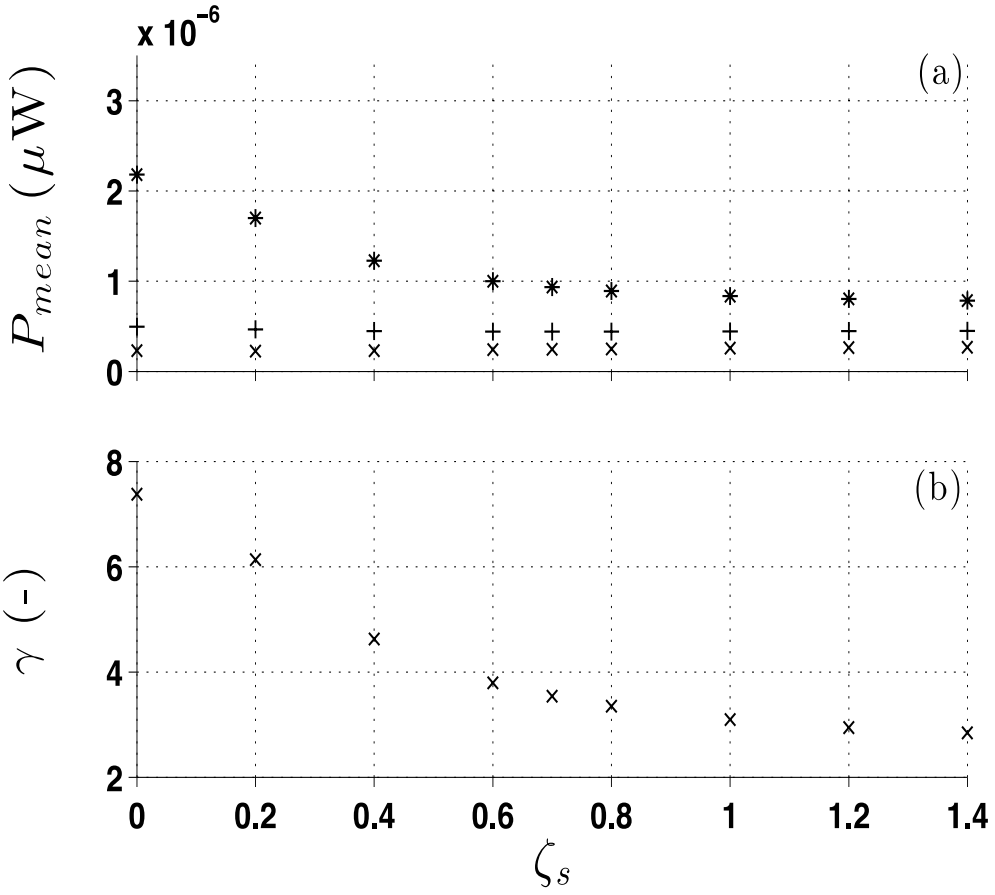

Figure 4.20: A plot showing the (a) computational power output and (b) power ratio (γ) against the structural damping ratio (ζs). For (a); x - bending, + - 36mm (*a*) offset, * - 72mm (2*a*) offset.

Ideally, the shaker tests should have been performed over a range of frequencies in order to obtain comprehensive results. Also, it would have been desirable to experimentally determine the damping ratio of the system to be compared with the computational result. However, given the electrical and flexible nature of the PVDF, it is not trivial to eliminate electrical and viscoelastic damping effects in the experiments. Moreover, since the main focus of this work is to identify the effect of bending and torsional vibrations on the power output during fluid-induced flutter, extensive shaker tests were not performed. Although the 0.7 damping ratio match was only a logical approximation, Figure 4.20 indicated the effect of damping on the increase in power output for all the three test cases. It indicated that for all the damping ratios, the power ratio was greater than 2, indicating that the coupled bending-torsion configurations provided higher power output at all cases. It was however important to investigate if these offset configurations performed similarly when excited by fluid flow. Thus, in the following section, wind-tunnel experimental results performed with symmetrical, asymmetrical and vertical-stalk arrangements of the energy harvesters are explained.

4.6.2 Wind-tunnel tests

4.6.2.1 Power output

The output power was measured and recorded for two minutes for each wind speed, once flutter manifested for each configuration. The results for the mean power output at each wind speed with standard deviation for the symmetrical, *a*-offset and *2a*-offset configurations are shown in Figure 4.21. The error bars shown in the plots in this chapter are the standard deviations observed during the recorded period of time. This was done to specifically observe the time-varying behaviour of these harvesters.

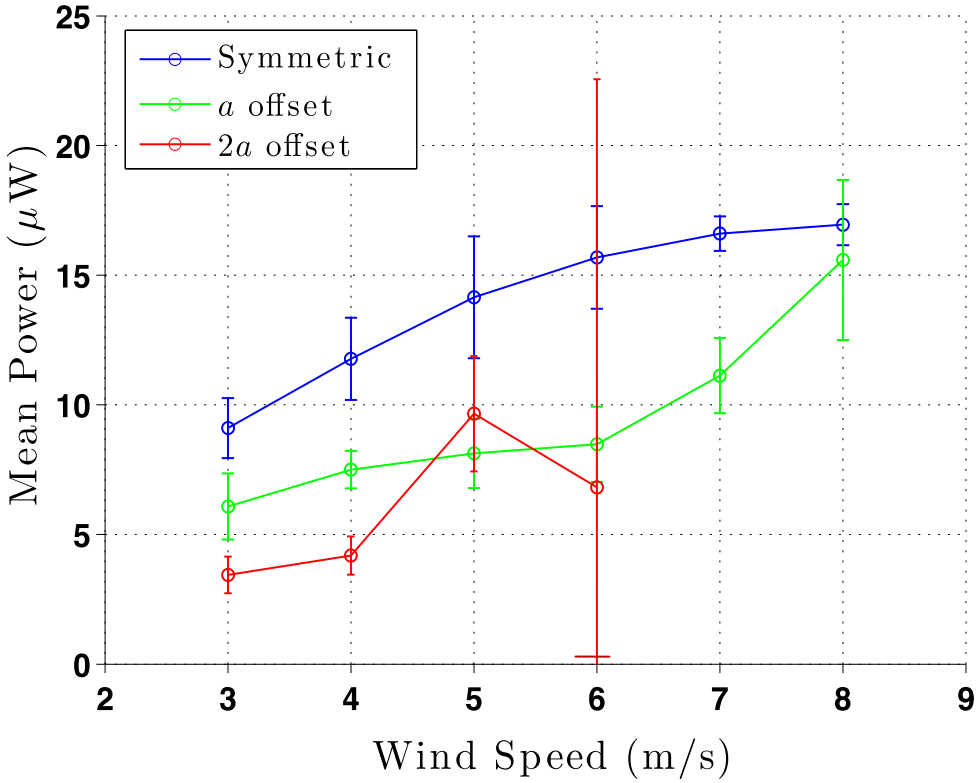

Figure 4.21: Power output of three horizontal stalk piezo configurations versus wind speed.

For the symmetric configuration, it was evident that as the wind speed increased, the power output also increased. This could be deduced visually from the experiments; as the wind speed increased, the flutter frequency of the PVDF patch also increased (equations (4.11) and (4.12)). Also, it was clear that the patch was subjected to only transverse bending due to the nature of fluid pressure impinging on leaf-stalk. A maximum power output of about 17μW was observed at a wind speed of 8.0m/s. Flutter of this configuration consisted of limit-cycle oscillations with no random snap-through events occurring, similar to the flutter observed at

higher flow speeds for a uniform filament in a parallel flow (Connell and Yue, 2007). This explained the relatively low output-power deviation at the higher wind speeds.

For the *a*-offset configuration, the power output increased as the wind speed increased but surprisingly, the power output remained lower than that of the symmetrical configuration for every wind speed. This was contrary to the dynamic test results and the work of Abdelkefil et al. (2011), both of which suggested that the *a*-offset configuration would output more power due to coupled bending-torsion vibrations. Furthermore, the *2a*-offset configuration showed no particular trend of the power output with monotonic increases in wind speed. The system had transitioned to flutter with large, nonlinear deformations (explained in next section) and hence the system output power with high deviation in the case of the 5.0 and 6.0m/s wind speeds. At the higher wind speeds of 7.0m/s and 8.0m/s, the system interfered with the base clamp due to its chaotic flapping motion. Hence, the power output was not recorded at these wind speeds.

The vertical-stalk experiments were performed in a similar manner to the horizontal-stalk experiments. The load resistance was maintained at 5.6MΩ throughout the experiment. The power outputs, along with standard deviations of the vertical-stalk configuration, are compared with horizontal-stalk pure bending configuration at different wind speeds in Figure 4.22.

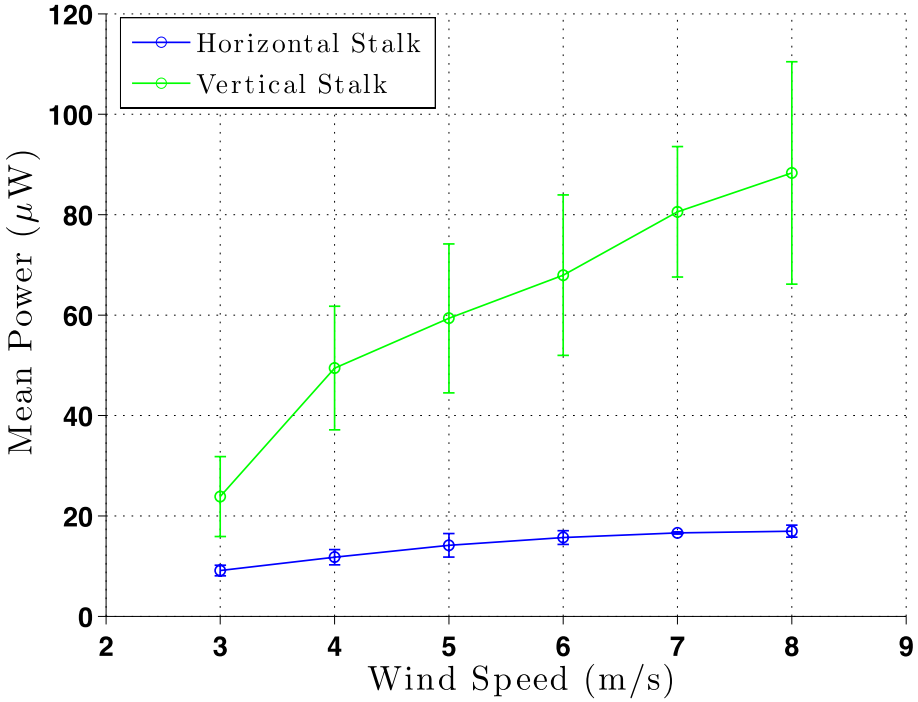

Figure 4.22: Power output vs. wind speed.

The vertical-stalk configuration clearly provided more power output than the horizontal-stalk configuration, for all wind speeds tested. A maximum power of 88.3µW was observed at a wind speed of 8m/s from the vertical-stalk configurations. Note that this power output could have been further increased by tuning the load resistance for this configuration at 8m/s, given its non-optimal load matching as mentioned above. From visual inspection, it was suspected that the PVDF stalk was subjected to excessive nonlinear bending. However, due to the high flapping frequencies (8-25Hz), high speed capture of the leaf-stalk was required to confirm the hypothesis. Also, the standard deviations remained higher for the vertical-stalk configuration, indicating that the flutter pattern was less harmonic compared to the horizontal-stalk configuration. The cause for the excessive power output is explained with the help of high-speed video results in the next section.

4.6.2.2 High-speed footage

High-speed imagery of the symmetrical configuration indicated that the PVDF was subjected to transverse bending at every wind speed. In the *a*-offset configuration, it was clearly seen that this configuration was subjected to coupled bending-torsional modes. However, the amplitude remained lower than that of the pure bending configuration at every wind speed. In Figure 4.23, the point of maximum deflection for the symmetrical configuration is compared with that of the *a*-offset configuration at 6.0m/s. In all the high-speed footage and images, the wind has to be visualized as if flowing out of the images and the camera positioned as shown in Figure 4.18. The author also recommends the reader to view the high-speed videos from the DVD attached at the back of the printed version of this thesis. It can be seen from Figures 4.23a and 4.23b that the bending amplitude of the offset configuration was lower than that of the symmetrical configuration, meaning lower bending strain. However, it is also seen that the PVDF was subjected to some amount of torsional strain in the offset configuration.

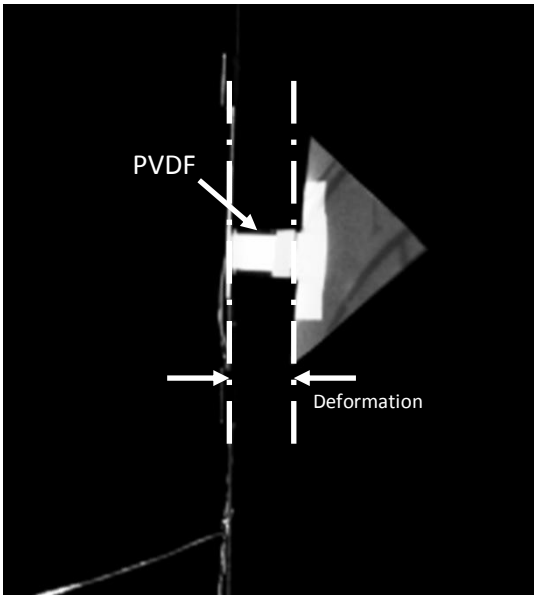

Figure 4.23a: Maximum deflection of the symmetrical case at 6.0m/s.

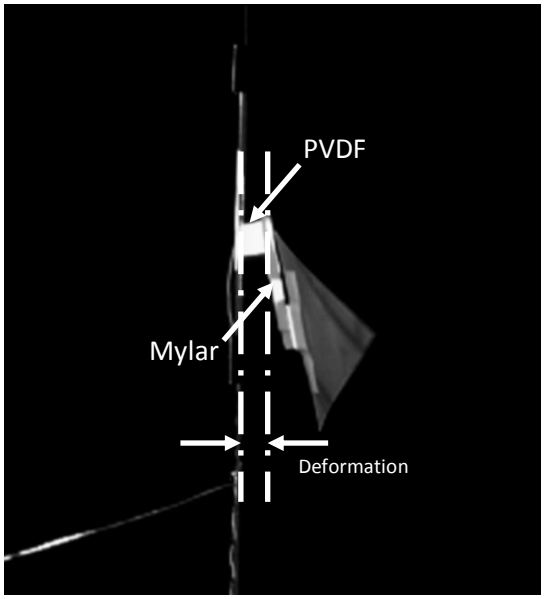

Figure 4.23b: Maximum deflection of the *a*-offset case at 6.0m/s.

In the asymmetrical cases, due to their geometry, the fluid forcing function impinging on the structure was no longer the same as the forcing function in the symmetrical configuration. In the dynamic tests performed earlier, the input forcing function was identical for all three cases. However, when the harvesters were immersed in a flow, there was a lack of direct control of the input fluid forcing function at a given wind speed, as it was totally driven by the structure's geometry (notwithstanding the flow properties being kept constant across all three test cases). However, comparing the flutter modes for each case provided some insight into the nature of the fluid forcing. Although the *a*-offset configuration experienced a small level of torsional strain, it was observed that the bending deflections were lower than the symmetrical configuration (Figure 4.23). As explained earlier, coupled bending-torsion vibrations involve bending and torsional strains. Although the *a*-offset configuration experienced torsional strain, the amount of bending strain would have remained lower compared to that of the symmetrical bending configuration. This was perhaps the cause for lower power outputs in the *a*-offset configuration.

It was interesting to observe the flutter pattern of the *2a*-offset configuration. Since the Mylar was longer, the system did not show evidence of limit-cycle oscillations, but rather manifested flutter in the chaotic regime, i.e. where irregular deformation magnitudes and random snap-through events occurred. The maximum deformation of the *2a*-offset configuration at 6m/s may be seen in Figure 4.24. The average power output recorded for this configuration was lower with a high standard deviation (Figure 4.21). At wind speeds of

7.0m/s and 8.0m/s, the flapping was very chaotic, to an extent that the leaf entangled itself with the base clamping strip and stalled. It has been shown elsewhere that maximum strain energy is acquired only when flutter eventuates in limit-cycle oscillations (Alben and Shelly, 2008). Thus, during chaotic flapping, the power output reduces significantly. The characteristics of different flutter regimes can also be found in Yamaguchi et al. (2000).

The two types of flutter, namely limit-cycle oscillatory and chaotic flutter, may be distinguished visually from experiments; however, the existence of chaotic flutter may be more readily perceived by inspection of the output-voltage spectral density. Where limit-cycle oscillations over time produce a distinct peak at the flutter frequency, chaotic flutter characterizes a more broadband response, as can be seen in Figure 4.25. The power spectral estimates of the voltage signals were calculated using Welch's modified periodogram technique (Welch, 1967). The flutter bending-mode harmonics are clearly seen in Figure 4.25a, whereas in Figure 4.25b, a peak in the signal approximately one-half of the dominant limit-cycle frequency manifested; a common indication of transition to chaotic flutter (Connell and Yue, 2007). Note that the dominant frequency in the bending case was higher and more pronounced than the *2a*-offset case, despite the constant wind speed, as noted by Argentina and Mahadevan (2005), which partly lends to the greater output power of the bending case. Interestingly, the output-power deviation was almost identical between the bending and 2*a*-offset cases (Figure 4.21).

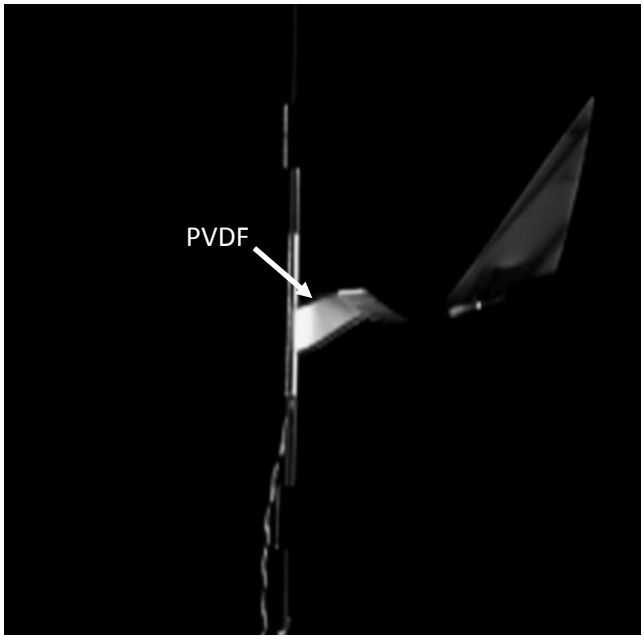

Figure 4.24: Maximum deformation of *2a*-offset configuration at 6.0m/s.

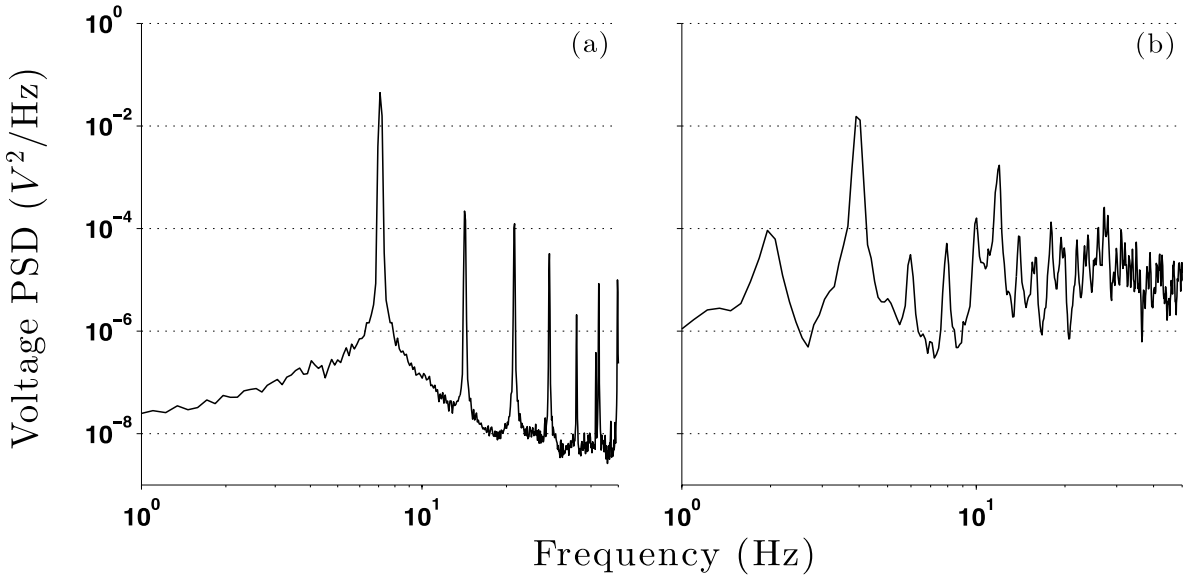

Figure 4.25: Voltage spectral density at 5.0m/s for the a) bending-only and b) *2a*-offset cases.

In any piezoelectric material, the power output depends on its operational mode. Piezoelectric materials subjected to transverse bending operate in the d_{31} mode. However, when the material is subjected to torsion, in-plane shear strains and axial strains along the edges are experienced. Due to the poling, design and electrode configuration of the PVDF examined, the shear strains (the conventional d_{15} mode) do not contribute to the harvestable power. The bending strains induced by torsion alone contribute to the harvestable power. The induced strains along the width of the material operate primarily in d_{32} mode (Figure 4.26). In general, commercially available PVDF piezoelectric materials are not designed to work in the d_{32} mode and hence their corresponding strain coefficients are very low (Table 4.1). Thus, it is evident that although torsional vibrations induce combined strains, it cannot be a substitute for energy harvesting from transverse bending as only the bending strains induced by torsion contribute to the power output unless the PVDFs are fabricated with high d_{15} values. It could only act as an additional source of power output. It is therefore essential to achieve more strain in d_{31} mode to obtain more power output. These asymmetrical configurations, although induced torsional vibrations, could not induce enough bending strains compared to the pure bending configuration. Also, the very low value of d_{32} conversion coefficient indicated that torsional vibrations do not help in providing more power output if sufficient amount of strain in *31*-mode is not achieved. It is however important to note that the power output is proportional to the time rate of change of strains in any direction. Therefore, the comparison

of the piezo coefficients only provides a limited understanding of the piezo's behavior and does not provide any conclusive result.

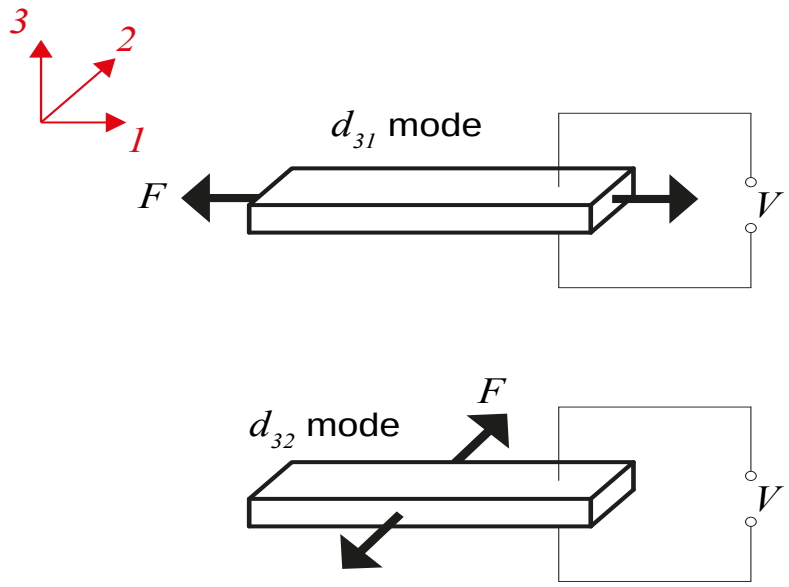

Figure 4.26: Piezo operational modes : d_{31}-pure bending; d_{32}-strain direction due to torsion.

Another practical drawback that was noted in these asymmetrical configurations was their low fatigue life. PVDF's subjected to excessive bending and torsional strain are prone to chaotic flapping and hence increased fatigue (picture of damaged PVDF patch is later shown in Figure 4.30). During chaotic flapping, the PVDF was often subjected to high amounts bending and twisting, thereby causing high stress concentrations along the edges leading to reduced fatigue life. Also, since the power output was already lower compared to the pure bending case and more prone to chaotic flapping and fracture in a short amount of time, it would not seem to be economically viable to design a harvester with an asymmetrical configuration discussed here, to be excited by fluid flow, unless these PVDFs are specifically manufactured to work in bending-torsion modes of vibration.

In the vertical stalk configuration, the flutter characteristics were entirely different. The maximum deformation of the PVDF stalk in the vertical configuration, at a wind speed of 3.0 m/s is shown in Figure 4.27. It is evident from this figure that the PVDF stalk was subjected to large transverse bending. This bending strain was augmented by a torsional strain at this point of maximum deformation. However, the amount of torsion induced in the stalk was considerably less compared to the bending. This behavior was also observed at other wind speeds. Thus, the increased power output in the vertical stalk configuration could be

attributed to large nonlinear bending deformations augmented by relatively small torsional deformations.

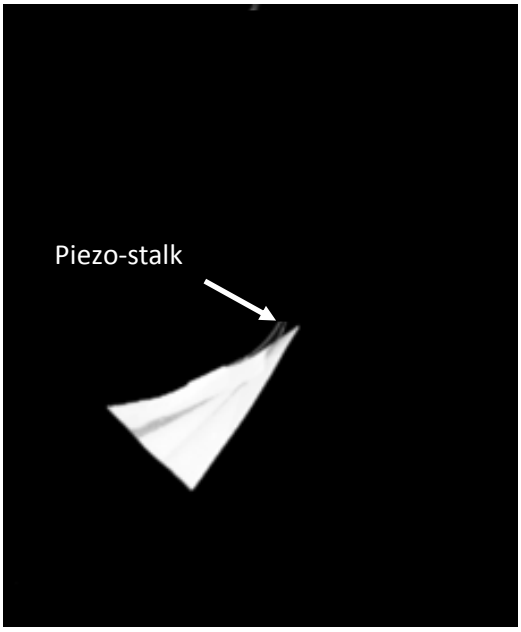

Figure 4.27: Maximum deformation of the PVDF stalk at 3.0 m/s.

The larger bending deformations in the vertical leaf-stalk arrangement were caused by the different nature of the aerodynamic forces impinging on the leaf, compared with the horizontal configuration. In the static-stable state (i.e. no flutter), the axis of rotation of the hinge was vertical with respect to the ground plane, for both configurations (Figure 4.1). However, the disparity in the aerodynamic forces arose once the system began to flutter. In the vertical-stalk case, the hinge axis of rotation also tilted with the system. Figure 4.28 is an image of the flapper at 5.0m/s, where the hinge axis is virtually horizontal with respect to the ground plane. In contrast, the hinge always remained vertical with respect to the ground plane for the horizontal configuration during flutter. Given that the leaf-stalk flutter was mainly driven by the leaf, the leaf geometry did not change between the horizontal and vertical configurations, and the wind speeds tested were identical in both cases, it is proposed that unsteady lift forces were chiefly driving the vertical-stalk cycle. That said, it has not been quantitatively determined whether the magnitude of the lift forces were larger in the case of the vertical-stalk case. It can be argued that the changing direction and orientation of the lift forces did indeed act constructively out of phase with the structural deformations occurring in the piezoelectric stalk, with the vertical-stalk case. An in-depth investigation into the unsteady lift forces governing the motion of the vertical-stalk case was not included in the work here, but might be worthy of further study (mentioned in Chapter 6).

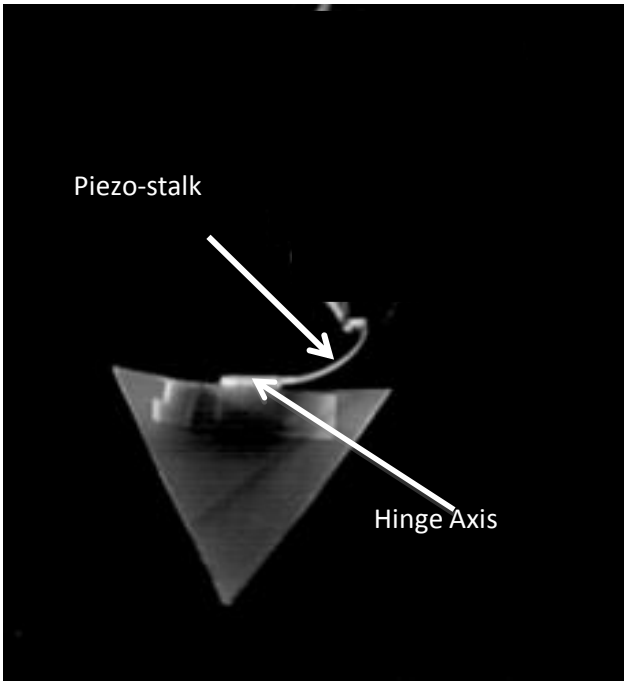

Figure 4.28: Entire surface of leaf facing the wind with an instantaneous horizontal hinge axis, at 5.0m/s.

Due to the large structural deformations, the stalk-leaf system would strike the base clamping strips during every flutter cycle. This behavior was observed at wind speeds of 5.0m/s and higher. The piezo-leaf system would rotate almost 180° and impact the base clamping strips. The interference of the clamping strips on the motion of the flapper could have also been the cause for a marginal decrease in the gradient of the power curve after 4.0m/s (Figure 4.22). However, this issue was not resolved simply because the base of the stalk required secure clamping. An image of the flapper at 8.0m/s is shown in Figure 4.29, where the base clamp is seen to be interfering with the flutter motion of the piezo-leaf system.

Although the large deformations result in increased power output, one major drawback is the fatigue life of the PVDF stalks. After three experimental trials at 8 m/s, it was found that the piezoelectric patches cracked at the clamping location (Figure 4.30). This was probably due to the combination of excessively large bending displacements and fatigue. However, one way that this issue could be resolved is by increasing the stiffness of the stalk, by stacking the PVDF patches. The patches could be stacked with or without an air gap, which would reduce the large deformations prevalent using a single stalk. At the same time, relatively high power outputs could be obtained since the stalks could be electrically connected in parallel, thus the charge from each piezoelectric patch would be cumulative. It remains to be seen whether the lower deformations of a stacked configuration would trade off with the additional current

provided in a stacked configuration. This would form a part of the future work in this configuration.

Figure 4.29: Image at 8.0m/s. Clamping strip interfering flapper motion.

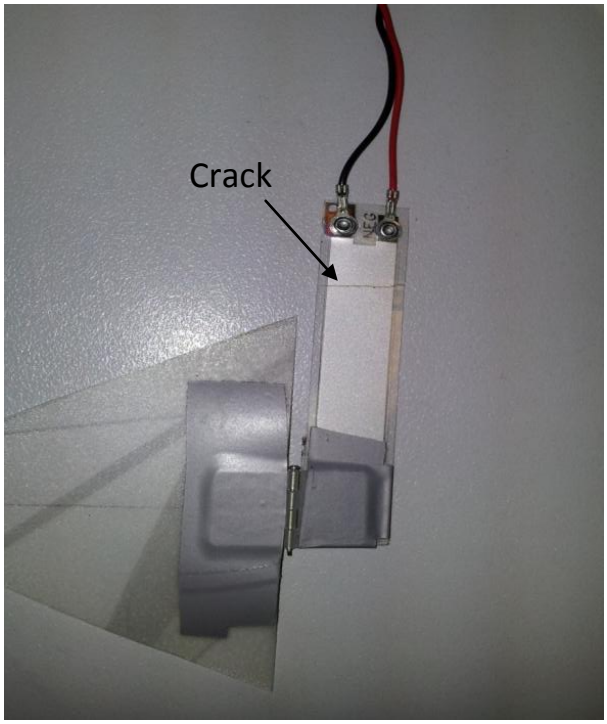

Figure 4.30: Crack observed at the clamping edge of the vertical stalk after 3 experimental trials.

4.7 A note on performance of harvesters in outdoor flow conditions

The power output and high-speed video results indicated that the offset (asymmetrical) configurations do not increase the power output, when excited by smooth fluid flow. Also,

the vertical stalk configurations were subjected to highly nonlinear strains and reduced fatigue life. Thus, the results clearly suggested that out of the different configurations tested, the horizontal symmetrical configuration performed the best under smooth flow conditions.

The symmetrical nature of the horizontal configuration aided in highly repeatable limit-cycle oscillations (LCO). However, in reality, flow conditions are not necessarily symmetrical. Wind can approach the harvesters from any direction. Also, outdoor flow conditions are usually turbulent. In this regard, comprehensive studies were conducted by McCarthy et al. (2014) in a complimentary research project. In this research, the horizontal symmetrical configuration was positioned at different yaw and pitch angles: first in smooth flow, and later in replicated atmospheric boundary layer (ABL) turbulent flow conditions (12.7% intensity, 310 mm longitudinal integral length scale). The key findings are quoted below (McCarthy et al., 2014):

'At non-zero yaw and pitch angles, the harvester departure from LCO's resulted in lower mean output power. When placed in replicated ABL turbulence, the turbulent flow structures apparently acted as a damping mechanism when the harvester fluttered in LCO's, reducing the power output and diminishing the effect of the vortex shedding. However, at higher pitch and yaw angles the turbulence generally appeared beneficial to the output power compared with smooth flow.'

Thus, it is important to note that the concept of an artificial tree is highly challenging, given the lower power outputs of these harvesters under non-parallel flow conditions. This emphasises the need for optimizing the harvester design to suit realistic urban turbulent flow conditions. Also, the base clamp has to be passively aligned to the wind such that the harvester is constantly parallel to the flow to maximize the power output. These are suggested to form a part of the future work.

4.8 Summary

Energy harvesting from PVDF using coupled bending-torsion vibrations was investigated. Literature suggested that asymmetrical configurations would output more power compared to symmetrical configurations, when excited by mechanical vibrations, due to coupled bending-torsion strain. Dynamic tests were performed using a shaker to measure the power output for symmetrical and asymmetrical configurations and these effects were also computationally investigated. From both the experimental and computational results, it was clear that the

offset configurations provided more power output compared to pure bending configurations. However, it was observed that the power generated could be significantly affected by the amount of structural damping present in the system.

Wind-tunnel tests were carried out for these configurations by coupling these configurations with an artificial leaf using a free hinge. It was somewhat surprising to find out that the offset configurations resulted in lower power outputs compared to the symmetrical pure bending configuration. However, high-speed video images indicated that amount of bending deformations induced in the offset configurations were lower. Due to the difference in geometry and flexibility of the configurations, the input fluid forcing function no longer was maintained constant. Thus, the amount of bending strain in the offset configurations remained lower. Also, the offset configurations, due to their flexibility, were more prone to chaotic flapping, thereby reducing the average power output. Most importantly, PVDFs subjected to coupled bending-torsion flutter partly operate in the d_{32} mode which has a relatively low piezoelectric conversion coefficient. Thus, the amount of power generated by the offset configurations remained low compared to the pure bending configuration at all wind speeds.

It was found that the vertical-stalk configuration provided much more power output compared to the symmetrical horizontal-stalk configuration. High speed videos indicated that this was because of excessive nonlinear transverse bending strain augmented by small amounts of torsional strain experienced by the PVDF. However, it was observed that these PVDF films were prone to fatigue and fracture due to the large amounts of strain. Thus, it was found that harvesters subjected to coupled bending and torsion modes of flutter were more prone to chaotic type of flapping and fatigue, hence they produced lower amounts of power. This also indicated that it is probably not economically viable to design a harvester, subjected to bending-torsion modes of flutter, unless the piezoelectric materials are specially designed to withstand high bending and torsional strains (higher d_{15} values). Also, due to the current design of most commercially available PVDFs which operate primarily in d_{31} or d_{33} modes, it is understood that energy harvested in fluid flow from torsion could only act as a low-value peripheral supplement to the energy harvested from bending.

Chapter 5
Proximity Effects of Energy Harvesters

5.1 Introduction

In order to harvest sufficient amount of energy to power ULP devices and LED lights, these harvesters have to be scaled up in number and deployed in a given space. By doing so, it is important to understand how these harvesters would interact with each other, when placed in close proximity. The presence of a flapping harvester closer to another similar harvester may have an impact on their power outputs due to their vortex interactions.

As mentioned earlier in Section 2.10.2, Pobering and Schwesinger (2004) presented a harvester array concept, where the power outputs were assumed to be unaffected, when operating in tandem. Since these harvesters work on FSI, this assumption is worth investigating. In this regard, Bryant et al. (2011) investigated two harvesters operating in tandem and identified that the downstream harvester's power output increased by 30% when positioned at a specific distance away from the upstream harvester. However, it is important to note that this harvester design was different from the one investigated here. Bryant et al. (2012) conducted smoke-wire flow visualization studies to understand the flow pattern around their harvesters. However, the focus was not to identify the cause for increase in downstream harvester power.

In the previous chapter, results indicated that out of the harvesters investigated, the horizontal configuration proved to be the most efficient and reliable (although the vertical-stalk configuration provided more power output, it is not considered due to fatigue issues). Thus in this work, two such horizontal symmetrical configurations were immersed in smooth parallel flow, and displaced in three orthogonal directions for a range of spacing separations.

In the following sections, experimental setup, methodology and results are explained. The phase lags between the harvesters were measured and used to understand the cause of any variation in power output. These phase-lag results were later used along with smoke-wire flow visualization, primarily conducted by McCarthy et al. (2014), to understand the behaviour of these harvesters.

5.2 Methodology

In order to determine the proximity effects, there are several ways in which the harvesters can be positioned and oriented in a three-dimensional space. However, the potential test matrix would become extremely large. Thus, only certain specific positions were selected in order to understand the basic behaviour of these harvesters.

Having more than two harvesters operating at once may result in complex vortex interactions, thereby making it highly challenging to understand the harvesters' behaviour. Thus, only two harvesters at any given time were investigated in this study.

Two harvesters were placed in the following directions, one at a time (as shown in Figure 5.1):

1. Stream-wise (longitudinal) direction.
2. Cross-stream (lateral) direction.
3. Vertical direction.

In each direction, the separation distance (d) between the harvesters was varied. This distance was normalized with respect to the single leaf-stalk length (L) and expressed as (d/L). The two harvesters were positioned at a normalized separation distance (d/L) of 0, 1 and 2. Every arrangement was tested in a wind-speed range of 3-8 m/s in smooth parallel flow. Therefore, there were 54 test cases in total. Each test case was repeated twice to ensure repeatability.

In the cross-stream direction, for the $d/L = 0$ case, the separation distance was 10 mm. This was due to the fact that harvesters with no separation distance would virtually act as a bimorph. A relatively small separation distance of 10 mm ensured no physical contact with each other. However, for the other cases, the separation distances were maintained as explained above. Figures 5.1a, 5.1b and 5.1c show the schematic setup of the harvesters in stream-wise, vertical and cross-stream directions respectively.

Time-varying voltages from both the harvesters were recorded simultaneously. These voltages were post-processed to determine two important parameters: mean power output and phase lag between the harvesters. The power output from each of the harvester was normalised with respect to its stand-alone power output (i.e. the power output, when flapping along with another harvester, was compared with its power output, when it flapped alone). Thus, the normalised power (λ) is defined as:

$$\lambda = \frac{P_{actual}}{P_{stand-alone}} \tag{5.1}$$

The phase lag was measured in order to identify the flutter pattern of these harvesters and to determine the cause for increase/decrease in power output (the consequence of phase-lag analysis is explained later in this chapter). The phase-lag measurement technique is explained in Section 5.3.1.1.

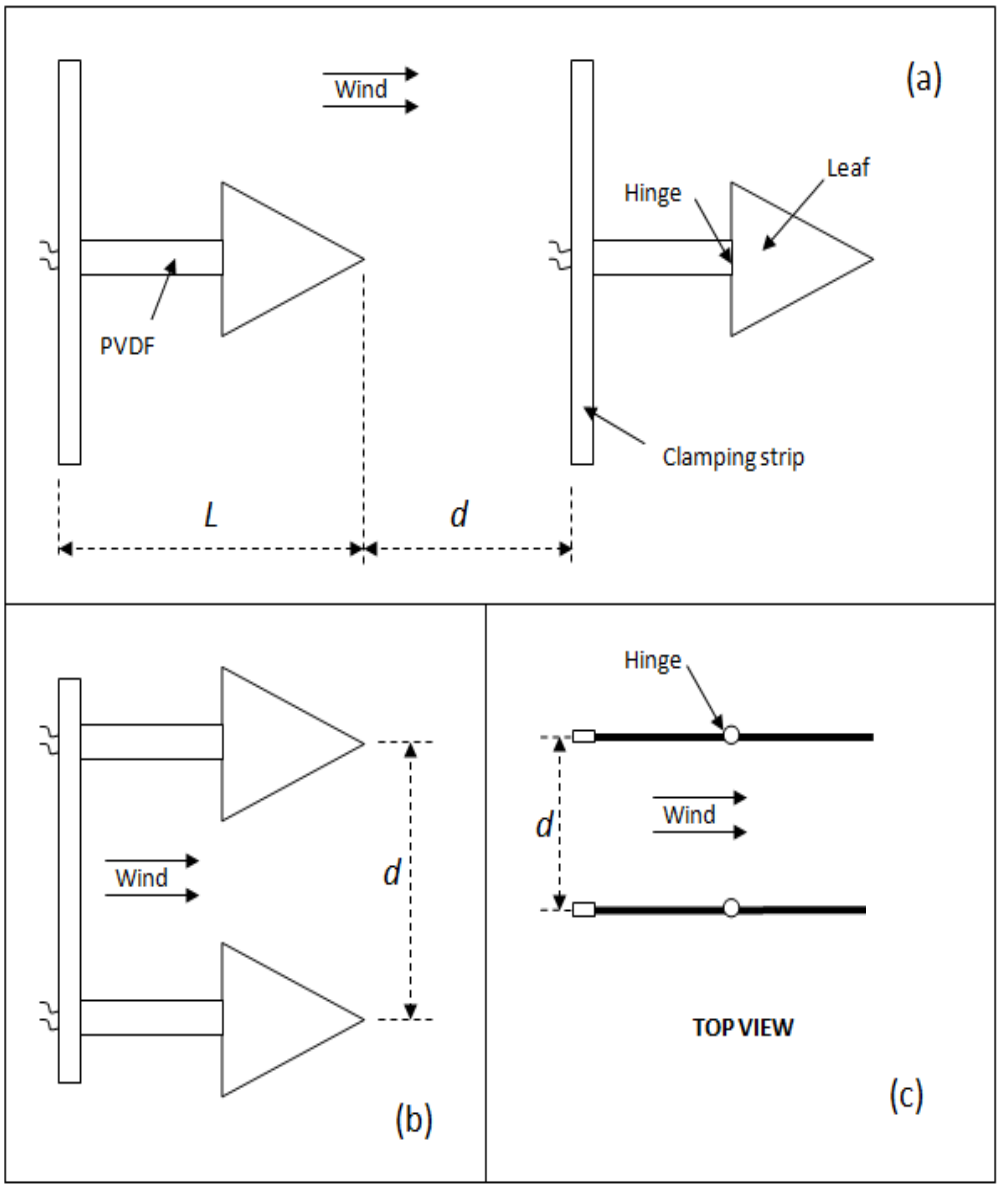

Figure 5.1: Schematic of the harvesters in (a) stream-wise, (b) vertical and (c) cross-stream directions.

5.3 Experimental setup

All experiments were conducted in RMIT University's AWT (details mentioned in Section 3.6.1). The symmetrical harvester configuration used in the experiments was described in Section 4.5.4.2. The PVDF stalk, hinge and the polymeric leaf together forms a length of 158 mm. The clamping stand has a width of 12 mm (explained in Section 3.6.2). Thus, the single leaf-stalk length (L), along with 10 mm of clearance, was set at 180 mm. The separation distance (d) between the harvesters was therefore set at 10 mm, 180 mm and 360 mm (d/L = 0, 1 and 2). Figure 5.2 shows the setup of the harvesters in the wind tunnel.

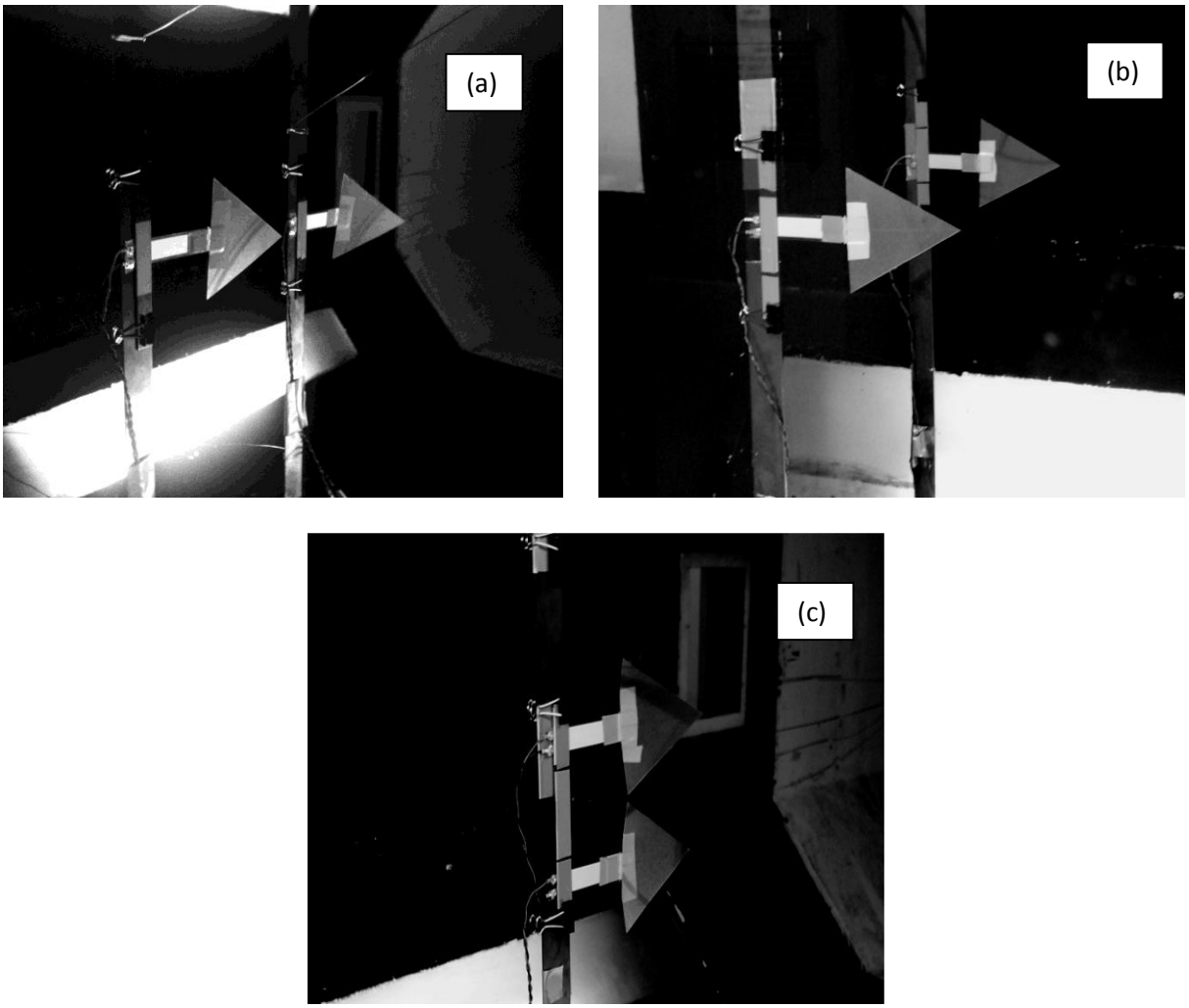

Figure 5.2: Experimental setup of the harvesters in (a) stream-wise, (b) cross-stream and (c) vertical directions.

Smoke-wire flow visualization was carried out on a specific arrangement by McCarthy with the author's assistance. The camera, smoke-wire and light setup can be found in McCarthy et al. (2013). The flow visualization revealed that the base clamping stand, along with the strips

and clips, did not have any significant impact on the flow to affect the performance of these harvesters.

5.3.1 Simultaneous Voltage measurements

The load matching, data logging and power calculation details were similar to the previous tests as explained in Section 4.5.5 in Chapter 4. However, the same setup was extended for both the harvesters and the data was recorded simultaneously. Since the sampling rate was 1kHz, and the multiplexing rate in the data acquisition unit (DAQ) was several orders of magnitude higher (1MHz), the delay in data logging between the harvesters were considered negligible. Figure 5.3 shows the electrical setup for the harvesters displaced in stream-wise direction. The same setup was used for other arrangements as well. GE-8115 shown in the figure is the differential probe with an internal impedance of 60 MΩ.

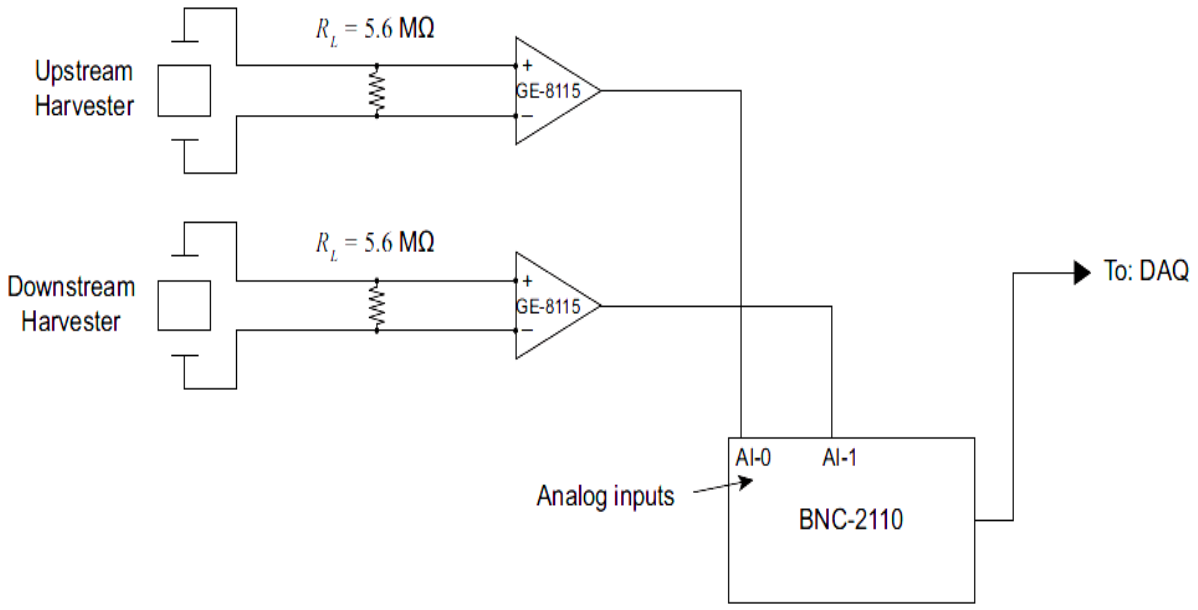

Figure 5.3: Diagram showing the electrical setup for voltage measurements.

5.3.1.1 Phase-lag calculations

When two harvesters were flapping at a given wind speed, it was visually spotted that the harvesters were not flapping in phase for most of the arrangements. To investigate this, the exact phase lag between the harvesters was calculated at every wind speed from the time-varying voltage data.

The voltage data for every test case were recorded for a period of 2 minutes. Therefore, the number of cycles for which the data were recorded depended on the wind speed (as the

harvesters would complete more cycles over a fixed time length at higher wind speeds). Also, it was considered useful to observe the time-varying behaviour of frequency and phase differences between the harvesters. Therefore, the frequency of each harvester, along with the phase differences between harvesters, was calculated for every cycle of flapping at a given wind speed.

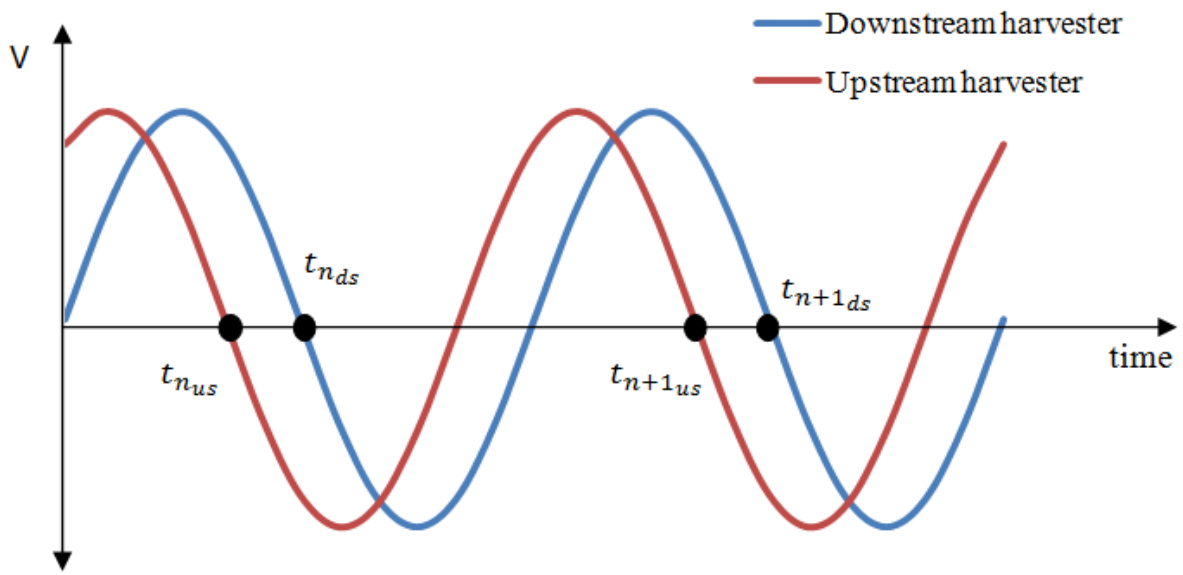

Figure 5.4: Schematic of the simultaneous voltage data acquired during the experiments.

Figure 5.4 shows a sample voltage data of the harvesters, when displaced in stream-wise direction, where $t_{n_{us}}$ and $t_{n_{ds}}$ represent the instantaneous times of the upstream and downstream harvesters respectively.

The n^{th} cycle time, T_n was calculated as:

$$T_{n_{us}} = t_{n+1_{us}} - t_{n_{us}}$$
$$T_{n_{ds}} = t_{n+1_{ds}} - t_{n_{ds}} \quad (5.2)$$

Therefore, the frequency for n^{th} cycle, f_n was calculated as:

$$f_{n_{us}} = \frac{1}{T_{n_{us}}}$$
$$f_{n_{ds}} = \frac{1}{T_{n_{ds}}} \quad (5.3)$$

The average cycle times for the harvesters were estimated as:

$$T_{mean} = \frac{1}{n}\sum_{i=1}^{n} T_i \tag{5.4}$$

The phase lag for n^{th} cycle, based on the upstream harvester, was therefore calculated as:

$$\theta_n = \frac{t_{n_{ds}} - t_{n_{us}}}{T_{mean}} \times 360^o \tag{5.5}$$

The mean phase lag was estimated as:

$$\theta_{mean} = \frac{1}{n}\sum_{i=1}^{n} \theta_i \tag{5.6}$$

Due to the digital sampling of the analog data at 1 kHz, the instantaneous times, t_{n+1} and t_n were approximations as these points do not always coincide with changes in voltage polarities (positive to negative change in voltage). Thus the frequency and phase lag estimations appeared slightly fluctuated. A spectral analysis of the data may provide a better estimation of the flapping frequency. However, since the time-varying behaviour of the harvesters was required to be observed, this method was preferred. Also, this method was justified due to the very low standard deviation values determined during the phase lag and frequency analysis.

5.4 Results and discussion

In order to observe any variation in power output of the harvester, when operating in close proximity with a similar harvester, the power outputs of the individual harvesters were recorded first in their stand-alone positions (i.e. when operating alone in the wind tunnel). The two harvesters used in this experiment were named 'harvester 1' and 'harvester 2' respectively. Each harvester was tested at least three times for its stand-alone power output at every wind speed to ensure repeatability.

Figure 5.5 shows the stand-alone power outputs of harvester 1 and harvester 2 for a wind-speed range of 3 - 8 m/s. The piezoelectric stalks used in both the harvesters were the same (LDT-028K/L with rivets, Measurement Specialties). The polymeric leaf used in each

harvester was cut out from the same sheet (isosceles triangle of base and height 8cm each). Also, the hinges used were identical, as shown in Section 4.5.4.1.

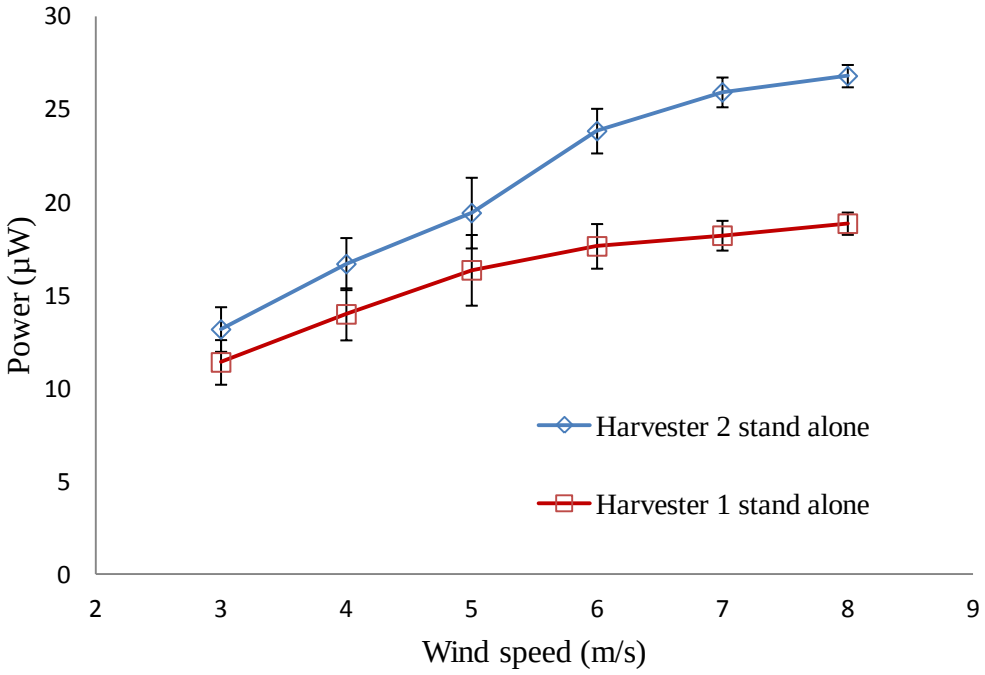

Figure 5.5: Power output comparison of individual harvesters in their stand-alone positions.

The graph clearly indicates that although the harvester configurations were identical, the power outputs differed. At first instance, the disparities in power outputs were attributed to frictional differences in the hinges. It is known that additional stiffness in hinges would increase the flutter frequency (see Appendix C), and hence the power output as power output is proportional to cube of the flutter frequency (equation (2.27)).

However, comparison of flutter frequencies of both the harvesters at every wind speed revealed that the flutter frequencies of the harvesters were essentially identical (see Figure 5.6: Note that the error bars in all the frequency plots in this chapter are the standard deviations observed for the period of time the data were recorded (2 minutes for each case)). This negated any differences in stiffness between the harvesters. Also, during the experimental trials, the leaves and hinges between the harvesters were swapped. However, they did not seem to alter the power outputs. Therefore, the disparity in power outputs could be attributed to the electromechanical properties of the PVDF stalk. Although the PVDFs used were of the same model and from the same source, the electromechanical coupling coefficients appear to be different. However, no conclusion could be drawn unless these properties are measured independently. This was not included in the scope of this work.

However, in order to overcome these differences, when the harvesters were placed together at different positions, each power output from the harvester was normalised to its own stand-alone power output at a given wind speed (as per equation (5.1)). This normalised power (λ) is used in the following sections to observe the increase/decrease in power outputs for every arrangement.

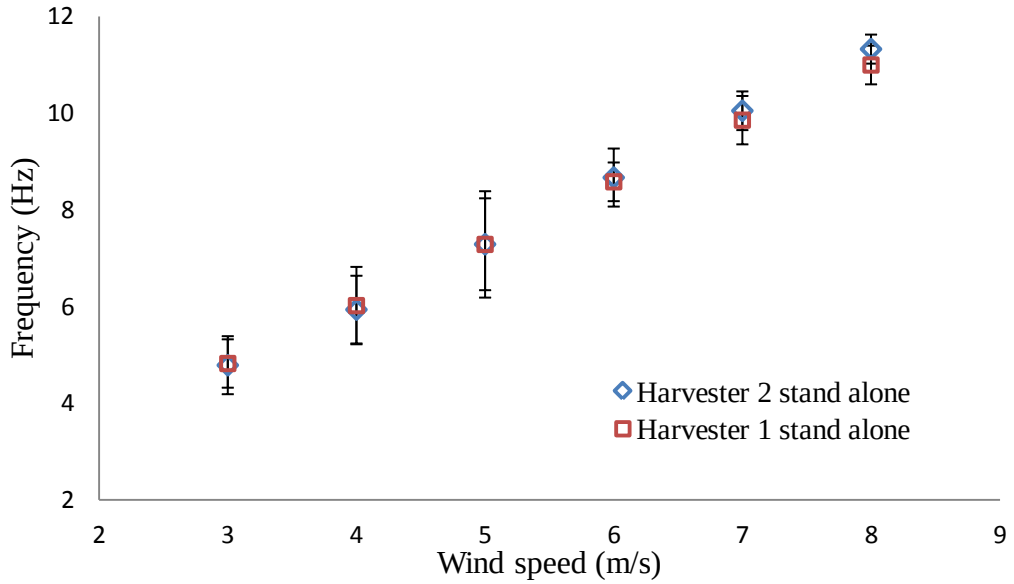

Figure 5.6: Flutter frequency comparison of the two harvesters in stand-alone positions.

5.4.1 Cross-stream proximity

In these tests, two similar harvesters were displaced laterally (side by side) and the separation distance between them were kept at d/L= 0, 1 and 2. Figure 5.7 shows the schematic of the arrangement for easier interpretation of the results. Note that for d/L = 0, the actual separation distance was 10 mm.

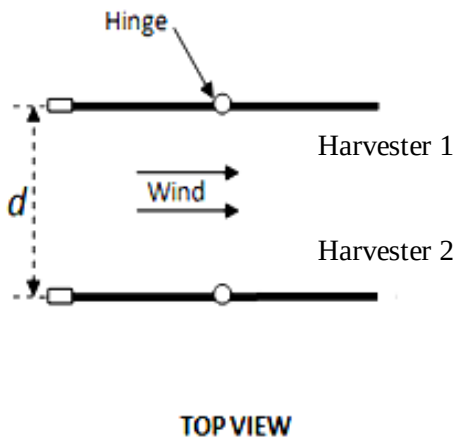

Figure 5.7: Cross-stream separation of the harvesters.

Figure 5.8 shows the normalised power output for harvester 1, and Figure 5.9 shows the same for harvester 2 for all the separation distances. Since the results from the experimental trials were identical, error bars were not required.

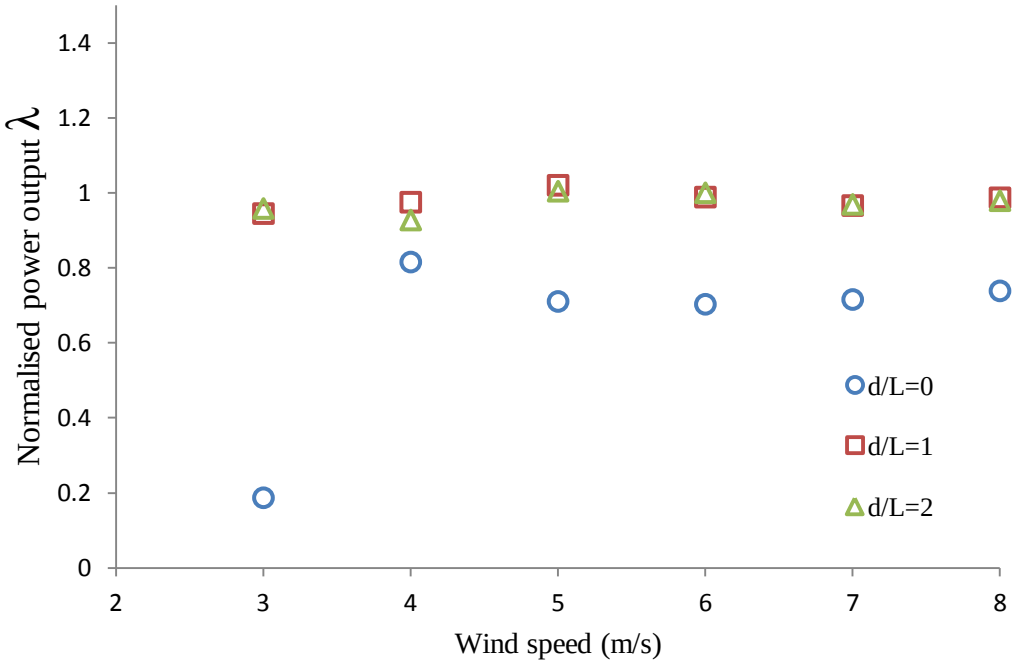

Figure 5.8: Normalised power output (λ) of harvester 1 in cross-stream proximity tests.

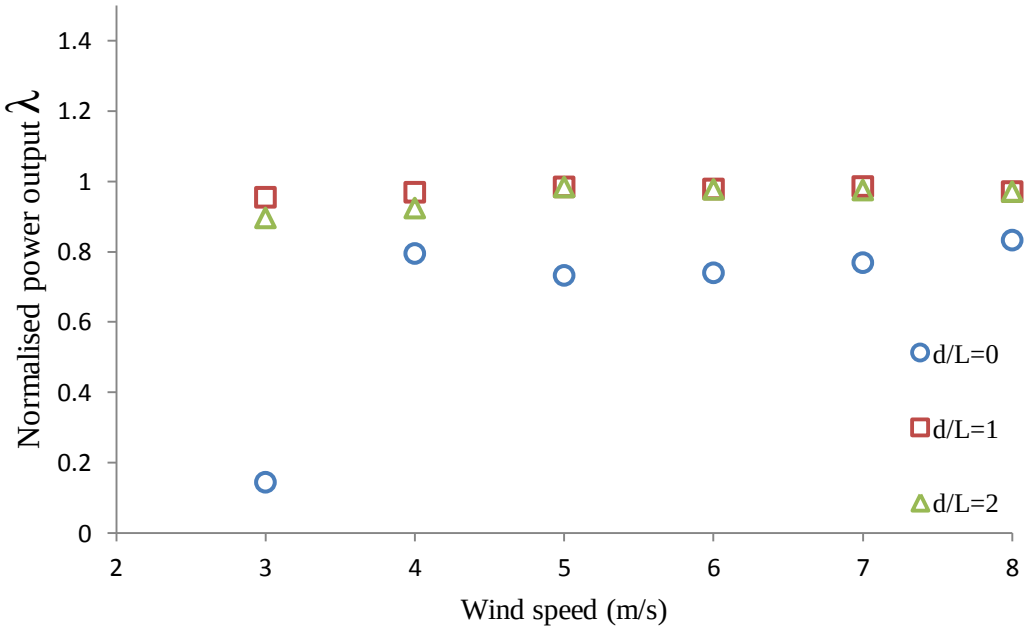

Figure 5.9: Normalised power output (λ) of harvester 2 in cross-stream proximity tests.

Since both the harvesters experience the same flow nominally at the same time, the behaviour of the harvesters were expected to be similar. This similar behaviour was clearly reflected in Figures 5.8 & 5.9.

At a lateral separation distance of 10 mm (d/L = 0), it was observed that the power output of the harvesters dropped significantly compared to their stand-alone case. For d/L = 0, at 3 m/s, it was observed that the harvester provided only 18% of their stand-alone power output. Given the very small separation distance, the system had different fluid boundary conditions. It is postulated that the system behaved like a single bimorph unit with air space (as discussed in Section 2.9.3 in Chapter 2). Thus, the harvesters had a reduction in the effective compliance thereby reducing the power output.

In Figure 5.10, the flutter frequency of harvester 1 in its stand-alone and d/L = 0 positions is compared. Reduction in flutter frequency for d/L = 0 position clearly explained the reduction in its corresponding power output. A very similar behaviour was observed for harvester 2 as well. A reduction in flutter amplitude was visually spotted for this position. This indicated that at a small separation distance, the harvesters destructively interacted with each other.

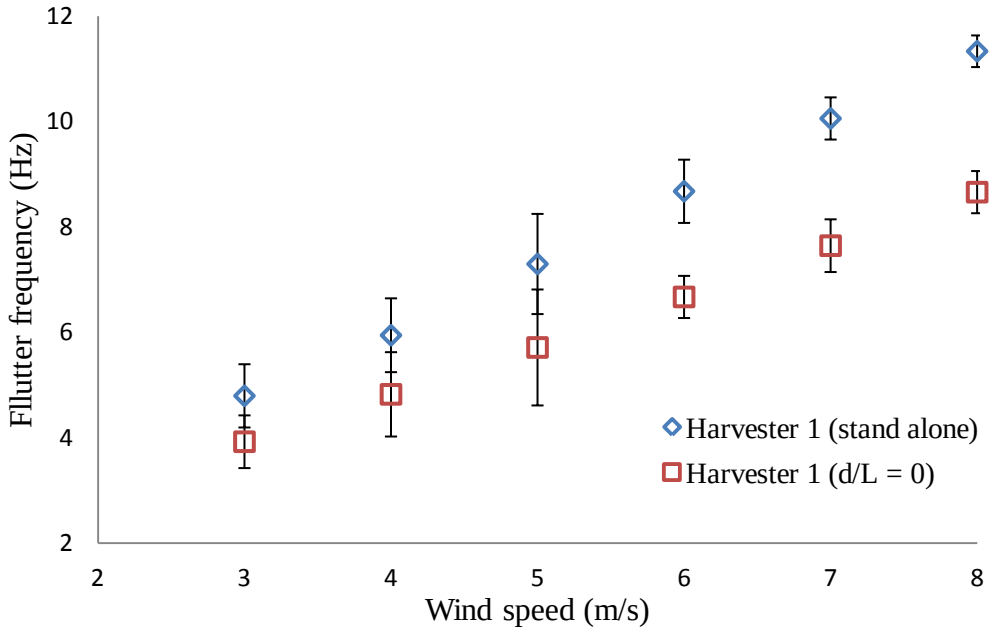

Figure 5.10: Flutter frequency comparison of harvester 1 in stand-alone and d/L = 0 positions.

For d/L = 0, at 3 m/s, owing to higher effective stiffness of the combined harvester system, it was visually noted that the limit-cycle flutter was not fully manifested. At other wind speeds, flutter frequencies of harvester 1 and harvester 2 were identical, and had a constant phase lag between the harvesters. This phase lag was measured at every wind speed, and for the range

of 4 - 8 m/s, the phase lag remained relatively constant (as shown in Table 5.1). This phase-lag behaviour was repeatable, as for both the experimental trials, similar phase-lag values were calculated. Also, this phase-lag behaviour remained constant over the number of cycles recorded (for a period of 2 minutes). Figure 5.11 shows the phase lag between the harvesters at 5 m/s. This constant phase lag clearly indicated an interaction between the harvesters at this position. The in-phase (approximately 10^0) behaviour also supported the postulation of an air-spaced bimorph-style behaviour.

Table 5.1: Phase lag values for d/L = 0 position.

Wind speed (m/s)	Phase lag (degrees)	
	Trial 1	**Trial 2**
4	10.37	9.86
5	9.09	9.24
6	8.01	8.63
7	7.40	8.03
8	8.63	9.12

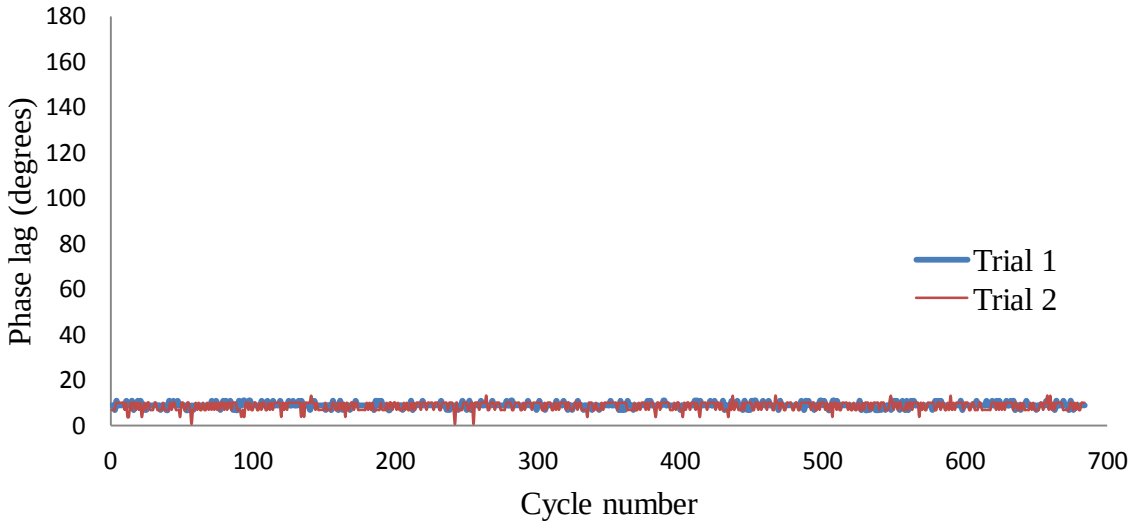

Figure 5.11: Phase lag between the harvesters for d/L = 0 position at 5 m/s.

However, at separation distances of 180 mm and 360 mm (d/L = 1 and 2), there was no significant interaction and the harvesters fluttered independent of each other. This was reflected in the λ values (approximately 1) at these distances for all wind speeds (see Figure 5.8 & 5.9). At these separation distances, the flutter frequencies of the individual harvesters

varied by 1 - 2 %, thereby not experiencing any phase-locking behaviour. The existence of independent fluttering motion of the harvesters, with no constant phase lag, suggested that as the separation distance in cross-stream direction increased, the harvesters behaved similar to their stand-alone cases.

5.4.2 Vertical proximity

In vertical proximity experiments, two similar harvesters were placed one below the other, and their interaction with each other was observed in a similar manner to the cross-stream proximity experiments. Figure 5.12 shows the schematic of the arrangement for easier interpretation of results.

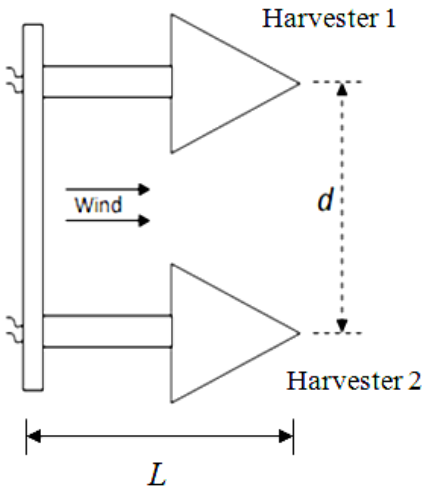

Figure 5.12: Vertical separation of the harvesters

Figure 5.13 shows the normalised power output (λ) for harvester 1 and Figure 5.14 shows the normalised power output for harvester 2 for all the separation distances. The figures indicate that for all the test cases, both the harvesters behaved similarly. This was justified from the fact that the harvesters experienced the same flow, at the same time, due to the symmetrical nature of the arrangement.

λ values were approximately 1 for all the test cases (as seen in Figures 5.13 & 5.14), with a maximum variation in power output of 6% observed at 5 m/s for d/L = 1 position. The two trials conducted for all the arrangements indicated that the results were repeatable (average values plotted in the graphs). These λ values indicated that there were no significant interactions between the harvesters to affect the power output for all the test cases.

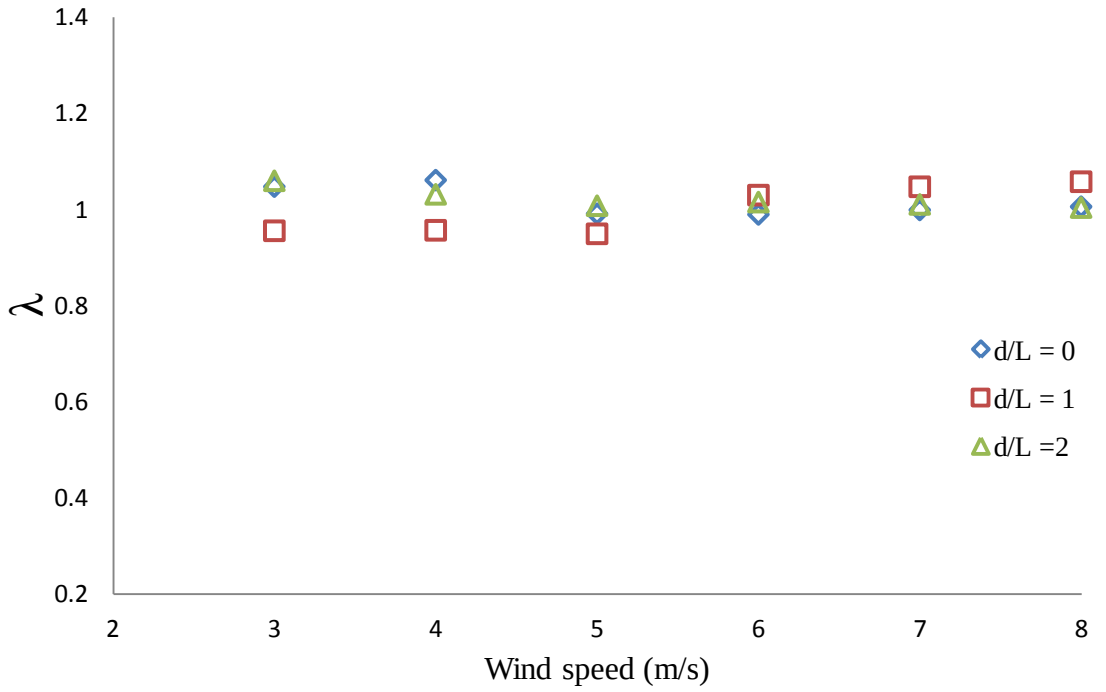

Figure 5.13: Normalised power output (λ) of harvester 1 in vertical proximity tests.

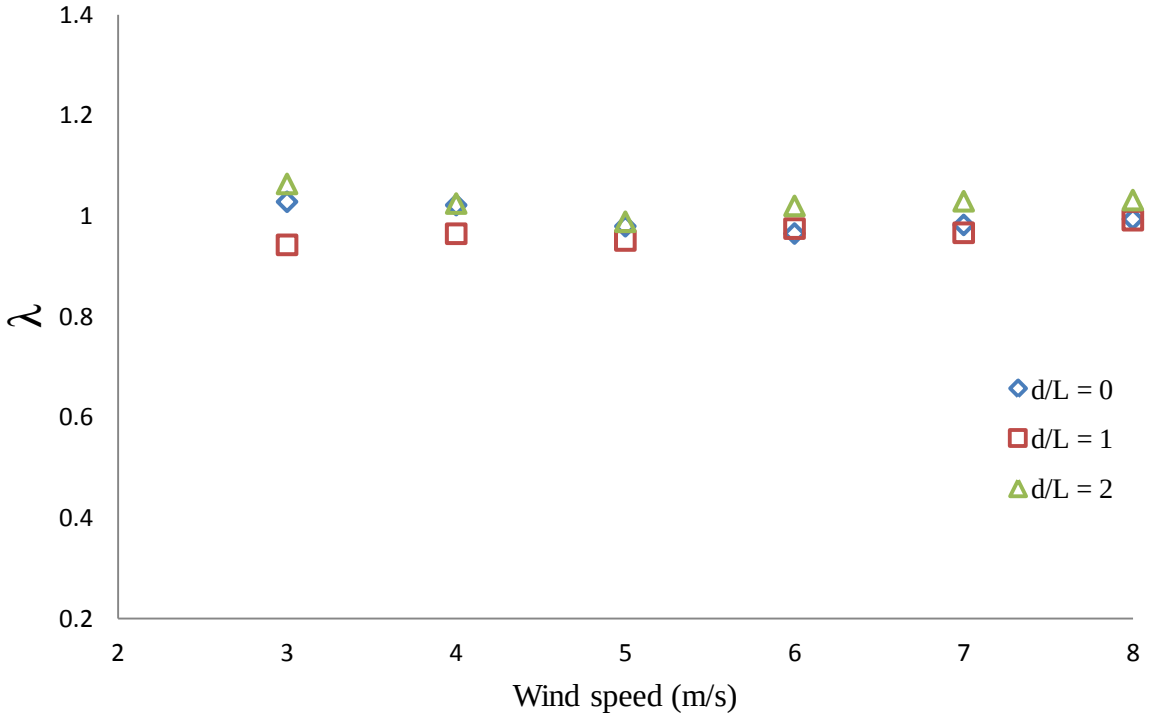

Figure 5.14: Normalised power output (λ) of harvester 2 in vertical proximity tests.

Although there were no significant variations in λ values indicative of any aerodynamic interaction between the harvesters, phase-lag analysis indicated that for $d/L = 0$ position, the harvesters locked in to a specific frequency, thereby experiencing a constant phase lag, at a given wind speed.

Figure 5.15 shows the frequencies for d/L = 0 position for wind-speed range of 3 - 8 m/s. Figure 5.16 shows the average phase-lag behaviour of the harvesters for wind speed range of 5 - 8 m/s. At wind speeds of 3 m/s and 4 m/s, it is postulated that the aerodynamic forces were not sufficient to create a phase-locking behaviour. This was supported by higher standard deviation values of frequencies at these wind speeds over the recorded period of time (Figure 5.15). Figure 5.17 shows the time-varying behaviour of the phase lag at 7 m/s. A similar behaviour was observed at other velocities.

From Figure 5.16, it can be seen that there was no specific relationship between the phase-lag and wind speed for d/L = 0 position. However, no significant conclusion can be drawn due to the insufficient number of data points obtained. Since there were no beneficial interactions in terms of power output, this behaviour was not analysed in detail. Nevertheless, the existence of a phase-lag behaviour at certain wind speeds indicated that aerodynamic interactions were occurring between the harvesters, when placed in close proximity. For positions of d/L = 1 and d/L = 2, due to small variations in frequencies between the harvesters (1 - 2 %), no phase-lag behaviour was observed, indicative of no aerodynamic interactions.

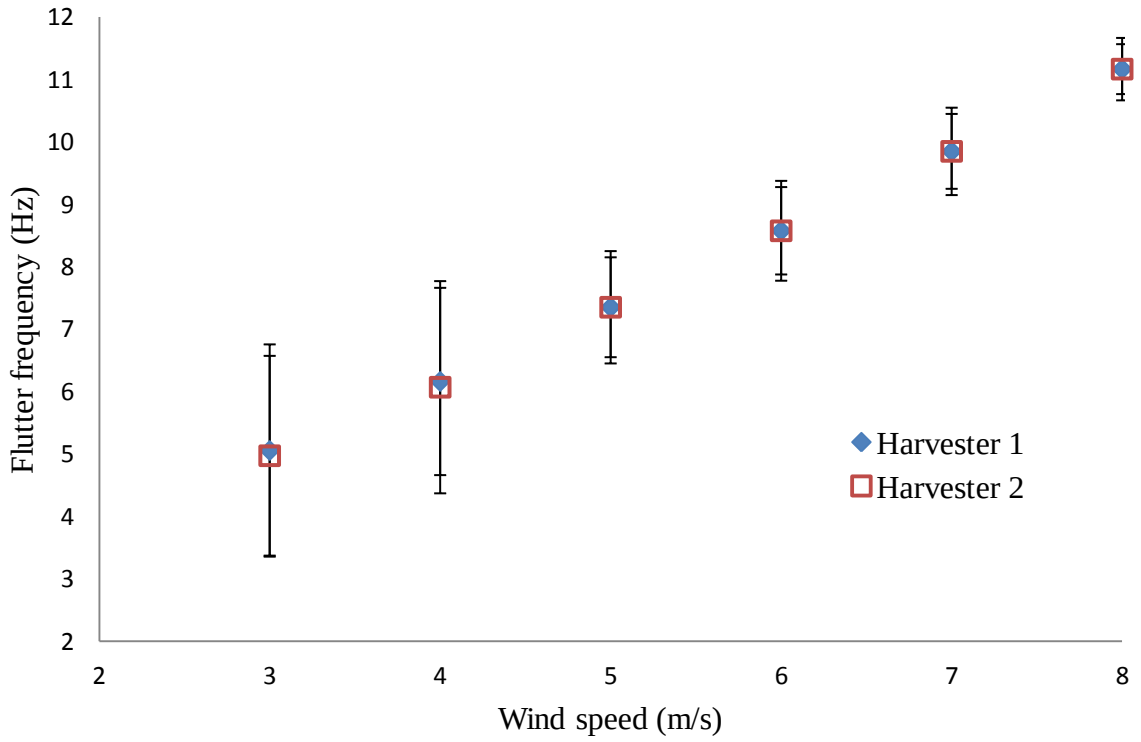

Figure 5.15: Flutter frequencies of the harvesters for d/L = 0 position.

.

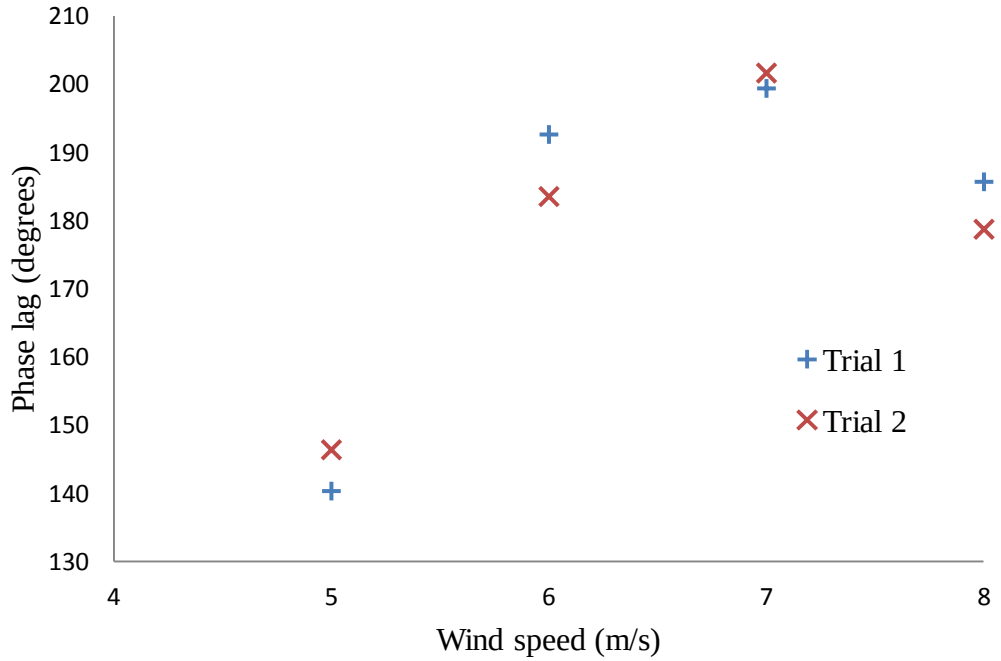

Figure 5.16: Phase lag vs. wind speed (for $d/L = 0$)

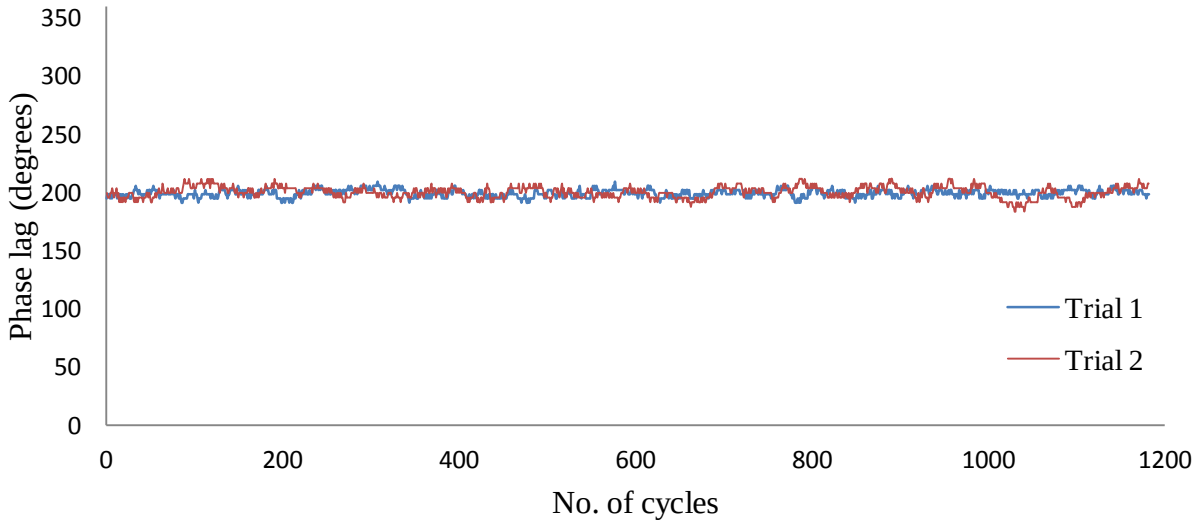

Figure 5.17: Phase lag between harvesters for $d/L = 0$ position at 7 m/s.

5.4.3 Stream-wise proximity

For these experiments, two identical harvesters were displaced in the direction of wind, one behind the other. Schematic of the arrangement is shown in Figure 5.18. The harvesters are referred as 'upstream harvester' and 'downstream harvester'. Figure 5.19 shows the λ values of the upstream harvester, for all the separation distances, tested in the wind-speed range of 3 - 8 m/s.

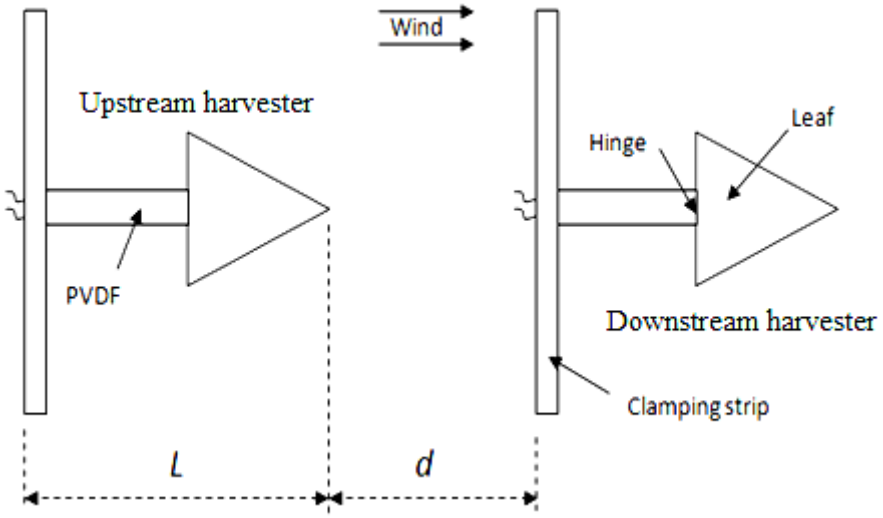

Figure 5.18: Stream-wise separation of harvesters.

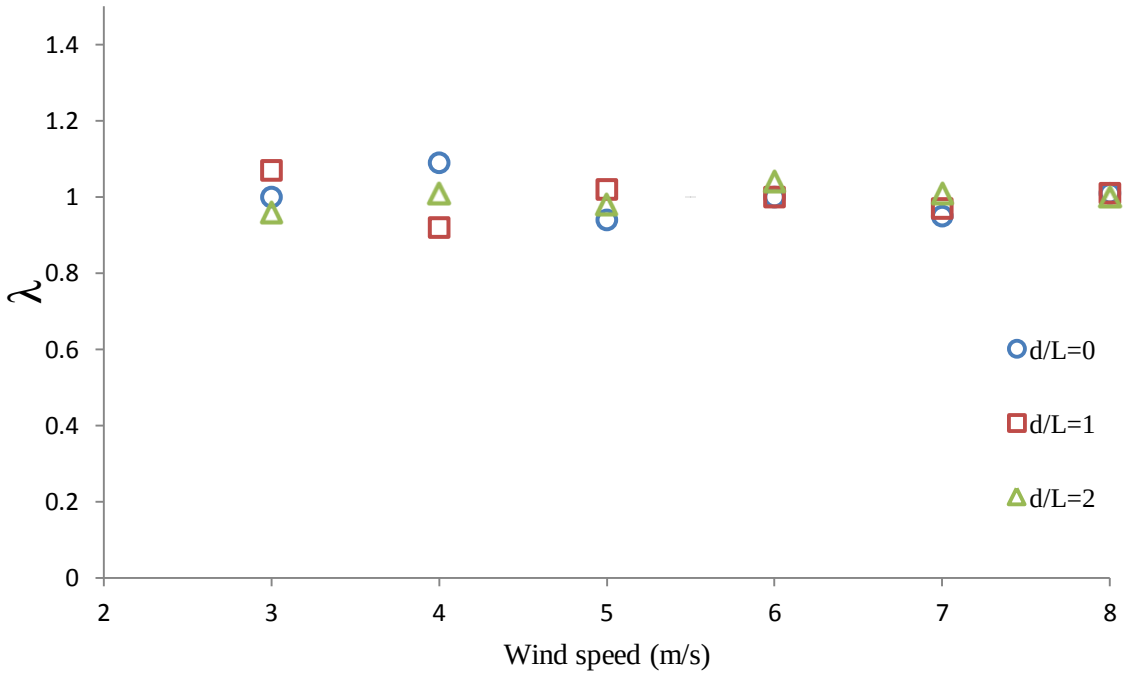

Figure 5.19: Normalised power output (λ) of upstream harvester in stream-wise proximity tests.

Figure 5.19 indicates that the λ value remained close to 1 irrespective of the separation distances at all wind speeds for the upstream harvester. This meant that the upstream harvester was not affected by the downstream harvester, when the downstream harvester's distance from the upstream one was varied. It is also important to mention that at lower wind speeds, the variation of power was more, which reflected in the higher variation of λ at 3m/s and 4m/s (+/- 8%).

However, it was interesting to observe the λ values of the downstream harvester, when the separation distance was varied. Figure 5.20 indicates the λ values of the downstream harvester, when fluttering in tandem. The figure indicates that, for all the separation distances, the λ values were found be greater than 1, with a maximum value of 1.41 at a wind speed of 8m/s. The graph reveals that for a separation distance of d/L = 1, the downstream harvester provided more power output compared to the other separation distances. This implied that there existed a specific distance (d/L = 1 in this case) between the upstream and downstream harvesters, where the power output of the downstream harvester remained higher compared to the other separation distances.

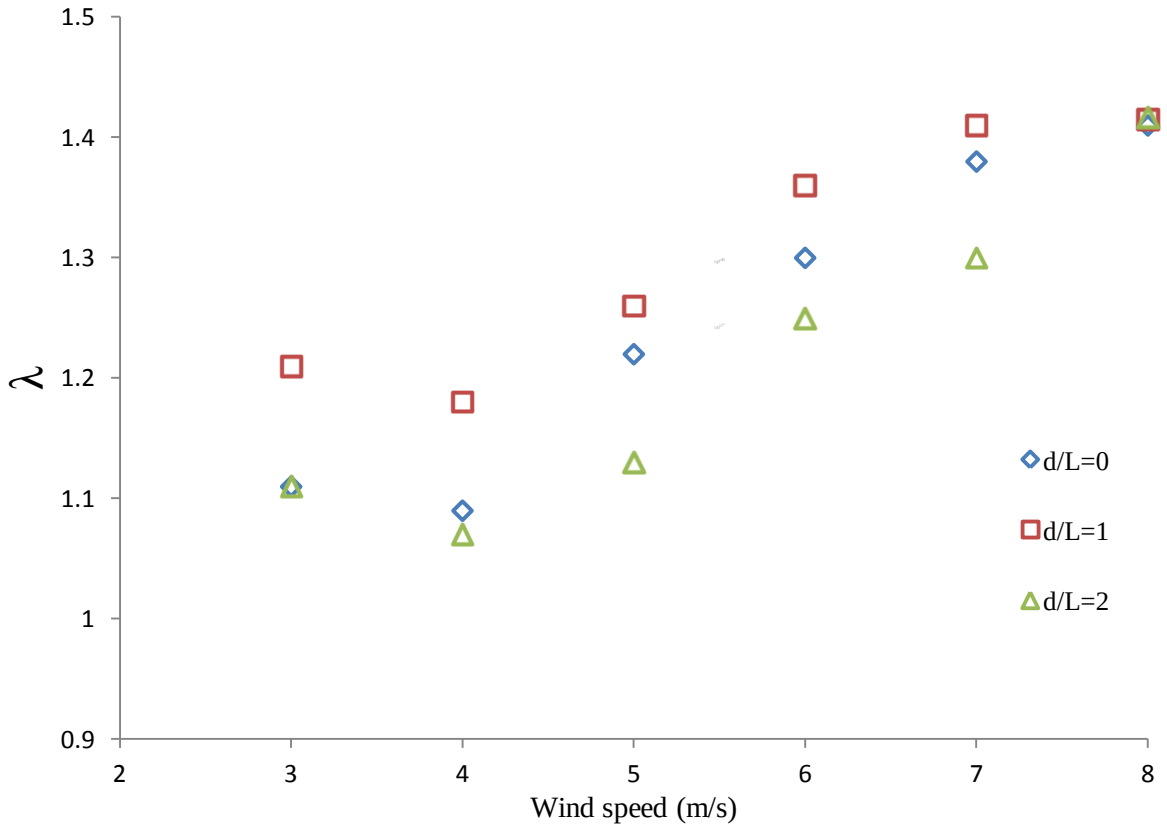

Figure 5.20: Normalised power output (λ) of downstream harvester in stream-wise proximity tests.

Since a unique increase in power output was observed for the downstream harvester at d/L = 1 position, this test case was repeated thrice to measure its power output and phase lag with the upstream harvester. These results indicated that the tests were very repeatable (as seen in Figure 5.21).

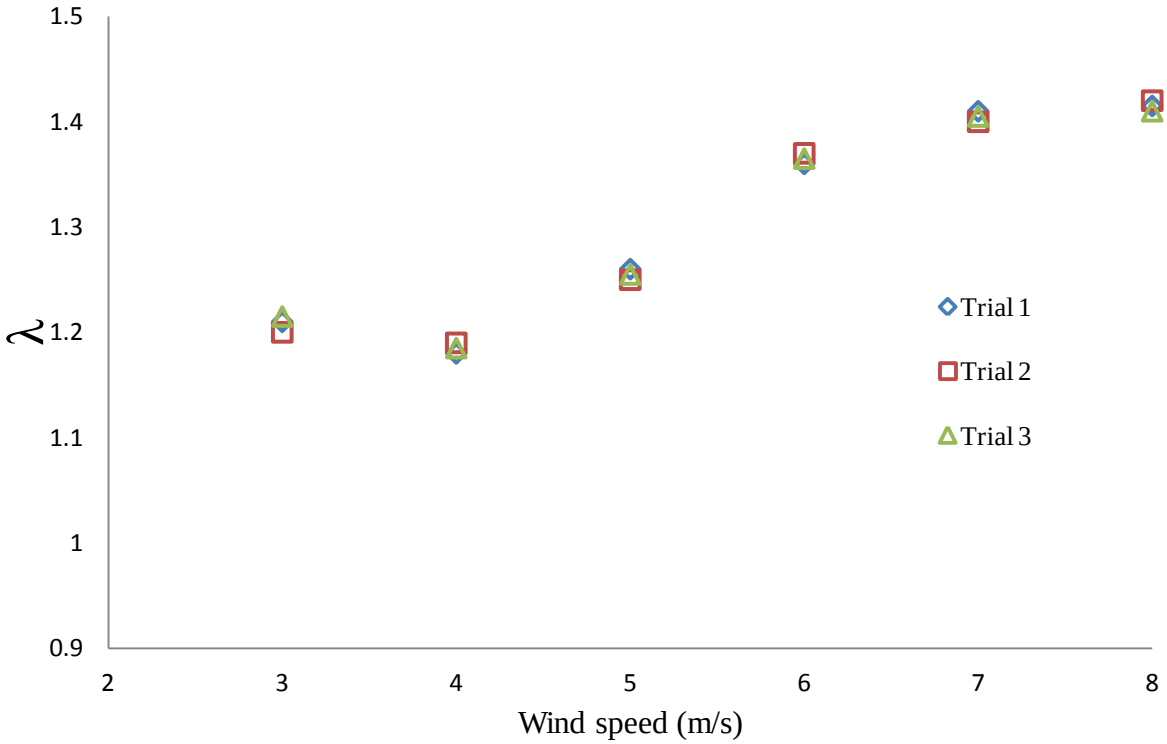

Figure 5.21: Normalised power output (λ) of downstream harvester at d/L = 1 position in stream-wise proximity tests.

In order to identify the cause for this increase in power output, smoke-wire flow visualization was conducted in the wind tunnel. The author acknowledges that the flow visualization was primarily conducted by Jesse McCarthy, with author's support in the experimental setup. The full details can be found in McCarthy et al. (2013; 2014). Only the key findings are presented in this section.

The high-speed video indicated two main flow structures:

1. Leading-edge vortex, shed from the leading edge of the upstream harvester.
2. Cone-shaped horseshoe vortex, shed from the triangular leaf.

While the leading-edge vortex was not found to have any significant impact on the downstream harvester, the horseshoe vortex was visually observed to be impinging on the downstream harvester. Figure 5.22 shows the vortex formation and separation from the upstream harvester. Figure 5.23 shows these horseshoe vortices approaching the downstream harvester. The figure also shows the phase-lag behaviour between the harvesters. The flow visualization was carried out at a wind speed of 4 m/s since at higher wind speeds, the smoke streamlines were not well defined.

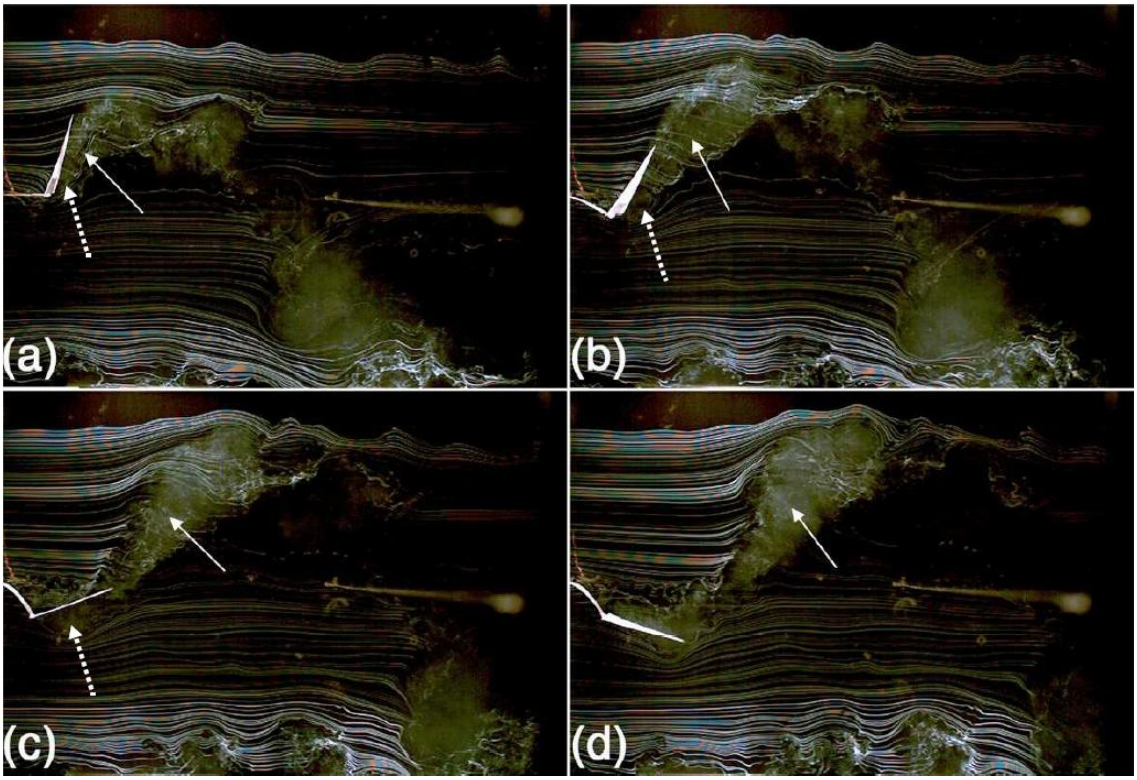

Figure 5.22: Images time sequenced from (a) to (d). Horseshoe vortex (solid-line arrow) and leading edge vortex (dashed-line arrow) forming, separating and propagating downstream from the upstream harvester (McCarthy et al., 2013).

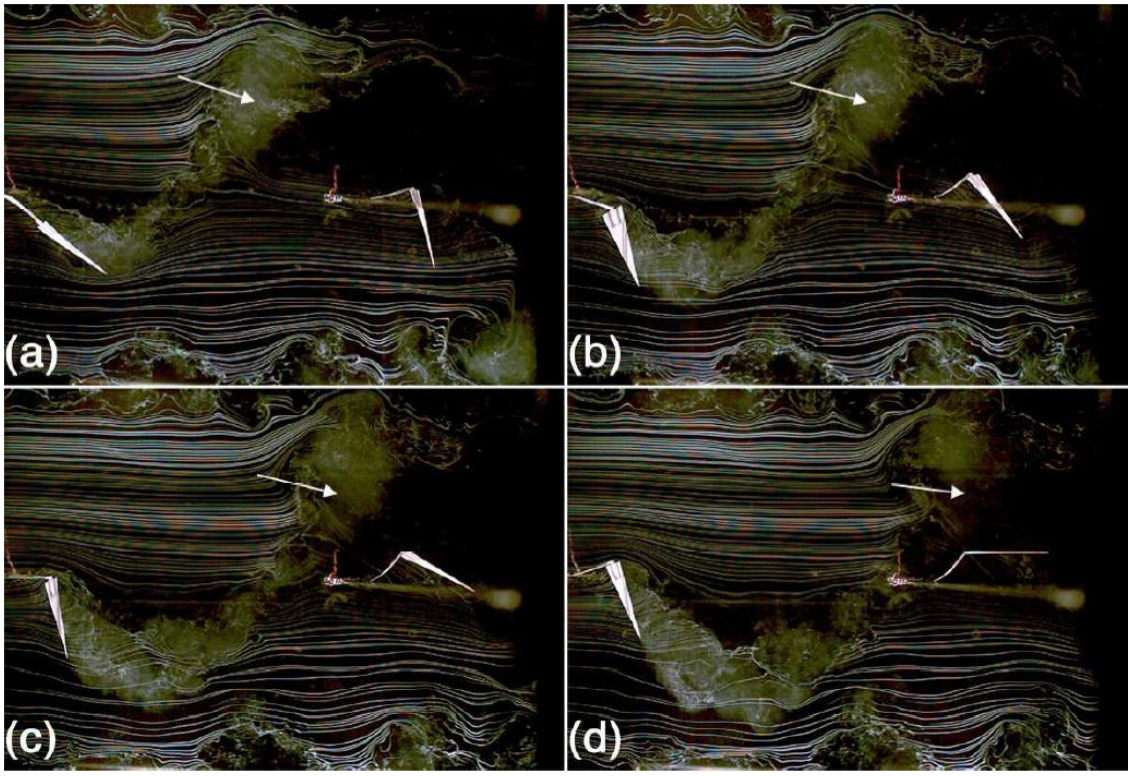

Figure 5.23: Images time sequenced from (a) to (d). Horseshoe vortex propagating downstream and interacting with downstream harvester (McCarthy et al., 2013).

It is postulated that as the horseshoe vortex approaches the downstream harvester, the pressure gradient created by the vortex adds suction, drawing the downstream harvester to the vortex core (as seen in the sequence of images shown in Figure 5.23). This additional suction would have caused increased strain rate on the PVDF stalk, leading to higher power outputs. The existence of a phase-locking behaviour (as seen in Figure 5.23) is also attributed to this interaction of downstream harvester with the horseshoe vortex. A dual-camera image capture, from two orthogonal directions, also revealed the three-dimensional nature of these vortices. It is suggested that this three-dimensional nature of the vortex would have also been the cause for the existence of a phase-locking behaviour, observed in vertical proximity tests for d/L = 0 position (explained in Section 5.4.2).

For the stream-wise proximity tests, phase-lag analyses were carried out, specifically for d/L = 1 position. Two different load resistances (5.6 MΩ and 3.4 MΩ) were used to observe if the electrical circuitry and load matching had any impact on the phase-lag behaviour (circuit diagram shown in Figure 5.3). Table 5.2 shows the phase lag between the harvesters at d/L = 1 position under both the loading conditions.

Table 5.2: Phase lag between two harvesters at d/L = 1 position in stream-wise proximity tests.

Wind speed (m/s)	Phase lag (degrees)	
	@ 5.6MΩ Load resistance	@3.4MΩ Load resistance
3	5.9	9.2
4	46.1	42.6
5	-	-
6	-	-
7	51.4	48.4
8	71.5	67.6

From the above table, it is clearly evident that the phase lags were slightly different at different wind speeds with the greatest discrepancy at 3m/s and it was also observed that the standard deviations were higher. This could be attributed to the lack of dynamic stability of harvesters at such low wind speeds. Also, at wind speeds of 4, 7 and 8 m/s, it is clearly seen that there was not much variation in the phase lags. This proved that there was no significant effect of the electrical circuit on the phase relationship between the upstream and downstream piezos. Also, it indicated that the phase relationship was fairly repeatable and consistent at

these wind speeds. Figure 5.24 shows the time-varying behaviour of phase lag at 4 m/s between the upstream and downstream harvesters. It clearly indicates that the phase locking behaviour remained constant over the number of cycles recorded. A similar behaviour was observed at 7 and 8 m/s.

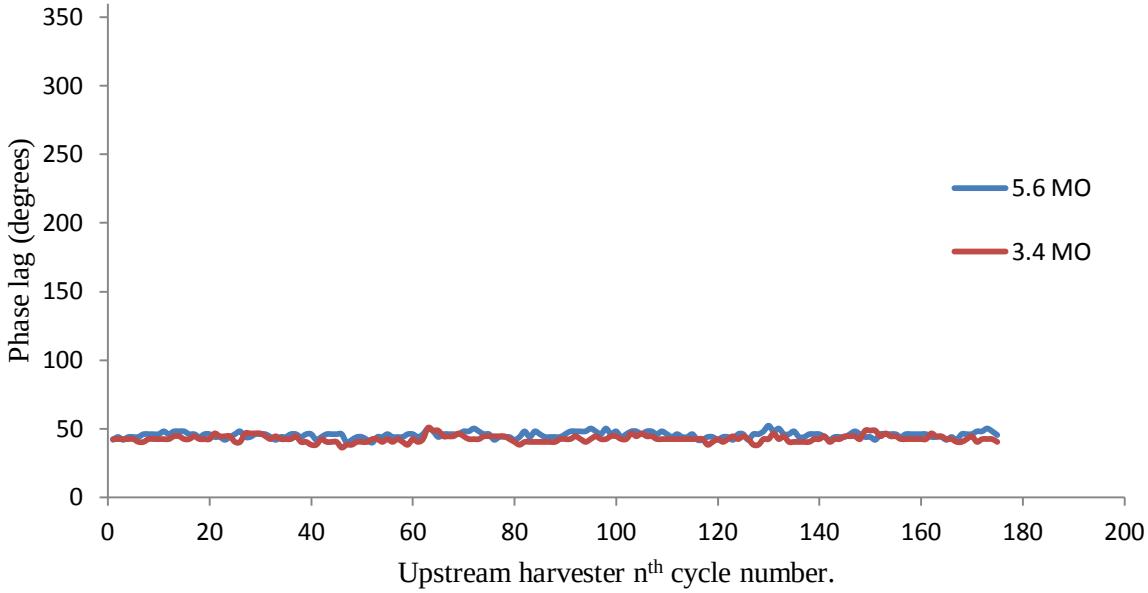

Figure 5.24: Phase lag between the harvesters at 4m/s.

However, at 5 and 6 m/s, it was observed, somewhat surprisingly, that there was not a constant phase lock between the upstream and downstream harvesters. The phase lag varied from 0 to 360 degrees over time. Figure 5.25 shows the variation of phase lag for the number of cycles recorded at 6 m/s. This graph shows that there was no constant phase-locking behaviour between the upstream and downstream piezo-leaf system. However, the data also indicates that the phase locked and unlocked at regular intervals of time. In order to understand this behaviour, the frequencies of the harvesters at this wind speed were investigated. Figure 5.26 shows the frequencies of flutter of the harvesters over the recorded number of cycles at 6m/s. The frequencies were calculated based on each cycle time and hence have a relatively coarse resolution (as explained in Section 5.3.1.1). However, that did not affect the findings of this analysis. It can be seen that the frequency of the downstream harvester dropped at regular intervals at this wind speed, and at the rest of the time, remained closer to the frequency of the upstream harvester. Thus the downstream harvester slowed down at regular intervals creating a phase lag to vary from 0^0 to 360^0. Also it was also

observed that the amplitude of flutter of the downstream piezo remained larger compared to the upstream piezo throughout the test run resulting in a higher average power output.

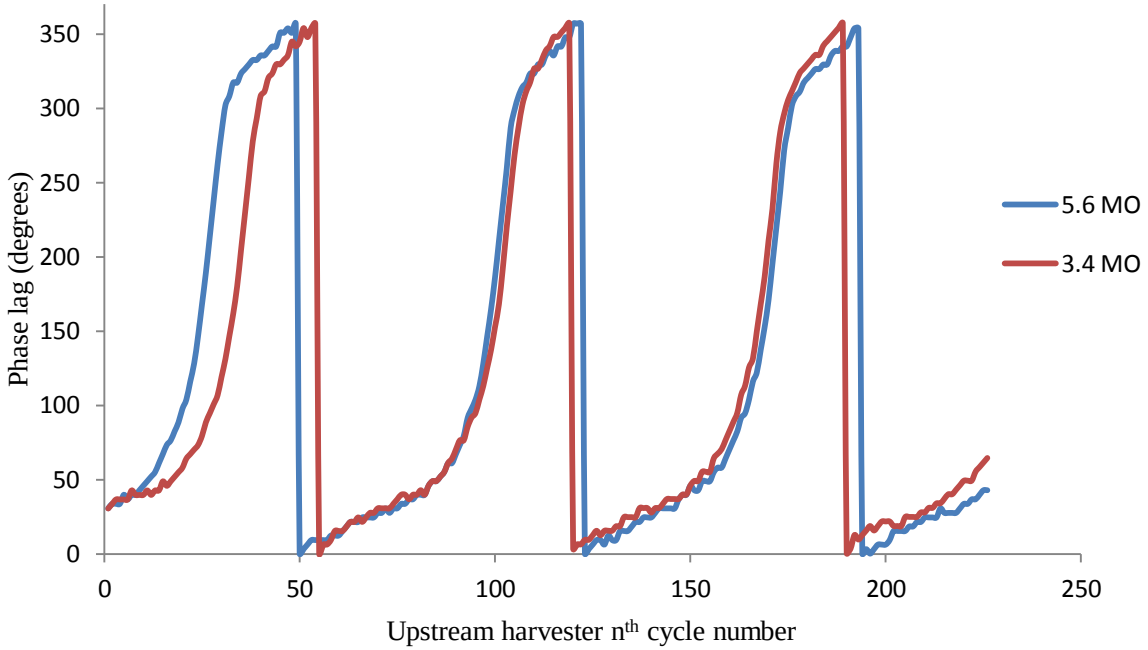

Figure 5.25: Phase lag between the harvesters at 6m/s for *d/L* = 1 case.

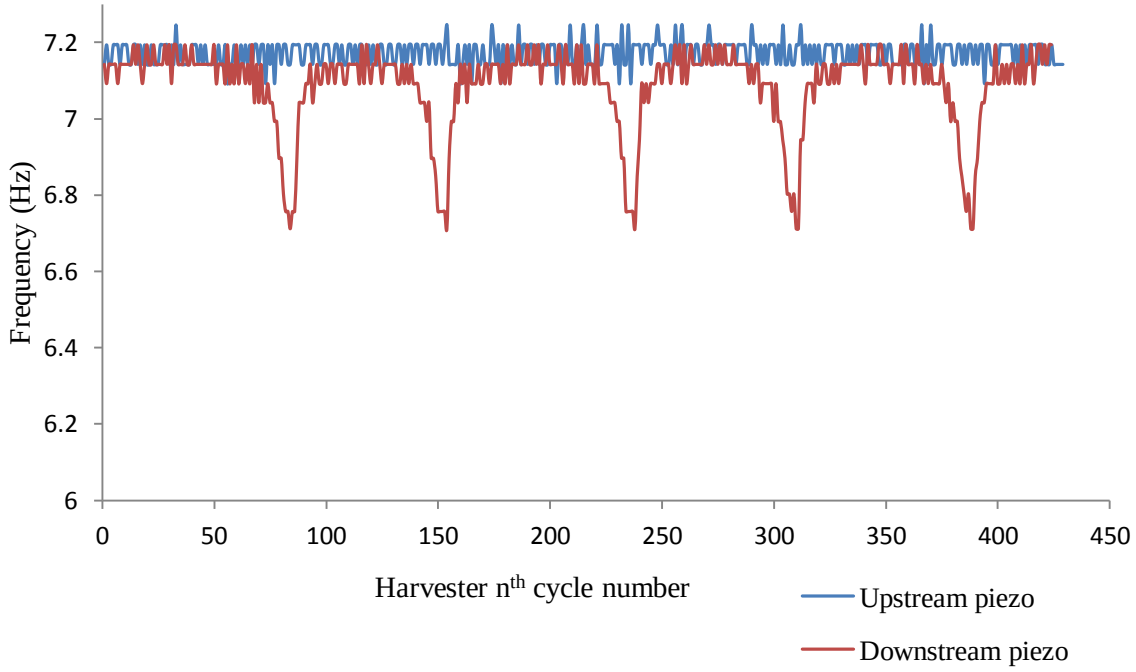

Figure 5.26: Phase lag between the harvesters at 6m/s for *d/L* = 1 case.

It is postulated that the vortices shed from the upstream harvester, when impinging on the downstream harvester, can have a constructive or a destructive impact on the power output. At a separation distance of one harvester length, it was observed that there was clearly a more constructive influence compared to other separation distances. Also at 5m/s and 6m/s, for this particular separation distance (d/L = 1), it is believed that there was a destructive influence at regular intervals, due to the vortices shed from the harvester upstream. However, this did not affect the average power output of the system as it was observed that the flutter amplitude of the downstream harvester always remained higher than the upstream harvester (as seen in Figure 5.27). Due to smoke dissipation effects at higher wind speeds (> 4 m/s), the flow structures were not visualized. At wind speed of 8 m/s, it was observed that the normalized power output was 1.4 for all the separation distances (as seen in Figure 5.20). It was observed that the phase lags, at this wind speed, were different for different separation distances, leading to higher power outputs.

However, the reason for the existence of a specific phase lag at every wind speed is still unclear. Although the flow visualization provided useful insights towards answering the cause of increased power output, it was only a qualitative study. A detailed quantitative study using Particle Image Velocimetry (PIV) technique would reveal the localized flow velocities and pressure gradients of the horseshoe vortex shed from the upstream harvester. This should form a part of the future work.

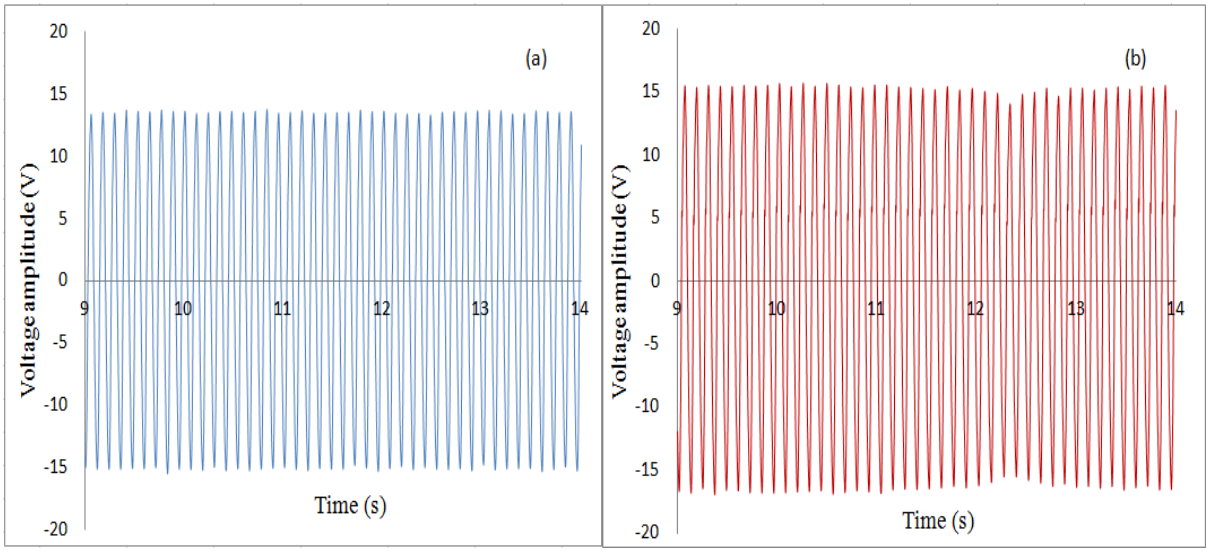

Figure 5.27: Voltage amplitudes of the upstream harvester (a) and the downstream harvester (b) observed at the point when the downstream harvester's frequency dropped (at 6 m/s).

Elsewhere, in a completely different context, a similar behaviour was observed. Akhtar et al. (2007) investigated a tandem flapping foil configuration in view to develop propulsion and

maneuvering systems for underwater vehicles. This work was biologically inspired, capturing and replicating fin motions in fishes. The dorsal-tail fin interactions in a swimming bluegill sunfish were observed, and the fin motions were computationally simulated. From the simulations, it was found that the thrust forces generated by the tail fin, when operating in tandem, were significantly higher compared to its stand-alone case. Simulations clearly revealed that the vortex shed from the dorsal fin constructively interacted with the tail fin, altering its flutter characteristics to increase its thrust force. However, when the phase relationship between the fins was varied in the simulations, it was found that the thrust forces varied significantly. This experiment demonstrated the importance of the phase-locking behaviour on the flutter characteristics of the downstream flapper.

The pitching-heaving motion observed in fish fins is similar to the motion of polymeric leaf of the harvesters observed in the work presented in this section. It is believed that fishes, through evolution, would have actively optimized the phase-locking behaviour to increase the thrust forces, and hence reduce their muscle activity. However, in the work presented here, the phase-locking between the harvesters were naturally established due to vortex interactions. The flow visualization videos suggested that the synchronization of vortices with the oscillations of the downstream harvester played a significant role in increasing the power output. Therefore, the phase relationship, and hence the power output of the downstream harvester depends on:

1. Stiffness and geometry of upstream harvester (which determines the vortex strength)
2. Separation distance between harvesters
3. Flow velocity

It is highly challenging to analytically or empirically determine the phase relationship as a function of the above mentioned parameters. The author acknowledges that further investigative studies may be useful to analytically understand this unique behaviour, and to further exploit the vortex interactions for improving the efficiency of the system. It is also important to note that these vortex interactions can be exploited only in the stream-wise direction, provided the flow remains parallel to the tandem harvesters. In other cross-stream and vertical directions, due to the lack of vortex interactions, no significant increase in power output could be achieved.

5.5 Proof-of-concept experiment

Based on the proximity tests conducted, an array of harvesters was placed in the wind tunnel to demonstrate the working of these devices for practical energy harvesting and lighting purposes. In this experiment, twelve similar harvesters were placed in smooth parallel flow. The harvesters were arranged such that four columns, each containing three harvesters were used. The three harvesters were placed vertically within a column, with a separation distance of 180 mm (d/L = 1). Two columns were laterally placed with the same separation distance, and the other two columns were placed downstream to these columns, again with d/L = 1. Therefore, the total volume occupied by the harvesters was approximately 0.035 m^3. The experimental setup is shown in Figure 5.28.

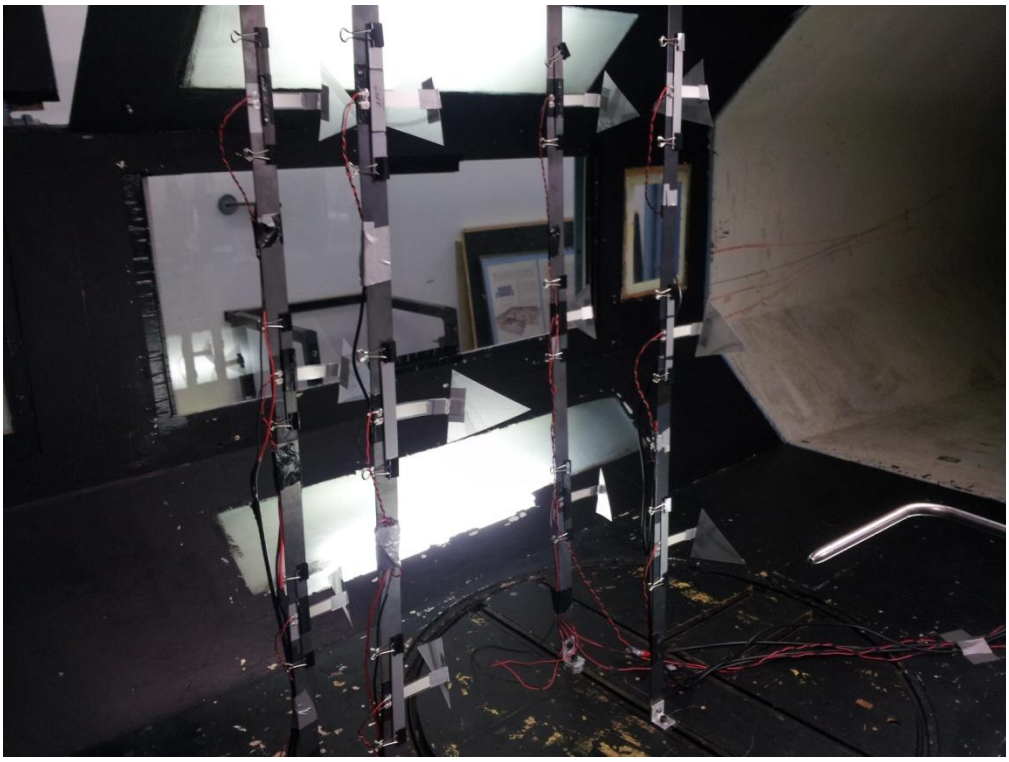

Figure 5.28: Experimental setup of twelve harvesters in wind tunnel.

The experiment was conducted at a wind speed of 5 m/s. In order to charge a battery or to power LED lights, the AC supply from these harvesters have to be rectified to DC supply. However, due to the phase relationship observed among these harvesters, individual rectifiers were essential for these harvesters. Given the economical rates of commercially available simple full-wave rectifiers, this may not add any significant effect to the overall costing, if these harvesters are commercialized and mass produced.

PVDF stalks are high-voltage, low-current devices. Thus, power conditioning electronics are essential to convert the raw power to usable power. Since the harvesters were used to power only a simple lighting system in this experiment, a simple zener diode was used to limit the voltages from the harvesters. Each harvester, after rectification, generated 14 μW at 5 m/s. These harvesters were connected electrically in parallel. Therefore, the energy density of these harvesters was estimated to be 4.8 mW/m^3. Although the power density was very low, this could have been improved significantly by designing suitable electronic systems. However, it was beyond the scope of this work.

A simple flasher and sequencer circuit was used to power LED lights in a specific order. LED lights were arranged to form the letters "RMIT", with 10 LEDs for each letter (see Figure 5.29). For this simple experiment, no intermittent storage device was required. However, in reality, power conditioning and storage devices are mandatory. Under the experimental conditions, the LED flashing was successful, with the system working as long as sufficient flow existed in the wind tunnel. The circuit diagram is shown in Appendix E. This simple experiment demonstrated the practical viability of the energy harvesting system. Also, some important electrical aspects to be considered for efficient functioning of multiple harvesters were established. This proof-of-concept video can be viewed from the DVD attached at the back of this thesis in the printed version. Online version is also available at https://www.youtube.com/watch?v=pfgK9hl1p_w&list=UUd02uOEOHtXAujBvrH6NHNQ

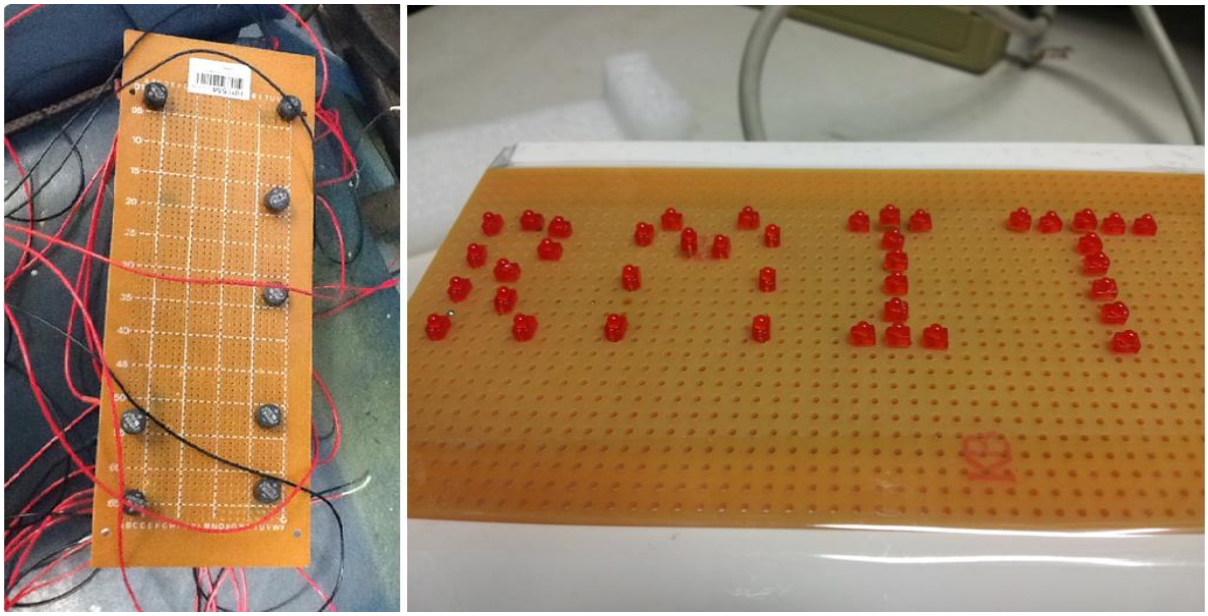

Figure 5.29: Individual rectifiers used in the experiment (a) and 'RMIT' in LED lights: One letter flashing at a time.

5.6 Summary

In this work, proximity effects of leaf-stalk harvesters were investigated. Two similar harvesters were placed in close proximity and their separation distances were varied in three orthogonal directions. It was found that the stand-alone power outputs of these harvesters were not identical, and hence the power outputs were normalized to their respective stand-alone power outputs in the experiments.

In cross-stream proximity experiments, when two harvesters were placed in close proximity, it was found that the power outputs dropped significantly. The harvesters produced only 18 % of their stand-alone power output at a wind speed of 3 m/s. It was postulated that when the harvesters were in close lateral proximity, they behaved like an air-spaced bimorph. This reduced the effective compliance, and hence reduced the power output at lower wind speeds significantly. For other separation distances, the harvesters were independent in operation, with no significant impact on power output. The normalized behaviour of the harvesters was identical, given the symmetrical nature of the arrangement with respect to wind flow.

In vertical proximity experiments, no significant impact on the power output was observed, for all the separation distances. A maximum variation of only 6 % in power output was observed. When the harvesters were placed in close proximity (with no separation distance), a unique phase relationship was observed. There existed a specific phase lag between the harvesters, and this phase lag varied at different wind speeds. Smoke-wire flow visualization revealed that the vortex shed from the harvesters were three-dimensional, and was responsible for establishing this phase relationship. The normalized performances of the harvesters were also found to be identical.

In stream-wise proximity experiments, while the upstream harvester remained unaffected, a significant increase in power output was observed in the downstream harvester at all wind speeds tested. A maximum of 40% increase in power output was observed at 8 m/s. Of all the separation distances, when the harvesters were displaced by one harvester length, the power outputs of the downstream harvester remained the highest. Flow visualization suggested that the horseshoe vortex, shed from the polymeric leaf of the upstream harvester, when approached the downstream harvester, created a pressure gradient and provided additional suction. This suction increased the flutter amplitude, and hence the strain rate and power output of the downstream harvester. The unique phase relationship observed between the harvesters were also attributed the vortex interactions with the downstream harvester.

These proximity tests provided a clear indication on how these harvesters can be arranged in space to develop an efficient harvesting system. By placing a harvester at the wake of an identical harvester, the power output can be significantly increased. However, these vortex interactions can be exploited only if the flow remains parallel to the harvesters at any given time. It still remains to be seen if this unique vortex interaction and power-output increase can be found, when multiple harvesters are placed in tandem. A proof-of-concept experiment established some of the basic electrical aspects to be considered while designing the system. The experiment suggested that these harvesters when scaled up in number and aesthetically well arranged, has the potential to harvest sufficient energy for powering LEDs and other ULP devices. The author acknowledges that this harvester system cannot be used as an alternative to conventional wind energy extraction methods in the current context. However, this technology shows potential to be pursued further.

Chapter 6
Conclusions and Recommendations

At the end of Chapter 2, having reviewed the relevant literature, research gaps were noted, which led to formulating specific research questions. These questions were answered in the subsequent chapters. Here, the research questions are restated and the answers, which are the findings of this research work, are provided. Also, the practical implications of this research and some important recommendations for future work are mentioned in this chapter.

6.1 Answers to research questions

1. *How are the physical and geometric properties of a three-dimensional highly compliant beam affecting its flutter onset and flutter frequency in a simple cantilever system?*

In order to understand the dependence of flutter onset velocity and flutter frequency on physical and geometrical properties of three-dimensional compliant beam, three different materials (polypropylene, paper and Mylar) with several different cantilever lengths were evaluated in a series of wind-tunnel tests. For a constant width of the beam, the results clearly indicated the variation of flutter onset velocity and frequency as a function of the beam properties. By obtaining constants of proportionality, two-dimensional theoretical scaling laws were extended to a three-dimensional experimental environment. These results implied that for a given width, a single experimental case is sufficient to obtain the constants of proportionality, and use the empirically obtained constants to precisely determine the flutter onset velocity and frequency of any material of any cantilever length. This finding is expected to have practical implications in the design of these harvesters. These findings are explained in detail in Section 3.8.1 in Chapter 3.

2. *What is the effect of the hinge, when placed at different positions along a beam, on the flutter frequency and onset velocity in a connected body system?*

As part of the original contribution to the field, flutter analysis of a connected body system was undertaken. Since the literature indicated that flutter onset velocity is proportional to the beam's natural frequency, analytical structural analyses were performed to identify the natural frequency variations of a connected body system with respect to hinge positions along the

beam. Computational analyses were carried out to validate the analytical results. Experimental samples were prepared with varying hinge positions and tested for their flutter onset velocities under smooth and parallel flow conditions. The experimental results followed the same trend as analytical results when the hinge position was varied from leading edge to the midpoint of the beam. However, it was observed that as the hinge position varied towards the trailing edge, the flutter onset velocity increased, unlike the analytical predictions. High-speed images indicated that as the hinge position moved towards trailing edge, the system transitioned to higher flutter modes. This work revealed that the presence of hinge reduces the flutter onset velocity in general, which is beneficial for energy harvesting purposes. However, the hinge position plays a crucial role in flutter mode of the system, thereby altering the onset velocity. These results can be found in Section 3.8.1.3 in Chapter 3.

3. *What is the possibility of increasing the power output using vertical leaf-stalk and other asymmetrical configurations for energy harvesting applications under smooth fluid flow conditions?*

Prior work from literature had shown that when excited by mechanical vibrations, asymmetrical configurations provided 30% more power compared to symmetrical configurations. Thus, in order to investigate the possibility of energy harvesting from asymmetrical configurations, simple dynamic tests and computational analysis were conducted. When excited by simple mechanical dynamic forces (via a shaker), asymmetrical piezo configurations were capable of producing more power output compared to symmetrical configurations due to coupled bending-torsional vibrations. However, when excited by fluid flow (in the wind tunnel), it was observed that the power output of the asymmetrical configurations remained lower. High-speed videos indicated that the nature of fluid forces differed between the symmetrical and asymmetrical configurations as the forcing function was completely governed by the geometry of the system. Thus, the asymmetrical configurations were subjected to lower bending strains. Also, due to asymmetry, the configurations were more prone to chaotic flapping, leading to reduced fatigue life and power outputs. Detailed discussion of these results can be found in Section 4.6 in Chapter 4.

In the vertical-stalk configuration, the power outputs were significantly higher compared to the symmetrical configuration. High-speed videos indicated that due to the nature of lift forces, the piezo stalk in vertical-stalk configuration was subjected to excessive nonlinear strains, leading to higher power outputs. However, the experiments suggested the piezo stalks

were prone to fatigue due to excessive amounts of strain. The experiments suggested that harvesters subjected to coupled bending-torsional type flutter are more prone to chaotic flapping and fatigue, and hence not suitable for energy harvesting from fluid flow, unless the piezoelectric materials are specifically designed for harvesting from coupled bending-torsional type flutter.

4. *What are the proximity effects of two identical flapping piezo-leaf systems in smooth flow on their power outputs when displaced in three orthogonal directions?*

Two piezoelectric energy harvesters were placed in parallel smooth wind flow in three orthogonal directions, one direction at a time, and the separation distance between the harvesters were varied. Results indicated that when the harvesters were displaced in the direction of the wind (stream-wise), the downstream harvester provided 20-40% more power output (depending on the wind speed) compared to its stand-alone case, and the maximum increase was at a separation distance of $d/L = 1$. When the harvesters were displaced in the cross-stream direction with a very small separation distance (10mm), the harvesters produced only 18% of their stand-alone power indicating that the harvesters destructively interacted with each other. In all the other directions and separation distances, the harvesters' operation was relatively independent of each other.

For the cases where the harvesters were displaced in the stream-wise direction, simultaneous voltage measurements revealed that there existed a specific phase lag between the harvesters at every wind speed, and that the phase lag and wind speed did not have any obvious linear relationship. It was postulated, with the help of smoke-wire flow visualization, that the vortex shed from the upstream harvester, when approaching the downstream harvester, created additional suction, and hence had a constructive impact on the power output of the downstream harvester. Also, at certain wind speeds, the upstream vortex regularly disturbed the flutter pattern of the downstream harvester. The reason for a specific phase lag between the harvesters in tandem is still to be understood in full. However, it is clear that if these piezoelectric harvesters were scaled up in number for energy generation, they could be intelligently placed in space to increase the overall power output. Detailed discussion of these results can be found in Section 5.4 in Chapter 5.

6.2 Practical implications of this research

In Chapter 1, some fundamental FSI analyses were presented, where the dependence of flutter characteristics on the material and geometric properties were clearly established. This would facilitate the material and cantilever length selections while designing the energy harvesting system. To maximize the power output, harvesters must have a low flutter onset velocity and high flutter frequency, and the experimentally validated scaling laws could be effectively utilized to make important design choices.

The connected body analysis, shown in Chapter 1, revealed that in a connected body system, a revolute hinge generally reduced the flutter onset velocity. This reinforced the concept of a clamped-hinged-free connected body system for energy harvesting purposes. Also, by moving the hinge position across the beam towards trailing edge, it was found that the system transitioned to higher modes of flutter. This analysis could be significant in choosing the hinge position in a harvester system to initiate flutter in its fundamental flexible mode, where maximum energy can be extracted.

Investigation of asymmetrical configurations for energy harvesting from fluid flow revealed two important aspects: 1. Input fluid-induced forces on a harvester is governed purely by the geometry of the harvester, and hence the input fluid forces differed for symmetrical and asymmetrical configurations. Thus the asymmetrical configurations were subjected to lower bending strains compared to symmetrical configurations. Since bending strains are essential for harvesting energy from commercially available piezoelectric materials, the experiments clearly indicated the disadvantages of asymmetrical configurations. 2. Any asymmetry in geometry could make the system more prone to chaotic flapping, thereby reducing the average power outputs. A reduction in fatigue life was also noted due to chaotic flapping. Although the asymmetrical configurations could increase power output under mechanical excitations, when extended to fluid flow, these asymmetrical configurations were not effective. Since no literature studies were found on asymmetrical configurations under fluid excitations, these experiments were essential to identify the above mentioned aspects which are useful for designing the harvester system.

Proximity experiments of two identical harvesters provided useful knowledge on how these harvesters can be placed in space for a scalable energy harvesting system. The results indicated that up to 40 % increase in power output could be achieved by placing the harvester

at a specific distance downstream to another identical harvester. Thus, the overall efficiency of the system can be significantly improved by placing these harvesters in certain strategic positions.

A proof-of-concept experiment suggested that the power outputs remained significantly low compared to wind turbines and other solar devices. Also, literature indicated that the overall efficiency of a fluttering-type piezoelectric harvester is less than 1%. Thus, the author acknowledges that significant improvements have to be made in fluid-mechanical and mechanical-electrical energy transductions to make these harvesters commercially viable. However, this research appears to have contributed to an increased understanding of piezoelectric energy harvesting from fluid flow.

6.3 Recommendations for future work

Fundamental FSI studies could be conducted with simple cantilever and interconnected beams with varying shapes to further understand the three-dimensional effects on flutter characteristics. Analytical modeling of fluid forces impinging on these slender beams could also significantly help in understanding flutter onset behaviour.

Although the vertical leaf-stalk configurations were found to yield higher power outputs, they were subjected to excessive strains, with a high risk of fracture. Future investigative studies could be conducted by employing a bimorph configuration for the stalk. This would increase the effective stiffness and hence reduce the amount of net effective strain, while extracting power from both the PVDF patches. This would however require increased wind speeds, which might not result in increased energy output, given the relatively low wind speeds in urban settings. However, a trade-off study between the amount of strain and power output remains to be studied.

In the proximity studies, only two harvesters were investigated in tandem. Investigation of multiple harvesters, operating in tandem configuration, would indicate if this beneficial vortex interaction can be exploited further downstream. Also, the effect of outdoor environmental influences (e.g. ultraviolet radiations and moisture) on the long-term electro-mechanical properties of the leaf and PVDF stalk should be investigated. Due to the turbulent nature of the atmospheric wind, and excessive strains experienced by these harvesters, fatigue analysis should form an important part of any future work.

Appendix A

Mesh details of connected-body analysis

The following table is a screenshot from the report generated by ANSYS® for the connected body analysis performed. A standard pre-defined mesh size was utilised in the modal analysis. Given the simplicity of the analysis, no further mesh refinements were required.

Table A.1: Mesh setup for connected body analysis.

Model (J4) > Mesh	
Object Name	*Mesh*
State	Solved
Defaults	
Physics Preference	Mechanical
Relevance	0
Sizing	
Use Advanced Size Function	Off
Relevance Center	Fine
Element Size	Default
Initial Size Seed	Active Assembly
Smoothing	Medium
Transition	Fast
Span Angle Center	Coarse
Minimum Edge Length	3.5e-004 m
Inflation	
Use Automatic Inflation	None
Inflation Option	Smooth Transition
Transition Ratio	0.272
Maximum Layers	5
Growth Rate	1.2
Inflation Algorithm	Pre
View Advanced Options	No
Patch Conforming Options	
Triangle Surface Mesher	Program Controlled
Patch Independent Options	
Topology Checking	Yes
Advanced	
Shape Checking	Standard Mechanical
Element Midside Nodes	Program Controlled
Straight Sided Elements	No
Number of Retries	Default (4)
Extra Retries For Assembly	Yes
Rigid Body Behavior	Dimensionally Reduced
Mesh Morphing	Disabled
Defeaturing	
Pinch Tolerance	Please Define
Generate Pinch on Refresh	No
Automatic Mesh Based Defeaturing	On
Defeaturing Tolerance	Default
Statistics	
Nodes	7150
Elements	952
Mesh Metric	None

Appendix B

Tensile tests for paper and polypropylene

In order to obtain the elastic modulus of the samples, tensile tests were conducted. Since Mylar samples were already obtained along with the mechanical data sheet, the tests were performed only for paper and polypropylene. Three specimens of each material were tested and the data were plotted as a standard stress-strain plot. Figures B.1 and B.2 show the stress-strain variations of the materials as an example. A nonlinear curve was fit and the elastic modulus was evaluated only for the elastic portion of the curve. Since the transition from elastic to plastic region was not obvious, to estimate the yield point, 0.2 % offset line was used. However, the yield stresses were not utilised in any analysis presented here. Table B.1 shows the elastic modulus evaluated for all the samples of paper and polypropylene.

Table B.1: Elastic modulus of the test specimens.

	Elastic modulus (MPa)	
	Polypropylene	Paper
Specimen 1	1194	2151
Specimen 2	1277	2089
Specimen 3	1312	2132
Average:	**1261**	**2124**

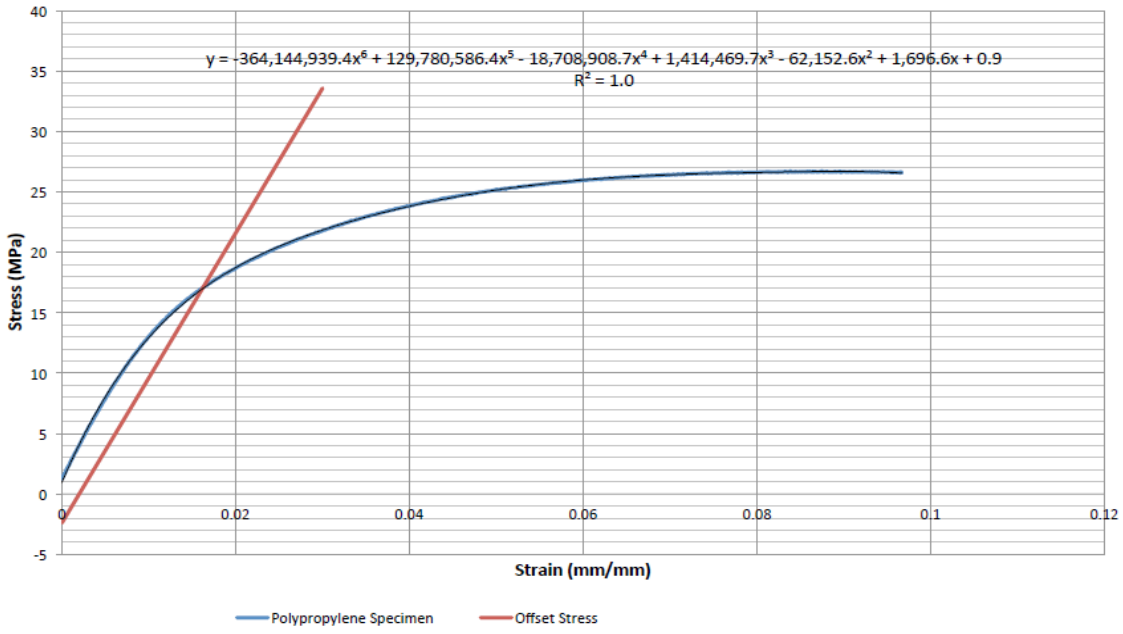

Figure B.1: Stress-strain plot of polypropylene specimen 2.

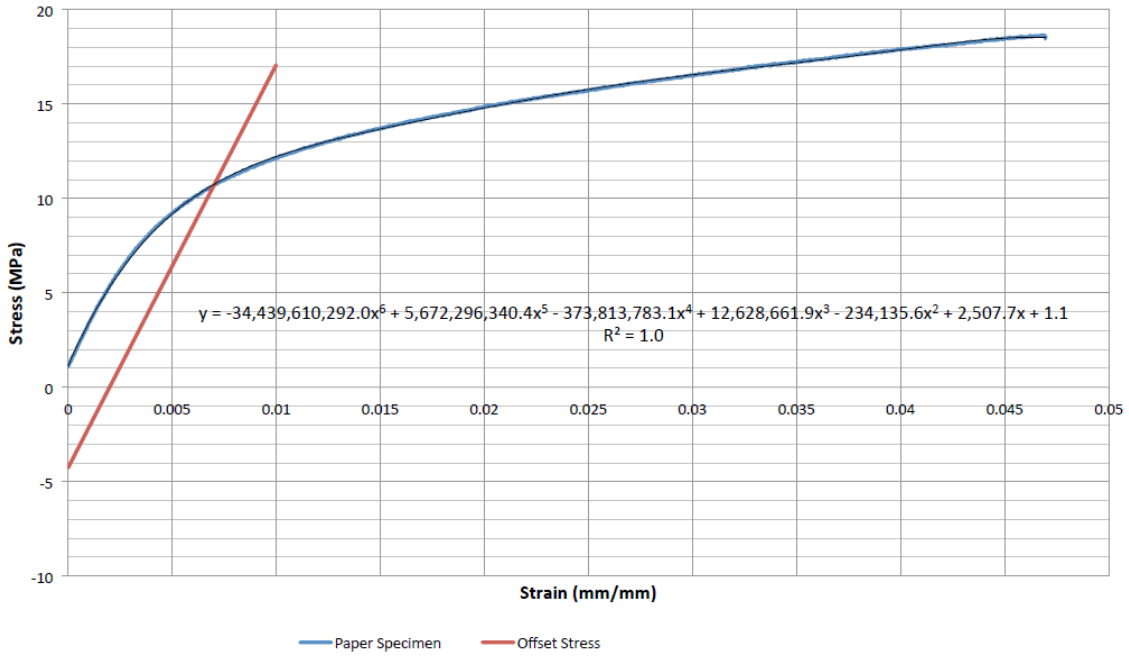

Figure B.2: Stress-strain plot of paper specimen 3.

Appendix C

Effect of hinge stiffness on flutter onset

Manufacturing of a negligible-stiffness and mass hinge is practically challenging. At first, commercially available hinges were investigated. However, due to the significant addition in mass and stiffness, the hinges were not used in the experiments. Therefore, in the experiments, two differing hinge thread materials, cotton and Kevlar®, were trialled, and disparity between the results was observed. Given that the hinges both were threaded as shown in Figure 3.12, the hinge torsional stiffness was the identified factor causing the dissimilarity. To further elucidate the effect of torsional stiffness, a brief computational study utilising the ANSYS® Mechanical™ model was carried out, and the impact on the value of R_2 for a given hinge position was evaluated.

The normalised critical flutter speed, v plotted for both hinge thread materials against normalised hinge position, η is shown in Figure C.1. The trend resulting from the Kevlar-hinged specimens appears somewhat erratic at η = 0.4 and 0.9. Hysteresis, either causing an apparent delay (η = 0.4) or quickening (η = 0.9) of flutter onset, was ruled out as the contributing factor, since for all three replicates the beam samples were initiated with no transverse deflection. Fabrication of the Kevlar hinges involved first twisting the thread about its longitudinal axis, so that the thread became thinner for threading through the holes punched in the beams. If the thread was twisted insufficiently, the Kevlar fibres 'caught' and temporarily inhibited motion. This could be an explanation for the delay of flutter at η = 0.4, though this does not explain the apparent acceleration of flutter onset for η = 0.9. Nevertheless, it is more likely that due to this construction technique exclusive to the Kevlar hinge specimens (the cotton-threaded beams did not require this technique, and thus were far simpler to construct), these inconsistencies arose; however, no conclusions may be drawn. There were two other noteworthy points regarding the results in Figure C.1:

1. The global trend outlined by the Kevlar-hinged specimens is shifted upwards from the cotton-threaded specimens.
2. It is evident that v is greater than unity for the Kevlar-threaded specimens.

The computational model was used to conduct a parametric study by varying the revolute hinge torsional stiffness of the model and evaluating the impact on the second modal natural frequency ratio, R_2. For this study, a hinge position of η = 0.5 was chosen. The results are shown in Figure C.2. In the limit of zero torsional stiffness, R_2 asymptotes to the zero-

stiffness value of about 0.45, as expected (Figure 3.5). More interestingly, R_2 asymptotes to a value slightly greater than unity with a large value of torsional stiffness, indicating that the hinge had actually become stiffer than the bending rigidity of the uniform beam. Without doubt, the hinge stiffness would affect the vibratory amplitude and frequency, and hence the power output of a piezoelectric stalk. Also, based on the experiments, cotton hinges were chosen for further analysis.

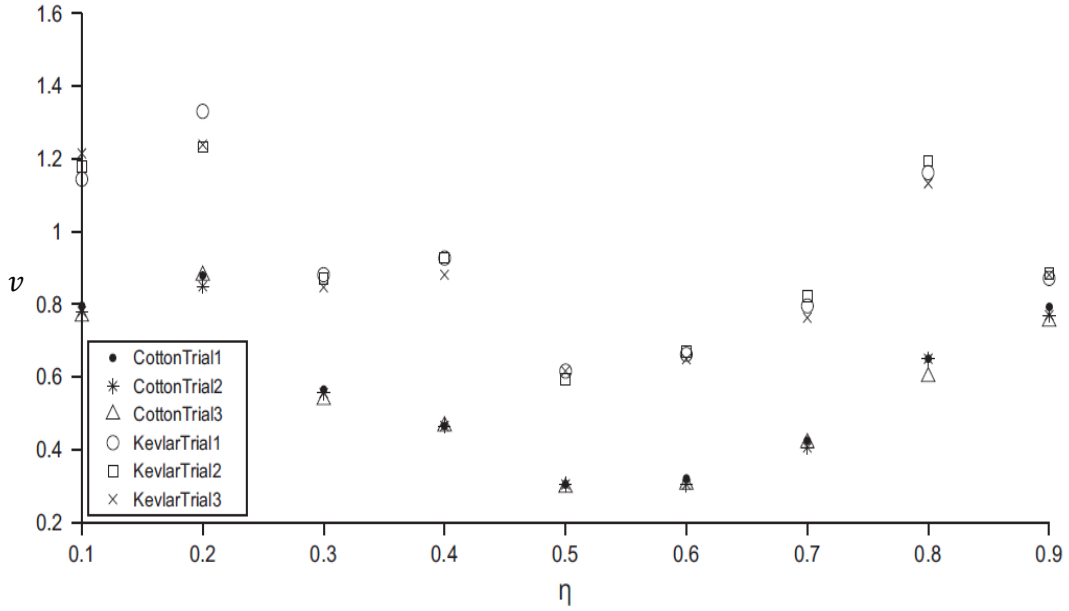

Figure C.1: Normalized critical flutter speed ($\boldsymbol{v}$) against normalized hinge position ($\boldsymbol{\eta}$) for Kevlar and cotton-hinged beams.

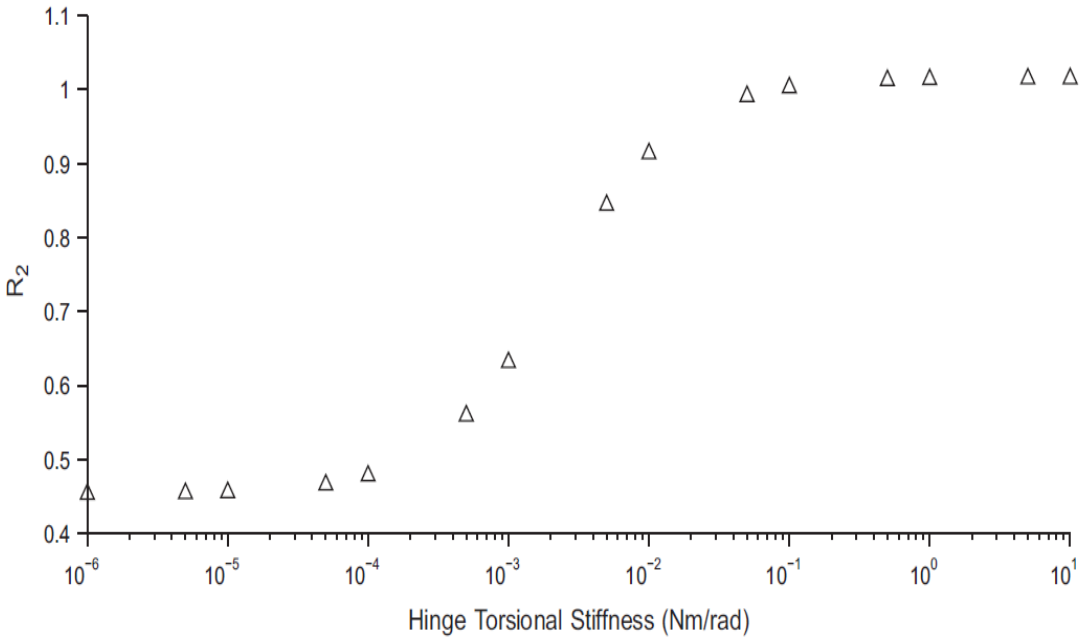

Figure C.2: Normalized frequency ratio (R_2) against torsional hinge stiffness for $\boldsymbol{\eta}$ = 0.5

Appendix D

User-defined codes for electromechanical analysis in ANSYS®

Since piezoelectric analysis is not a readily available feature in ANSYS® R14 workbench, certain user-defined functions were inserted to impart electromechanical and structural properties of PVDF to the material, and to model the electrical loading for post-processing of the power output results. These commands are listed below:

```
/gopr  ! RESUME LISTING TO SOLUTION OUTPUT
C--------------------------------------------------------------------
C-------- DEFINE PIEZOELECTRIC ELEMENT TYPE-----------------------------
C--------------------------------------------------------------------
et,matid,226,1001       ! PIEZOELECTRIC ELEMENT TYPE
C--------------------------------------------------------------------
C------------ DENSITY (Kg/m3) ----------------------------------------
C--------------------------------------------------------------------
rho = 1780
C--------------------------------------------------------------------
C-------- ISOTROPIC ELASTIC MODULUS (N/m2) -----------------------------
C--------------------------------------------------------------------
modulus = 3.0e9
C--------------------------------------------------------------------
C----------------- POISSON'S RATIO (-) -----------------------------------
C--------------------------------------------------------------------
poisson = 0.34
C--------------------------------------------------------------------
C-------------- DIELECTRIC CONSTANTS (PERMITTIVITIES) (F/m) --------------
C--------------------------------------------------------------------
ep11 = 1.13e-10/8.854e-12
                ep22 = 1.13e-10/8.854e-12
                                ep33 = 1.13e-10/8.854e-12
C--------------------------------------------------------------------
C---------- PIEZOELECTRIC MATRIX VALUES (C/m2) --------------------------
C--------------------------------------------------------------------
e11 = 0          $e12 = 0          $e13 = 0
e21 = 0          $e22 = 0          $e23 = 0
e31 = 0.216      $e32 = 0.003            $e33 = -0.33
e41 = 0          $e42 = 0          $e43 = 0
e51 = 0          $e52 = 0          $e53 = 0
e61 = 0          $e62 = 0          $e63 = 0
C--------------------------------------------------------------------
```

```
C--- DELETE PREEXISTING MATERIAL PROPERTIES ASSIGNED TO THIS BODY
C--------------------------------------------------------------------------
mpde,all,matid
tbde,all,matid
C--------------------------------------------------------------------------
C------- ASSIGN VALUES DEFINED ABOVE TO THIS BODY ------------------------
C--------------------------------------------------------------------------
mp,perx,matid,ep11
mp,pery,matid,ep22
mp,perz,matid,ep33
tb,piez,matid,,18
tbdata,1,e11,e12,e13,e21,e22,e23
tbdata,7,e31,e32,e33,e41,e42,e43
tbdata,13,e51,e52,e53,e61,e62,e63
mp,dens,matid,rho
mp,ex,matid,modulus
mp,nuxy,matid,poisson
/nopr  ! DISCONTINUE LISTING TO SOLUTION OUTPUT

C--------------------------------------------------------------------------

!    Commands inserted into this file will be executed just prior to the
Ansys SOLVE command.
!   These commands may supersede command settings set by Workbench.
!    Active UNIT system in Workbench when this object was created:  Metric
(m, kg, N, s, V, A) with temperature units of C
/prep7
ddel,all,volt
!
et,30,CIRCU94,0
r,30,5e6
!
cmsel,s,terminal1,node
cp,next,volt,all
*get,term1_node,node,0,num,min
cmsel,s,terminal2,node
cp,next,volt,all
*get,term2_node,node,0,num,min
!
type,30 $ real,30
e,term1_node,term2_node
!
outres,esol,all
!
fini
/solu
```

Appendix E

Flasher and sequencer circuit

A 555 Timer is generally used to generate a pulse of required frequency. However, since the current produced from the harvesters were very low, it was important to opt for more efficient electronic devices. In this regard, a simple comparator (LMC7215) was used to produce a positive signal for 10 ms, every 2 seconds (duty cycle - 0.5%). By using this comparator, an average current of only 6 μA was consumed. The flasher circuit is shown in Figure E.1. In order to have the letters of RMIT flashing, one at a time, a 4017 decade counter and AND gates were used (circuit diagram shown in Figure E.2). Each letter had 10 LEDs, consisting of two sets of 5 serial LEDs, connected in parallel. Although the circuit worked for demonstration purposes, the author acknowledges that the efficiency of the circuit could be further increased by designing specific ULP devices for practical lighting purposes.

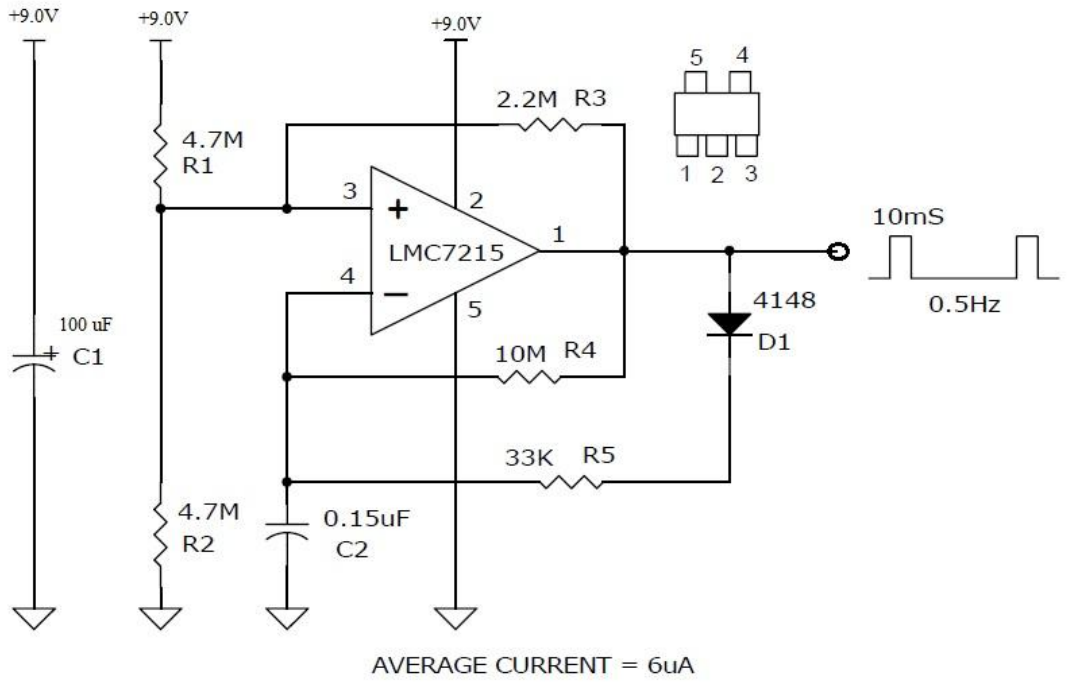

Figure E.1: Flasher circuit for proof-of-concept experiment (adapted from: http://discovercircuits.com; designed by: Dave Johnson)

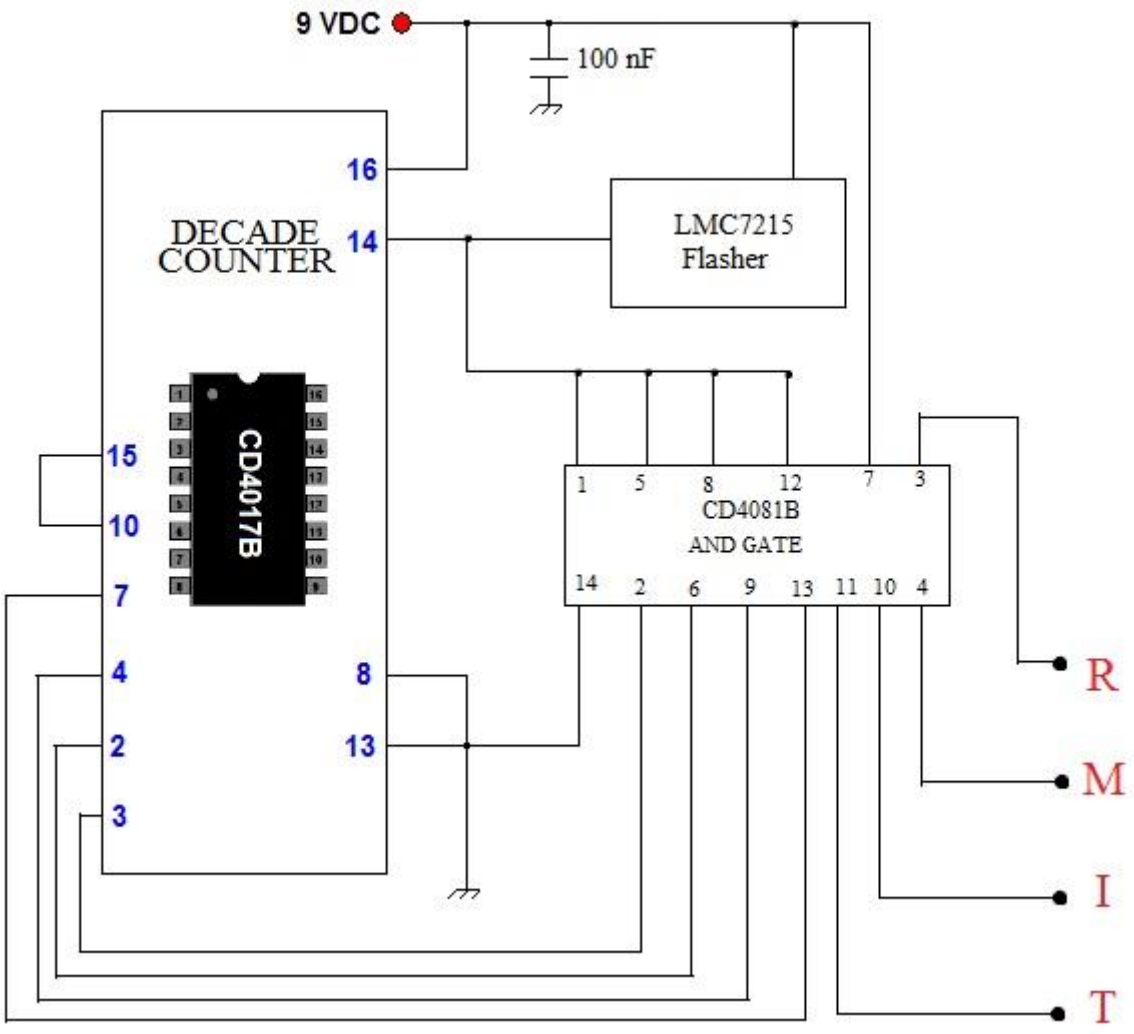

Figure E.2: Circuit for "RMIT" flashing and sequencing.

References

Abdelkefil, A, Najar1, F, Nayfeh, AH and Ben AS 2011, 'An energy harvester using piezoelectric cantilever beams undergoing coupled bending–torsion vibrations'. *Journal of Smart Materials and Structures*, Vol. 20, 115007 (11pp).

Akaydin, HD, Elvin, N & Andreopoulis, Y 2010, 'Energy harvesting from highly unsteady fluid flows using piezoelectric materials', *Journal of Intelligent Material Systems and Structures*, vol. 21, 1263–1278.

Akhtar, I., Mittal, R., Lauder, GV. and Drucker, E 2007, 'Hydrodynamics of a biologically inspired tandem flapping foil configuration', *Theoretical and Computational Fluid Dynamics*, Vol. 21, 155-170.

Alben, S., Shelley, M.J. 2008, 'Flapping states of a flag in an inviscid fluid: bistability and the transition to chaos'. *Physical Review Letters* 100 (7). 074301-1-4.

Allen, JJ. and Smits, AJ 2001, 'Energy harvesting eel', *Journal of Fluids and Structures*, vol. 15, no. 3-4, 629–640.

Allen, JJ & Smits, AJ 2001, 'Energy harvesting eel', *Journal of Fluids and Structures*, vol. 15, no. 3-4, 629–640.

Anton, RS, Sodano, AH 2007, 'A Review of Power Harvesting Using Piezoelectric Materials', *Smart materials and structures*, 16, R1-R21.

ANSYS® 2010. Mechanical, Release 13.0, no. Theory Reference: Eigen value and Eigen vector Extraction in Help System, ANSYS, Inc.

APC Internationa;, Ltd., *'Piezoelectric Constants'*, URL: https://www.americanpiezo.com/knowledge-center/piezo-theory/piezoelectric-constants.html, viewed: 25/2/2014.

Argentina, M & Mahadevan, L 2005, 'Fluid-flow-induced flutter of a flag', *Proceedings of the National Academy of Sciences of the United States of America*, vol. 102, no. 6, 1829–34.

Baker, J, Roundy, S and Wright, P 2005, 'Alternative geometries for increasing power density in vibration energy scavenging for wireless sensor networks', *Proc. 3rd Int. Energy Conversion Engineering Conf. (San Francisco, CA, Aug.),* pp 959–70.

Baker, J, Roundy, S and Wright, P 2005, 'Alternative geometries for increasing power density in vibration energy scavenging for wireless sensor networks', *Proc. 3rd Int. Energy Conversion Engineering Conf. (San Francisco, CA, Aug.),* pp 959–70.

Beards CF 1996. *Structural Damping: Analysis and Damping*. Elsevier, ISBN: 978-0-340-64580-2.

Betz, A. 1966, Introduction to the Theory of Flow Machines, (D. G. Randall, Trans.) Oxford: Pergamon Press.

Blevins, R.D. 1979, *'Formulas for Natural Frequency and Mode Shape'*. ISBN: 0-442-20710-7, Van Nostrand Reinhold Company, New York.

BP statistical review of world energy, 2007: http://www.neb-one.gc.ca/clf-nsi/rnrgynfmtn/nrgyrprt/nrgyftr/2007/nrgyftr2007chptr2-eng.html

Bryant, M, Mahtani, R & Garcia, E 2011, 'Synergistic wake interactions in aeroelastic flutter vibration energy harvester arrays', In *ASME Conference on Smart Materials, Adaptive Structures and Intelligent Systems, SMASIS*, September 18 - September 21, American Society of Mechanical Engineers, Scottsdale, AZ, United States.

Bryant, M, Mahtani, RL & Garcia, E 2012, 'Wake synergies enhance performance in aeroelastic vibration energy harvesting', *Journal of Intelligent Material Systems and Structures*, vol. 23, no. 10, 1131 – 1141.

Burton, T, Sharpe, D, Jenkins, N & Bossanyi, E 2001, *Wind Energy Handbook*, ISBN:978-0-471-48997-9, John Wiley & Sons.

Cady, WG 1964, *'Piezoelectricity: An Introduction to the theory and applications of electromechanical phenomena in crystals*', Dover Publications, New York, 1-20.

Churchill, DL, Hamel, MJ, Townsend, CP & Arms, SW 2003, 'Strain energy harvesting for wireless sensor networks', In *Smart Structures and Materials 2003. Smart Electronics, MEMS, BioMEMS, and Nanotechnology*, 3-5 March, vol. 5055, SPIE-Int. Soc. Opt. Eng, USA, pp. 319–27.

Connell, BSH & Yue, DKP 2007, ‘Flapping dynamics of a flag in a uniform stream’, *Journal of Fluid Mechanics*, vol. 581, 33–67.

CSE India, 2011: http://capitalmind.in/2012/03/fuel-prices-must-in-the-budget/

Datta S.K. and Gottenberg W.G. 1975, 'Instability of an elastic strip hanging in an airstream'. *Journal of Applied Mechanics*, Vol. No. 42, pp 195–198.

Dickson, R 2008, *New Concepts in Renewable Energy*, Lulu Enterprises, Inc.

Dosch, JJ, Inman, DJ & Garcia, E 1992, ‘A self-sensing piezoelectric actuator for collocated control’, *Journal of Intelligent Material Systems and Structures*, vol. 3, no. 1, 166–185.

Dragon, D 1998, 'Ferroelectric, dielectric and piezoelectric properties of ferroelectric thin films and ceramics', *rep. Prog. Phys.*, 61(9), 1267-1324.

Eloy C, Souilliez C. and Schouveiler L. 2006, 'Flutter of a rectangular cantilevered plate'. *Proceedings of the Sixth FSI, AE & FIV + N Symposium, ASME PVP 2006/ICPVT-11 Conference*. Vancouver, Canada.

Encraft 2009, Final Report (Warwick Microwind Trial project), Tech. rep., URL http://www.warwickwindtrials.org.uk/2.html, viewed (28/12/2011).

Erturk, A and Inman, D 2011, *'Piezoelectric Energy Harvesting'*, John Wiley & Sons, Ltd., United Kingdom.

Erturk, A. and Inman, D.J. 2008. 'On Mechanical Modeling of Cantilevered Piezoelectric Vibration Energy Harvesters', *Journal of Intelligent Material Systems and Structures*, 19:1311_1325.

Erturk, A. and Inman, DJ 2008, ‘Issues in Mathematical Modeling of Piezoelectric Energy Harvesters', *Smart Materials and Structures*, 17:065016 (14pp).

Gipe, P 2003, ‘*Noise from small wind turbines: An unaddressed issue*’, URL: www.wind-works.org/articles/noiseswt.html, viewed (2/1/2012).

Golding, EW 1955, ‘Electrical energy from the wind’, in *Proceedings of the IEEE - Part A: Power Engineering*, vol. 102, pp. 677–687.

Grimes, R.G., Lewis, J.G., Simon, H.D. 1994. 'A shifted block lanczos algorithm for solving sparse symmetric generalized eigenproblems'. *SIAM Journal on Matrix Analysis and Applications* 15 (1), 228–272.

Guan, MJ and Liao, WH 2007, 'On the efficiencies of piezoelectric energy harvesting circuits towards storage device voltages', *Smart Mater. Struct.*, 16, 498–505.

Guyomar, D, Badel, A, Lefeuvre, E and Richard, C 2005,'Toward Energy Harvesting Using Active Materials and Conversion Improvement by Nonlinear Processing', IEEE Transactions On Ultrasonics, Ferroelectrics, And Frequency Control, vol. 52, no. 4.

Hermann von Helmholtz 1868, 'On the discontinuous movements of fluids', *Monthly Reports of the Royal Prussian Academy of Philosophy in Berlin*, 23: 215–228.

Hobeck, DJ, Inman, JD 2011, 'Energy harvesting from turbulence-induced vibrations in air flow: Artificial piezoelectric grass concept', In *ASME Conference on Smart Materials, Adaptive Structures and Intelligent Systems, SMASIS*, September 18 - September 21, American Society of Mechanical Engineers, Arizona, United states, No. 5053.

Huang, L 1995, 'Flutter of cantilevered plates in axial flow', *Journal of Fluids and Structures*, vol. 9, 127–147.

IPCC 2007a, Climate Change 2007: Synthesis Report - Contribution of Working Groups I, II and III to the Fourth Assessment Report of the Intergovernmental Panel on Climate Change, Tech. rep., Intergovernmental Panel on Climate Change (IPCC).

Jun, Z, Childress, S, Libchaber, A & Shelley, M 2000, 'Flexible filaments in a flowing soap film as a model for one-dimensional flags in a two-dimensional wind', *Nature*, vol. 408, 8359.

Karami, AM, Farmer, RJ, Bressers, S, Priya, S, Inman, JD 2011, 'Parametrically excited non-linear piezoelectric wind energy harvester', In *ASME Conference on Smart Materials, Adaptive Structures and Intelligent Systems, SMASIS*, September 18 - September 21, American Society of Mechanical Engineers, Arizona, United states, No. 5042.

Kholkin, A, Jadidian, B, Safari, A 2002, In *'Encyclopedia of Smart Materials*', Schwartz, MM (Eds.), ISBN: 0-471-17780-6, John Wiley & Sons, Inc. New York, Vol. 1, 139-148.

Kong, N, Ha, DS, Erturk, A and Inman, DJ 2010,'Resistive Impedance Matching Circuit for Piezoelectric Energy Harvesting', *Journal of Intelligent Material Systems and Structures,* 21: 1293.

Kornecki, A, Dowell, EH & O'Brien, J 1976, 'On the aerodynamic instability of two-dimensional panels in uniform incompressible flow', *Journal of Sound and Vibration,* vol. 47, no. 2, 163–178.

Kundu, P and Cohen , I 2002, '*Fluid Mechanics*', Academic press, page 130.

Lee, CS, Joo, J, Han, S and Koh, SK 2004, 'Multifunctional transducer using polyvinylidene fluoride active layer and highly conducting poly-3,4-ethylenedioxythiophene electrode: actuator and generator', *Appl. Phys. Lett,.* 85, 1841–3.

Lee, CS, Joo, J, Han, S, Lee, JH and Koh, SK 2005, 'Polyvinylidene fluoride transducers with highly conducting poly-3,4-ethylenedioxythiophene electrodes', *Proc. Int. Conf. on Science and Technology of Synthetic Metals,* vol. 152, pp 49–52.

Li, S & Lipson, H 2009, 'Vertical-stalk flapping-leaf generator for wind energy harvesting', In *ASME Conference on Smart Materials, Adaptive Structures and Intelligent Systems, SMASIS2009,* September 21 - September 23, vol. 2, American Society of Mechanical Engineers, Oxnard, CA, United states, pp. 611–619.

Li, S, Yuan, J and Lipson, H 2011. 'Ambient wind energy harvesting using cross flow fluttering'. *Journal of Applied Physics*, 109, 026104.

Lord Kelvin 1871, 'Hydrokinetic solutions and observations'. *Philosophical Magazine* 42:362–377.

Lord Rayleigh, 1879, Proceedings of the London Mathematical Society, vol. X, pp. 4–13.

Mateu, L and Moll, F 2005, 'Optimum piezoelectric bending beam structures for energy harvesting using shoe inserts'. *J. Intell. Mater. Syst. Struct.*, 16, 835–45.

MATLAB®, 2010. Numerical Algorithms, MUPad Help Manual, SciFace Software GmbH & Co. KG.

McCarthy, JM, Deivasigamani, A, John, SJ, Watkins, S and Coman, F 2012. 'The Effect Of The Configuration Of The Amplification Device On The Power Output Of A

Piezoelectric Strip'. *ASME conference Smart Materials, Adaptive Structures and Intelligent Systems (SMASIS)*, Georgia, United States, SMASIS2012-7951.

McCarthy, JM, Deivasigamani, A, John, SJ, Watkins, S, & Coman, F 2013, 'Energy Harvesting from Flows Using Piezoelectric Patches', Chapter in *Non-linear Approaches in Engineering Applications*, Springer publications, Editors - Reza Jazar & Liming Dai, Springer Publications.

McCarthy, JM, Deivasigamani, A, Watkins, S, John, S, Coman, F, & Petersen, P 2013, 'Downstream flow structures of a fluttering piezoelectric energy harvester', *Experimental Thermal and Fluid Science*, 51: 279 - 290.

McCarthy, J, Deivasigamani, A, Watkins, S, John, S, Coman, F, & Petersen, P 2014, 'On the visualization of flow structures downstream of fluttering piezoelectric energy harvesters in a tandem configuration', *Experimental Thermal and Fluid Science*, 57: 407 - 419.

McCarthy, J, Deivasigamani, A, Watkins, S, John, S, & F. Coman 2013, 'A parametric study of wind-induced flutter of piezoelectric patches for energy harvesting'. In *15th Australian International Aerospace Congress, AIAC15*, Paper No. 194, Melbourne, Australia.

Nam, Y & Sasaki, M 2002, 'Strain rate self-sensing for a cantilevered piezoelectric beam', *KSME International Journal*, vol. 16, no. 3, 310–319.

Ng, TH and Liao, WH 2004, 'Feasibility study of a self-powered piezoelectric sensor', *Proc. Smart Structures and Materials Conf.*; *Proc. SPIE*, 5389, 377–88.

Ng, TH and Liao, WH 2005, 'Sensitivity analysis and energy harvesting for a self-powered piezoelectric sensor *J. Intell. Mater. Syst. Struct.*, 16, 785–97.

Ottman, GK, Hofmann, HF, Bhatt, AC and Lesieutre, GA 2002, 'Adaptive Piezoelectric Energy Harvesting Circuit for Wireless Remote Power Supply', IEEE Transactions On Power Electronics, Vol. 17, No. 5.

Paidoussis, M 1998, *'Fluid-Structure Interactions - Slender Structures and Axial Flow'*, Vol. 1, Elsevier Academic Press.

Païdoussis M. 2004, *Fluid-Structure Interactions - Slender Structures and Axial Flow.* Vol. No. 2, Elsevier Academic Press.

Piezo Systems, Inc., *'Piezo terminology*' , URL: http://www.piezo.com/tech1terms.html, Viewed: 25/2/2014.

Pobering, S & Schwesinger, N 2004, 'A novel hydropower harvesting device', In *International Conference on MEMS, NANO and Smart Systems, ICMENS 2004*, August 25 - August 27, IEEE Computer Society, Banff, Alta., Canada, pp. 480–485.

Porritt 2006. 'Sustainable development', diagram at Cornell Sustainability Campus: http://www.sustainablecampus.cornell.edu/csi.cfm

PPC 2009, 'Polymer Plastics Company, LC', URL http://www.polymerplastics.com, viewed: 1/4/2011.

Priya S, Chen C T, Fye D and Zahnd J 2005, 'Piezoelectric windmill: A novel solution to remote sensing' *Japan. J. Appl. Phys.* 244 L104–7

Priya, S 2005, 'Modeling of electric energy harvesting using piezoelectric windmill', *Appl. Phys. Lett.* 87, 184101.

Priya, S 2007, 'Advances in energy harvesting using low profile energy harvesters', *Journal of Electroceramics*, 19, 165-182.

Priya, S, Chen, CT, Fye, D and Zahnd, J 2005, 'Piezoelectric windmill: A novel solution to remote sensing', *Japan. J. Appl. Phys.* 244 L104–7.

Raju, M 2008, '*Energy Harvesting: ULP Meets Energy Harvesting*', URL: www.ti.com/corp/docs/landing/cc430/graphics/slyy018 20081031.pdf.

Ramadass, KY and Chandrakasan, AP 2010, 'An Efficient Piezoelectric Energy Harvesting Interface Circuit Using a Bias-Flip Rectifier and Shared Inductor', *IEEE Journal Of Solid-State Circuits*, VOL. 45, NO. 1, 189-204.

Rastegar, J, Pereira, C and Nguyen, HL 2006, 'Piezoelectric-based power sources for harvesting energy from platforms with low frequency vibration', *Proc. Smart Structures and Materials Conf.*; *Proc. SPIE,* 6171, 617101.

Renewable Energy Policy Network for 21st century (REN21) 2013, *'Renewables Global Status Report*', URL: http://www.ren21.net/gsr

Roundy, S and Wright, PK 2004, 'A piezoelectric vibration based generator for wireless electronics', *Smart Mater. Struct.* 13, 1131–42.

Roundy, S, Leland, ES, Baker, J, Carleton, E, Reilly, E, Lai, E, Otis, B, Rabaey, J, Wright, PK and Sundararajan, V 2005, 'Improving power output for vibration-based energy scavengers', *IEEE Pervasive Comput.* 4, 28–36.

Roundy, S, Wright, PK and Rabaey, J 2003, 'A study of low level vibrations as a power source for wireless sensor nodes', *Comput. Commun.* 26, 1131–44.

Shu, YC, Lien, IC 2006, 'Analysis of power output for piezoelectric energy harvesting system', *Smart Materials and Structures*, 15, 1499-1512.

Sirohi, J and Mahadik, R 2011, 'Piezoelectric wind energy harvester for low-power sensors', *Journal of Intelligent Materials Systems and Structures (JIMSS)*, 22, 2215.

Smart Material Corp. 2012, URL: www.smart-material.com/MFC-product-main.html

Sodano, HA, Park, G. and Inman DJ 2001. 'Estimation of electric charge output for piezoelectric energy harvesting'. *Strain*, Vol. 40, 49-58.

Sodano, HA, Inman, DJ and Park, G 2005a, 'Comparison of piezoelectric energy harvesting devices for recharging batteries', *J. Intell. Mater. Syst. Struct.*, 16, 799–807.

Sodano, HA, Park, G and Inman, DJ 2004, 'Estimation of Electric Charge Output for Piezoelectric Energy Harvesting', Strain, 40, 49–58.

Taylor, GW, Burns, JR, Kammann, SM, Powers, WB and Welsh, TR, 2001, 'The energy harvesting eel: A small subsurface ocean/river power generator', *IEEE Journal of Oceanic Engineering*, vol. 26, no. 4, 539–547.

Theodore von Kármán 1963, Aerodynamics, McGraw-Hill: ISBN 978-0-07-067602-2. Dover (1994): ISBN 978-0-486-43485-8.

Theodorsen, T., 1935, 'General Theory of Aerodynamic Instability and the Mechanism of Flutter', Technical Report No. 496, *National Advisory Committee for Aeronautics*.

Timoshenko, SP 1953, *'Strength of Materials*', McGraw-Hill, New York.

Van Dyke, M 1982, *An Album of Fluid Motion*, The Parabolic Press, Stanford, California.

Watanabe Y, Isogai K, Suzuki S, and Sugihara M. 2002a, 'A theoretical study of paper flutter'. *Journal of Fluids and Structures*. Vol. No. 16 (4), pp 543–560.

Watanabe Y, Suzuki S, Sugihara M, and Sueoka Y. 2002b, 'An experimental study of paper flutter'. *Journal of Fluids and Structures*. Vol No. 16 (4), pp 529–542.

Weaver Jr.W, Timoshenko, SP and Young, DH 1990. *Vibration problems in engineering*. Fifth edition, John Wiley and Sons, Ltd.

Webb, A 2007, *The Viability of Domestic Wind Turbines for Urban Melbourne*, Tech. rep., Alternative Technology Association.

Welch, P 1967, 'The use of fast fourier transform for the estimation of power spectra: A method based on time averaging over short, modified periodograms.', *IEEE Trans. Audio Electroacoust.*, vol. AU-15, 70–73.

Wilson, A 2009, '*The folly of building-integrated wind*', URL: http://www.buildinggreen.com/auth/article.cfm/2009/4/29/The-Folly-of-Building-Integrated-Wind, viewed (2/1/2012).

World Commission on Environment and Development 1987, *Our Common Future*, Oxford: Oxford University Press. p. 27. ISBN 019282080X.

WWEA 2011, *World Wind Energy Report 2010*, Tech. rep.,WorldWind Energy Association, Bonn, Germany.

Yamaguchi, N, Sekiguchi, T, Yokota, K & Tsujimoto, Y 2000a, 'Flutter limits and behaviours of a flexible thin sheet in high-speed flow–II: experimental results and predicted behaviours for low mass ratios', *ASME Journal of Fluids Engineering*, vol. 122, 74–83.

Yamaguchi, N, Yokota, K & Tsujimoto, Y 2000b, 'Flutter limits and behaviours of a flexible thin sheet in high-speed flow–I: analytical method for prediction of the sheet behaviour', *ASME Journal of Fluids Engineering*, vol. 122, 65–73.

YTC America Inc. 2008, Structure of PZT. JPEG, URL: http://www.ytca.com/lead_free_piezoelectric_ceramics, viewed: 28/11/2012.

Zhang, QM, Bharti, V, Kavarnos, G, Schwartz, M 2002, 'Poly-vinylidene fluoride (PVDF) and its copolymers' In: *Encyclopedia of smart materials*, Vols 1-2, Wiley, New York, pp 807-825.

Zhu, X 2010, 'Piezoelectric Ceramics Materials: Processing, Properties, Characterization and Applications', In: *Piezoelectric Materials: Structure, Properties and Applications*, Nelson WG (Eds.), ISBN: 978-1-60876-272-9, Nova Science Publishers, Inc., New York, 1-34.